Physical and chemical aspects of A10(_x)/PET gas barrier composites

Barker, Campbell Preston

University of Durham

A Thesis entitled

Physical and Chemical Aspects of AlO_x/PET Gas Barrier Composites

submitted by

Campbell Preston Barker
B.Sc. (Dunelm)

A candidate for the degree of Doctor of Philosophy

Hatfield College, September 1994.

PHYSICAL AND CHEMICAL ASPECTS OF AlO_X/PET GAS BARRIER COMPOSITES

Campbell P. Barker, submitted for the Degree of Doctor of Philosophy

---

Variable stoichiometry aluminium oxide (AlO_X)/polyethylene terephthalate (PET) gas barrier films, deposited using an adapted metallization chamber *via* controlled oxygen introduction, have been studied. Products of the metallization (Al/PET) and reactive evaporation processes (metal- and oxygen-rich AlO_X/PET) were analyzed to determine the effect of oxygen introduction upon chemical and physical properties.

Permeability measurements determined that better gas barriers were associated with metal/oxide interfaces in both Al/PET and metal-rich AlO_X/PET as determined by X-ray photoelectron spectroscopy (XPS). Oxygen-rich AlO_X/PET contains no free metal.

Oxide species detected in the reactively evaporated films arise from the gas phase reaction of aluminium with oxygen; the similarity between analyses of the gas phase reactions by optical emission spectroscopy (OES) corresponds to similar interfacial chemistries. Morphologies of these layers (*via* atomic force microscopy) at the micrometer scale are characteristic of the PET base film, while at the sub-micrometer level fine-grained deposits typical of thin film deposition under moderate vacuum are observed.

Layer chemistry dictates the performance of the composites under uniaxial stretching. Al/PET's more ductile 'metallic' interface results in greater 'stretchability' prior to gas barrier loss than the purely oxide system. Metal-rich AlO_X/PET exhibits intermediate behaviour because of the free metal in its subsurface. All coatings exhibit cracking at 3% elongation. Oxygen-rich AlO_X/PET's gas barrier degenerates at low degrees of stretching (< 2%): it can be 'healed' by exposure to water vapour and oxygen. Metal-rich AlO_X/PET cannot.

Polypropylene surface chemistry (XPS) and morphology (AFM) after corona treatment have been modified by the introduction of a low molecular weight saturated hydrocarbon resin to the films. The level of oxygen incorporation is only slightly affected whereas the size of the globules associated with corona discharge treatment is reduced.

To all sources of inspiration

"The philosophers have only interpreted the world in various ways; the point is to change it."

Karl Marx

" The shadows are lengthening for me. The twilight is here. My days of old have vanished tone and tint; they have gone glimmering through the dreams of things that were. Their memory is one of wondrous beauty, watered by tears, and coaxed and caressed by the smiles of yesterday. I listen vainly, but with thirsty ear, for the witching melody of faint bugles blowing reveille, of far drums beating the long roll. In my dreams I hear again the crash of guns, the rattle of musketry, the strange mournful mutter of the battlefield. But in the evening of my memory, always I come back to West Point. Always there echoes and re-echoes in my ears - Duty - Honour - Country."

General Douglas MacArthur

" One of the greatest pains to human nature is the pain of a new idea."

Walter Bagehot

MEMORANDUM

- The work in this thesis was carried out at the University of Durham between September 1991 and August 1994. Except where acknowledged by reference, it is the original work of the author and has not been submitted for any other degree.

- The copyright rests with the author. No part of this thesis should be reproduced without the author's prior written permission, and any information taken from the thesis should be acknowledged.

- Results arising from this work have been submitted to the following journals as papers:

  - An AFM and Permeability Study of Stretching-induced Gas Barrier Loss of AlO_x Layers, C. P. Barker, K.-H. Kochem, K. M. Revell, R. S. A. Kelly, J. P. S. Badyal, submitted to *Thin Solid Films*.

  - The Interfacial Chemistry of Metallized, Oxide Coated, and Nanocomposite Coated Polymer Films, C. P. Barker, K.-H. Kochem, K. M. Revell, R. S. A. Kelly, J. P. S. Badyal, submitted to and accepted by *Thin Solid Films*.

Other publications:

- Plasma-enhanced Chemical Vapour Deposition of TiO_2/Polymer Composite Layers, P. J. Ratcliffe, J. Hopkins, A. D. Fitzpatrick, C. P. Barker, J. P. S. Badyal, *J. Mater. Chem.* 4 (1994), 1055.

- The Growth and Reactive Ion Etching of Organosilicon Plasma Polymers, J. L. C. Fonseca, S. Tasker, C. P. Barker, J. P. S. Badyal, *Proceedings of the International Symposium on Plasma Polymerization/Deposition: Fundamental and Applied Aspects* (1993), 20.

- Glow Discharge Oxidation of Plasma Polymerized Organosilicon Layers, J. L. C. Fonseca, C. P. Barker, J. Hopkins, J. P. S. Badyal, submitted to *Chemistry of Materials*.

- Glow Discharge Oxidation of Polycyclohexamethylsilane and Polyphenylmethylsilane Thin Films, J. L. C. Fonseca, C. P. Barker, J. P. S. Badyal, submitted to *Chemistry of Materials*.

- Plasma Assisted Decomposition of Titanium Tetraisopropoxide, P. J. Ratcliffe, J. Hopkins, A. D. Fitzpatrick, C. P. Barker, J. P. S. Badyal, *Proc. Int. Symp. Plasma Chem. 11* (1993), 1154.

PERSONAL ACKNOWLEDGEMENTS

- Barrie and Pauline for their determination, sacrifice and, most importantly, giving me every opportunity to learn;

- Dr. Jas Pal Badyal, my supervisor, for giving me the opportunity to carry out this research. Roger Kelly, Bob Kimmel, Karl-Heinz Kochem, Gunther Schloegl, Nils Nilsson and Ken Revell for an enjoyable introduction into industrial research. Their respective companies, Camvac (Europe) Limited and Hoechst Aktiengesellschaft, for their interest and support;

- Everyone in Lab. 98, past and present, for their help, support and humour: Rachel, Phil, Ze, Christiane, Pete, Simon, Gav, Janet, Olly, Martin, Beth, Alan, Vicki, Susanne, Colin and Rob;

- D.U.W.B.C 1992-3;

- John, Tim, Al and Tex for true education, hospitality and a host of good times too numerous and dangerous to mention;

- Procter & Gamble for their confidence in me, and giving me the job I wanted;

- Finally, to all of the moulders of my character through experience, teaching and conversation. I owe special debts to John Lever, Andrew Wolters, John Kerr , David Conner and Carole Seheult.

ACKNOWLEDGEMENTS

Experimental work not undertaken by the author:

- Sample deposition performed by Mr. Ken Revell and his colleagues at Camvac (Europe) Limited;

- Electron microscopy (Chapter 1) carried out at Hoechst AG, Werk Kalle-Albert, Wiesbaden, Germany courtesy of Dr. Karl-Heinz Kochem and colleagues;

- Atomic force micrographs (Chapters 4, 6 and 7) accumulated by Dr. Jas Pal Badyal, Chemistry Department, University of Durham;

- Optical emission spectra (Chapter 5) courtesy of Ms. Anne Byrnes, Rees Instruments Limited;

- Stretched gas barrier samples (Chapter 6) provided by Dr. Karl-Heinz Kochem and colleagues, Hoechst AG, Werk Kalle-Albert, Wiesbaden, Germany;

- Resin-containing polypropylene films (Chapter 7) prepared at Hoechst AG, Werk Kalle-Albert, Wiesbaden, Germany courtesy of Dr. Karl-Heinz Kochem and colleagues.

TABLES OF CONTENTS

CHAPTER 1

INTRODUCTION 1-31

CHAPTER 2

PERMEABILITY OF AlO_x/PET FILMS 32-61

CHAPTER 3

AN XPS STUDY OF THE SURFACE AND INTERFACIAL CHEMISTRY OF AlO_X/POLYMER FILMS 62-103

CHAPTER 4

ATOMIC FORCE MICROSCOPY OF AlO_x/PET FILMS

104-122

CHAPTER 5

OPTICAL EMISSION SPECTROSCOPY OF AlO_x THIN FILM DEPOSITION 123-148

CHAPTER 6

PROCESS-RELATED GAS BARRIER DETERIORATION OF AlO_x/PET FILMS 149-178

CHAPTER 7

POLYPROPYLENE SURFACE ENGINEERING *VIA* RESIN ADDITION AND CORONA TREATMENT 179-208

CHAPTER 8

CHAPTER 1

INTRODUCTION

The aim of this thesis is to show that the chemical and physical properties of gas barrier films deposited onto flexible polyethylene terephthalate (PET) films by metallization with aluminium can be modified by the introduction of oxygen into the evaporant stream. Reactive evaporation produces AlO_X/PET composites with variable 'x' [1]. Many techniques have been used to identify the mechanisms through which such changes are effected by the reactive evaporation process. This work was performed under the European Commission's BRITE/EURAM programme, the aim of which is to foster international co-operation between companies and academia in areas of strategic commercial importance. In this instance, Camvac (Europe) Limited's patented process [1] is designed to compete with gas barrier packaging systems developed in Japan and the United States of America [2]. Hoechst Aktiengesellschaft and the University of Durham complete the project team.

The packaging industry has recently progressed from a reliance upon aluminium foil and metallized polymers [1] to more advanced, transparent oxide coatings [3-12] such as SiO_2, SiO_X, and Al_2O_3. Oxide coated polymer films are of commercial interest since they offer a number of advantages over conventional metallized plastics for gas barrier applications, including transparency for easier product identification, microwave transparency, and potential recyclability [7]. Silicon oxides are dominant in this sector of the market [12]. Such systems are typically deposited by plasma-enhanced techniques [4,5,7] which require completely different deposition apparatus

modifications to the conventional metallization process described herein that are academically and commercially appealing.

Metal-polymer interfaces represent the union of dissimilar structures: the close-packed structure of a metal and the loose, interwound structure of complex molecular units in a polymer [13]. As such they are of great academic and commercial interest. DiNardo [14] recently summarized the approach used in this area thus:

"The great potential to apply scientific discoveries in surface and interface science to microelectronics device and processing technology has been realized in many ways. Much of the scientific work has been focused on clean and adsorbate-covered metal and semiconductor surfaces. Surface chemists direct their attention towards catalytic processes and surface modification through chemistry. Surface physicists and materials scientists involved in microelectronics technology have concentrated much effort in understanding the growth and control of semiconductor surfaces and the formation of metal-semiconductor interfaces...

We identify another area of surface and interface research which has applied established surface science methods to advanced technological requirements - coupling surface chemical and structural investigations to macroscopic adhesion at the metal-polymer interface."

This approach is transferable to many emerging areas of materials technology. This author's aim is to transfer these ideas to the understanding of the effect of oxygen introduction into the process of conventional metallization.

Although this thesis does not aim to probe adhesion, the phenomena associated with work in that area are important. Most crucially, the concept of interphase formation upon coating deposition is central to the issues this author will be addressing. An interphase has a finite volume and distinct physical properties (or a gradient of properties) [15]. Properties such as stress transfer and permeation are thought to be interphase-dependent.

While some work has been performed upon metallized films for barrier applications [16-20], the authors have not examined the effect of

coating chemistry as influenced by introduction of oxygen into the process. Recent work on glassy oxide systems for the new generation of packaging materials [3-12] tends to be more related to announcing companies' capabilities and products than a true investigation of materials' properties for the understandable reason of maintaining the confidential nature of proprietary knowledge.

This thesis therefore represents a union of several areas of materials' science.

The structure of the thesis will now be introduced. Each chapter has associated with it a single phenomenon. The format is of self-contained units fitting together to make the whole as opposed to the more usual clustering of all experimental information in one chapter, all results in another, and so on. This author's aim is to maintain close proximity between background literature, experimental details, results, discussion and conclusions associated with each phenomenon.

The remainder of this introductory chapter is dedicated to a review of high rate coating techniques and their important parameters. Chapter 2 deals with gas transport phenomena associated with AlO_x/PET films. Chapters 3 and 4 probe the chemistry and morphology of the films, respectively. Chapter 5 probes gas phase mechanisms occurring during the deposition of the films *via* optical emission spectroscopy. Chapter 6 analyzes an important area of gas barrier composite performance, their resistance to stretching-induced gas barrier loss. Chapter 7 represents a natural development of the project into technology transfer from PET films to PP, and investigation of the parameters influencing the gas barriers of these films after AlO_x coating. Finally, Chapter 8 contains the conclusions and a proposed mechanism for the chemical and physical phenomena encountered in the preceding work.

1.1 METALLIZATION OF POLYMERS

Resistive evaporation of metals is one of the oldest methods of metallization, and it is still the most common [21]. The first evaporation experiments were performed by Faraday under a nitrogen atmosphere by passing an electric current through a wire. Deposits were poorly adhered to substrates, primarily because of the high pressures reducing the mean free path of the evaporating metal. Performing the experiments under vacuum, later workers (Pohl and Pringsheim, 1912) improved the nature of the deposit. World War II saw the demand for non-reflective optical coatings increase, and deposition technology was advanced to meet these requirements. Post-war development of polymer technology burgeoned, and the merging of these two technologies gave rise to vacuum metallization of polymers for many applications, some of which are listed below [21,22]:

- Decorative: automobile trim; decorations; jewellery; cosmetic caps; glassware; labels; and trophies.
- Electrical: audio/video tapes; capacitors; electrical contacts; electromagnetic radiation shielding; floppy discs; integrated circuits; resistors; and solar cells.
- Optical: architectural glass; camera lenses/filters; compact discs; headlamps; aeroplane canopies; mirrors; road reflectors; sunglasses; and telescopes.
- Physical: solid lubricants; food packaging, including microwave susceptors; corrosion resistance; and tool hardening.

Requirements for metallization are: (i) adequate vacuum for deposition; (ii) sufficient energy for source vaporization; and (iii) substrate manipulation such that adequate coverage is obtained [21].

The deposition rate for metallization is dependent upon the substrate material and temperature, the sticking coefficient of the condensing species to the substrate, and the probability of re-evaporation [23].

1.1.1 Resistive evaporation

Resistively heated vapour sources must be electrical conductors, have a melting point higher than that of the material to be evaporated, and a vapour pressure lower than it, as well as being chemically inert to the evaporant or other materials encountered during the deposition process [21]. Source heating is achieved by passing direct electrical current through the material, typically from a power supply rated at between 20 and 55 kW. The exact nature of the power supply characteristics will depend upon the number of evaporant sources and the source temperature required for deposition.

A plethora of suitable source materials are available for resistance heated sources but their precise suitability is process-dependent [21]. Refractory metals such as tungsten, molybdenum and tantalum are typically used for wire-based evaporant source designs since they have high melting points (especially tungsten) and low vapour pressures. Powders have to be contained, and are typically evaporated from a refractory 'boat' of these metals. Very large charges of evaporant, or evaporants which will react with the refractory boats, are contained in crucibles. Those for use with the latter category of evaporants are lined with a protective coating such as alumina or carbon.

latter category of evaporants are lined with a protective coating such as alumina or carbon.

All of these sources share the same disadvantage, namely that they are only capable of evaporating one charge of material before the process must be stopped and 'refuelled'. Many metallization processes are performed under semi-continuous operation, *i.e.*, the process is one of extended batch operation. Polymer film metallization uses such a technique; indeed, due to the length of industrial polymer film reels (typically many thousands of metres), operation in any other way would be unfeasible. Semi-continuous deposition requires a semi-continuous source of evaporant. This is achieved by using an automatic wire feed system in which evaporant is paid off from a coil onto the resistively heated source [21,22], typically an intermetallic 'boat' of boron nitride, titanium diboride and aluminium nitride mixed and pressed to give the desired resistivity [21].

Evaporation is a simple process. Its advantages are: a high deposition rate; relatively low equipment costs; and the use of simple materials as evaporants. To its disadvantage, evaporation is relatively hard to control and can deposit only a limited range of materials [22].

1.1.2 Coating growth

Classically the growth of evaporated films has been considered in terms of island or nucleus growth at favoured sites on the substrate [24]. High gas pressures can lead to decreases in the kinetic energy of the gaseous species and concomitant microstructure degradation. At sufficiently high pressures, small (nanometer-scale) particles are formed.

1.1.3 Uniformity of coating

Because of the directionality of evaporation [24,25], the mass deposited per unit area is dependent upon the angle of the receiving surface relative to the incident flux. Evaporative processes rely upon small area sources for the material to be deposited [22]; for the coating of flexible polymer film, for example, a homogeneous deposit is achieved by placing a bank of evaporant sources, equally spaced, in a line perpendicular to the direction of film spooling [24]. Coating thickness from a single source at any point on the substrate is given by:

- $d/d_o = 1/[1+(r/h)^2]^2$

where d/d_o is the ratio of the film thickness at any point to that directly above the evaporant source, r is the radial distance from the centre of the source, and h is the distance of the substrate above the source.

1.1.4 Comparison of resistive evaporation with other deposition technologies

1.1.4.1 Induction heated deposition

Induction heating of evaporant [21] relies upon the placing of a crucible, containing the evaporant material, inside a primary current coil which induces a current either in the evaporant itself or, if the evaporant is non-conducting, metal bands built into the crucible.

Advantages of this technique are that: results are easily reproduced; a wide range of currents and voltages can be used; and the sources are easy to

change. Disadvantages are that the process is a batch one and the evaporation process generates excess heat.

1.1.4.2 Electron beam evaporation

Electrons are generated by thermionic emission from a hot filament, typically tungsten, and focused upon the evaporant source [21,26]. This process is highly energy efficient, is capable of semi-continuous operation, and allows temperatures high enough for refractory metal evaporation to take place. However, low pressures are required to produce and maintain stable electron beams, and capital costs are high.

1.1.4.3 Sputter deposition

Sputter deposition is older than vacuum evaporation by ~50 years, and, until it was surpassed by that technique, was used for the deposition of gold and silver for decorative and optical applications. The contaminated nature of the product at that time meant that vacuum evaporation was preferred [22].

Process gas ions are generated then accelerated towards a target of the material to be deposited where they sputter the target. Sputtered species then deposit on the substrate. This process yields high adhesion coatings to polymers because of the high kinetic energy of the impinging species [21,22], and allows the deposition of refractory metals and ceramics since source material transfer to the gas phase is not a thermal process. For the same reason there are no fractionation processes, and the reactive sputtering technique allows the deposition of complex alloys, carbides, nitrides and borides which cannot be achieved by other means [22]. To its detriment,

deposition rates are slow, equipment is expensive, source material must be in sheet form, and large degrees of substrate heating can occur.

1.1.4.4 Ion plating

Evaporation of metal under conditions when the substrate is biased (-2 to -5 kV), known as ion plating [24], leads to improvement of adhesion relative to simple evaporation due to increased evaporant kinetic energy and substrate sputtering effects induced by the electric potential.

1.2 PLASMA-ENHANCED CHEMICAL VAPOUR DEPOSITION

Plasmas are commonly referred to as the fourth state of matter [27] since they can be formed by heating gases to very high temperatures, analogous to the phase transitions at lower temperatures. Under these conditions the gas starts to ionize, producing a mixture of electrons, ions and neutral species in local thermodynamical equilibrium [28]. The high temperatures preclude the use of such equilibrium plasmas in heat-sensitive materials' processing.

Plasmas can be formed by another method, however. Subjecting gas to high electric or magnetic fields allows free electrons in the gas to gain energy. Since these species are much less massive than the surrounding ions and neutrals they gain more energy. Hence these plasmas are characterized by their non-equilibrium nature. For polymer applications, low pressure (0.01-0.2 Torr) radio-frequency excited plasmas are often used.

Film deposition from non-equilibrium plasmas containing reactant gases is termed plasma-enhanced chemical vapour deposition (PECVD). This has been described by the following qualitative steps:

- Reactant transport to the deposition zone;
- Reactant mass transport to the substrate surface;
- Reactant adsorption on the substrate surface;
- Physical and/or chemical reactions leading to product formation, both film and by-product;
- By-product desorption;
- By-product transport to the gas stream;
- Transport of by-products away from the deposition zone.

Recently this view has been changed by the observation of particle formation in the gas phase [29-35].

PECVD has been applied to the deposition of clear gas barrier coatings [4-7,36]. Low deposition rates were a problem until advances by Felts [8] in the deposition of SiO_2 by PECVD. In this case either hexa- or tetramethyldisiloxane are decomposed in the plasma in a mixture of oxygen and helium to yield 20-30 nm coatings. This method is preferred over the reactive evaporation of SiO since it exhibits better layer densification.

Plasmas are, however, more difficult to control than simpler processes since there are more controlling parameters: gas pressures; feed gas flows for all reactants; and the power and tuning of the plasma.

1.3 REACTIVE EVAPORATION

Reactive evaporation is usually a convenient - and occasionally the only - method for depositing compounds with high melting points [37] when direct evaporation is precluded by processing problems. The reactive evaporation process entails evaporation into an atmosphere of reactive gas.

Typical oxidizing gas pressures are between 5 x 10^{-3} and 0.2 Torr. Aluminium oxide dissociates upon evaporation [37] to yield Al, O, AlO, Al_2O, O_2 and $(AlO)_2$ [24,25], and has a vapour pressure of only 10^{-2} Torr at 1800°C [24]. It is therefore unsuitable for direct evaporation. When aluminium is evaporated into an oxygen atmosphere reaction can theoretically occur in three regions of the deposition chamber [38]: the substrate surface; the gas phase; the metal evaporant surface; or a combination of all three. Each of the possible reaction sites has a chemical concept associated with it [25]: vapour condensation at the substrate surface; particle-particle interactions as vapour traverses the source-substrate distance; and the solid/liquid to gas phase transition at the evaporant pool surface.

Different authors' discussions show that the exact location of reaction varies with the system and operating conditions [24]. In general, if the mean free path of the system is greater than the source-substrate distance reaction will take place at the substrate surface, while introduction of more reactants, leading to the mean free path becoming less than that distance, leads to vapour phase reactions [37].

Limiting parameters in these systems are the substrate chemistry and temperature, the nature of the metal and oxidant, their impingement rates/partial pressures, and condensation coefficients.

1.4 DEPOSITION APPARATUS AND PARAMETERS

The vacuum chamber used for the deposition of AlO_x/PET has four principal components: vacuum pumps; polymer film unwinding and winding apparatus, with its concomitant system of rollers; aluminium and

oxygen reactant introduction; and deposit monitoring techniques. The deposition chamber is represented schematically in Figure 1.4.1.

Base pressure of 3×10^{-3} Torr is maintained by oil diffusion pumps backed by mechanical pumps. However, indicated pressures in semi-continuous processes are known to be an inaccurate measure of the residual pressure since gases such as oxygen and water vapour are consumed by the reactive aluminium metal during processing [17]. Such data should be interpreted with caution.

Polymer films for AlO_x thin film deposition are loaded onto the supply reel of the polymer spooling system and wound through the deposition zone over a chilled capstan roll [22], allowing control of substrate temperature in order that the polymer is not damaged by process heat. Industrially it has been found that substrate temperature can rise to 400 K [39]. Polymer web is finally rolled onto the take-up reel which is removed after the deposition has finished and the chamber has been vented to atmosphere.

Evaporant aluminium is provided by ceramic heater boats fed semi-continuously with aluminium wire at a controllable rate. So that the system can be readied prior to deposition, the evaporant sources can be isolated from the polymer film by means of a shutter. Multiple sources equally spaced across the width of the chamber ensure coverage of the reel's full width. Oxygen gas is introduced through nozzles connected directly to a gas supply, and must be placed close to the evaporant aluminium source otherwise pressure in the chamber rises beyond tolerable limits and the product film does not have desirable properties. The source-substrate separation is 0.25 m.

In situ monitoring relies upon measurement of deposited film optical density prior to take-up using collimated light sources which are directed through the plane of the spooling film towards a corresponding array of

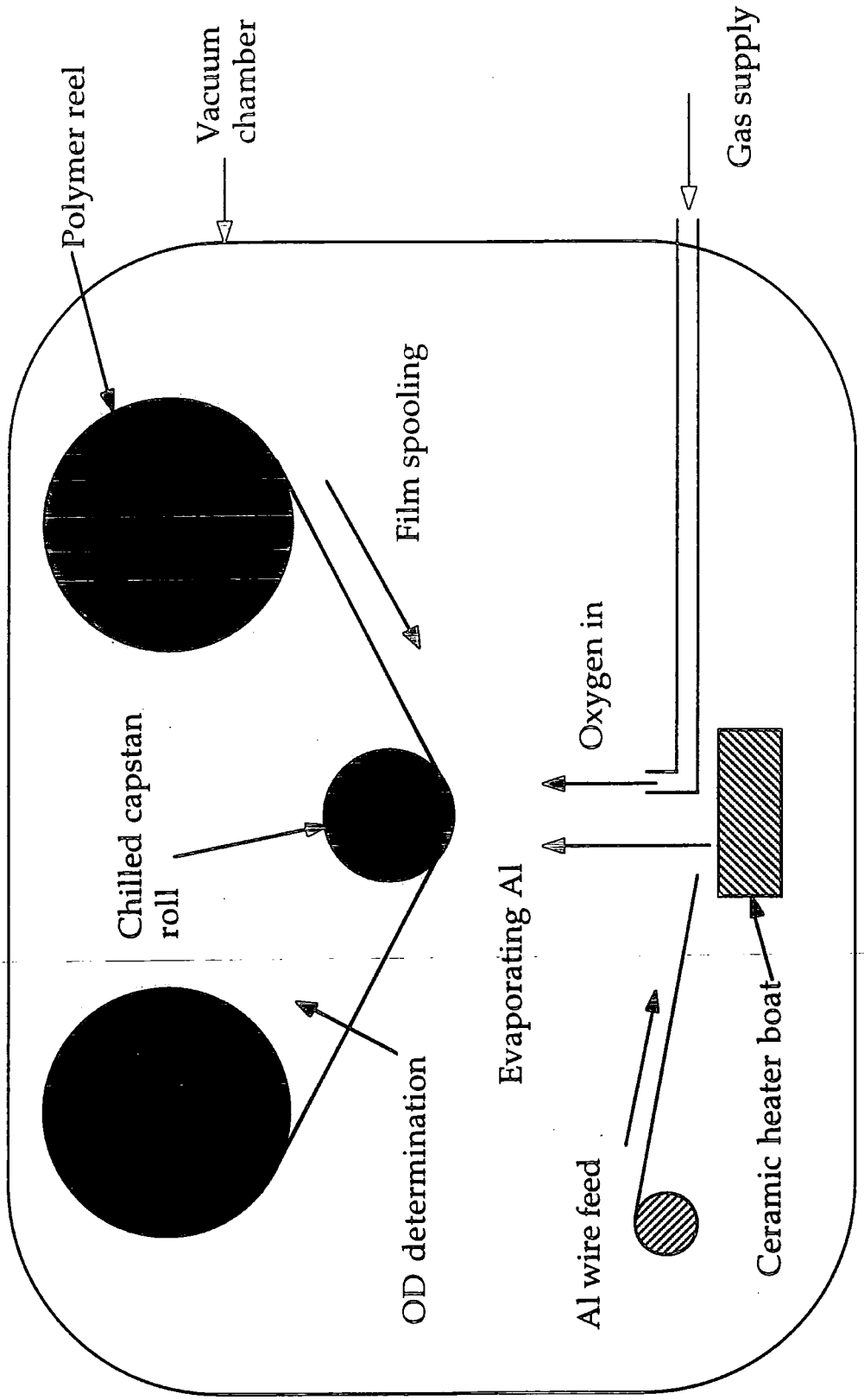

Figure 1.4.1: Schematic diagram of adapted metallization chamber.

photocells. Optical density (OD) is a measure of the film's opacity, and is defined as below:

- $OD = -\log_{10}(I_{tr}/I_o)$

where I_{tr} is the transmitted light intensity through the film and I_o the unattenuated intensity [40].

Parameters for AlO_x/PET gas barrier film deposition are: resistive heater voltage, controlling the temperature of the ceramic heater boats; polymer film speed; aluminium wire feed rate; and oxygen flow rate. They are shown in Table 1.4.1.

Film type	OD	O_2 flow rate /l min^{-1}	Al wire feed rate /inch min^{-1}	PET web speed/ m min^{-1}	Heater voltage/ V
Al/PET	2.5	0	18	250	5.5
Metallization prior to O_2 introduction	0.8	0	6	250	5.5
Metal-rich AlO_x	0.4	2-3	6	250	5.5
Oxygen-rich AlO_x	0.2	3-5	6	250	5.5

Table 1.4.1: Production parameters associated with characteristic AlO_x barrier film products.

In this section the protocol of AlO_x/PET deposition will be elucidated with reference to the parameters listed above [1]. With the shutter separating the deposition zone from the polymer film, the ceramic heater voltages are increased and their temperatures allowed to equilibrate.

Polymer film spooling is commenced and its speed is increased to 250 m min^{-1}, at which point the shutter is opened and aluminium wire feed commenced. As aluminium condenses on the substrate the optical density of the film increases until it reaches its desired value of 0.8 above that of the substrate (the OD of the PET is 0.04). This value is substantially lower than that for conventional metallization since at an OD of 0.8 uniform gas barrier across the reel width is not achieved. Oxygen is then introduced and the optical density of the film falls. *In situ* ODs of 0.4 corresponds to metal-rich AlO_X/PET composite, and 0.2 to an oxygen-rich AlO_X/PET composite.

At this point it is pertinent to mention the notation that will be used in this work. The range of aluminium-containing samples are collectively referred to as AlO_X/polymer since all samples, even those produced with zero oxygen flow rates, do contain oxygen (see Chapter 3). Conventionally metallized samples are termed either 'metallized' or Al/polymer, and these terms are used interchangeably. Samples produced by reactive evaporation are referred to as either metal- or oxygen-rich AlO_X/PET.

Removal of the polymer reel from the deposition chamber and exposure to ambient atmospheric conditions results in a reduction of the deposits' ODs. This can be attributed to aerial oxidation of the species at the surfaces of the material. The observed ODs, both *in situ* and after extended exposure to ambient atmosphere, are tabulated in Table 1.4.2 [41].

Remembering that OD can be a measure of metallic aluminium content, observations of this kind can yield information on the chemistry occurring upon exposure to ambient atmospheric conditions. The above data clearly shows that aerial oxidation does not significantly reduce the metallic aluminium content of conventionally metallized PET. Thinner aluminium layers corresponding to metallization prior to oxygen introduction are similarly little effected.

Sample	*In situ* OD	Final OD
Al/PET	2.5	2.4
Metallization prior to O_2 introduction	0.8	0.7
Metal-rich AlO_X/PET	0.4	0.2
Oxygen-rich AlO_X/PET	0.2	0.1

Table 1.4.2: *In situ* and final AlO_X/PET optical densities.

Coatings produced by the introduction of oxygen are, however, more greatly affected. Most of the metallic aluminium contained in the layers can be oxidized by atmospheric gases. The amount of metal is lower for the oxygen-rich coating, consistent with deposition conditions. Note also that the *in situ* OD of the oxygen-rich coating corresponds to the *ex situ* OD of the metal-rich variant. Metal content of these two layers may be the same. No indication of the depth distribution of the metal can be obtained, however.

Visible inspection of the three gas barrier films after exposure to air and the concomitant 'fading' highlights the differences between them. Al/PET has a metallic lustre and is opaque. The metal-rich AlO_X/PET structure is transparent but has a grey colour. Oxygen-rich AlO_X/PET is essentially colourless and transparent although not as clear as uncoated PET.

A close analogue to this system is found in the deposition of cermet films [42,43], intimate mixtures of metal and ceramics, often formed by reactive evaporation. These are used for their variable electrical conduction mechanisms characterized by the proportion of metal in the films.

1.5 POLYMER SUBSTRATES FOR AlO_x DEPOSITION

The principal consideration for substrate choice is that of ultimate gas barrier achievable along with aesthetic factors such as clarity. Coating of PET for barrier applications is common since this polymer already possesses substantial barrier relative to polymers such as polyethylene and polypropylene [44].

PET is a crystalline polymer. Technical specifications of the polymer were withheld for commercial reasons. Its repeat unit is represented in Figure 1.5.1.

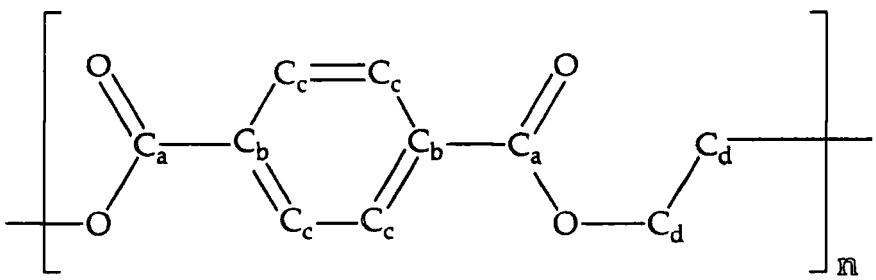

Figure 1.5.1: the structure of the PET repeat unit.

There are four types of carbon atom in the repeat unit, labelled a to d: carboxylic groups, a; phenyl carbons bonded to carboxylic groups, b; phenyl carbons, c; and ether carbons, d.

In this study the PET substrates are identical. Although the composition and properties of the polymer will affect those of the composite, they have not been varied and can be discounted from discussions concerning the effects of deposition conditions on the properties of resulting films. The particular formulation and structure of film used was chosen because it has been successfully metallized commercially by Camvac and was found to give good gas barrier upon AlO_x coating [41].

Critical parameters for polymer formulation in the case of PET are [45]: polymer molecular weight; and chemical natures and concentrations of carboxylic acid, catalyst deactivant, unreacted catalyst and slip additives. Once the film has been cast it is stretched, either uni- or biaxially. Its structure is metastable at this point. More stable structures are then reached by the annealing or heat-setting process with the following variables: temperature; fixed dimensions, under tension or a relaxed state; and different atmospheres. Properties such as tensile modulus, permeability, shrinkage, apparent crystal size, rate of hydrolysis, melting temperature, and percentage crystallinity are affected by the heat-setting conditions.

For PET heat-setting temperatures are typically between 100-240°C. Crystallinity in the cited study [45] increased with heat-setting temperature from ~30 to ~60%.

1.6 PRESSURE AND MEAN FREE PATH EFFECTS DURING DEPOSITION

Section 1.3, describing reactive evaporation, stated that mean free path considerations dictate the location of the reaction. In this section pressure and mean free path effects are considered for both metallization and reactive evaporation.

1.6.1 Aluminium vapour pressure considerations

Metallization is a pressure non-equilibrium and spatially non-isothermal process. It is important to demonstrate the effects that the latter phenomenon can have. In order to perform this task it is necessary to use aluminium vapour pressure data under equilibrium conditions [46], Table 1.6.1.1.

Supersaturation can be defined as the ratio of actual to equilibrium vapour pressure at a given temperature. The data presented below clearly shows that even if the actual vapour pressure of aluminium attained during metallization is orders of magnitude lower than the equilibrium value, substantial supersaturation will occur in the cooler regions of the deposition chamber. Supersaturation of metal vapour can lead to the formation of clusters in the gas phase [47-49]. Reviews of vacuum metallization [21,24] categorize the process as being one of simple evaporation and condensation, and state that the evaporant is merely transported from source to substrate. The reality may, in fact, be more complicated.

For the reactive evaporation of aluminium oxide films supersaturation is difficult to define since there is no vapour phase moiety of stoichiometry Al_2O_3. Qualitatively, the supersaturation is even greater in this situation.

Temperature (K)	p (Torr)
820	10^{-11}
862	10^{-10}
910	10^{-9}
960	10^{-8}
1020	10^{-7}
1090	10^{-6}
1175	10^{-5}
1265	10^{-4}
1370	10^{-3}
1495	10^{-2}
1650	10^{-1}
1845	10^{1}
2090	10^{2}
2410	10^{3}

Table 1.6.1.1: Equilibrium vapour pressure of aluminium as a function of temperature.

1.6.2 Mean free path effects

According to the kinetic theory of gases [50] the pressure of gas in a confining vessel results from the impingement of, and momentum transfer from, molecules with the walls of the container. When considering vacuum systems such as that used for the deposition of AlO_x thin films, an important parameter in the process is the mean free path (λ) of the gaseous species, defined as the average distance traversed by molecules between successive collisions with each other. When divided by the diameter (d) of the vessel through which the gas is flowing, the resultant dimensionless quantity is known as the Knudsen number (Kn) [51], itself a useful quantity since it allows differentiation between the flow regimes encountered by a gas as its pressure is reduced. d is taken as 0.25m in this case since this is the source-substrate distance.

There are four flow regimes for gases at low pressures [51]: turbulent; laminar; intermediate; and molecular. Turbulent and laminar flow are governed by the viscosity of the gas, *i.e.*, the interactions between the gaseous molecules/atoms, whereas molecular flow proceeds without intermolecular interactions. Intermediate flow is a function of both molecular and viscosity parameters. Laminar, intermediate and molecular gas flow can be characterized by the Knudsen number of a given system, Table 1.6.2.1.

Flow regime	Knudsen number
Laminar	$Kn < 9.1 \times 10^{-3}$
Intermediate	$9.1 \times 10^{-3} < Kn < 1$
Molecular	$Kn > 1$

Table 1.6.2.1: Gas flow regimes and their characteristic Knudsen numbers.

Tables 1.6.2.2, 1.6.2.3 and 1.6.2.4 contain results from calculations to show how the mean free paths, and the Knudsen numbers, change with pressure for aluminium in an aluminium atmosphere, aluminium in an oxygen atmosphere, and oxygen in an aluminium atmosphere, respectively. Calculations were performed for limiting cases of the variables concerned; for example, heater boat temperatures of 1700 K are employed during deposition which is carried out at room temperature, 298 K; the vapour pressure of aluminium at 1700 K is 0.16 Torr but it is possible, and probable, that the evaporation coefficient is less than unity due to the presence of impurities [25] (e.g., an oxide film on the surface of the evaporant pool) in the system; and the pressure of oxygen in the deposition chamber cannot be measured due to its entrainment in the evaporating aluminium stream [1]. However, these 'limiting case' calculations will show the effects possibly in operation. Molecular diameters are 0.293 nm for oxygen [52], and 0.286 nm for aluminium, twice the metallic radius of 0.143 nm [53].

T (K)	p_{Al} (Torr)	λ_{Al} (m)	Kn
1700	1.6×10^{-1}	3.03×10^{-3}	1.21×10^{-2}
1700	1×10^{-1}	4.84×10^{-3}	1.94×10^{-2}
1700	1×10^{-2}	4.84×10^{-2}	1.94×10^{-1}
1700	1×10^{-3}	4.84×10^{-1}	1.94
1700	1×10^{-4}	4.84	19.4
298	1.6×10^{-1}	5.31×10^{-4}	2.12×10^{-3}
298	1×10^{-1}	8.49×10^{-4}	3.40×10^{-3}
298	1×10^{-2}	8.49×10^{-3}	3.40×10^{-2}
298	1×10^{-3}	8.49×10^{-2}	3.40×10^{-1}
298	1×10^{-4}	8.49×10^{-1}	3.40

Table 1.6.2.2: Calculated aluminium mean free paths and Knudsen numbers, for limiting case temperatures and pressures of aluminium species, for AlO_X thin film deposition.

T (K)	p_{O2} (Torr)	λ_{Al} (m)	Kn
1700	1	6.56×10^{-8}	2.62×10^{-7}
1700	0.1	6.56×10^{-7}	2.62×10^{-6}
1700	1×10^{-2}	6.56×10^{-6}	2.62×10^{-5}
1700	1×10^{-3}	6.56×10^{-5}	2.62×10^{-4}
1700	1×10^{-4}	6.56×10^{-4}	2.62×10^{-3}
298	1	1.15×10^{-8}	4.60×10^{-8}
298	0.1	1.15×10^{-7}	4.60×10^{-7}
298	1×10^{-2}	1.15×10^{-6}	4.60×10^{-6}
298	1×10^{-3}	1.15×10^{-5}	4.60×10^{-5}
298	1×10^{-4}	1.15×10^{-4}	4.60×10^{-4}

Table 1.6.2.3: Calculated aluminium mean free paths and Knudsen numbers for limiting case temperatures and pressures of oxygen species, for AlO_x thin film deposition.

T (K)	p_{Al} (Torr)	λ_{O2} (m)	Kn
1700	1	9.47×10^{-8}	3.79×10^{-7}
1700	0.1	9.47×10^{-7}	3.79×10^{-6}
1700	1×10^{-2}	9.47×10^{-6}	3.79×10^{-5}
1700	1×10^{-3}	9.47×10^{-5}	3.79×10^{-4}
1700	1×10^{-4}	9.47×10^{-4}	$3.79\backslash \times 10^{-3}$
298	1	1.66×10^{-8}	6.64×10^{-8}
298	0.1	1.66×10^{-7}	6.64×10^{-7}
298	1×10^{-2}	1.66×10^{-6}	6.64×10^{-6}
298	1×10^{-3}	1.66×10^{-5}	6.64×10^{-5}
298	1×10^{-4}	1.66×10^{-4}	6.64×10^{-4}

Table 1.6.2.4: Calculated oxygen mean free paths and Knudsen numbers for limiting case temperatures and pressures of aluminium species, for AlO_x thin film deposition.

Under almost all of the cases considered above the mean free paths characteristic of this system (using the assumptions outlined above) are less than the source-substrate distance. Gas phase interactions will therefore be important since the gas flow is either laminar or intermediate.

1.7 FURTHER INFORMATION

Cross-sectional transmission electron microscopy (TEM) was performed upon the AlO_x/polymer samples by Hoechst [54]. Thicknesses measured are tabulated below. Electron diffraction showed that the oxides present in both metal- and oxygen-rich AlO_x/PET were amorphous, and that the metal-rich variant contained aluminium clusters ~1-1.5 nm in diameter.

Sample	Thickness (nm)
Al/PP	25
Al/PET	40
Oxygen-rich AlO_x/PET	25
Metal-rich AlO_x/PET	20

Table 1.7.1: AlO_x layer thicknesses as determined by cross-sectional TEM.

1.8 CONCLUSIONS

- A modified metallizing chamber has been used to deposit variable stoichiometry AlO_X/polymer composites *via* the introduction of oxygen into the stream of evaporating aluminium.

- The principle advantage of this technique is its simplicity and low cost.

- Post-deposition 'fading' of the AlO_X coatings indicates that the stoichiometries of the films change upon exposure to ambient atmospheric conditions. Optical density data shows that all films undergo aerial oxidation. The extent of fading relative to the initial, *in situ* OD is greatest for metal- and oxygen-rich AlO_X/PET. The *in situ* OD of the oxygen-rich coating is the same as the *ex situ* OD of the metal-rich variant.

- 'Limiting case' calculations of gaseous mean free paths indicate that reactions are likely to take place in the gas phase, and, because of the temperature gradient in the chamber, vapour phase interactions due to supersaturation are likely to be important even in the absence of oxygen.

1.9 REFERENCES

[1] Bowater Packaging Limited, Patent Application 8928706.4.

[2] BRITE/EURAM Programme, *Synopses of Current Projects 1990-1991*, Commission of the European Communities, Luxembourg, 1991.

[3] R. W. Phillips, T. Markantes, C. LeGallee, *Society of Vacuum Coaters' 36th Annual Technical Conference Proceedings* (1993), 293.

[4] M. Izu, B. Dotter, S. R. Ovshinsky, W. Hasegawa, *Society of Vacuum Coaters' 36th Annual Technical Conference Proceedings* (1993), 333.

[5] P. Ang, *Society of Vacuum Coaters' 36th Annual Technical Conference Proceedings* (1993), 518.

[6] T. Krug, R. Ludwig, G. Steiniger, *Society of Vacuum Coaters' 36th Annual Technical Conference Proceedings* (1993), 302.

[7] J. E. Klemberg-Sapieha, L. Martinu, M. Kuttel, M. R. Wertheimer, *Society of Vacuum Coaters' 36th Annual Technical Conference Proceedings* (1993), 445.

[8] J. T. Felts, Airco Coating Technology, Concord, California.

[9] C. Missiano, E. Simonetti, P. Cerolini, S. Staffetti, G. Taglioni, A. Pasqui, F. Fusi, *Society of Vacuum Coaters' 36th Annual Technical Conference Proceedings* (1993), 307.

[10] J. S. Smith, N. A. Peppas, *J. Appl. Polym. Sci.* **43** (1991), 1219.

[11] C. Missiano, E. Simonetti, S. Staffetti, G. Taglioni, F. Rimediotti, *Society of Vacuum Coaters' 35th Annual Technical Conference Proceedings* (1992), 28.

[12] S. Schiller, M. Neumann, H. Morgner, N. Schiller, *Society of Vacuum Coaters' 36th Annual Technical Conference Proceedings* (1993), 278.

[13] P. S. Ho, *Appl. Surf. Sci.* **41/42** (1989), 559.

[14] N. J. DiNardo, in *Metallized Plastics 1: Fundamental and Applied Aspects*, Eds. K. L. Mittal, J. R. Susko, Plenum Press, New York, 1989, 137.

[15] J. D. Miller, H. Ishida, in *Fundamentals of Adhesion*, Ed. L.-H. Lee, Plenum Press, New York, 1991, Chapter 10.

[16] E. H. H. Jamieson, A. H. Windle, *J. Mater. Sci.* 18 (1985), 64.

[17] J. Weiss, *Thin Solid Films* 204 (1991), 203.

[18] P. Mercea, L. Muresan, V. Mercea, *J. Memb. Sci.* 24 (1985), 297.

[19] P. Mercea, L. Muresan, V. Mercea, D. Silipas, I. Ursu, *J. Memb. Sci.* 35 (1988), 291.

[20] T. A. Beu, P. Mercea, *Mater. Chem. Phys.* 26 (1990), 309.

[21] K. M. Anetsberger, in *Metallized Plastics 1: Fundamental and Applied Aspects*, Eds. K. L. Mittal, J. R. Susko, Plenum Press, New York, 1989, 29.

[22] C. T. Wan, K. A. Taylor, D. L. Chambers, G. T. Susi, in *Metallized Plastics 2: Fundamental and Applied Aspects*, Ed. K. L. Mittal, Plenum Press, New York, 1991, 81.

[23] J. E. Curran, J. S. Page, U. Pick, *Thin Solid Films* 97 (1982), 259.

[24] R. F. Bunshah, in *Deposition Technologies for Films and Coatings*, Ed. R. F. Bunshah, Noyes Publications, Park Ridge, 1982, Chapter 4.

[25] *Handbook of Thin Film Technology*, Eds. L. I. Maissel, R. Glang, McGraw-Hill, New York, 1970, Chapter 1.

[26] E. B. Graper, *J. Vac. Sci. Technol.* 8 (1971), 333.

[27] *CRC Handbook of Chemistry and Physics*, Ed. R. C. Weast, CRC Press, Boca Raton, 1982, F-107.

[28] R. Reif, W. Kern, in *Thin Film Processes II*, Eds. J. L. Vossen, W. Kern, Academic Press, London, 1991, Part IV-I.

[29] N. Braithwaite, B. Graham, New Scientist 140 (1993), 34.

[30] S. R. Turns, M. J. Funari, A. Khan, *Combust. Flame* 75 (1989), 183.

[31] A. Garscadden, *Proc. Int. Symp. Plasma Chem.* 11 (1993), 785.

[32] T. Fukuzawa, M. Shiratani, Y. Watanabe, *Proc. Int. Symp. Plasma Chem.* 11 (1993), 1125.

[33] Y. Nakano, K. Sugiyama, Y. Takeuchi, T. Matsuda, *Proc. Int. Symp. Plasma Chem.* 11 (1993), 1422.

[34] M. Shiratani, H. Tsuroka, T. Fukuzawa, H. Kawasaki, Y. Watanabe, *Proc. Int. Symp. Plasma Chem.* 11 (1993), 1469.

[35] J.-F. Bilodeau, P. Proulx, F. J. Moura, R. J. Munz, *Proc. Int. Symp. Plasma Chem.* 11 (1993), 365.

[36] F. Garbassi, M. Morra, E. Occhiello, Polymer Surfaces: From Physics to Technology, J. Wiley & Sons, Chichester, 1994, Chapter 11.

[37] R. F. Bunshah, in *Science and Technology of Surface Coating*, Eds. B. N. Chapman, J. C. Anderson, Academic Press, London, 1974, 361.

[38] M. Ohring, *The Materials Science of Thin Films*, Academic Press, New York, 1992, Chapter 3.

[39] J. F. Silvain, A. Arzur, M. Alnot, J. J. Ehrhardt, P. Lutgen, *Surf. Sci.* 251/252 (1991), 787.

[40] J. Weiss, C. Leppin, W. Mader, U. Salzberger, *Thin Solid Films* 174 (1989), 155.

[41] K. M. Revell, R. S. A. Kelly, Camvac (Europe) Limited, private communication.

[42] H. Birey, *Appl. Phys. Lett.* 23 (1973), 316.

[43] J. Beynon, M. M. El-Samamoudy, *J. Mater. Sci. Lett.* 6 (1987), 1447.

[44] T. M. Aminabhavi, V. S. Aithal, *J. Macromol. Sci. Rev. Macromol. Chem. Phys.* C31 (1991), 117.

[45] R. M. Gohil, *J. Appl. Polym. Sci.* 52 (1994), 925.

[46] R. E. Honig, D. A. Kramer, *RCA Rev.* 30 (1969), 285.

[47] A. Hoareau, B. Cabaud, P. Melinon, *Surf. Sci.* 106 (1981), 195.

[48] O. F. Hagena, *Surf. Sci.* 106 (1981), 101.

[49] R. S. Bowles, J. J. Kolstad, J. M. Calo, R. P. Andres, *Surf. Sci.* **106** (1981), 106.

[50] A. Roth, *Vacuum Technology*, 2nd Edition, North-Holland, Amsterdam, 1983, Chapter 3.

[51] A. Roth, *Vacuum Technology*, 2nd Edition, North-Holland, Amsterdam, 1983, Chapter 2.

[52] P. W. Atkins, *Physical Chemistry*, 3rd Edition, Oxford University Press, Oxford, 1986, 653.

[53] J. G. Stark, H. G. Wallace, *Chemistry Data Book*, 2nd Edition, John Murray, London, 1988, 27.

[54] K.-H. Kochem, Hoechst AG, private communication.

CHAPTER 2

PERMEABILITY OF AlO_x/PET FILMS

2.1 INTRODUCTION

The aim of this first experimental chapter is to determine any differences in gas transport behaviour between the AlO_x films deposited under different conditions. More accurately, it can be seen as an exercise in problem definition since the quest of this thesis is to understand the differences that may or may not be observed.

Prior to a discussion of the experimental results, the next sections of this chapter will deal with the fundamental aspects of polymer permeability and its measurement, and the gas transport properties of metallized films.

So that a study of this nature could be initiated in this author's laboratory, a suitable permeability measurement system was required. The equipment designed is described in the experimental section, Section 2.2. In this system the equilibrium partial pressures of permeant within the vacuum chamber are measured, and data is quoted as the mean equilibrium permeant partial pressure (MEPPP).

Metallization can be used to alter the gas transport characteristics of polymer films in two ways [1]: by reducing the overall rate of gas transport through the film, *i.e.*, the gas barrier effect; or by changing the selectivity of gas separation. Both effects will be considered in this chapter.

2.1.1 Gas transport processes in polymers

Permeability (P), the steady-state flux of permeant through a medium, is the product of the solubility (or sorption) and diffusion coefficients (S and D, respectively) in that medium [2,3]:

- $P = DS$

- $D = D_0 \exp(-E_D/RT)$
- $S = S_0 \exp(-\Delta H_S/RT)$

where D_0 and S_0 are the pre-exponential factors, E_D is the activation energy of diffusion, ΔH_S is the heat of solution, R is the gas constant, and T is temperature [4].

2.1.1.1 Sorption

Sorption in glassy polymers below the glass transition temperature, into which category PET falls at room temperature, is, phenomenologically, the immobilization of penetrant within the polymer and can be described by two distinct penetrant populations [2,5,6] within the dual-mode sorption model. For simple gases the concentration is very low [7]; indeed, it is this factor that accounts for the simplicity of the relationship between permeability and diffusivity. Firstly, there is the Henry's Law population for which the equilibrium concentration, governed by classical dissolution, is linearly proportional to pressure. There is also a Langmuir population of penetrant species which reside in microvoids (unrelaxed molecular-scale gaps in the host polymer's structure [8]). Overall, the concentration of

penetrant species in a host polymer matrix can be described by the following summation of the contributions from both mechanisms:

- $c = k_D.p + C'_H.bp/[1+bp]$

where c is the concentration, p is pressure, k_D is the Henry's Law solubility constant, C'_H is the hole saturation constant and b is the hole affinity parameter. For inert gases the Langmuir capacity of the host polymer matrix is small [8]. Pace and Datyner [6] have drawn attention to the difference between hole-forming mechanisms for smooth-chained polymers (such as PE and PET) and those with flexible side-groups: in the former case it is the 'kinking' of the main chain itself that leads to the formation of microvoids, while in the latter case the motion of unrestrained side-chains will also affect the available volume for uptake of penetrant in the Langmuir population.

Chemical interactions are neglected in the dual-mode sorption model [9] as it applies to inert gases. Simulations [10] have shown that it is the physical properties of the penetrant and the polymer that dominate the solubility process, and that the role of gas-polymer interactions is secondary. However, one study [11] simulated the sorption of water (a 'reactive' species) to a polymer repeat unit and found that the water molecules interacted strongly with alcohol functional groups *via* attractions between the partial charges on the water molecule and the oxygen of the alcohol group.

2.1.1.2 Diffusion

Fick's First Law is a fundamental consideration in gas transport processes, and states that the flux of penetrant diffusing through a medium is proportional to the concentration gradient across that medium:

- $F_x = -D(\partial c/\partial x)$

where D is the diffusion coefficient, c is the concentration and x is the direction of diffusion being considered [12,13]. The activation energy of diffusion is proportional to the diameter of the penetrant for simple gases [14].

The energy required to move a molecule from its equilibrium position is small compared to that required to create a 'hole' in the polymer network [15]. Understanding the segmental motion of polymers is therefore important for study of the diffusion process. Pace and Datyner have produced a series of papers upon the diffusion of simple penetrants in polymers [14,16,17]. Their model combines thermodynamic and molecular aspects of gas transport. Starting from the assumption that amorphous polymers have local order on the scale of several nanometres (backed up by the very small differences in density between the amorphous and crystalline phases of a polymer), they envisage a collection of parallel chain bundles, best described as a series of parallel 'ropes' packed together. Two modes of diffusion are then conceptualized: firstly, motion along the axis of the polymer chain bundles; and, secondly, motion perpendicular to the bundle axis. The former has virtually no activation energy while the latter requires sufficient energy to separate the parallel polymer chain bundles before diffusion can take place, the magnitude of this quantity being determined by factors such as the inter-chain potential, chain-bending modulus and equilibrium chain separation. This idealized system does assume that the polymer chains are smooth and uniformly flexible in nature, and that the penetrant species are hard and spherical.

When applied to polymers such as PET these assumptions are challenged by the deviations between experiment and theory.

Underestimation of diffusion coefficients has been attributed to the neglection of the effects of atomic-scale irregularities (with radii of curvature comparable to the radii of the smallest penetrants) in the polymer chain which allow more diffusion than predicted *via* the calculated diffusion coefficients.

Computer modelling has been applied to the diffusion of species through amorphous polymer networks such as polyethylene [18], polypropylene [19], polyisobutylene [20,21] and polydimethylsiloxane [22]. These have clearly shown the hopping mechanism by which diffusion takes place, and that, as the size of the penetrant decreases, the individual hops become increasingly ill-defined. As the hop occurs, the hopping species is thought to be momentarily translationally 'hot' [21].

One advance in this area stands out for particular comment. Muller-Plathe *et al.* [20] have shown that changing the amorphous polymer model structure from one relying upon a united atom approach to the methyl side-groups of polypropylene to an explicit, all-atom approach produces a better match between experimental and calculated values. This result was rationalized in terms of wider channels between adjacent cavities in the polymer structure for the united atom approach which artificially inflated the diffusion coefficient.

2.1.1.3 Predictive methods in polymer permeability

As discussed above, the diffusion and solubility coefficients can be described thus:

- $D = D_0 \exp(-E_D/RT)$
- $S = S_0 \exp(-\Delta H_S/RT)$

- $D = RT.A_\alpha.\exp(-B_\alpha/f)$
- $\Delta H_S = \Delta H_{cond} + \Delta H_1$
- $\Delta H_1 = v_1(\partial_1-\partial_2)^2.\Phi^2$

where A_α is a parameter dependent upon the size and shape of the penetrant, B_α describes the efficiency of using the available free volume fraction, f, ΔH_{cond} is the molar heat of condensation, ΔH_1 is the partial molar heat of mixing, v_1 is the partial molar volume of the penetrant, ∂_1 and ∂_2 are solubility parameters, and Φ is the volume fraction of polymer in the mixture [4]. For gases such as He, N_2 and O_2 the molar heat of condensation is very small at room temperature.

Overall, the permeability of a polymer system can be seen as a function of the tightness of the polymer supramolecular structure (as expressed by the free volume) and the interaction between the polymer chains (the cohesive energy).

2.1.2 Gas transport through oriented PET

Permeation of simple gases (such as He, Ar, N_2, O_2) through polymers has been recognized as a method of gaining information about their microstructures since these systems are effectively without chemical interaction [23]. Crystallinity is a crucial indicator of structure. Crystallites are thought to act as barriers to gas transport [24]. Slee *et al.* [24] showed that the ratio of the permeability of crystalline PET (P) to that of amorphous PET (P_a) can be related to the crystalline fraction (f_c) present in the polymer thus:

- $P/P_a = 2(1-f_c)/(2+f_c)$

PET has an almost planar conformation in which all but the three bonds in the ether segment of the chain are rigid and inflexible because of the extended delocalization owing to the adjacence of the unsaturated ring and ester groups [17]. Hence most of the gas transport through amorphous PET films will occur through motion of this section of the polymer.

2.1.3 Methods of gas transport measurement

2.1.3.1 Steady-state methods

When considering the transport of penetrants through a uniform plane of polymer with constant concentrations on either side of the film, steady state is reached when the concentrations at all points within the polymer are constant [13]. At this point, if the pressures on both sides of the polymer are known and the diffusion coefficient is constant, the rate of transfer of permeant (F) can be expressed thus:

- $F = P(p_1-p_2)/l$

where P is the permeability coefficient, p_1 and p_2 are the pressures on the up- and down-stream sides of the polymer, respectively, and l is the thickness of the polymer.

2.1.3.2 Time-lag method

Prior to the establishment of a steady state situation as described above, the point of initial introduction of the penetrant under study into the polymer film environment can be envisaged. Initially there is no penetrant on either side of the polymer. Any penetrant is continually removed from

the downstream side of the polymer, and the penetrant flux is time-dependent. As time increases (and tends towards infinity) the relationship between the flux and the system's constants tends towards a line corresponding to the equation:

- $Q_t = DC_1/l.(t - l^2/6D)$

where Q_t is the flux, D is the diffusion coefficient, C_1 is the concentration on the upstream side of the polymer, t is time, and l is the polymer thickness. The t-axis is intercepted at point L where [13,24]:

- $L = l^2/6D$

Since the polymer thickness is known, the diffusion coefficient can be calculated. Once steady state conditions are achieved the permeability coefficient is also determined.

2.1.4 Experimental systems

2.1.4.1 'Prior art'

Partition cells are a common method of measuring the permeability of polymers [13]. In such experiments, the pressure on either side of the polymer is tightly controlled. Typically the downstream compartment of the apparatus is evacuated and the upstream compartment filled with penetrant gas. The pressure rise in the downstream compartment can be taken as a valid experimental measurement since, if the pressure is held low enough, the pressure in this compartment is still effectively zero relative to that in the upstream area. Since it is an activated process, temperature

control is important for accurate experimentation. Other experimental variables to be considered are the area of polymer exposed to the gas supply, and possible edge effects (caused by different mechanical deformations at the edges of different polymer samples).

2.1.4.2 Experimental methods based upon UHV systems

Laurenson and Dennis [25] have used a gas permeability system based upon a UHV system fitted with a quadrupole mass spectrometer in which the sample to be tested was placed in a chamber pumped through an orifice of known size to test the permeabilities of elastomers commonly used in vacuum systems. Base pressure of their system was not quoted. They did identify the critical sources, in their opinion, of experimental error.

Mass spectrometer sensitivity was found to change with time in the relatively high pressure range (5×10^{-7} to 4×10^{-5} Torr), perhaps because of the presence of 'poisonous' gases outgassing from the polymer samples. This problem was overcome by using a needle valve to introduce gases into the chamber and correlating the response of the quadrupole mass spectrometer relative to the ion gauge; changes in ion gauge sensitivity are found to be much less likely and of smaller magnitude than the fluctuations observed for mass spectrometers. Nash [26], however, does not concur. He maintains that accurate calibration and subsequent reliability of vacuum pressure measurement devices are difficult to maintain over extended periods of time.

Holden *et al.* have also used a mass spectrometric device in the determination of polymer film permeability [24], but in their case the total pressure was determined, not the partial pressure.

2.1.5 Gas transport properties of metallized polymer films

The absence of perfect gas barrier of aluminium foils laminated to polymers was studied as early as 1959 [27]. This effect has also been observed for polymers vapour deposited with metal [28-30]. The quest for improvement in the imperfect gas barrier of metallized films led to the investigation of the phenomena responsible for such observations.

Jamieson and Windle [31] studied industrially deposited Al/PET gas barrier structures in their 1985 publication. Transport of oxygen gas was thickness independent for between 20 and 40 nm layers. Measurements of pinholes in the metal layers allowed calculation of the oxygen permeability. Experimentally determined permeabilities were found to vary linearly with those calculated. There was a non-zero intercept, consistent with the idea that pinholes were responsible for some, but not all, of the exhibited permeability. Pinhole formation was assigned to the presence of atmospheric dust particles on the film during coating deposition (the size distribution of the pinholes matched that of atmospheric dust over the 1-10 μm range), thereby masking parts of the film from metal coverage and therefore gas barrier.

Much of the work in this field has been performed by Mercea and various co-workers since 1985 [28-30]. They have considered these films both experimentally and *via* calculations. Their work's underlying hypothesis is that all gases which are unable to dissolve in metals cannot permeate through them [28]; any gas transport must therefore be due to layer defects.

Palladium, nickel and copper films of 50 nm thickness were resistively evaporated under high vacuum conditions (5×10^{-6} Torr) onto 30 μm PET (industrially produced) in the first of these papers [28]. SEM showed that these layers were not continuous when viewed on the micrometer scale: fine cracks were observed with widths < 1 μm. The authors were not

able to produce defect-free layers and proposed that these cracks were introduced during the cooling of the deposited metal (from the deposition temperature of 80°C) by the differing thermal expansion coefficients of the PET film and metal. Indeed, differences in the permeabilities of the Ni-, Cu- and Pd-coated PET films were taken to correspond to the qualities of the deposited layers. Hydrogen, able to dissolve in the metals themselves, exhibited enhanced permeation relative to the other gases after metallization with Pd or Ni.

Mercea and co-workers' later publication [29] carries the defect theory further by monitoring the transport through Pd/PET membranes of Ar, He, N_2 and CO_2 (which do not dissolve in Pd) and H_2 (which does). By their choice of gases the authors hoped to distinguish between two effects: the gas barrier effect, and the gas-selective effect, increasing the throughput of a given gas by tailoring the chemistry of the system in order to promote dissolution and diffusion through the metal layer itself. By changing the orientation of the Pd coating relative to the feed gas supply, *i.e.*, either facing the Pd towards or away from the gas source, it was shown that for the non-dissolving gases the permeation was unaffected while for H_2 the permeation was greater when the Pd layer was exposed to the H_2 supply. For other, non-reactive gases permeation through pinholes (diameter distribution peaking at ~4μm) was invoked for the lack of perfect gas barrier. They determined that ~0.75% of the polymer was uncoated.

Calculations performed using a pinhole model [30] indicated that this did not account fully for the difference between theory and experiment. Gas barrier improvement factors were calculated at 20, independent of the penetrant. Experimental data shows that the gas barrier improvement factor changes with permeant species. This was rationalized in terms of channels, ~10 nm in width, through which the permeants could flow. This model allows the gas-dependence of permeability to be explained *via* preferential

molecular flow through defects smaller than the mean free path of the gas in question.

Weiss concluded in his paper [32] that the major effect for gas barrier is the amount of filler particles in the PET base film when metallized under industrial conditions. Such protrusions can be considered to induce defects in the metal layer.

2.2 EXPERIMENTAL

2.2.1 Sample definition and preparation

All samples are as defined in Chapter 2 unless otherwise stated.

Samples referred to as HCl-etched were prepared as follows. Barrier layers were etched with ~2 mol dm^{-3} aqueous hydrochloric acid by placing the films in a large beaker of acid for 6 hours, after which time the film was removed and washed extensively with ultrapure water then dried under ambient atmospheric conditions for at least two days.

2.2.2 MEPPP determination

The permeability measuring system, based upon the sample preparation chamber of a Kratos ES300 X-ray photoelectron spectrometer, is represented schematically in Figure 2.2.2.1. Base pressure, typically 2×10^{-10} Torr, was maintained by a liquid-nitrogen-trapped diffusion pump with rotary pump backing, and monitored with a Vacuum Generators ultra-high vacuum ion gauge (VIG 24) and controller. A Vacuum Generators SX200 quadrupole mass spectrometer, interfaced to an IBM-compatible personal computer running data accumulation and analysis software developed in-

house, allowed compositional analysis of the gaseous species in the chamber by mass-to-charge ratio (m/e).

Calibration experiments to determine the response of the quadrupole mass spectrometer to known pressures of gas were performed using high purity helium, argon and oxygen gases (BOC, 99.995, 99.999, and 99.6 %, respectively) which were introduced into the chamber by means of a leak valve. Mass spectra were recorded at ion gauge indicated pressures of 10^{-7} Torr which were converted to meaningful quantities using ion gauge sensitivity factors [33]. By correlating these pressures with the intensities of the relevant m/e signals, the mass spectrometer's response per unit pressure was calculated. Nash's observations concerning the unreliability of ionization gauges over extended periods of time [26] have been neglected since the vast majority of this work was performed within the first year of a new gauge's life.

Discs of sample films were placed in the permeability probe, as shown schematically in Figure 2.2.2.2, with the coating facing the high pressure gas supply. Based upon two drilled-out UHV flanges, one with its knife-edge removed, the copper gasket gave a leak-tight seal for the sample holder. The probe was connected to the UHV system by means of stainless steel tubing welded to the modified flange which was inserted through the chamber's rotatable gate valve.

Sample films were then exposed to gas supplied through the vacuum system's roughing line (base pressure 5×10^{-2} Torr) to a pressure of 1000 Torr, Figure 2.2.2.3. Mean equilibrium permeant partial pressures (MEPPPs) of gases were determined after suitable equilibration of the system and removal of ambient gases from the m/e trace. Measured gas permeation was in the steady-state regime where the concentration of permeant on either side of the membrane is constant and the flow of permeant through the membrane is allowed to reach equilibrium.

Terminology in this area of study is sometimes confusing in its interchangeability of terms. For clarity these are discussed now. Permeability is a measure of the flux of permeant through a medium. In gas barrier film work this term is often superseded by 'gas barrier', a qualitative, colloquial expression for the inverse of the permeability. Experimental data in this work will be referred to by its correct term, MEPPP, as outlined below, since permeability is not actually measured but a quantity proportional to it.

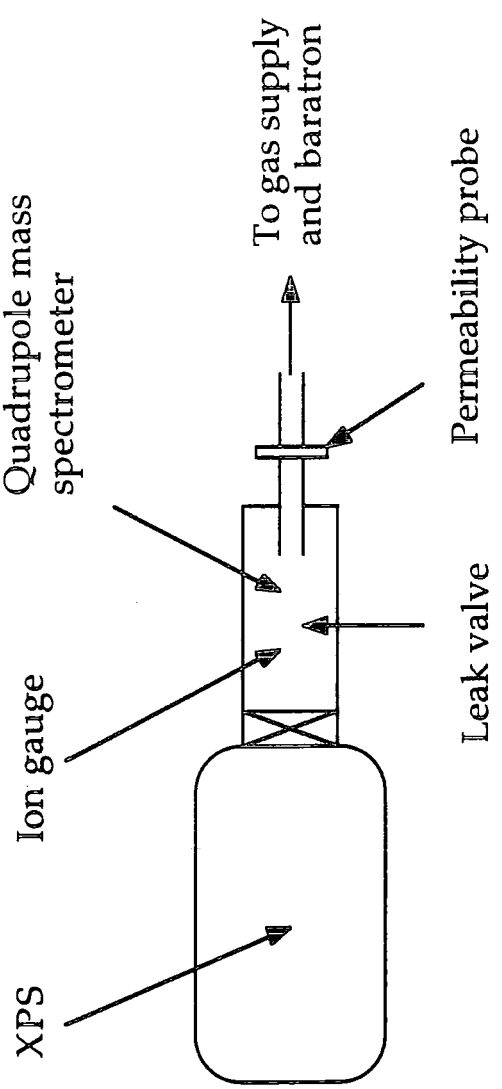

Figure 2.2.2.1: schematic diagram of ES 300 surface analysis instrument

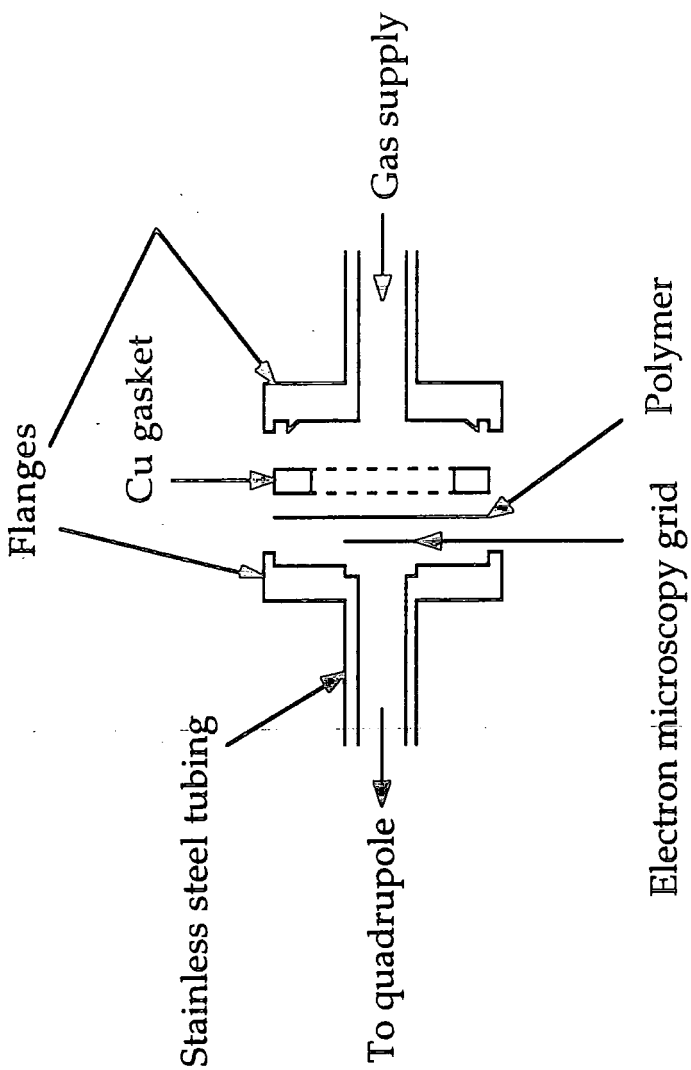

Figure 2.2.2.2: Sample holder of mass spectrometric permeability analysis system

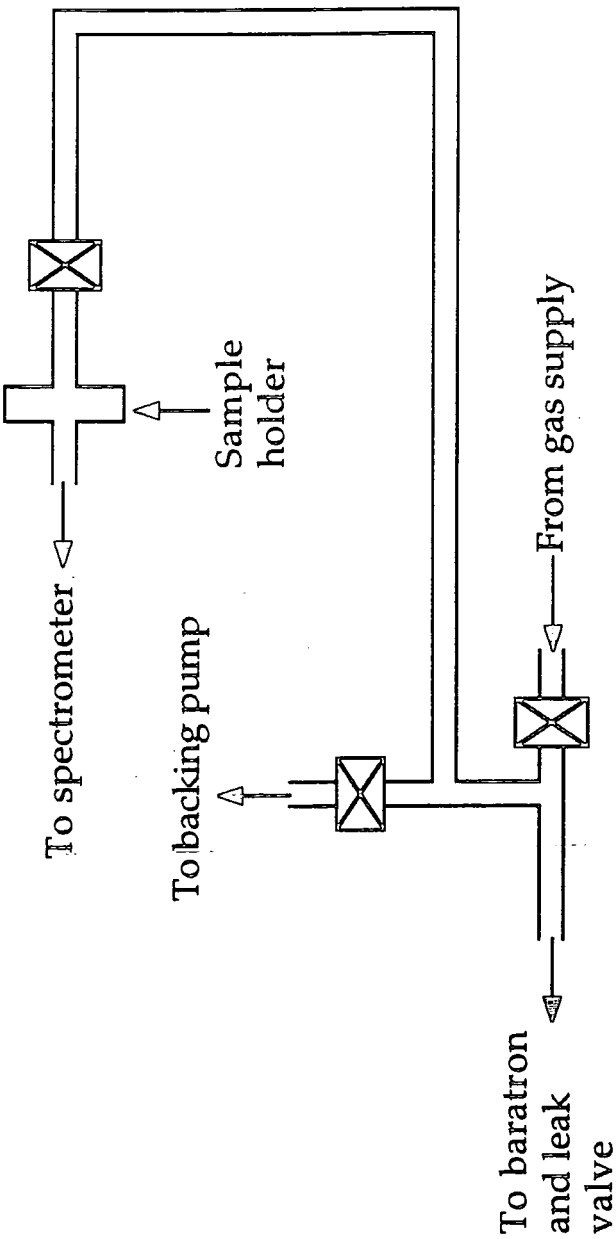

(b) Gas inlet system

Figure 2.2.2.3: Schematic representation of gas inlet system.

2.3 RESULTS

2.3.1 Uncoated PET

Experiments on uncoated PET were performed in order to test the applicability of this system to the determination of permeabilities of thin polymer films. Data for uncoated PET is presented in Table 2.3.1.1 along with the permselectivities relative to argon which are compared with those from the literature [34].

Permeant	MEPPP (10^{-9} Torr)	Permselectivity (rel. to Ar)	Literature permselectivity
Ar	0.93 ± 0.01	1.00 ± 0.01	1.0
He	53.70 ± 0.62	57.74 ± 0.90	50
O_2	1.02 ± 0.01	1.10 ± 0.02	1.5

Table 2.3.1.1: MEPPP and permselectivity data for uncoated PET.

Although not a perfect match between the experimental and literature values and those of the author, the permselectivity values are reproducible and similar. Indeed, the goal in mind when developing this system was to achieve reliability and reproducibility such that results could be compared validly between samples, and not to generate results which could be converted into standard units.

2.3.2 AlO_X/PET films

MEPPPs of Ar, He and O_2 are presented in Table 2.3.2.1 and Figures 2.3.2.1 (a)-(c), respectively. Differences in the observed MEPPPs are close to, or within, the limits of experimental error for all gases except He.

	MEPPP (10^{-9} Torr)		
Sample	Ar	He	O_2
Al/PET	0.039 ± 0.001	1.27 ± 0.05	0.027 ± 0.004
Metal-rich AlO_X/PET	0.035 ± 0.001	1.03 ± 0.06	0.025 ± 0.003
Oxygen-rich AlO_X/PET	0.034 ± 0.001	1.86 ± 0.05	0.025 ± 0.002

Table 2.3.2.1: MEPPPs of Ar, He and O_2 for Al/PET, and metal- and oxygen-rich AlO_X/PET.

The higher the MEPPP of a gas passing through the sample and into the UHV chamber, the greater the difference between the MEPPPs for that gas for the various AlO_X coated films. Oxygen's MEPPP is the lowest of all three gases for all three coated films, and there are no significant differences between the MEPPPs for Al/PET, and metal- and oxygen-rich AlO_X/PET. Argon's MEPPPs are slightly higher, and the experimental results are more divergent than those for oxygen, the Ar MEPPP for Al/PET being slightly higher than those for metal- and oxygen-rich AlO_X/PET. Helium has a yet higher MEPPP under these experimental conditions, and the differences between the MEPPPs for the three barrier films is more pronounced than the argon case: the He MEPPP for oxygen-rich AlO_X/PET is significantly

higher than for Al/PET, itself slightly higher than that for metal-rich AlO_x/PET.

2.3.3 Gas barrier improvement factors

Consideration of the improvement in gas barrier upon AlO_x coating is made in this section; data is presented in Figure 2.3.3.1. The gas barrier improvement factor is calculated by dividing the MEPPP of uncoated PET for each gas by the MEPPP for the respective gas as determined for the coated samples. Gas barrier improvement is gas-dependent, and this gas-dependence varies with stoichiometry of the gas barrier coating as in the previous section: oxygen and argon gas barrier improvements are affected little by deposition conditions while the helium improvement factor depends strongly upon the type of coating. Metallization and metal-rich AlO_x deposition improve the He gas barrier to a greater extent than does oxygen-rich AlO_x deposition. Metal-rich AlO_x deposition attenuates He transport better than metallization.

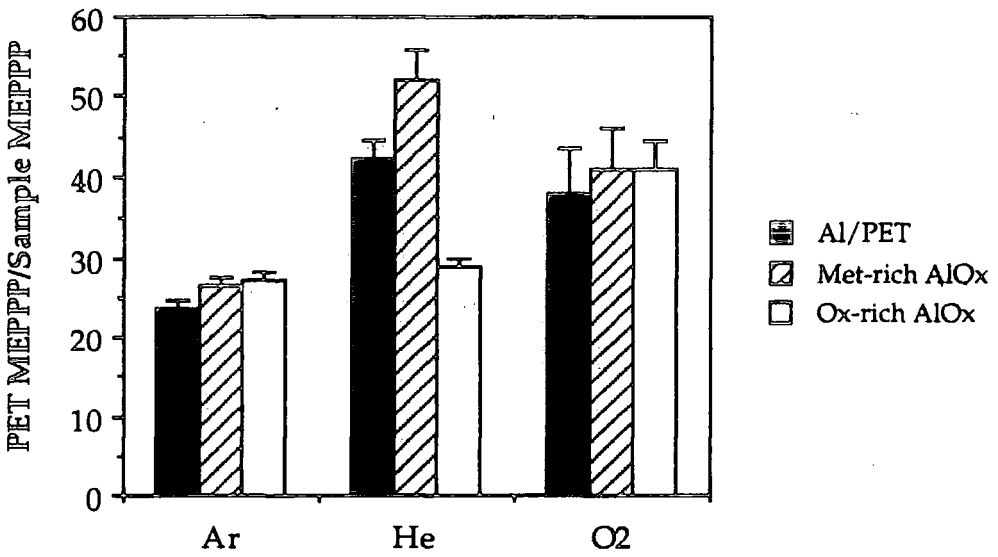

Figure 2.3.3.1: Gas barrier improvement factors for Al/PET, and metal- and oxygen-rich AlO_X/PET.

2.3.4. Permselectivities of AlO_X/PET films

Permselectivity is calculated by dividing the MEPPP of He and O_2 by the Ar MEPPP. Argon was chosen since it has similar MEPPPs for all AlO_X gas barriers and will not be susceptible to reactions in UHV as oxygen can be. Hence an insight can be gained into the mechanism of gas transport through the gas barrier film by comparing the selectivities with those of the uncoated polymer system.

	Permselectivity (rel. to Ar)	
Sample	He	O_2
Al/PET	32.56 ± 1.53	0.69 ± 0.10
Metal-rich AlO_X/PET	29.43 ± 1.91	0.71 ± 0.09
Oxygen-rich AlO_X/PET	54.71 ± 2.18	0.74 ± 0.06
PET	57.74 ± 0.90	1.10 ± 0.02

Table 2.3.4.1: Permselectivities (relative to Ar) of He and O_2 for Al/PET, and metal- and oxygen-rich AlO_X/PET.

Permselectivity data, Table 2.3.4.1 and Figures 2.3.4.1 (a) and (b), show that the selectivity of AlO_X/PET gas barrier films varies with deposition conditions used. Helium permselectivity of Al/PET and metal-rich AlO_X/PET, Figure 3.3.4.1 (a), are within experimental error of each other, with a value of ~30, substantially lower than the values for oxygen-rich AlO_X/PET and uncoated PET, both ~55. Oxygen permselectivity displays different behaviour, however, Figure 3.3.4.1 (b): the values for all three gas barrier films fall within experimental error at ~0.7, appreciably lower than that of uncoated PET with its value of ~1.1. Oxygen gas transport relative to argon is therefore relatively insensitive to the deposition conditions used whereas helium transport relative to argon is affected differently by the different deposition conditions: the metal-rich and metallized deposition environments result in coatings which block the transport of helium more effectively than oxide coating.

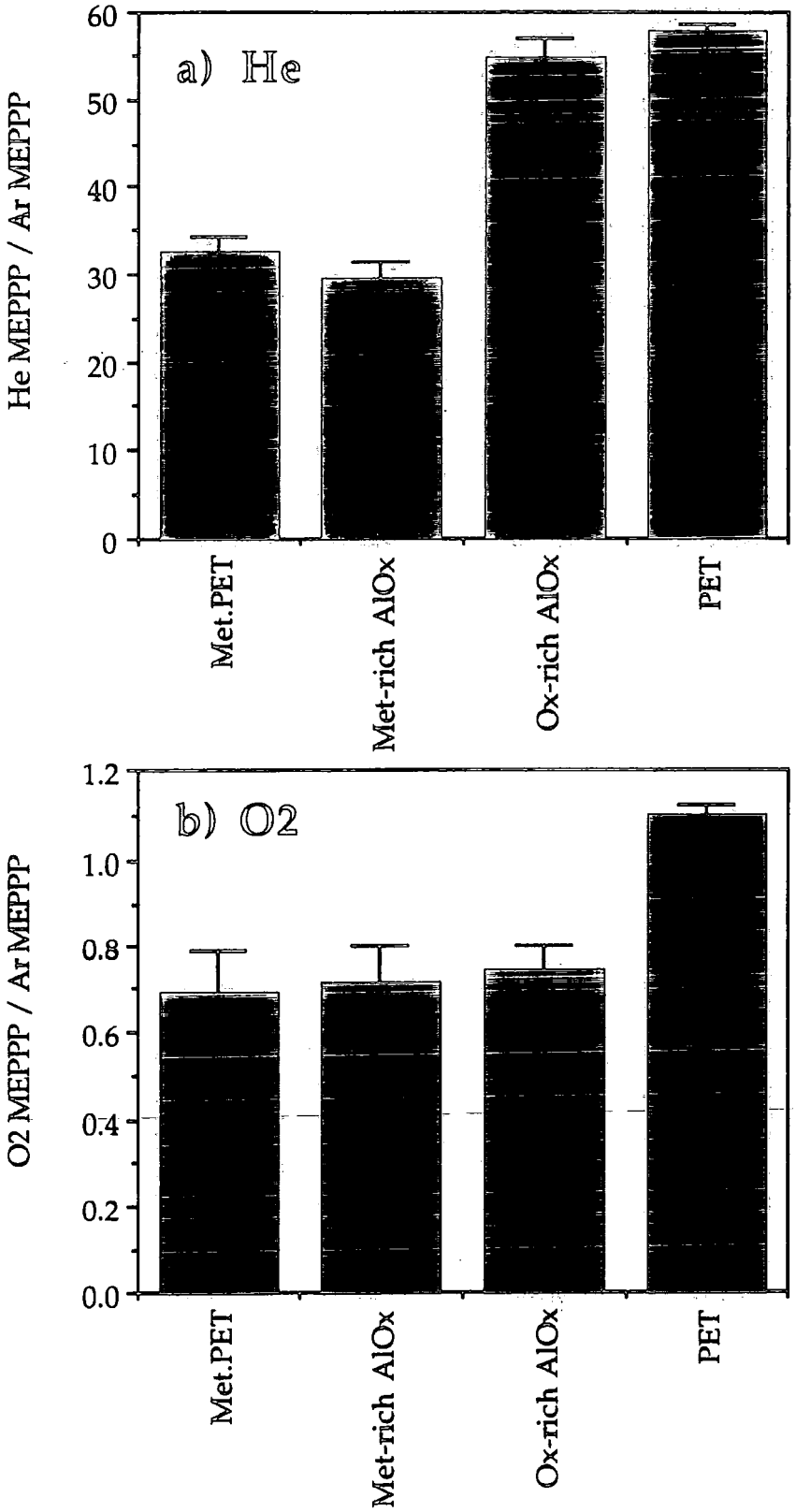

Figure 2.3.4.1: He and O_2 permselectivities compared for Al/PET, metal- and oxygen-rich AlO_x/PET, and uncoated PET.

2.3.5 AlO_x barrier coating etching

MEPPPs of Ar, He, and O_2 for all three etched barrier films are compared with those for uncoated PET in Table 2.3.5.1. For oxygen and argon, MEPPP values are greater for the etched films than uncoated PET in all cases, showing that removal of the barrier layer by HCl-etching does lead to complete loss of gas barrier. In the case of He, the MEPPPs observed for metal- and oxygen-rich AlO_x/PET are greater than those of the uncoated substrate while that of Al/PET is slightly less. Some residual gas barrier to helium is present in the case of Al/PET.

	MEPPP (10^{-9} Torr)		
Sample	Ar	He	O_2
HCl-etched Al/PET	1.10 ± 0.05	42.69 ± 2.16	1.23 ± 0.04
HCl-etched metal-rich AlO_x/PET	1.24 ± 0.06	57.45 ± 5.27	1.19 ± 0.17
HCl-etched oxygen-rich AlO_x/PET	1.31 ± 0.00	67.98 ± 1.82	1.16 ± 0.04
PET	0.93 ± 0.01	53.70 ± 0.62	1.02 ± 0.01

Table 2.3.5.1: Mean equilibrium permeant partial pressures of argon, helium and oxygen for HCl-etched Al/PET, metal- and oxygen-rich AlO_x/PET, and untreated PET.

2.4 DISCUSSION

2.4.1 Experimental apparatus

The experimental apparatus developed during the course of this work has reproducibly monitored the transport of gases through many polymer films, with and without coatings. When contrasting this system with those of Laurenson and Dennis [25], and Holden *et al.* [24], it is noteworthy that this author's system combines the good points of both systems with, hopefully, the bad points of neither, *i.e.*, the partial pressures are measured as by Laurenson and Dennis and the gas supply and sample handling procedures are similar to those of Holden *et al.*

2.4.2 Gas barrier improvement factors

Previously, gas-dependent gas barrier improvement factors have been rationalized by suggesting that selective molecular flow through defects in the metal layer occurs when the defect size is smaller than the mean free path of the permeating species [29,34]. This approach neglects the mechanism of permeation in polymers as outlined in previous sections of this chapter wherein discussions concerning the influence of microscopic polymer structural effects upon the gas transport properties were presented. Both hypotheses fit this study's experimental data since helium has the smallest diameter and longest mean free path of the penetrants considered and would therefore be affected the most by either mechanism. This data is analogous to the gas selectivities observed for PET deposited with SiO_2 [34]: in this study the authors did not improve the He gas barrier yet did so for every other gas considered. Differentiation between the two mechanisms requires chemical and microstructural studies of these systems.

2.4.3 Permselectivities

Permselectivity data shows that the mechanism responsible for the imperfect gas barrier of these materials must operate at a level which affects different gases according to their properties, and that this mechanism is the same for both metal-containing coatings. The presence of very large defects such as those discussed by Jamieson and Windle [31], and Mercea *et al.* [28-30] would not account for this. Again, this leaves either very small-scale defects or the chemistry of the layers and their interphases with the base polymer as the cause of the observed effects

Permselectivities of the AlO_X/PET films show that the transport of oxygen through the coated films is easier to attenuate than the transport of helium. The major difference between these two penetrants is their diameter: that of helium is substantially smaller than that of oxygen.

2.4.4 Barrier film removal

Lack of gas barrier after etching of the deposited metal layer is consistent with a previous study [29] in which the authors claimed that no modification of PET's permeation behaviour had occurred at the metal/polymer interface. A caveat should be introduced at this point: no modification of the permeation behaviour of PET has occurred at the metal/polymer interface *as probed by these experimental conditions.* It is quite possible that etching in hydrochloric acid has removed the modified species at the metal/polymer interface responsible for gas barrier effects, should they in fact exist.

2.5 CONCLUSIONS

- A novel mass spectrometric permeability analysis system has been developed for application to flexible polymer films.

- Reactive evaporation of aluminium oxide onto PET leads to gas barrier composites with similar performance to conventional metallized film.

- Gas barrier and permselectivities are a function of the permeant gas-coating chemistry combination.

- Helium (which has the smallest diameter of the gases studied) gas barrier is affected differently by the deposition parameters employed whereas those of argon and oxygen are relatively insensitive. This correlates with effects observed for polymer systems wherein smaller penetrants are affected more by microscopic structural changes.

- The presence of unoxidized aluminium metal in the AlOx layers results in better gas barrier to helium for Al/PET and metal-rich AlO_x/PET

- No significant gas barrier is found after the coatings are removed by etching, eliminating the possibility that a robust interfacial 'skin', resistant to acid attack, is responsible for gas barrier.

2.6 ACKNOWLEDGEMENTS

- Mr. Jim Hodgson, Mr. Mel Higham and Mr. Neil Holmes, Chemistry/Biology Mechanical Workshops, University of Durham, for the construction of the permeability probe.
- Mr. George Rowe and Dr. Tony Royston, Chemistry Department, University of Durham, for the development of the quadrupole mass spectrometer interface, and data accumulation and analysis software, respectively.

2.7 REFERENCES

[1] P. Mercea, L. Muresan, V. Mercea, D. Silipas, I. Ursu, *J. Memb. Sci.* **35** (1988), 291.

[2] C. E. Rogers, in *Polymer Permeability*, Ed. J. Comyn, Elsevier, London, 1985, Chapter 2.

[3] T. M. Aminabhavi, V. S. Aithal, *J. Macromol. Sci. Rev. Macromol. Chem. Phys.* **C31** (1991), 117.

[4] L. Jia, J. Xu, *Polym. J.* **23** (1991), 417.

[5] R. M. Conforti, T. A. Barbari, P. Vimalchand, M. D. Donohue, *Macromolecules* **24** (1991), 3388.

[6] R. J. Pace, A. Datyner, *J. Polym. Sci. Polym. Phys.* **18** (1980), 1103.

[7] V. Stannett, in *Diffusion in Polymers*, Eds. J. Crank, G. S. Park, Academic Press, London, 1968, Chapter 2.

[8] W. J. Koros, R. T. Chern, V. Stannett, H. B. Hopfenberg, *J. Polym. Sci. Polym. Phys.* **19** (1981), 1513.

[9] J. S. Vrentas, C. M. Vrentas, *Macromolecules* **24** (1991), 2404.

[10] I. C. Sanchez, P. A. Rodgers, *Pure & Appl. Chem.* **62** (1990), 2107.

[11] J. L. Valles, J. W. Halley, *J. Chem. Phys.* 92 (1990), 694.

[12] J. Comyn, in *Polymer Permeability*, Ed. J. Comyn, Elsevier, London, 1985, Chapter 1.

[13] J. Crank, G. S. Park, in *Diffusion in Polymers*, Eds. J. Crank, G. S. Park, Academic Press, London, 1968, Chapter 1.

[14] R. J. Pace, A. Datyner, *J. Polym. Sci. Polym. Phys. Ed.* 17 (1979), 465.

[15] C. A. Kumins, T. K. Kwei, in *Diffusion in Polymers*, Eds. J. Crank, G. S. Park, Academic Press, London, 1968, Chapter 4.

[16] R. J. Pace, A. Datyner, *J. Polym. Sci. Polym. Phys. Ed.* 17 (1979), 437.

[17] R. J. Pace, A. Datyner, *J. Polym. Sci. Polym. Phys. Ed.* 17 (1979), 453.

[18] P. V. Krishna Pant, R. H. Boyd, Macromolecules 25 (1992), 494.

[19] F. Mueller-Plathe, *J. Chem. Phys.* 96 (1992), 3200.

[20] F. Muller-Plathe, S. C. Rogers, W. F. van Gunsteren, *Macromolecules* 25 (1992), 6722.

[21] F. Muller-Plathe, S. C. Rogers, W. F. van Gunsteren, *J. Chem. Phys.* 98 (1993), 9895.

[22] R. M. Sok, H. J. C Berendsen, W. F. van Gunsteren, *J. Chem. Phys.* 96 (1992), 4699.

[23] J. A. Slee, G. A. J. Orchard, D. I. Bower, I. M. Ward, *J. Polym. Sci. Polym. Phys. Ed.* 27 (1989), 71.

[24] P. S. Holden, G. A. J. Orchard, I. M. Ward, *J. Polym. Sci. Polym. Phys. Ed.* 23 (1985), 709.

[25] L. Laurenson, N. J. M. Dennis, *J. Vac. Sci. Technol.* A3 (1985), 1707.

[26] P. J. Nash, *Vacuum* 37 (1987), 643.

[27] W. Prins, J. J. Hermans, *J. Phys. Chem.* 63 (1959), 716.

[28] P. Mercea, L. Muresan, V. Mercea, *J. Memb. Sci.* 24 (1985), 297.

[29] P. Mercea, L. Muresan, V. Mercea, D. Silipas, I. Ursu, *J. Memb. Sci.* 35 (1988), 291.

[30] T. A. Beu, P. Mercea, *Mater. Chem. Phys.* 26 (1990), 309.

[31] E. H. H. Jamieson, A. H. Windle, *J. Mater. Sci.* 18 (1985), 64.

[32] J. Weiss, *Thin Solid Films* 204 (1991), 203.

[33] Vacuum Generators pressure measurement technical information.

[34] P.-V. Mercea, M. Bartan, *J. Memb. Sci.* 59 (1991), 353.

CHAPTER 3

AN XPS STUDY OF THE SURFACE AND INTERFACIAL CHEMISTRY OF AlO_x/POLYMER FILMS

3.1 INTRODUCTION

Chapters 1 and 2 have shown that the introduction of oxygen into an adapted metallization chamber leads to AlO_x/PET composite structures that exhibit similar gas barrier behaviour to conventional metallized polymers. Gas barrier improvement factors and permselectivities of these structures are affected by coating deposition conditions. The aim of this chapter is to probe the chemistry of both the AlO_x layers themselves and the AlO_x/PET interphases using X-ray photoelectron spectroscopy (XPS).

Previous work on metal-polymer interfaces can be divided into two broad categories: studies designed to develop understanding of metallization as employed in the semiconductor industry, mainly using polyimides as substrate materials, and those for other applications, including gas barrier packaging and decorative products. Within each of these areas of work, two main approaches have been adopted. Firstly, *in situ* , low rate metal deposition under UHV conditions followed by analysis, aiming to probe the changes in composition and electronic structure as a function of deposited metal coverage without the presence of contaminants [1]. And, secondly, post-deposition analysis of samples prepared under industrial or simulated industrial conditions [2-5]. Clearly these two *modus operandi* are attacking the same problem from opposing ends of the technical spectrum. The former, a building-up under strict experimental control, contrasts with the

latter, designing experiments to probe the (buried and inaccessible) metal-polymer interface indirectly.

Burkstrand has outlined the general principles gained from his XPS studies of Cu, Ni and Cr deposited onto polystyrene (PS), polyvinyl acetate (PVAC), polyethylene oxide (PEO), polymethyl methacrylate (PMMA) and polyvinyl alcohol (PVA) [6]. After metal deposition onto oxygen-containing polymer surfaces, the metal atom can interact strongly with the oxygen-containing groups on the surface, forming a metal-oxygen-carbon complex. Extents of reaction for the different metals are rationalized in terms of the dissociation energy of the metal oxides: that for copper oxide is less than that of those of nickel and chromium, correlating with the lesser degree of XP spectral modification observed upon deposition of this metal.

Adhesion of the metal to the polymer is of prime importance in many applications. Several factors are thought to contribute to the performance of the composite in this area [7,8]: mechanical interlocking; elimination of weak boundary layers; electrostatic forces; and chemical bonding. Clearly XPS can only probe the chemical factors responsible for the adhesion.

3.1.1 Metal/polyimide interfaces

By far the greatest attention has been paid to this area of metallization technology because of its importance in microelectronics' fabrication [9], an area of enormous economic significance, where metal-polymer interfacial integrity and stability is of prime importance.

Much attention has been addressed to the contrasting metals Cu and Cr, weakly and strongly interacting, respectively. Preferential attenuation of XP features characteristic of carbonyl groups is observed for Cr deposition [1]. Cu deposition, on the other hand, attenuates all features more evenly,

leading to the conclusion that the metal-polymer interaction is non-selective. Hence the reactivity of the metal influences the sites attacked upon deposition. In the case of d-block elements this reactivity has been linked to the number of d-electrons in the atom: the greater the number of d-electrons, the less reactive the metal at the metal/oxygen-containing polymer interface.

The task of bridging the gap between surface sensitive studies and the macroscopic phenomena of interest has been aided by the use of microstructural tools to elucidate the location and abruptness of the metal-polymer interface. Transmission electron microscopy (TEM) has shown that weakly reacting metals (such as Cu) agglomerate within the polyimide itself, beneath the polyimide surface, while metals exhibiting stronger chemical interactions (such as Cr) form a sharp interface [1]. While no definitive statement can be made concerning the possibility of atomic scale interdiffusion at the metal-polymer interface, it appears that Cu atoms, preferring to interact with themselves and not the polyimide, diffuse into the polymer and lower their energy by agglomeration [10]. No cluster formation is seen for Al/polyimide interfaces. Static SIMS studies of Cu and Cr layers deposited onto polyimide which were peeled apart [9] showed that, despite the difficulties in interpreting the SIMS data for the metal-polymer interfaces: failure occurs in an organic layer for both Cu and Cr. Metal-organic complexes observed are different for the two metals; and, after annealing, the Cu interface approaches the composition of the Cr interface. Cr disrupts the polymer's structure more than the less reactive metal Cu. However, this does not seem to be intrinsic to the system since annealing appears to provide the energy necessary for more effective intermixing of the Cu and polyimide. Not only is the chemistry of the system dictated by the reactivity of the metal with the polymer but also some physical properties.

3.1.2 Al/PP interfaces

The driving force for much of this work has been adhesion improvement of the metal to the polymer [2-5,11]. Polypropylene has a low surface polarity [12]. Pretreatments are employed to enhance adhesion. Andre *et al.* [2-5] have used nitrogen and ammonia plasmas to improve the adhesion of *in situ* aluminized samples (layer thickness 15-30 nm, deposited by thermal evaporation). Adhesion improvement was independent of the observation of nitrogen-containing functional groups by XPS, and, from SIMS results, is assigned to the removal of hydrophobic, low molecular weight hydrocarbon species. The Al/PP interfacial oxide thickness is independent of sample preparation conditions at ~4 nm.

Modification of the chemical properties of PP is also achievable by the addition (by extrusion) of maleic-anhydride-grafted low molecular weight PP to untreated PP [12]. Higher maleic anhydride concentrations led to higher surface polarities. Adhesion properties exhibited a non-linear dependence upon the maleic anhydride concentration: this was rationalized in terms of two competing effects. At low concentrations, bond formation between the aluminium and polymer is enhanced by the presence of the maleic anhydride while higher concentrations lead to the presence of a weak boundary layer which reduces the measured adhesion of the sample.

3.1.3 Metal/PET interfaces

Much information can be gathered by comparing the metallization chemistry and adhesion performance of PET with a polymer containing no oxygen [7]. PET presents three possible reaction sites: carbonyl oxygen; ether oxygen; and π-electrons of the phenyl ring. PE, on the other hand, does not contain any selective reaction sites. *In situ* plasma treatments and Ag

deposition were performed in UHV, and the surface chemistry and adhesion of the product films were monitored [7]. Adhesion of Ag on untreated PET is much greater than that of Ag on untreated PE. Argon plasma treatments did not improve the adhesion whereas oxygen plasma treatments did. XPS shows that no interaction between Ag and untreated PE takes place. Introduction of ~12 % of oxygen into the surface region by the oxygen plasma leads to the observation of an Ag-O-C complex upon metal deposition *via* XPS chemical shifts. For the PET case, preferential attenuation of the carbonyl feature of the C 1s XP spectrum indicates that an Ag-O-C complex is formed. Intensity loss of the π-π^* shake-up is analyzed with caution since it is known that changes in the electronic properties of phenyl ring substituents can change the observed intensity of this feature. Oxygen plasma treatments of both substrates results in substantial increases in adhesion. Surface chemistry changes upon deposition are greater for treated PET than those for the untreated samples. Ag deposition onto PET [13], performed under UHV conditions, results in preferential reaction of the carbonyl groups, the number of reaction sites being increased by plasma treatment of the polymer substrate and the concomitant introduction of acid groups.

Ion plating [14], in which evaporated metal (Co in this case) is given kinetic energy by passing through a plasma and an accelerating potential, also results in increased adhesion.

Interfacial adhesion of sputter deposited Pd on PET [15] suggests the importance of interfacial oxidation for the adhesion of metal layers on polymers: high energy Pd atoms impinge on the PET and undergo oxidation, the oxygen for this process originating from either the polymer structure itself or the sputtering atmosphere when oxygen is introduced. The interfacial oxide is thicker than for samples prepared by simple evaporation.

3.1.4 Al/PET interfaces

Bou *et al.* recently studied the interfacial chemistry of Al/PET [16]: aluminium was resistively evaporated onto commercially available PET film (filler free with no cleaning or pretreatment prior to the experiments) under UHV conditions (10^{-10} Torr). At very low coverages the authors interpret their XPS results in terms of Al-O-C complex and aluminium cluster formation. Interfacial complex formation is observed most easily by monitoring the C 1s XP lineshape: the emergence of a feature at 283.7 eV (285.0 eV C-H reference) at low coverages; Al-C formation at higher coverages; and the preferential intensity decay of the C 1s feature assigned to the C=O group of the polymer structure support this assertion. Bou *et al.* conclude that interfacial complex formation occurs by complete reaction of the carbonyl groups, and partial reaction of the ether linkages and phenyl rings, with impinging aluminium atoms, the propensity for reaction following the trend of basicity of the polymer's functional group. A similar study by Silvain *et al.* [17] reinforces the idea that Al-O-C interfacial complex formation is important.

Several papers have been published which originate from Du Pont de Nemours in Luxembourg [18,19], generally pertaining to the more industrially applied aspects of metal-polymer adhesion. Recently, the influence of PET preparation parameters upon the adhesion and surface chemistry of the Al/PET composite has been studied [19]. Biaxially stretched PET films were prepared using different tensions and heat-setting conditions, thereby altering such properties as crystallinity, density and mechanical strains. Resultant films were then metallized under moderate vacuum (~10^{-4} Torr) to a nominal thickness of 50 nm and tested for adhesion. ISS results showed that differences in adhesion could be

rationalized in terms of three possible interfacial failure mechanisms: Type I, when the two peeled surfaces had compositions corresponding to PET and carbon; Type II, when both surfaces indicated the presence of aluminium-carbon mixed phases; and Type III; when one surface corresponded to PET and the other to an Al-O-C complex. Type II failure corresponds to the higher peel strengths, while both Types I and III lead to failure at lower peel strengths. Modification of the PET surface characteristics by heat transfer from the metal source has been considered under these deposition conditions where substrate temperatures of 140°C have been reported. Indeed, control of substrate temperature during metallization is one of the crucial variables in the deposition process since thin polymer films are heat-sensitive [20]. Diffusion between the polymer and incident metal is possible. RBS and SIMS experiments profiled the interfaces of samples exhibiting high and low peel strengths, determining that the interfaces of well-adhered samples were broader than those exhibiting poorer adhesion. Oxygen content is also lower at the interface corresponding to good adhesion, and aluminium grain sizes are smaller. Rationalization of the latter two effects was made in terms of adatom mobility on the surface: good adhesion, resulting from decreased adatom mobility, results in smaller grain sizes.

Plasma polymerization of acrylic and methacrylic acid onto PET substrates was found to increase the adhesion of aluminium layers by between 5 and 10 times following the introduction of polar functionalities (C-O, C=O, C=N) [18].

While most of the literature concerning the interfacial and surface chemistries of metallized polymer substrates deals with slight variations in experimental conditions, a recent paper [21] monitored changes in the surface chemistry and physical characteristics of the uncoated polymer films against their adhesion after metallization. Two samples were metallized: biaxially oriented PET and a poly (ethylene isophthalate-co-ethylene sodium

sulphoisophthalate)-coated PET, coated to a thickness of ~5 nm. The authors suggest that the adhesion of aluminium to the polymer films is dictated by two phenomena: firstly, the chemical interaction and, secondly, the mechanical interaction. Chemical observations at the metal-polymer interface show that the chemistry is the same, namely the presence of functionalities assigned to aluminium oxide and Al-O-C, the latter attributed to reaction between aluminium and the products of thermal degradation of the polymer, vinyl and carboxylic acid end-groups. TEM, however, indicated that the metal penetrated the copolymer coating to ~5 nm, *i.e.*, the coating's thickness, while very little penetration was observed for PET. The copolymer's lower crystallinity, glass transition temperature and melting point add to the plausibility of this hypothesis.

3.1.5 Surface chemistry of aluminium

The true gas barrier of metallized films has been assigned to a few nanometres of oxide that forms on the aluminium surface upon exposure to air [22]. Aluminium is a reactive metal, oxidizing readily in air to form a stable oxide surface [23] (thickness between 4-5 nm [24,25]) at both the outer and inner surfaces of the metal, protecting it from any further chemical attack due to its high electrical resistivity, preventing the electron flow necessary for the reaction [22] $O_2 + 4e^- \rightarrow 2O^{2-}$. The oxide's larger molecular volume (1.5 x that of aluminium metal) leads to compressive forces within the oxide film and prevents the exposure of fresh metal to the oxidizing atmosphere [24]. The oxide layer is amorphous when formed at low temperatures [26] with a structure thought to be similar to that of γ-Al_2O_3 [24] and hydrates readily [27] to form aluminium oxide hydroxides, AlO(OH), or hydroxides, $Al(OH)_3$.

Hydration of aluminium foil has been investigated industrially by Thorne *et al.* [28] with particular reference to adhesion performance. The authors had found that the adhesion levels exhibited by their aluminium foils to PE followed a seasonal pattern, being higher in the cooler and drier conditions of the winter than in the warmer and more humid summer. Oxygen 1s XPS showed that after extended periods (110 days) of storage under humid conditions the lineshape changes considerably, becoming broader and flatter as the component assigned to O-H increases at the expense of that assigned to O-Al. Conclusions were that the formation of hydroxides on the surface of the aluminium foil was irreversible but that storage under dry conditions resulted in the loss of weakly bound water and a consequent increase in the adhesion between the foil and polymer. Other workers [24] state that distinguishing between oxide and hydroxide species on the aluminium oxide surface is not possible via XPS since the O 1s binding energies are very close.

3.1.6 X-ray photoelectron spectroscopy

Under illumination of a sample by sufficiently energetic photons, one or more of the following photoionization processes can occur [29]: core-level ionization; X-ray fluorescence; or Auger processes. Core-level ionization is associated with the XPS experiment since these processes provide the technique with its beneficial qualities, namely the chemical shift information. Also, X-ray photoelectron spectroscopy is preferred for studying polymer systems since Auger spectra are more difficult to interpret as the process is two-electron in nature [30], and the surface damage induced by the incident beam is lower. Photoemission and Auger processes are represented schematically in Figure 3.1.6.1.

Critical parameters for the light source for the XPS experiment are the energy of the photons, their energy distribution and intensity. Line sources are common, typically either Al or Mg Kα X-rays. Their widths are, respectively, 0.85 and 0.7 eV. The use of these elements arises from the compromise between their sufficiently high energy and the lack of breadth characteristic of 'harder' radiation such as Cr Kα.

Photoelectron spectroscopies are best summarized as techniques for determining the binding energies of electrons emitted from solids irradiated with monoenergetic photons [30] as refined by Siegbahn. When compared with the other available surface-sensitive spectroscopies, electron spectroscopies are often preferred because: the information depth is small; electrons are easily counted and detected; and they can be analyzed readily for both energy and angular distributions. Binding energies are determined by use of the following equation:

- $E_{kin} = h\nu - E_b - e\Phi_{sp}$

where E_{kin} is the measured kinetic energy of the photoelectron, hν is the energy of the irradiating photons, E_b is the binding energy of the electron whose kinetic energy is measured, and $e\Phi_{sp}$ is a term correcting the observed binding energies for the effect of the work function of the spectrometer/sample entity since this may be different from that of the sample alone. Conservation of linear momentum dictates that the partition of energy occurs in inverse proportion to mass. The electron therefore carries virtually all of the energy away from the photoionization process [29]. The binding energies of photoemitted electrons are affected by electrostatic interactions with valence electrons of the sample [30], and can therefore yield important information on that bonding.

Koopman's theorem assumes that all other electrons in the system apart from the photoionized electron are frozen in their orbitals and are unaffected by the process. Thus the ionization energy of the electron is taken to be the energy of the orbital from which it departed. Although there have been doubts about the validity of this theorem, it is, nonetheless, extensively applied to spectral interpretation.

Information from the XPS experiment is 'carried' from the sample to the analyzer courtesy of the energy and momentum of the electron [31]. Scattering events, either elastic or inelastic, can result in the loss of that information. In this instance, inelastic scattering is the main concern. Such processes arise from electron-electron or electron-phonon interactions. The escape depth (d) of an electron of inelastic mean free path (λ) at a take-off angle (α) is given by:

- $d = 3\lambda\sin\alpha$

The inelastic mean free path is dependent upon the energy of the electron, passing through a minimum of just over one atomic layer at ~30 eV, Figure 3.1.6.2.

Electron analyzers are of two main types: retarding potential and dispersive analyzers. The former relies upon the application of a retarding potential prior to detection, and the effect of the retarding potential upon the transmission of electrons of differing energies. Electron analysis for XPS is typically dispersive. Commonly used for the XPS experiment is the concentric hemispherical analyzer. The basis of operation is that an electron will follow the equipotential surface between two hemispheres held at an electric potential under the conditions:

- $E_O = e\Delta V/[(R_2/R_1) - (R_1/R_2)]$

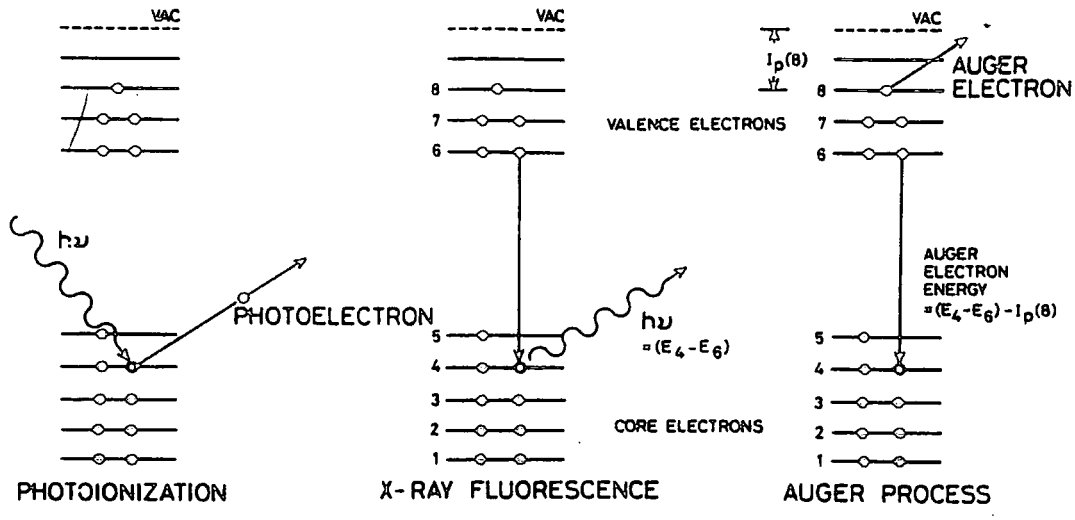

Figure 3.1.6.1: Schematic representation of photoemission and Auger processes.

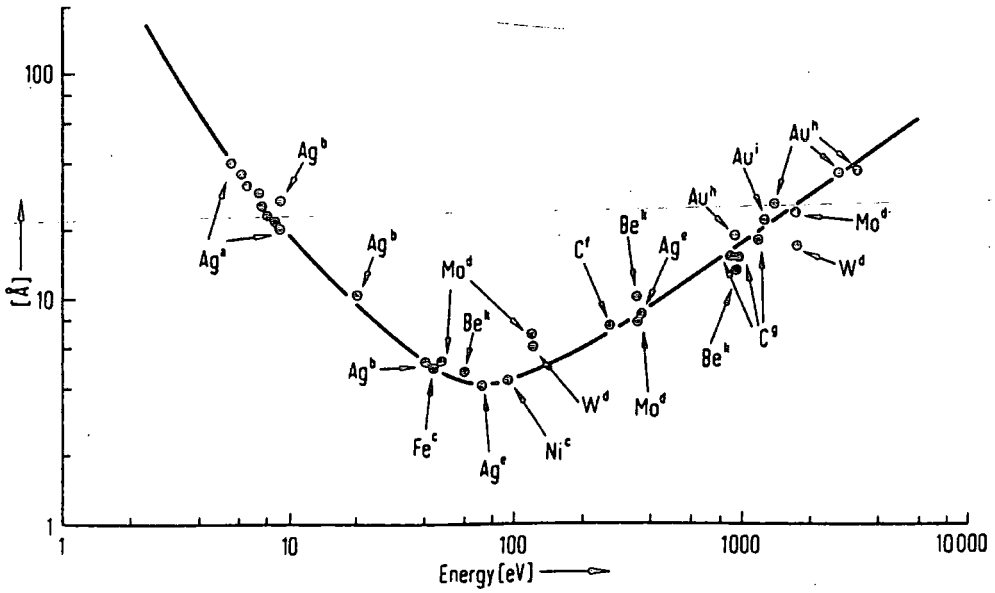

Figure 3.1.6.2: Electron inelastic mean free path versus electron kinetic energy.

where R_2 and R_1 are the radii of the outer and inner hemispheres, respectively, e is the electronic charge, E_o is the energy of the electron and ΔV is the potential difference between the hemispheres.

3.2 EXPERIMENTAL

3.2.1 Sample definition

Samples were analyzed as-received and are defined in Chapter 1. Hydrochloric acid etching was performed as outlined in Chapter 2.

3.2.2 XPS

X-ray photoelectron spectra were accumulated on a Kratos ES300 surface analysis instrument. Base pressure of 1×10^{-9} Torr was maintained by a turbomolecular pump (Alcatel) backed by a mechanical rotary pump (Edwards), and an ion pump (Varian). X-ray excitation was provided by a differentially pumped (Varian ion pump) dual anode X-ray source using the magnesium anode (Mg Kα line, 1253.6 eV) operating at an anode voltage of 12 kV and an emission current of 10 mA. Photoemitted electrons were collected at a take-off angle of 30°C to the surface normal and analyzed with a concentric hemispherical analyzer operating in the constant retarding ratio mode (CRR, 22:1). Sample insertion was realized by means of a rotatable gate (or ball) valve pumped by a mechanical rotary pump (Edwards, base pressure 5×10^{-2} Torr). Elemental sensitivity factors used for data analysis were determined experimentally and are as follows: carbon 1s, 1.00; oxygen 1s, 0.59; and aluminium 2p, 1.02.

The spectrometer was calibrated to the Au $4f_{7/2}$ level at 83.8 eV and the Ag $3d_{5/2}$ level at 367.9 eV. All binding energies are referenced to hydrocarbon at 285.0 eV.

Data accumulation and component peak analysis was performed on an IBM-compatible personal computer running software developed in-house.

3.2.3 Argon ion sputter depth profiles

Argon ion sputter depth profiles were performed on a Vacuum Generators CLAM 100 surface analysis instrument. Base pressure of 2×10^{-10} Torr was maintained by an oil diffusion pump backed by a mechanical rotary pump (Edwards). X-ray excitation was provided by a dual anode X-ray source using the magnesium anode (Mg Kα line, 1253.6 eV) operating at an anode voltage of 12 kV and an emission current of 20 mA. The electron energy analyzer (concentric hemispherical, multi-channel detector) was operated in constant analyzer energy mode (CAE) at a pass energy of 50 eV and an electron take-off angle of 20° to the surface normal, typically operating under the following conditions: 0.05 eV steps, electron counting for 0.5 seconds, over a 20 eV range. Sample insertion was realized by means of a modified gate valve, the atmospheric side of which was pumped by a rotary pump (1×10^{-3} Torr base pressure). Argon ion sputtering was carried out using a cold cathode ion gun (Vacuum Generators AG21) operating at a pressure of 2×10^{-6} mbar of argon (British Oxygen Company, Research Grade), 3 keV beam energy (characteristic energy spread 1-2%), and a constant ion beam current of 1 μA. An IBM-compatible personal computer was used for data accumulation and component peak analysis.

3.3 RESULTS

3.3.1 Surface XPS

3.3.1.1 Polymer film substrates

Elemental compositions, both experimental and theoretical, of PP and PET are shown in Table 3.3.1.1.1.

Sample	Experimental % C content (theoretical)	Experimental % O content (theoretical)
PET	71.9 ± 1.5 (71.4)	28.1 ± 1.5 (28.6)
PP	84.5 ± 0.2 (100)	5.5 ± 0.2 (0)

Table 3.3.1.1.1: Experimentally determined and theoretical proportions of carbon and oxygen in PP and PET.

Uncoated PET exhibits features in its XP spectrum attributed to carbon and oxygen functionalities, Figure 3.3.1.1.1 (a) and (b), respectively. Experimentally determined ratios of the polymer's functional groups agree well with theoretical and literature values [13], Table 3.3.1.1.1. XP lineshapes of PET C 1s spectra were fitted with three major components: C-H at 285.0 eV; C-O at 286.6 eV; and C=O at 289.0 eV. π-π^* shake-ups at 291.5 eV were also observed. As found in previous work [13], the ratio of the main components was found to be 3:1:1. The O 1s region of the PET XP spectrum could be fitted with two peaks: C=O, 532.9 eV; and C-O, 533.9 eV [13].

Polypropylene film used for metallization is corona treated in order to improve adhesion. Figure 3.3.1.1.2 (a) and (b) are C 1s XP spectra of untreated and corona treated polypropylene, respectively: the former

spectral feature is more symmetric than the latter since corona treatment introduces oxygenated functionalities into the polymer's surface, and these functionalities give rise to photoelectrons of lower kinetic energy than those characteristic of purely hydrocarbon environments. The degree of polypropylene oxygenation is, however, much smaller than that found for PET. Figure 3.3.1.1.3 (a) and (b) are O 1s XP spectra of the untreated and corona treated PP films. Introduction of oxygenated functionalities is evident.

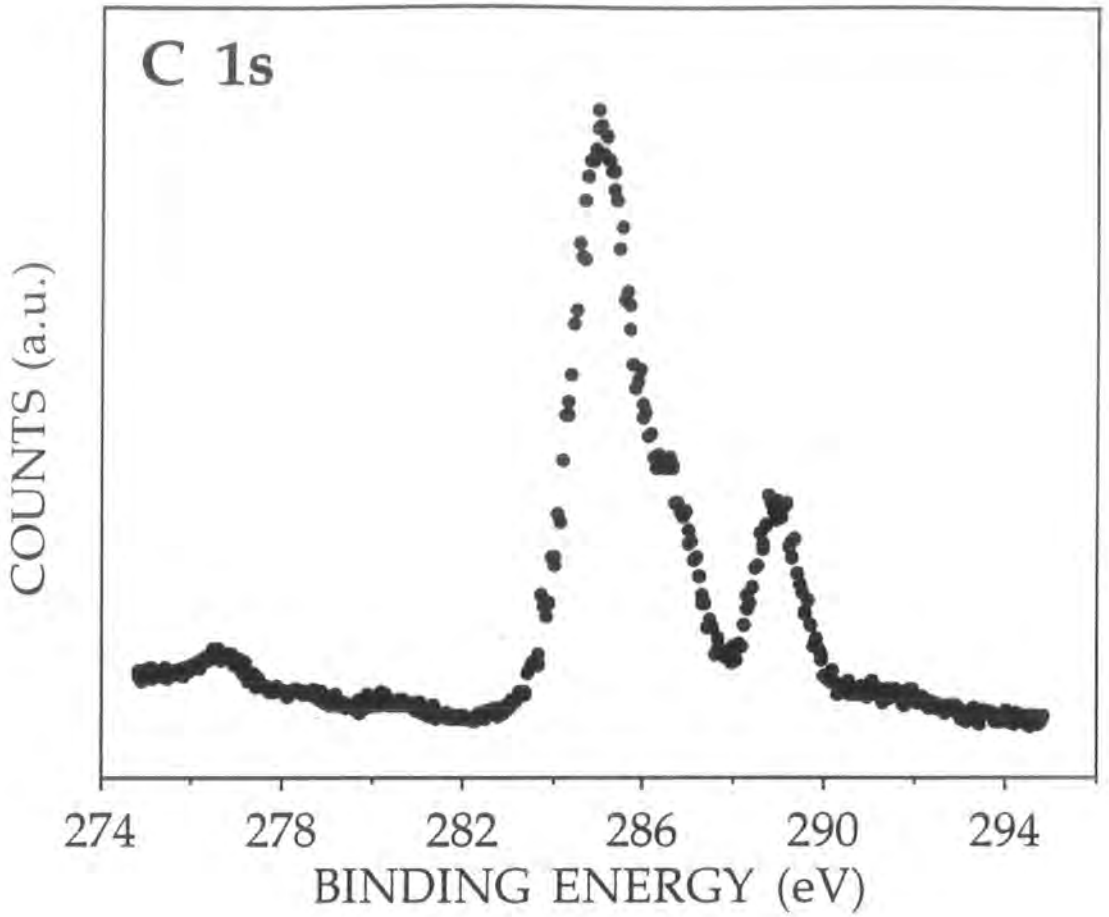

Figure 3.3.1.1.1 (a): C 1s XP spectrum of PET.

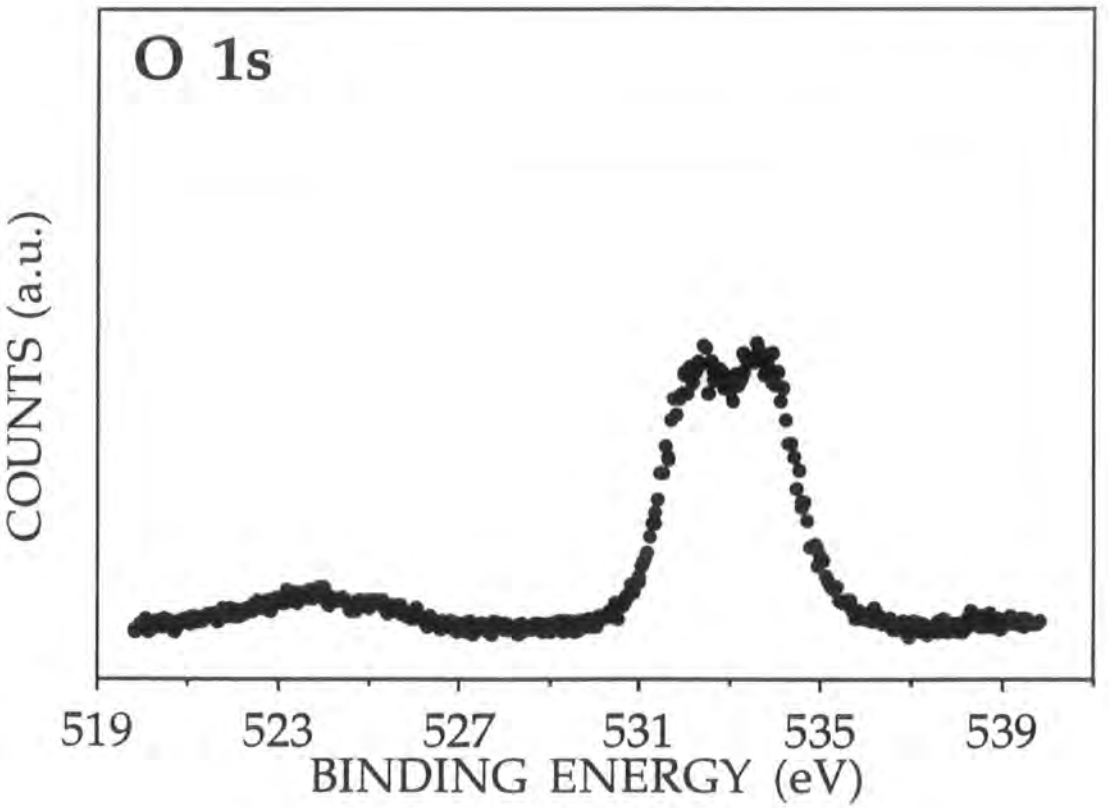

Figure 3.3.1.1.1 (b): O 1s XP spectrum of PET.

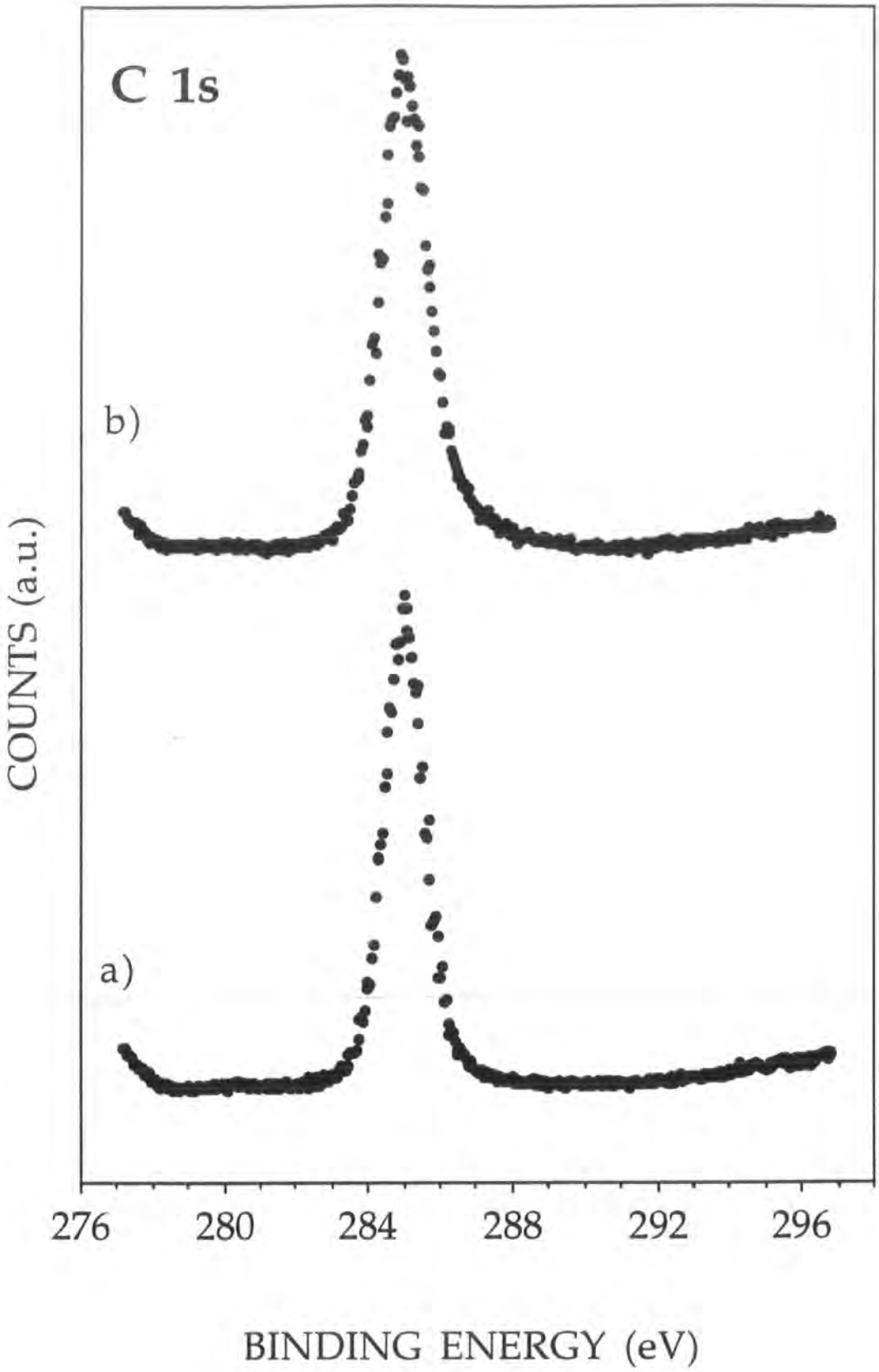

Figure 3.3.1.1.2: C 1s XP spectra of: (a) untreated PP; and (b) corona treated PP.

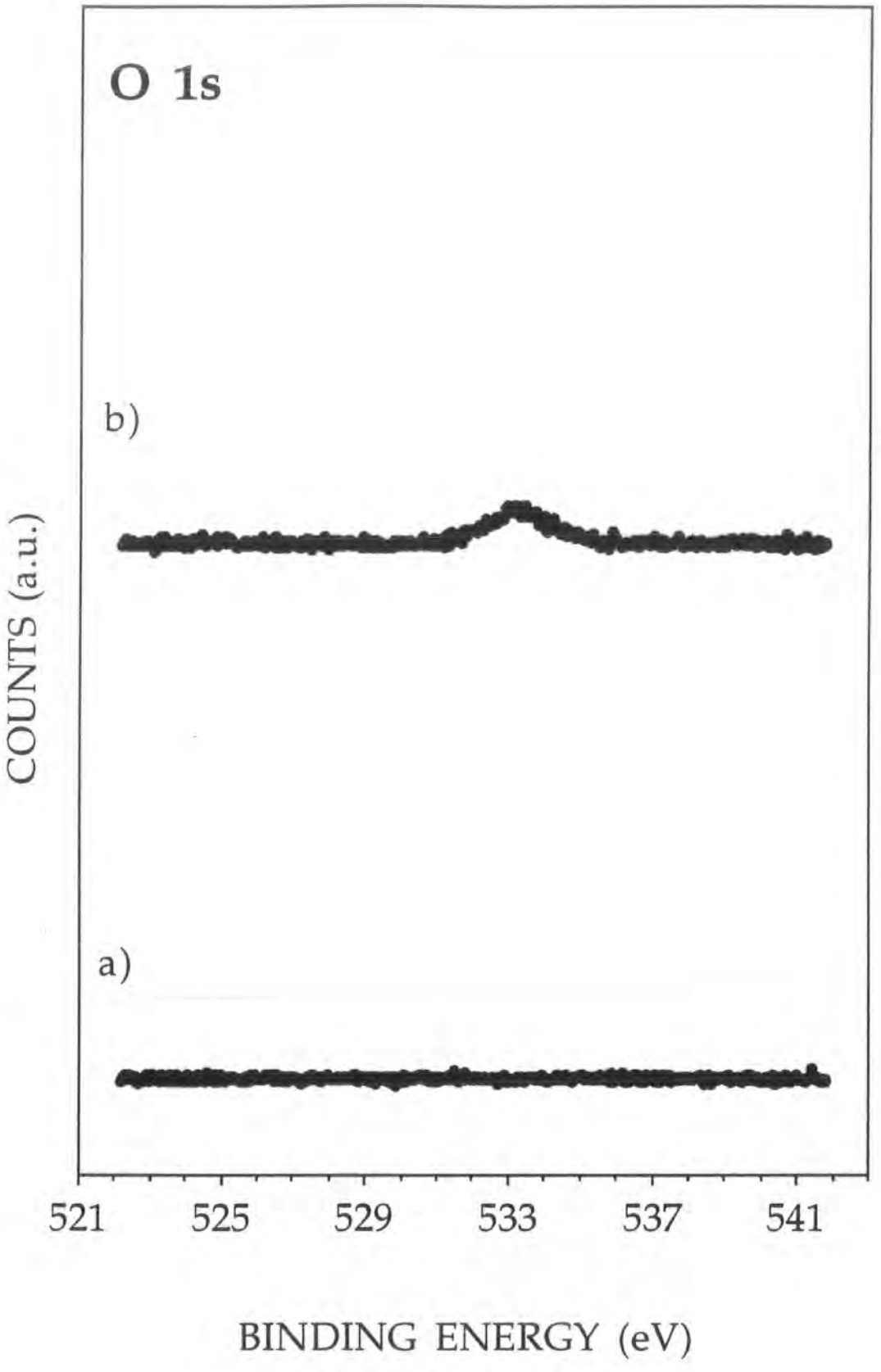

Figure 3.3.1.1.3: O 1s XP spectra of: (a) untreated PP; and (b) corona treated PP.

3.3.1.2 AlO_X coated polymer films

Survey spectra of all samples showed features corresponding only to carbon, aluminium and oxygen. The regions of the XP spectrum corresponding to emitted photoelectrons from these elements were then analyzed in greater detail. Al 2p, and C and O 1s photoemitted electrons were monitored in these experiments.

Elemental compositions of Al/PE, Al/PP and Al/PET, and metal- and oxygen-rich AlO_X/PET as determined by XPS are presented graphically in Figure 3.3.1.2.1. No comment concerning the importance of this observation will be made at this juncture; the data is presented for completeness. Lineshapes of the regions of the XP spectra corresponding to the three elements in question will be dealt with sequentially.

Al 2p XPS binding energies and lineshapes for the five coated polymer films are compiled in Table 3.3.1.2.1 and Figure 3.3.1.2.2, respectively. The Al 2p XPS envelopes for the three metallized polymer films exhibit two distinct features: bulk metal at ~72.4 eV [16], and oxidized aluminium at ~74.8 eV, Figure 3.3.1.2.2 (a)-(c). It should be noted that the latter possesses a much larger full-width-at-half-maximum (~2.3 eV versus ~1.5 eV) since it is characteristic of the +3 aluminium oxidation state in a variety of different inorganic environments (e.g. Al_2O_3, AlO(OH), $Al(OH)_3$) [16,24]. The fact that features from both the oxide and the underlying metal can be observed indicates that the oxide layer is thin: average thickness of the outermost oxide layer present on the metallized polymers was calculated [24] to be 3.6 ± 0.1 nm assuming that the system's composition is homogeneous.

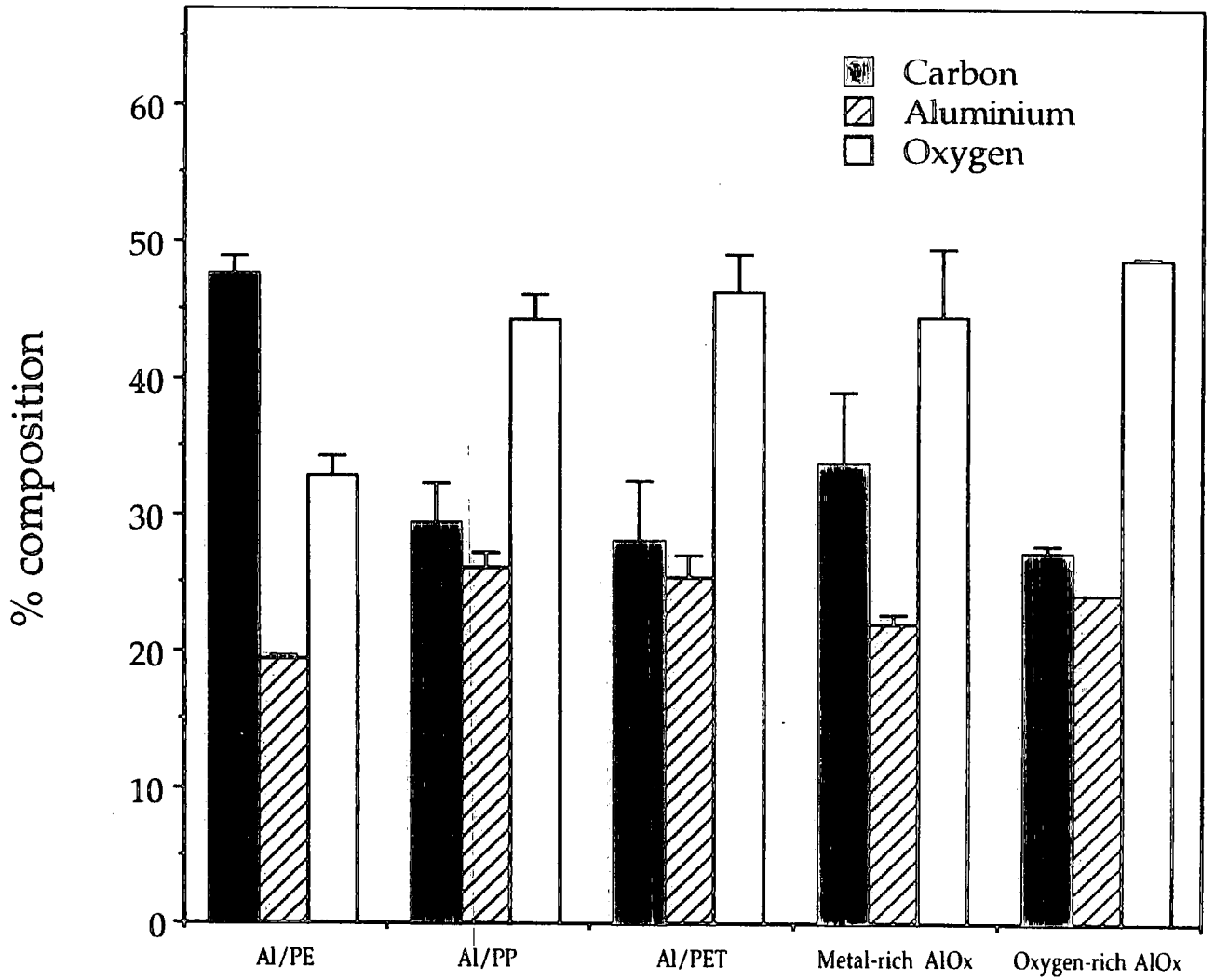

Figure 3.3.1.2.1: Elemental compositions of AlOx films as determined by XPS.

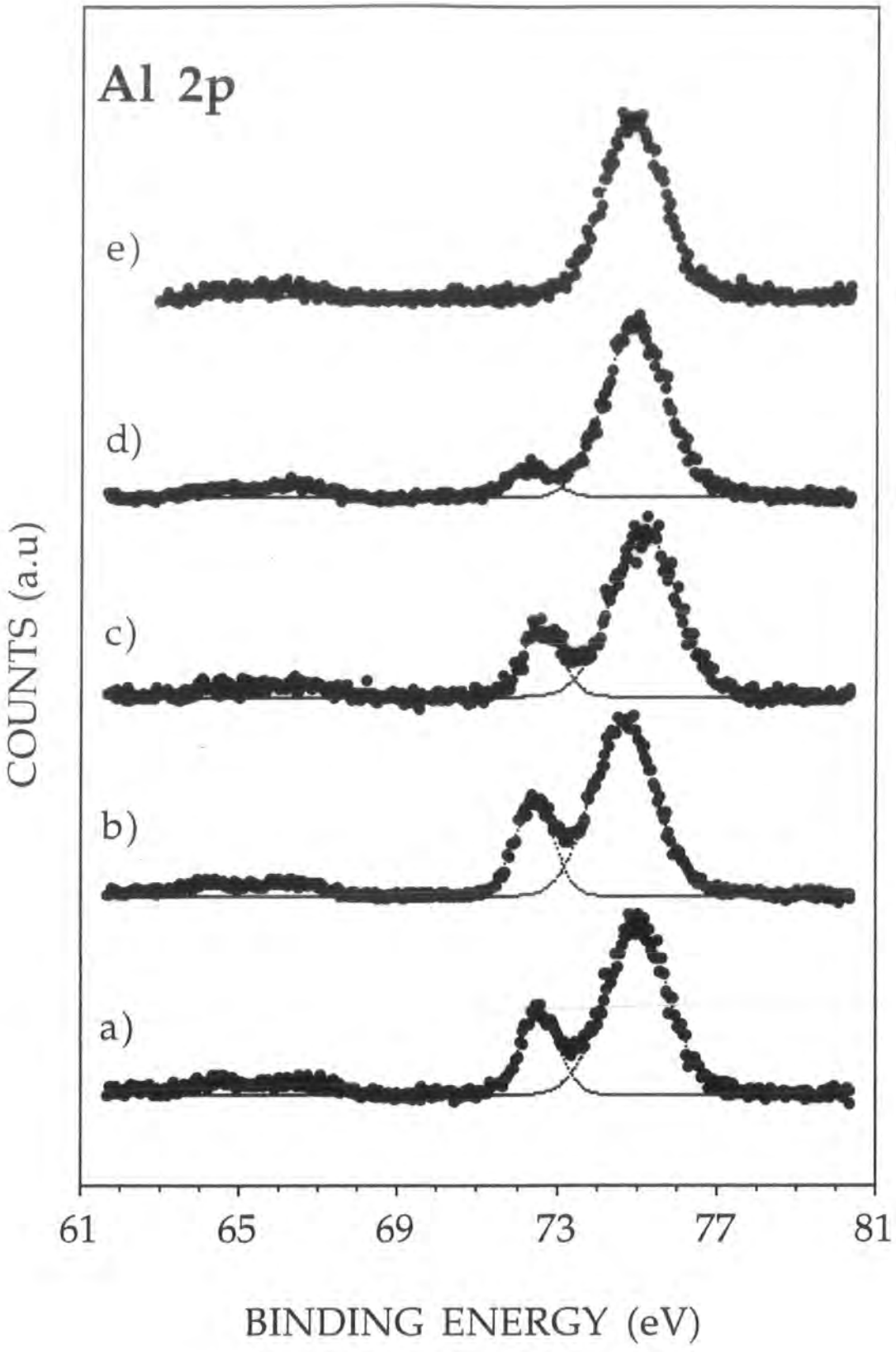

Figure 3.3.1.2.2: Al 2p XP spectra of (a) Al/PE; (b) Al/PP; (c) Al/PET; (d) metal-rich AlOx/PET; and (e) oxygen-rich AlOx/PET.

Sample	Al 2p Binding Energy / eV ± 0.1 eV	
	Al (0)	Al (III)
Al/PE	72.5	74.9
Al/PP	72.4	74.6
Al/PET	72.4	74.8
Metal-rich AlO_X/PET	72.3	75.0
Oxygen-rich AlO_X/PET	-	74.9

Table 3.3.1.2.1: Al 2p XP binding energies for AlO_X/polymer samples.

Metal-rich AlO_X/PET displays the same pair of Al 2p features as previously observed for the metallized polymer samples, Figure 3.3.1.2.2 (d). However, in this case, transmission electron microscopy (TEM) analysis shows the presence of aluminium clusters (face centred cubic) of approximately 1.0-1.5 nm in size which are dispersed throughout an amorphous aluminium oxide matrix, see Chapter 1. Such mixed metal-ceramic coatings are commonly referred to in the literature as 'cermet' films [32].

Oxygen-rich AlO_X/PET contains only one feature in its Al 2p XPS spectrum, which can be assigned to the +3 aluminium oxidation state, Figure 3.3.1.2.2 (e). In this case, the Al 2p binding energy is virtually the same as that measured for the surface aluminium (III) species found for the metallized films.

The relative amounts of each type of aluminium environment at the surface of the five coated polymer samples are summarized in Table 3.3.1.2.2. Whilst the percentages of the total areas under the Al 2p XPS lineshapes assigned to the metallic and oxidized environments are

approximately the same for the three metallized polymers, the Al 2p spectrum of metal-rich AlO_x/PET points to a much lower metallic aluminium content.

Sample	Percentage of total area under Al 2p XPS lineshape	
	Al (0)	Al (III)
Al/PE	23.8 ± 0.1	76.2 ± 0.7
Al/PP	24.7 ± 0.9	75.3 ± 0.9
Al/PET	21.1 ± 1.1	78.9 ± 1.1
Metal-rich AlO_x/PET	12.5 ± 2.0	87.5 ± 2.0
Oxygen-rich AlO_x/PET	-	100

Table 3.3.1.2.2: Percentages of total area under Al 2p XPS lineshape assigned to Al (0) and Al (III) species.

O 1s XP spectra of aluminium-containing compounds are of relatively little value for chemical state identification in these experiments because of the large degree of overlap between the spectral features expected for aluminium-oxygen species [24]. XP lineshapes for Al/PE, Al/PP and Al/PET, and metal- and oxygen-rich AlO_x/PET are similar in shape, Figure 3.3.1.2.3 (a)-(e), respectively. No detailed analysis was performed but centroid binding energies for the observed features correspond to those expected for aluminium oxides, Table 3.3.1.2.3. Literature values for the binding energies of O 1s core level electrons in aluminium-oxygen compounds are: 531.2 eV [33] and 531.3 eV for the oxide, and 532.8 eV [24] for the hydroxide.

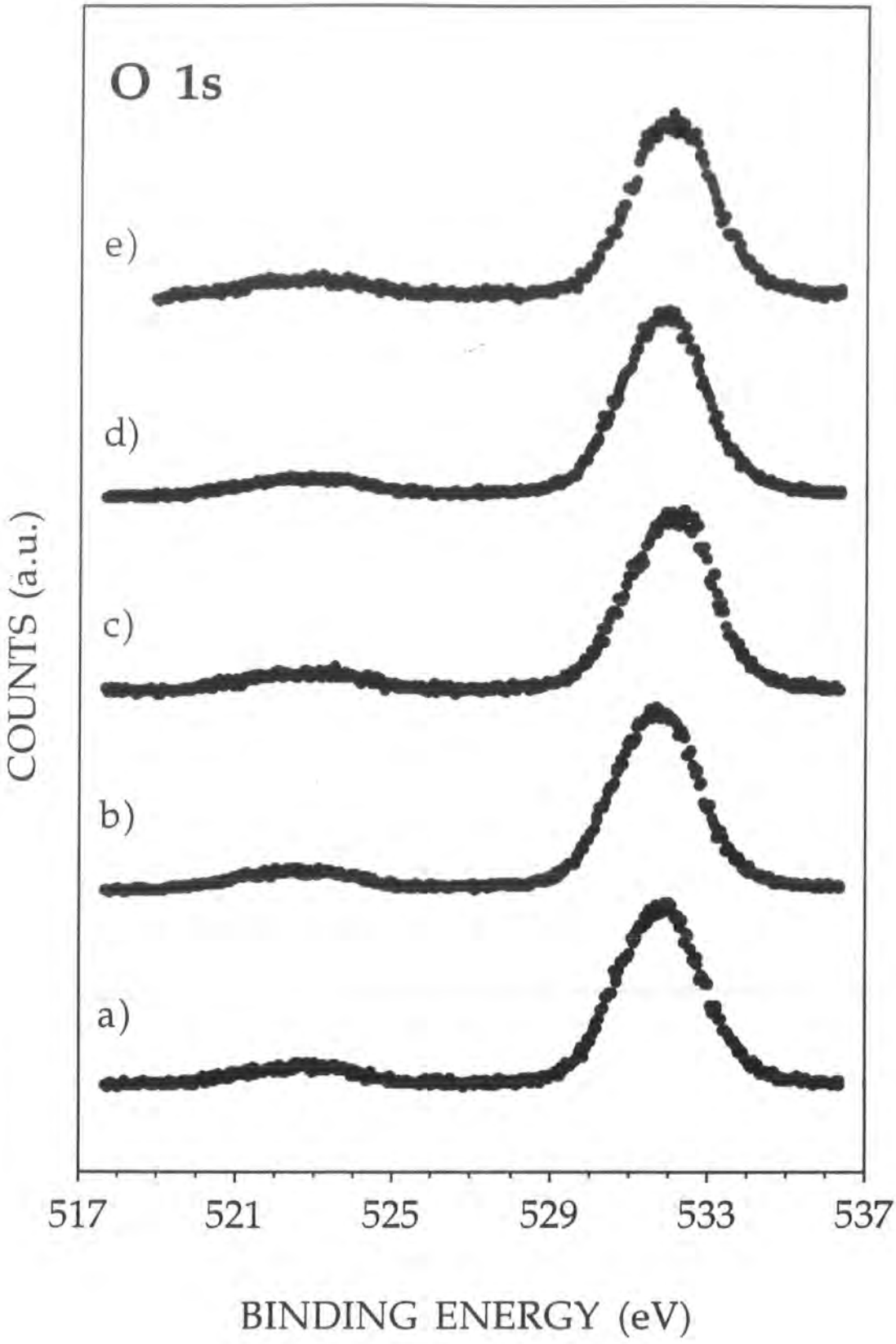

Figure 3.3.1.2.3: O 1s XP spectra of (a) Al/PE; (b) Al/PP; (c) Al/PET; (d) metal-rich AlOx/PET; and (e) oxygen-rich AlOx/PET.

Sample	Binding energy (eV)	FWHM (eV)
Al/PE	531.8 ± 0.0	3.1 ± 0.1
Al/PP	531.6 ± 0.1	3.0 ± 0.1
Al/PET	531.8 ± 0.1	3.2 ± 0.1
Metal-rich AlO_X/PET	532.0 ± 0.1	3.1 ± 0.1
Oxygen-rich AlO_X/PET	531.9 ± 0.1	3.2 ± 0.2

Table 3.3.1.2.3: O 1s XP spectra centroid binding energies and FWHMs for barrier films.

C 1s XP spectra lineshapes are plotted in Figure 3.3.1.2.4 (a)-(e). As with the O 1s region of the XP spectrum, lineshapes are similar for all samples studied.

The similarity of the C 1s XP spectra for all of the AlO_X/polymer films prompted further investigation into the origin of this phenomenon. There are three possible sources of the observed hydrocarbon moieties: the samples themselves; rotary pump oil from the fast insertion lock of the spectrometer; or residual gases in the analysis chamber of the spectrometer. Following standard experimental routines, as used in the studies of the AlO_X/polymer films, the effect of varying lengths of time exposed to the latter two possible sources of contamination was monitored.

Aluminium foil was ultrasonically cleaned in cyclohexane (BDH, 99%) for 10 minutes, dried in air and introduced into the analysis chamber of the Kratos ES300 surface analysis instrument. In the first set of experiments the sample was left in the analysis chamber of the spectrometer between analyses, whilst the second set were performed by extracting and then reintroducing the sample between analyses. Modest increases in the C

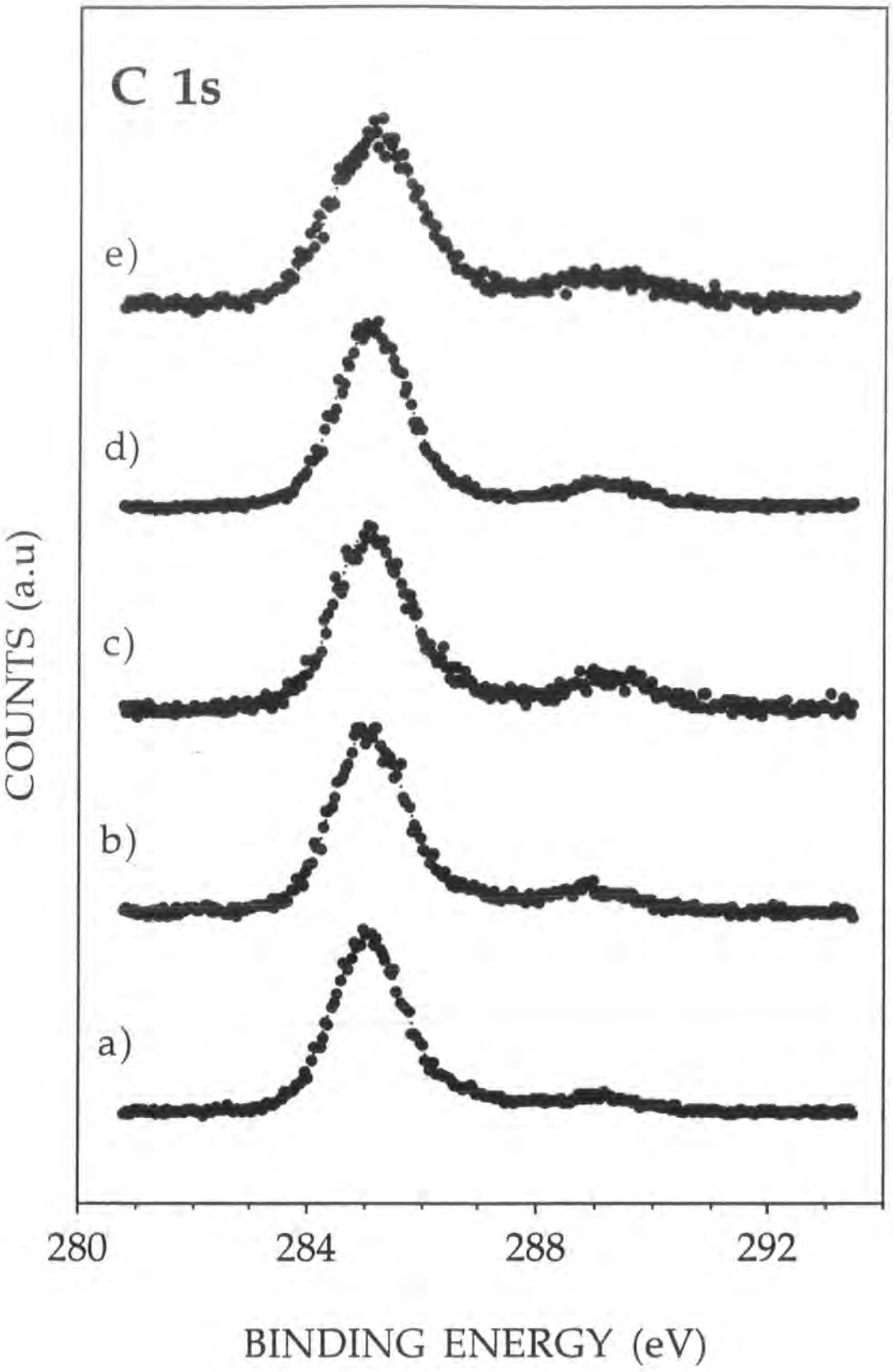

Figure 3.3.1.2.4: C 1s XP spectra of (a) Al/PE; (b) Al/PP; (c) Al/PET; (d) metal-rich AlOx/PET; and (e) oxygen-rich AlOx/PET.

1s signal intensity were observed in the former case, but much greater increases were determined for the latter. It is worthy of note that molecular sieves, used to 'trap' rotary pump oils, can be aluminium oxide particles.

3.3.2 Argon ion sputter depth profiles

Argon ion sputter profiles were carried out as a function of the ion beam current multiplied by sputtering time (henceforth referred to as current-time). These profiles have not been converted into units of depth since it is well known that there exists a difference in sputter yield between pure aluminium and aluminium oxide [34,35]. However, aluminium oxide is reported not to undergo reduction during argon ion bombardment [36] and does not suffer from preferential sputtering [4,19]. Data was normalized to the Al 2p peak area at the maximum of O 1s peak area in the subsurface region of the profile.

All of the coated polymer samples display an initial rise in the Al 2p signal, accompanied by a drop in the C 1s intensity during argon ion depth profiling, Figures 3.3.2.1-5. This is attributed to the accumulation of hydrocarbon contaminant at the surface during sample transfer from the metallization chamber to the XPS spectrometer, as described above.

Total Al 2p XPS peak area plotted against cumulative current-time (proportional, but not necessarily linearly so, to depth) displays four distinct regimes: (i) an initial increase in signal intensity at low current-times; (ii) a region of constant Al 2p peak area; then (iii) a decrease towards longer sputter current-times; and finally (iv) a gradual diminishing of aluminium species. This behaviour is comparable to previously reported SIMS [19,34], XPS [37] and AES [2,3] depth profiling studies of metallized polymers. Assuming that the average sputter rates of the three metallized films are approximately the same, Figure 3.3.2.2 shows that the aluminium layer on

PP substrate was approximately half the thickness of the aluminium layers on PE and PET films, consistent with film deposition conditions, Chapter 2. The third region of the sputter depth profiles is of prime interest, since it probes the metal-polymer interface. The residual aluminium signal observed over longer sputter periods might arise via either intermixing at the interface during sputtering [34], diffusion of aluminium atoms into the polymer matrix during the deposition process [8], or the area analyzed being of greater area than the area sputtered.

Normalized O 1s XPS peak areas for the three metallized films display two features of interest: a native oxide at the surface, and another at the aluminium-polymer interface, *i.e.* an interfacial oxide. This interfacial oxide region appears to be much broader but less oxygen rich compared to the native surface oxide; this may be attributed to either sputtering-induced effects, or perhaps the presence of a thicker oxygen-rich region at the metal-polymer interface, where the latter would be consistent with the penetration of aluminium into the substrate during reactive evaporation [8,21,34]. This interfacial oxide in metallized PET appears to be more oxygen-rich than for the other two polymers, PE and PP, and can be correlated to the molecular structure of PET, which already contains oxygen. Control argon ion sputtering experiments with uncoated PET demonstrated that oxygen is lost very rapidly (~200 μAs), thus discounting the possibility that the experimentally observed oxygen profiles are due to oxygen functionalities contained within the bulk polymer film.

A clear difference is evident between the XPS depth profiles of metal- and oxygen-rich AlO_X/PET, Figures 3.3.2.4 and 3.3.2.5. The Al 2p and O 1s peak profiles follow each other in the case of the oxygen-rich oxide coating, whereas there is a depletion of oxidized aluminium in the subsurface region of the metal-rich aluminium oxide barrier layer as indicated by a reduction in the oxygen profile. The metal-rich coating contains free aluminium

metal (clusters embedded into the aluminium oxide matrix as shown in Chapter 1); clearly any metal within 4-5 nm of the surface will have undergone aerial oxidation. Indeed, comparing the depth profiles of Al/PET and metal-rich AlO_x/PET it is evident that the surface oxide peak of the former is of similar dimensions (assuming similar sputter rates for this species) to that of the latter.

The depth profiles of metallized and oxide coated polymer films are markedly different in the region of the coating/polymer interface: in the case of the metallized films the oxygen profile is of much lower intensity than that of the aluminium, whereas for the oxide coated polymers there is a much higher concentration of oxygen, equating to the oxide found at the surface.

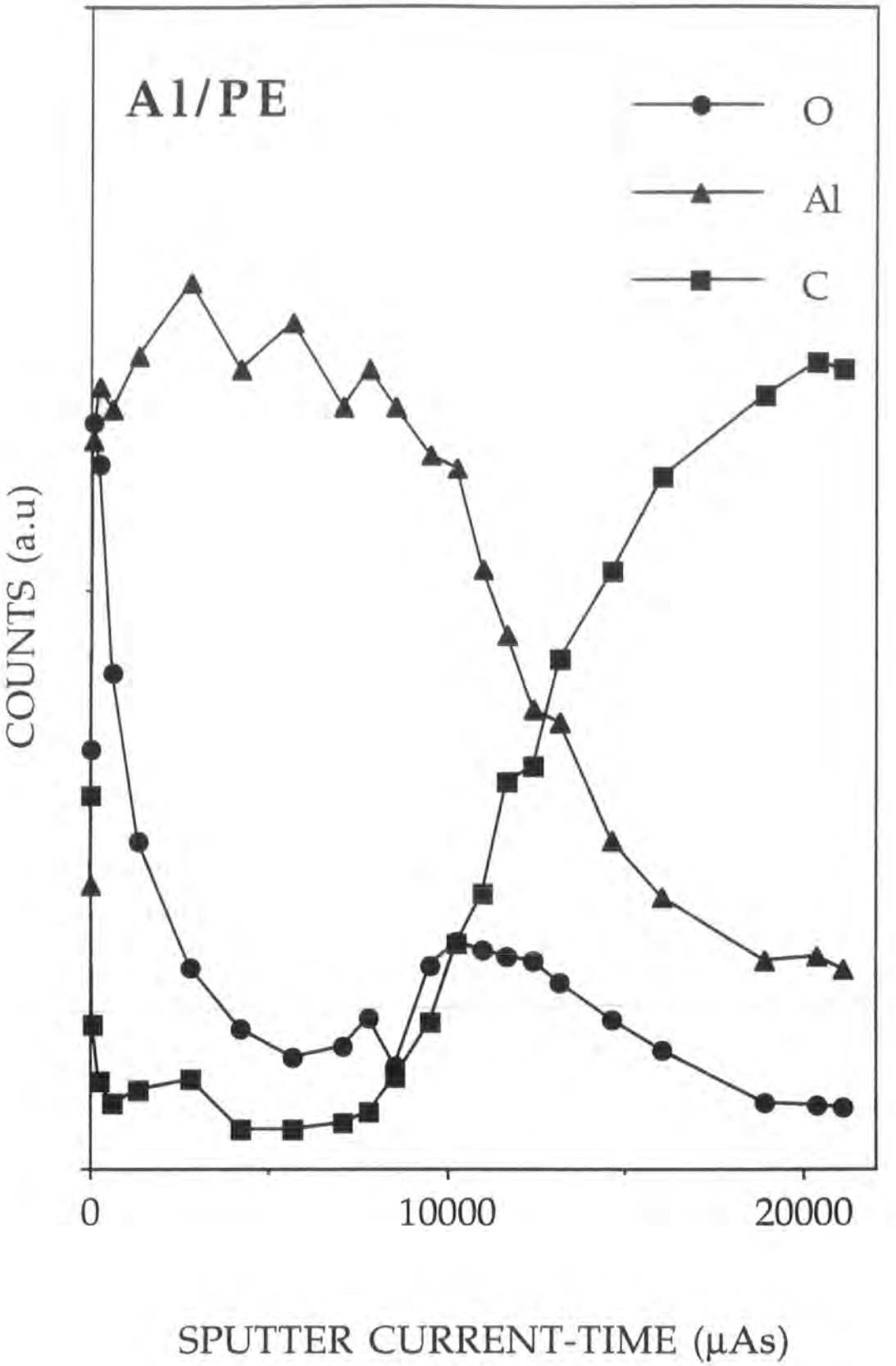

Figure 3.3.2.1: Argon ion sputter depth profile of Al/PE.

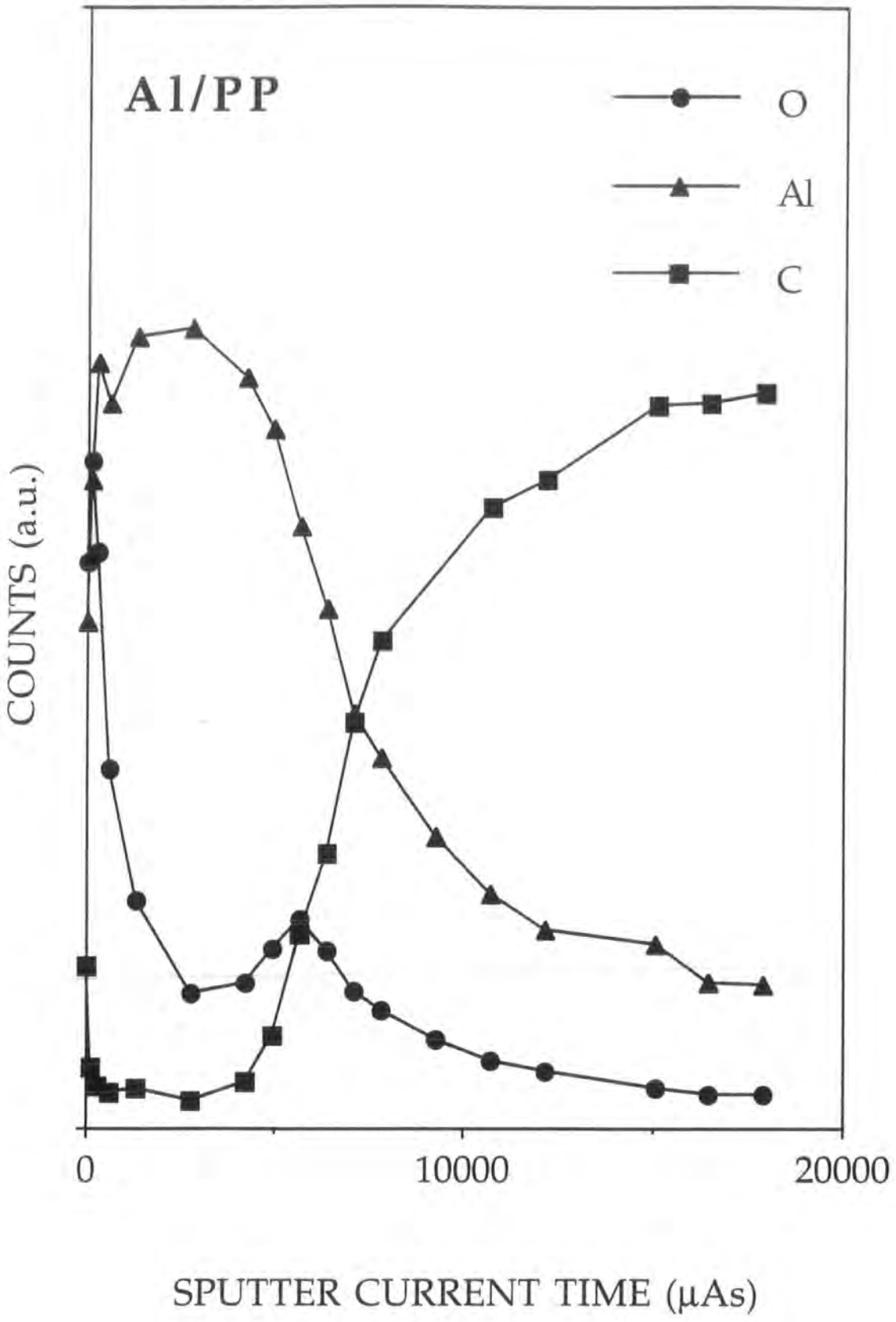

Figure 3.3.2.2: Argon ion sputter depth profile of Al/PP.

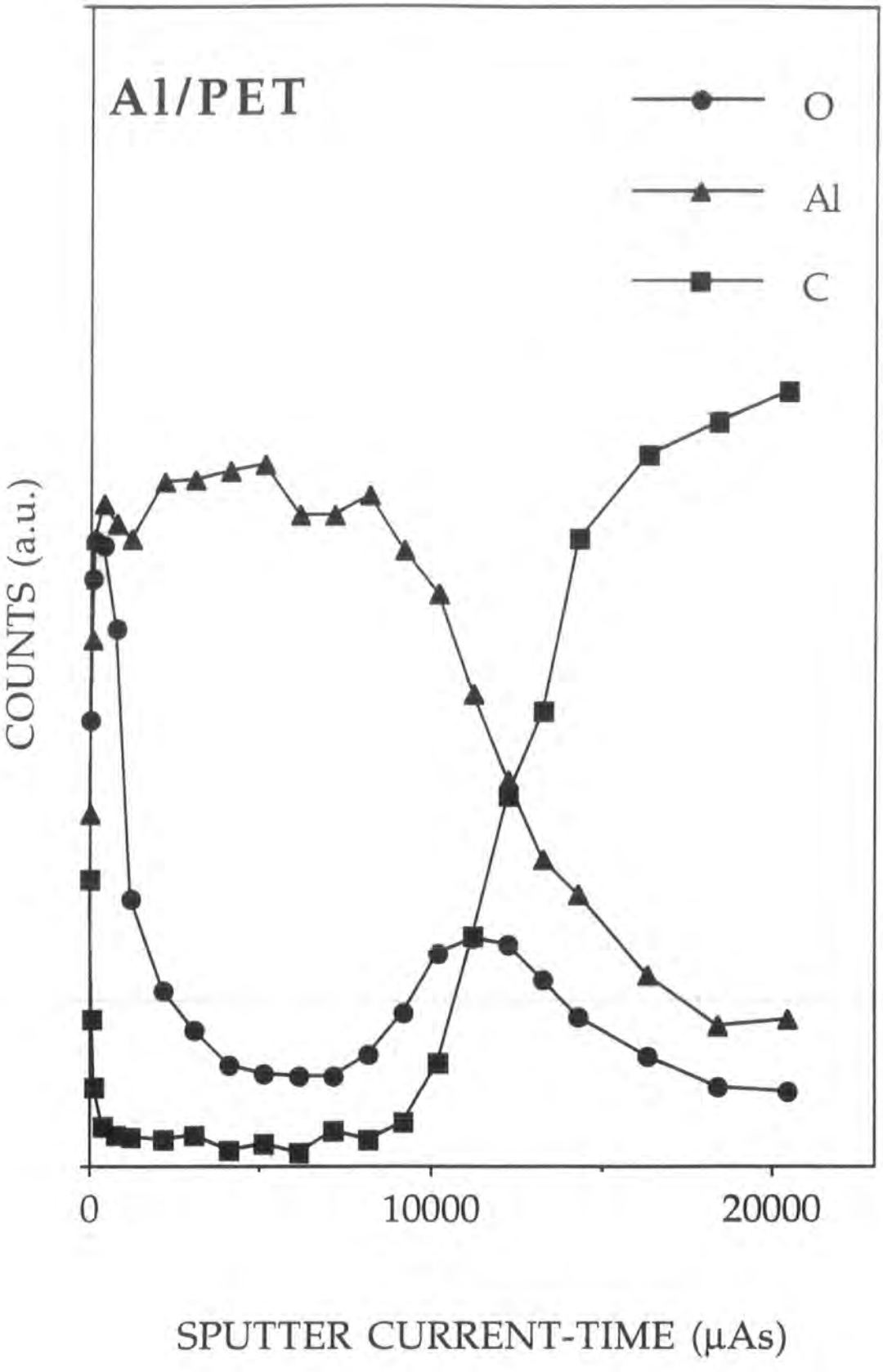

Figure 3.3.2.3: Argon ion sputter depth profile of Al/PET.

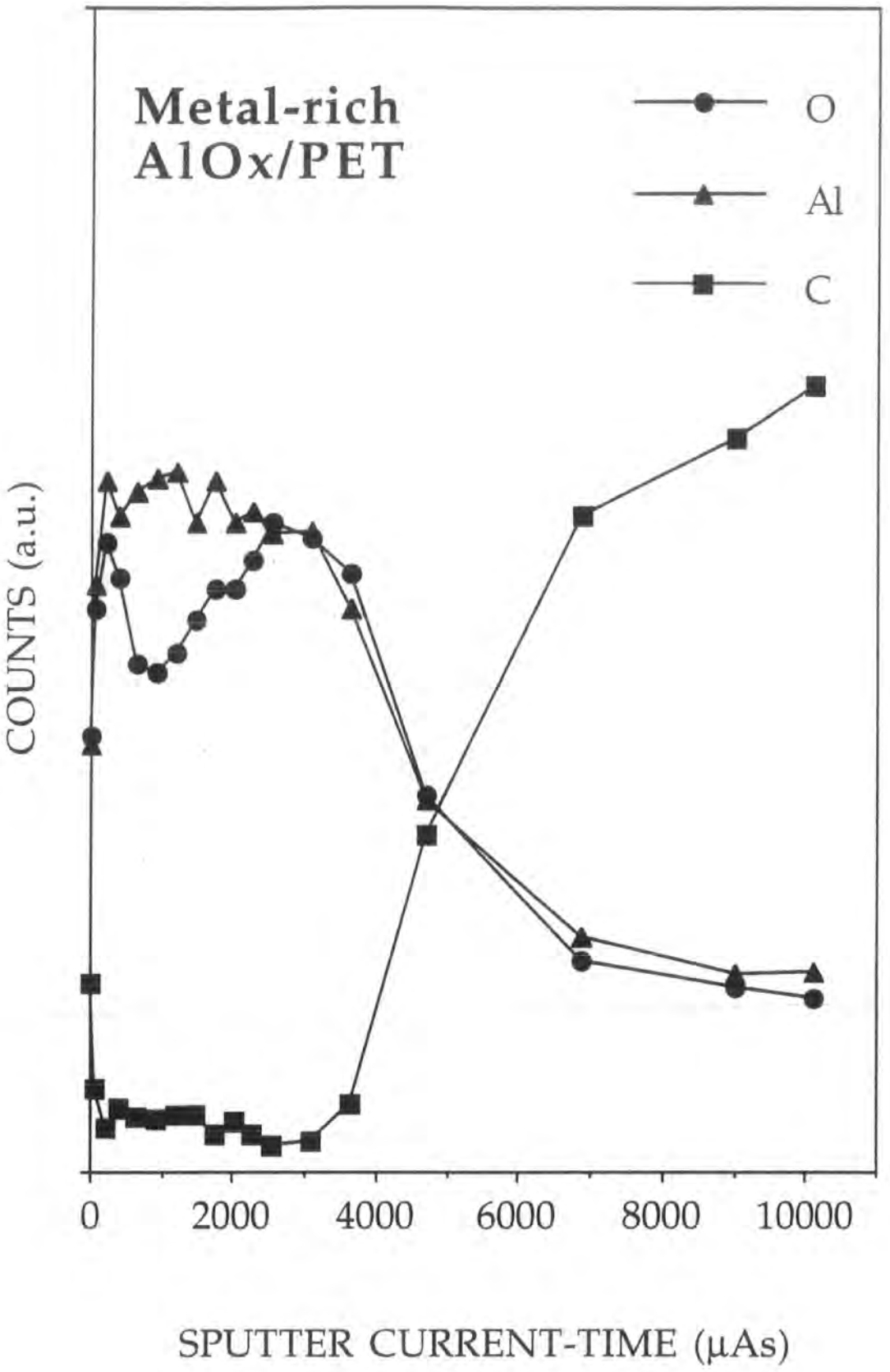

Figure 3.3.2.4: Argon ion sputter depth profile of metal-rich AlOx/PET.

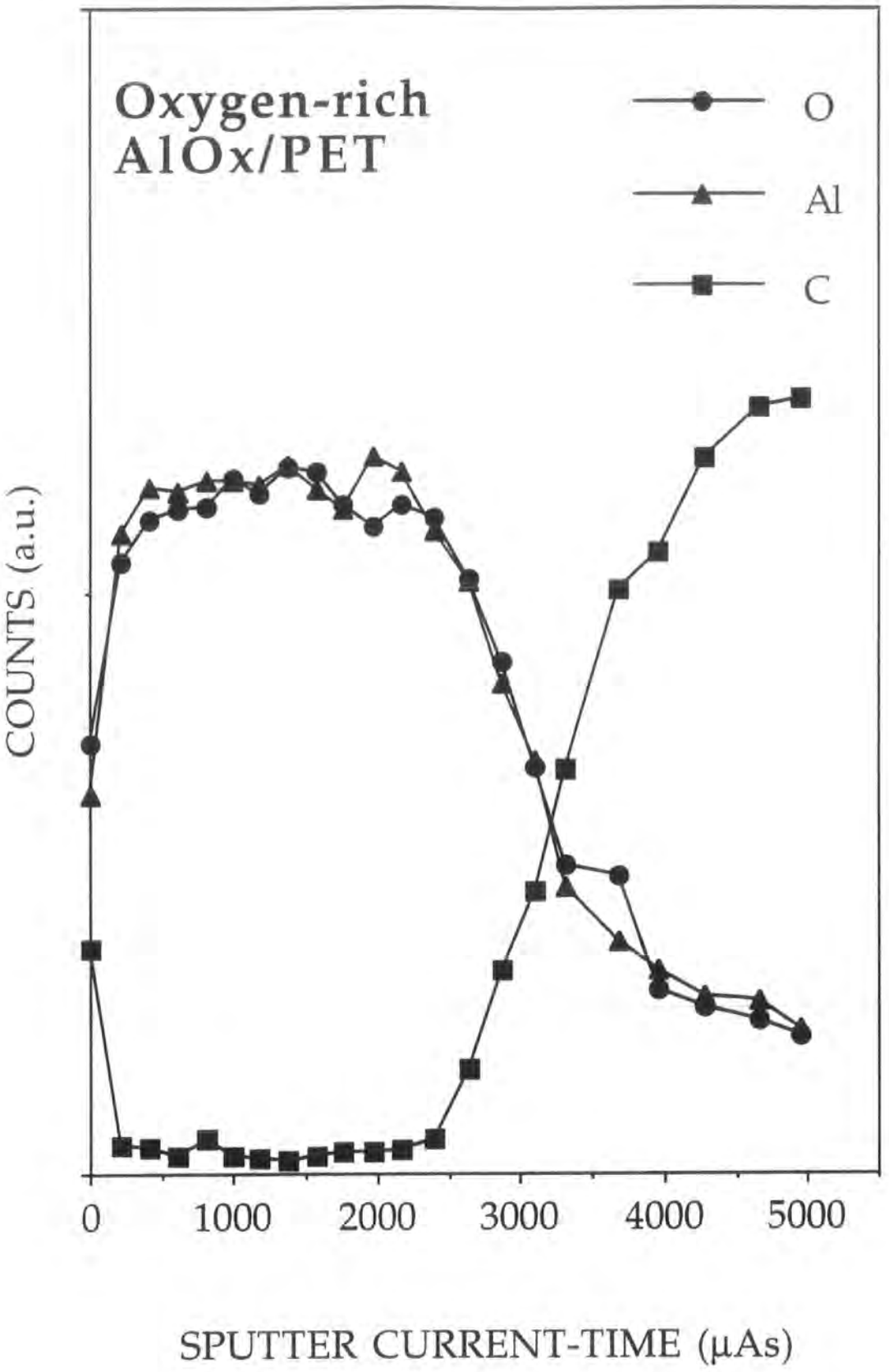

Figure 3.3.2.5: Argon ion sputter depth profile of oxygen-rich AlOx/PET.

3.3.3 Barrier film removal

No aluminium was detected in the surface regions of the etched barrier films apart from etched Al/PET, for which the aluminium signal accounted for 2.0 ± 0.2 % of the total XPS peak area even after four days etching. Since the O 1s region of the XP spectra is relatively uninformative attention will be directed to the C 1s region. Experimentally determined percentages of the total area under the carbon 1s envelope for the assigned functional groups are shown below in Figure 3.3.3.1.

Comparison of experimental data for untreated and HCl etched PET shows that there is a slight reduction in the $\underline{C}$=O peak area percentage and an increase in the $\underline{C}_xH_y$ peak. It is possible that etching in dilute hydrochloric acid chemically modifies the surface of the polymer, perhaps by removing surface-segregated portions of the overall structure. Literature data [15] states that PET's structure is unaffected by treatment with HCl. Etched oxygen-rich AlO_x/PET samples yield results that are within experimental error of those for HCl etched PET. The oxygen-rich AlO_x/PET deposition process has not chemically modified the polymer surface as detected by this experimental procedure.

Etching of metal-rich AlO_x/PET with hydrochloric acid, however, has altered the surface composition of the PET relative to both oxygen-rich AlO_x/PET and the control experiment, etched PET: the percentage of hydrocarbon is observed to increase; and the percentages of oxygenated carbon functionalities have decreased. No such trend is observed for Al/PET. However, the results for metallized PET do not follow this trend, its composition corresponding to those of etched PET and oxygen-rich AlO_x/PET.

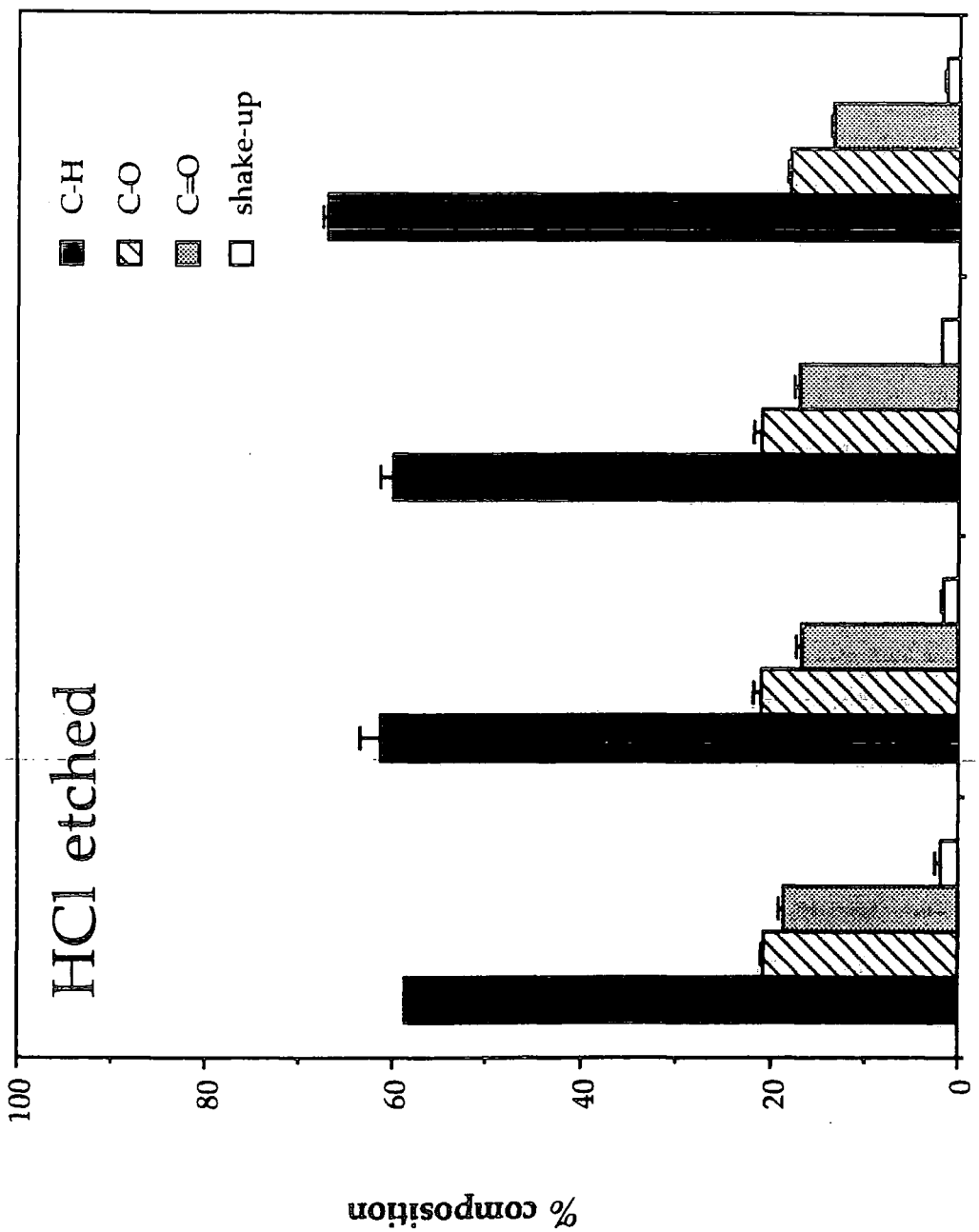

Figure 3.3.3.1: Proportion of C 1s XPS peak area assigned to functional groups for HCl-etched samples.

3.4 DISCUSSION

The overall stoichiometry of these AlO_X coatings can be controlled by varying the reactant oxygen: metal ratio during deposition.

In Chapter 1 the deposition process was described and, in particular, the post-deposition aerial oxidation of the AlO_X layer was highlighted: the more metal-rich the deposit, the greater the extent of optical density fading upon exposure to ambient atmospheric conditions, suggesting that the AlO_X coatings contain decreasing proportions of aluminium metal in the order Al/PE = Al/PP = Al/PET > metal-rich AlO_X/PET > oxygen-rich AlO_X /PET. The depth of aerial oxidation is known to be far less than the thickness of the coatings considered, and it is assumed that this depth of oxidation is equal for the three coating types.

Argon ion sputter depth profile studies of metallized polymer films have shown the presence of two oxide layers: one at the surface; and another at the metal/polymer interface [2,32,37]. The oxygenated species required for the formation of the oxide layer at the metal/polymer interface can arise from oxygen introduced during the deposition process, reaction with oxygen centres contained in the parent polymer structure or post-production aerial oxidation via permeation of oxygenated gases (O_2, CO_2, and H_2O) through the reverse side of the polymer substrate. Substrate oxygen content, known to influence the *in situ* reactions at the coating/polymer interface, may also be important since the interfacial oxide layer is more prominent for the Al/PET polymer than for the Al/PE and Al/PP. Andre *et al.*, studying the influence of PP plasma pretreatment upon the adhesion of *in situ* resistively evaporated aluminium layers [3], have shown by AES depth profiles that the introduction of functionalities at the polymer surface does not lead to a measurable difference between the interfacial chemistries of the aluminium layer deposited onto untreated and treated polymers when

analyzed under their conditions. This may well be due to the relatively low levels of oxygen incorporation into PP films and the consequently minor change in the overall stoichiometry of the polymer surface. However, when comparing the results of Al/PP with Al/PET in this author's study it is noteworthy that the difference in the level of oxygenation of the polymer surfaces is large between PP and PET, and that differences in the intensities of the interfacial oxide peaks are observed.

Interfacial reactions [10,29,39] resulting in $AlO_xC_yH_z$ formation account for the lack of oxygen concentration at the metal/polymer interface. Starting from the assumption that the penetration of aerial oxidation is the same for all coatings analyzed in this study, the Al/polymer systems provide a reference level of oxidation concomitant to exposure to ambient atmospheric conditions. Any extra oxygen species observed at or near the coating/polymer interfaces and in the bulk of the AlO_x coatings will therefore owe their presence to the deposition process itself and not either the polymer substrate surface chemistry or aerial oxidation. Argon ion sputter depth profiles of the metal- and oxygen-rich AlO_x/PET composites exhibit much higher levels of oxygen incorporation than found for the Al/polymer cases, and, based upon the assumptions outlined above, this oxygen arises from the deposition process. Thus information on the interfaces *as deposited and prior to aerial oxidation* can be inferred: while the Al/polymer interfaces are substantially $AlO_xC_yH_z$ in nature, their exact stoichiometry dependent upon the surface chemistry of the polymer, those of metal- and oxygen-rich AlO_x/PET are essentially identical and oxide-like.

Metal-rich AlO_x/PET exhibits metal near the surface of the coating. By using the above argument and relating it to the surface chemistry of this system, the presence of oxide at the surface can be seen to be due to aerial oxidation, leading to the conclusion that the metal is not deposited homogeneously throughout the metal-rich coating but instead resides at the

surface. Post-production exposure to oxidizing gases accounts for the presence of the surface oxide. Reaction of oxygenated carbon functionalities with oxide is less vigorous compared to that for metal surfaces [40].

3.5 CONCLUSIONS

- Introduction of oxygen into a conventional metallizing chamber has led to the deposition of mixed metal/oxide films containing less metal in their surface regions than metallized films, and purely oxide films.

- Argon ion sputter depth profiles have shown that the influence of substrate chemistry upon the interfacial compositions of Al/polymer gas barrier materials is small, and that these interfaces are substantially non-oxide like in nature, this being due to the interfacial reactions leading to Al-O-C complex formation.

- Al/PET depth profiles have been used as a reference material in attempting to understand the deposition chemistry of the AlO_X/PET systems. Both metal- and oxygen-rich AlO_X/PET exhibit stoichiometric oxides at the coating/polymer interface; this oxygen is proposed to have originated from the deposition process. Metal-rich AlO_X/PET also exhibits metal near the surface of the coating: due to the surface oxide peak's correspondence with that observed for metallized films, this metal is concluded to have been deposited at the surface and then undergone subsequent oxidation.

- Removal of AlO_X barrier layers does not show significant alterations to the chemical composition of the PET surface.

3.6 REFERENCES

[1] N. J. DiNardo, in *Metallized Plastics 1: Fundamental and Applied Aspects*, Eds. K. L. Mittal, J. R. Susko, Plenum Press, New York, 1989, 137.

[2] V. Andre, F. Arefi, J. Amouroux, Y. de Puydt, P. Bertrand, G. Lorong, M. Delamar, *Thin Solid Films* **181** (1989), 451.

[3] V. Andre, Y. de Puydt, F. Arefi, J. Amouroux, P. Bertrand, J. F. Silvain, in *Metallization of Polymers, ACS Symposium Series* **440** (1990), Eds. E. Sacher, J. J. Pireaux, S. P. Kowalczyk, 423.

[4] V. Andre, F. Arefi, J. Amouroux, G. Lorang, *Surf. Interf. Anal.* **16** (1990), 241.

[5] V. Andre, F. Tchoubineh, F. Arefi, J. Amouroux, Y. de Puydt, P. Bertrand, M. Goldman, "Improvement of adhesion of polypropylene..", copy of published article, provinence unknown.

[6] J. M. Burkstrand, *J. Appl. Phys.* **52** (1981), 4795.

[7] L. J. Gerenser, in *Metallization of Polymers, ACS Symposium Series* **440** (1990), Eds. E. Sacher, J. J. Pireaux, S. P. Kowalczyk, 431.

[8] L.-H. Lee, "The Chemistry and Physics of Solid Adhesion" in *Fundamentals of Adhesion*, Ed. L.-H. Lee, Plenum Press, New York, 1991, Chapter 1.

[9] W. J. van Ooij, R. H. G. Brinkhuis, J. M. Park, in *Metallized Plastics1: Fundamental and Applied Aspects*, Eds. K. L. Mittal, J. R. Susko, Plenum Press, New York, 1989, 171.

[10] P. S. Ho, *Appl. Surf. Sci.* **41/42** (1989), 559.

[11] R. Mauron, S. Nowak, G. Dietler, L. Schlapbach, *Surf. Interf. Anal.* **17** (1991), 535.

[12] J. Scultz, L. Lavielle, A. Carre, P. Comien, *J. Mater. Sci.* **24** (1989), 4363.

[13] L. J. Gerenser, *J. Vac. Sci. Technol.* **A8** (1990), 3862.

[14] K. Nakamae, S. Tanigawa, T. Matsumoto, in *Metallized Plastics 1: Fundamental and Applied Aspects*, Eds. K. L. Mittal, J. R. Susko, Plenum Press, New York, 1989, 235.

[15] F. Soeda, K. Hayashi, A. Ishitani, *J. Electr. Spec. Rel. Phenomena* **27** (1982), 205.

[16] M. Bou, J. M. Martin, Th. Le Mogne, L. Vovelle, *Appl. Surf. Sci.* **47** (1991), 149.

[17] J. F. Silvain, A. Arzur, M. Alnot, J. J. Ehrhardt, P. Lutgen, *Surf. Sci.* **251-252** (1991), 787.

[18] Y. Novis, M. Chtaib, R. Caudano, P. Lutgen, G. Feyder, *Brit. Polym. J.* **21** (1989), 171.

[19] Y. de Puydt, P. Bertrand, P. Lutgen, *Surf. Interf. Anal.* **12** (1988), 486.

[20] C. T. Wan, K. A. Taylor, D. L. Chambers, G. T. Susi, in *Metallized Plastics 2: Fundamental and Applied Aspects*, Ed. K. L. Mittal, Plenum Press, New York, 1991, 81.

[21] J. D. Rancourt, J. B. Hollenhead, L. T. Taylor, *J. Adhesion* **40** (1993), 267.

[22] E. H. H. Jamieson, A. H. Windle, *J. Mater. Sci.* **18** (1983), 64.

[23] I. P. Batra, L. Kleinman, *J. Electron. Spectroscop. Rel. Phenom.* **33** (1984), 175.

[24] B. R. Strohmeier, *Surf. Interf. Anal.* **15** (1990), 51.

[25] T. N. Wittberg, J. D. Wolf, P. S. Wang, *J. Mater. Sci.* **23** (1988), 1745.

[26] H. J. van Beek, E. J. Mittemeijer, *Thin Solid Films* **122** (1984), 131.

[27] H. Randhawa, *J. Vac. Sci. Technol.* **A7** (1989), 2346.

[28] N. A. Thorne, P. Thuery, A. Frichet, P. Gimenez, A. Sartre, *Surf. Interf. Anal.* **16** (1990), 236.

[29] P. K. Ghosh, *Introduction to Photoelectron Spectroscopy*, J. Wile & Sons, New York, 1983.

[30] G. Ertl, J. Kuppers, *Low Energy Electrons and Surface Chemistry*, Verlag Chemie, Weinheim, 1974.

[31] *Electron Spectroscopy for Surface Analysis*, Ed. H. Ibach, Springer-Verlag, New York, 1977.

[32] H. Demiyront, N. Tezey, *Thin Solid Films* **10** (1983), 345.

[33] C. D. Wagner, in Practical Surface Analysis, Vol. 1, Auger and X-ray Photoelectron Spectroscopy, 2nd Edition, Eds. D. Briggs, M. P. Seah, J. Wiley & Sons, New York, 1990, Appendix 5.

[34] Y. de Puydt, P. Bertrand, *Nuclear Instruments and Methods in Physics Research* **B 39** (1989), 86.

[35] G. Betz and G.K. Wehner, *Topics in Appl. Phys.* **52** (1983), 57.

[36] S. Hofmann, *J. Trace Microprobe Tech.* **1** (1982/83), 213.

[37] M. Chtaib, Y. Novis, R. Caudano, P. Lutgen, G. Feyder, in *Metallization of Polymers, ACS Symposium Series* **440** (1990), Eds. E. Sacher, J. J. Pireaux, S. P. Kowalczyk, 288.

[38] M. Bou, J. M. Martin, Th. Le Mogne, *Appl. Surf. Sci.* **47** (1991), 149.

[39] P. Bodo, J.-E. Sundgren, *Surf. Interf. Anal.* **9** (1986), 437.

[40] D. A. Drabold, J. B. Adams, D. C. Anderson, J. Kieffer, *J. Adhesion* **42** (1993), 55.

CHAPTER 4

ATOMIC FORCE MICROSCOPY OF AlO_X/PET FILMS

4.1 INTRODUCTION

Chapter 2 determined the differences in gas transport properties between Al/PET, metal- and oxygen-rich AlO_X/PET composites. Two effects were highlighted for study: the chemistry of these systems (Chapter 3) and the morphology. It is the aim of this chapter to determine, by atomic force microscopy (AFM), whether there are morphological differences between these coatings, and whether these differences can be used to elucidate the differences in gas transport behaviour between the AlO_X/PET composites.

4.1.1 Atomic Force Microscopy

Details of this technique were first published in 1986 [1]. This development represented a dramatic change from scanning tunnelling microscopy, reliant upon sample electrical characteristics, to the use of interatomic forces as a surface analytical tool. Excellent and complete reviews can be found in references [2] and [3].

Atomic force microscopy belongs to the burgeoning family of scanning probe microscopies which includes scanning tunnelling microscopy , lateral force microscopy and magnetic force microscopy. Many achievements have been made in this area, most notably the ability to position single atoms [4] and dissociate single absorbed molecules on surfaces [5]. Meyer [6] has described the conception and development of atomic force microscopy. It is not this author's intent to review all progress

in this area but rather to demonstrate the applicability of such systems to gas barrier film technology.

As an analytical tool for the study of polymeric and other electrically insulating surfaces, AFM has eliminated the sample preparation requirements of the STM experiment (metallization to allow electron tunnelling) [7], thus allowing high resolution to be achieved on the surfaces themselves [8].

The AFM experiment is represented schematically in Figure 4.1.1.1. The main components are: a sample attached to a piezoelectric stage; a tip supported on a cantilever; a laser; a photodiode array; and a feedback control loop to control the experiment.

Essential to the implementation of all operating modes is the bringing together of tip and sample. Ideally the approaching tip apex would be a single atom but such atomically sharp tips are thought unrealistic [9,10]. Instead, the tip-sample interaction is better described as that of a small sphere above a plane [11]. The mechanism is not understood [10]. At all times it should be remembered that the images produced by atomic force microscopes are a convolution of the sample and the tip [9,12], the latter having been approximated by a 50 nm spherical tip.

The forces experienced by a tip approaching a surface can be described as follows: at large separations the tip is in its rest position. As the tip-sample separation decreases, the tip bends towards the surface as it experiences attractive forces. This displacement reaches a maximum value before the overall force becomes repulsive as the minimum of the separation-energy curve is passed. It is at this point that the possibility of tip-induced damage to the sample becomes a probability rather than a possibility since the tip is being forced back from its equilibrium position by the surface. Such forces have, however, found uses in the area of

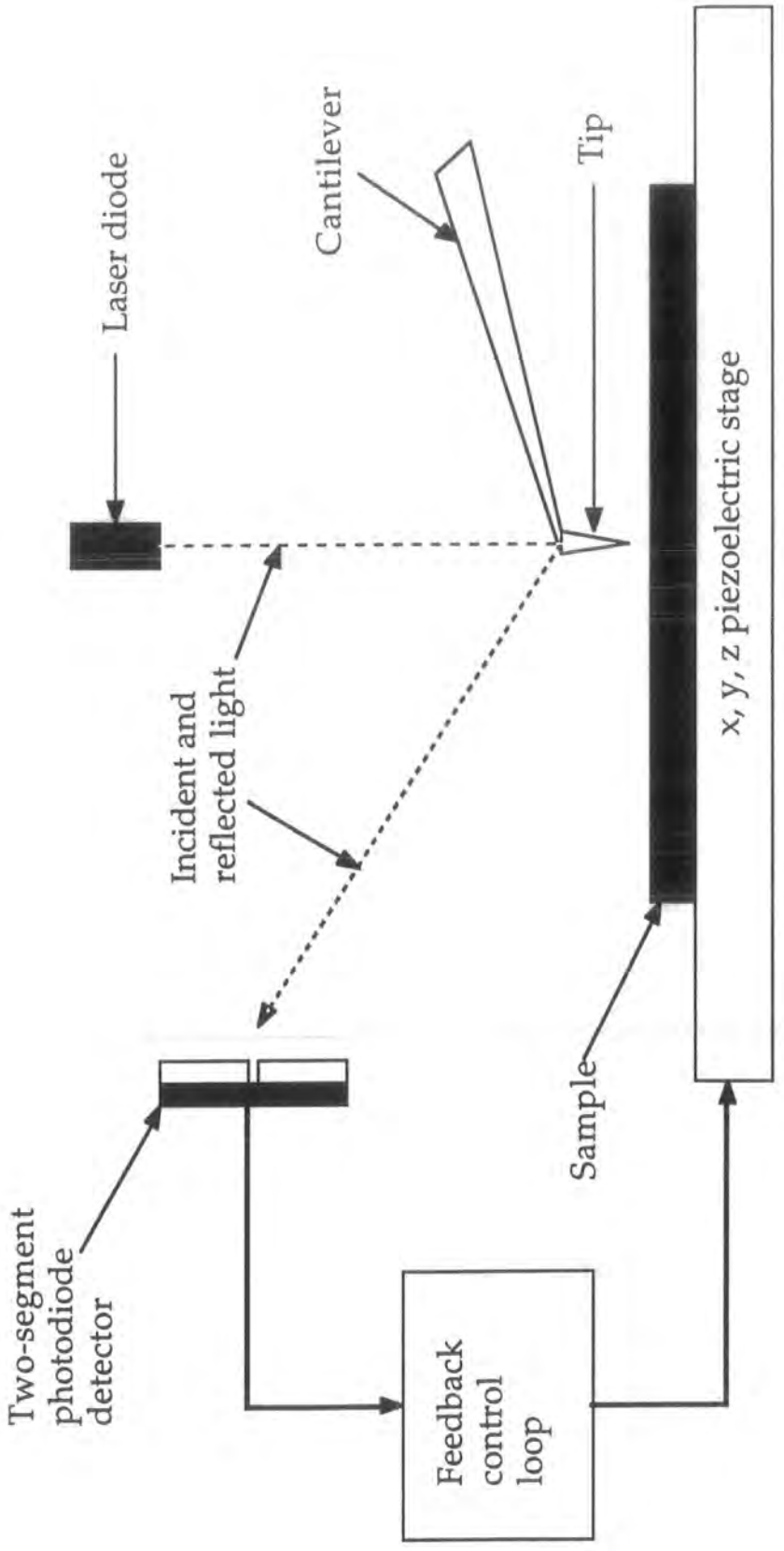

Figure 4.1.1.1: Schematic representation of AFM experiment.

nanometer-scale machining of surfaces [13]. For samples analyzed under ambient laboratory conditions there is also the effect of thin films of water to be taken into account; for relatively large-scale topographical determinations this was found to be of no concern [10].

4.1.2 Atomic force microscope operating modes

4.1.2.1 Contact mode

As for a generalized spring, the deflection of an AFM tip is described as:

- $F = -k\Delta z$

The contact mode maintains the tip deflection at a constant value [10,11]. As such, the topographical map of the surface represents a surface of constant force against/displacement of the tip. Typical forces are ~10^{-9} N. Values for an ionic bond are ~10^{-7} N, and ~10^{-11} N for a hydrogen bond [14]. Contact mode can lead to damage of the surface, especially those of soft samples such as polymers [11]. Indeed, intentional damage of polymer surfaces led to the observation of an oriented morphology perpendicular to the scanning direction [15].

4.1.2.2 Tapping mode

Digital Instruments, manufacturers of the instrument used in this study, developed a mode of operation for their atomic force microscope enabling reduction of the lateral forces experienced by the surface as the tip is raster-scanned over the surface [16,17], typical values being ~10^{-10} N. More

accurately described as a high-amplitude resonance mode, a high aspect ratio tip/cantilever combination is oscillated at its resonant frequency, typically between 300-400 kHz, with an amplitude of between 20-100 nm [18]. At the lowest point of the oscillation, intermittent contact occurs with the surface (hence the name 'tapping mode') and the amplitude is reduced. It is this reduction in oscillation that is monitored in a tapping mode experiment by measuring the root-mean-square of the cantilever deflection signal [18]. $\Delta\omega_{res}$, the change in resonant frequency, is given by:

- $\Delta\omega_{res} \sim (k - F)^{0.5}$

and equates to a force gradient [14]. Feed-back controls maintain this oscillation reduction at a constant level, yielding topographical maps corresponding to constant oscillation amplitude reduction surfaces above the sample surface. Resolution in this mode does not reach the levels observed in the contact mode.

4.1.3 Morphologies of evaporated aluminium thin films

Sundgren and Hentzell's review of hard-coating technology [19] noted that grain sizes for refractory compound films were typically less than 100 nm, and sometimes 5-10 nm due to low substrate temperatures during their deposition.

Aluminium layers on metallized films are polycrystalline and can exhibit a strong texture when deposited at high film speed [20] with grain sizes typically the same as the aluminium thickness. Crystallite sizes for 'fast evaporations' at substrate temperatures ~373 K are 50 nm. Electron micrographs show that the structure appears very fine-grained on ~10 μm

scales. As the substrate temperature is increased the grain size increases [20,21].

The extent of oxidation within the deposition system affects the deposit's morphology [22]. Greater oxidation reduces the grain size. Verkerk and co-workers have examined the effect of residual atmosphere upon the characteristics of evaporated aluminium coatings by introducing controlled pressures of water vapour [23] and oxygen [24]. Although evaporated at low deposition rates and exposed to relatively low pressures (maximum ~10^{-5} Torr), in both cases higher pressures led to the development of a fine-grained morphology. A more recent study [25] concluded that at ~1 Torr aluminium forms particulate films, the particles themselves being an agglomeration of 'dust' formed due to the high gas pressures. Entrainment of evaporated metals in relatively high pressures of gas (typically inert gases) is known to lead to particle formation [26,27]

4.2. EXPERIMENTAL

All experiments were performed upon as-received samples defined in Chapter 1. Reproducibility was tested by altering the scanning direction employed, scanning several regions of the same sample, and repeating for other samples.

Images were accumulated using a Digital Instruments NanoScope III atomic force microscope in the tapping mode for soft samples; the choice of mode was found to have no effects upon the imaging of the coated samples.

4.3 RESULTS

4.3.1 10 μm scale

Figure 4.3.1.1 is an atomic force micrograph of uncoated PET. The protrusions (lighter regions) dispersed across the surface are interpreted as filler particles in the polymer film. Their sizes and distribution is not regular on this scale. The vertical scale on this image is 50 nm; the surface is therefore quite rough.

At this scale all of the coated films exhibit the same gross morphology as uncoated PET. By way of example, Figure 4.3.1.2 is an AFM of Al/PET. Again, the lighter coloured protrusions are irregularly spaced across the surface and are assigned to filler particles from the base film protruding through, or coated by, the AlO_X coating. In contrast to the AFM of uncoated PET, some 'grain'-like features can be seen in this case. Their structure is elucidated below.

4.3.2 1μm/500 nm scale

Figure 4.3.2.1-4 are AFMs of PET, Al/PET, and metal- and oxygen-rich AlO_X/PET.

PET has a globular surface structure. The surface is smoother on this scale when compared to the previous image, Figure 4.3.1.1. The vertical scale is 10 nm. There is a protrusion evident to the right side of this image, and this may be a filler particle.

Al/PET also exhibits a smooth structure but its features are of different sizes to and far more distinguishable than those for the uncoated film. Particles observed are approximately 60 nm in diameter.

Metal- and oxygen-rich AlO_x/PET's structures are similar to those of the Al/PET variant with a smooth surface but the particles are smaller. These images are shown with 500 nm scales so as to highlight the difference between them. The vertical scale remains unchanged at 10 nm. Particles for the metal-rich variant are larger than those for the oxygen-rich at ~45 and ~25 nm, respectively. Note that the lower points of these micrographs, represented as dark areas, correspond to ~10 nm on the vertical scale. It is not clear whether these represent gaps in the coating since the probe tip is unlikely to be able to penetrate features of such a potentially high aspect ratio due to its finite size. Gaps in the coatings' coverage of the base films are present.

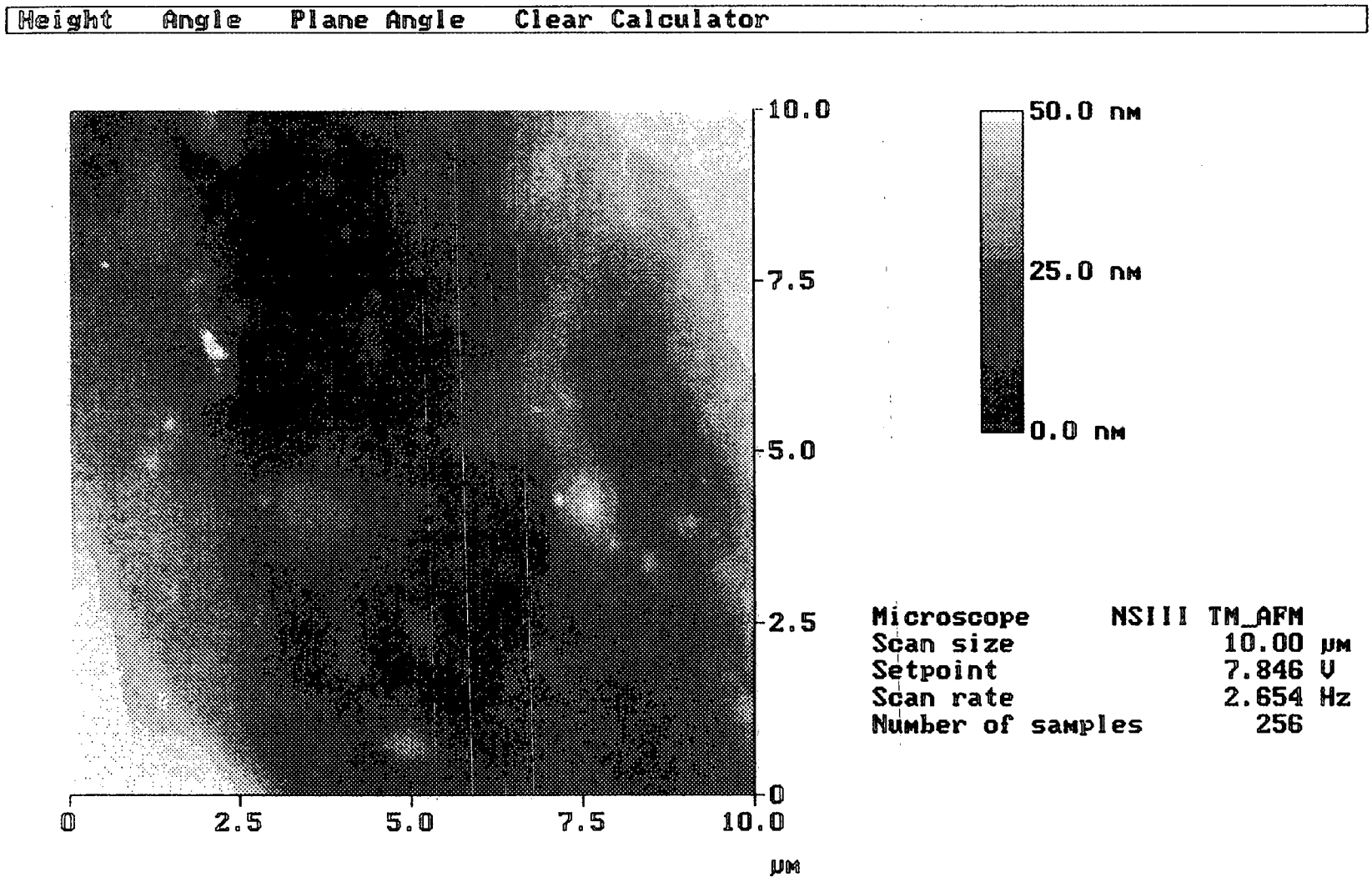

Figure 4.3.1.1: AFM of uncoated PET.

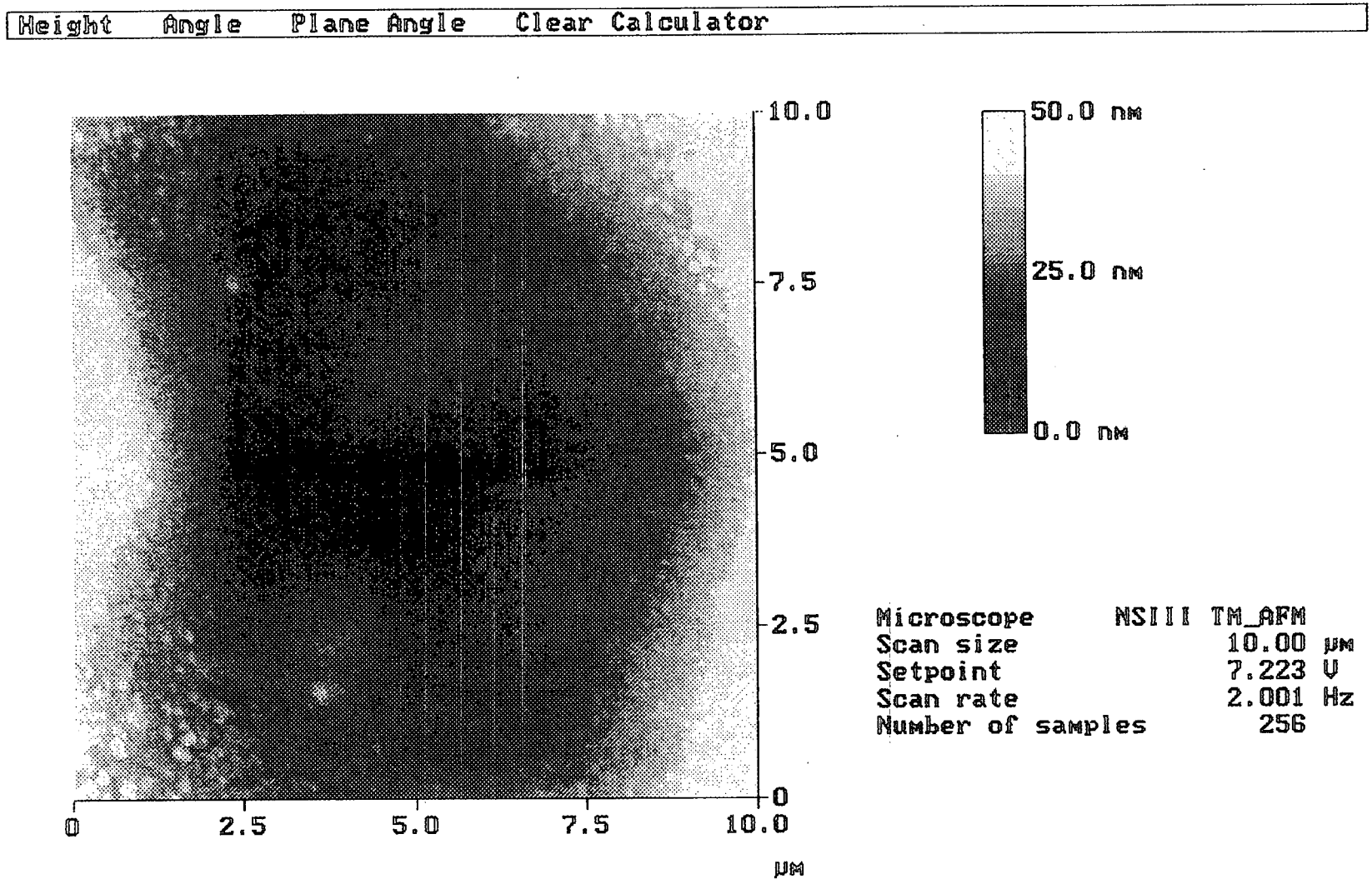

Figure 4.3.1.2: AFM of Al/PET.

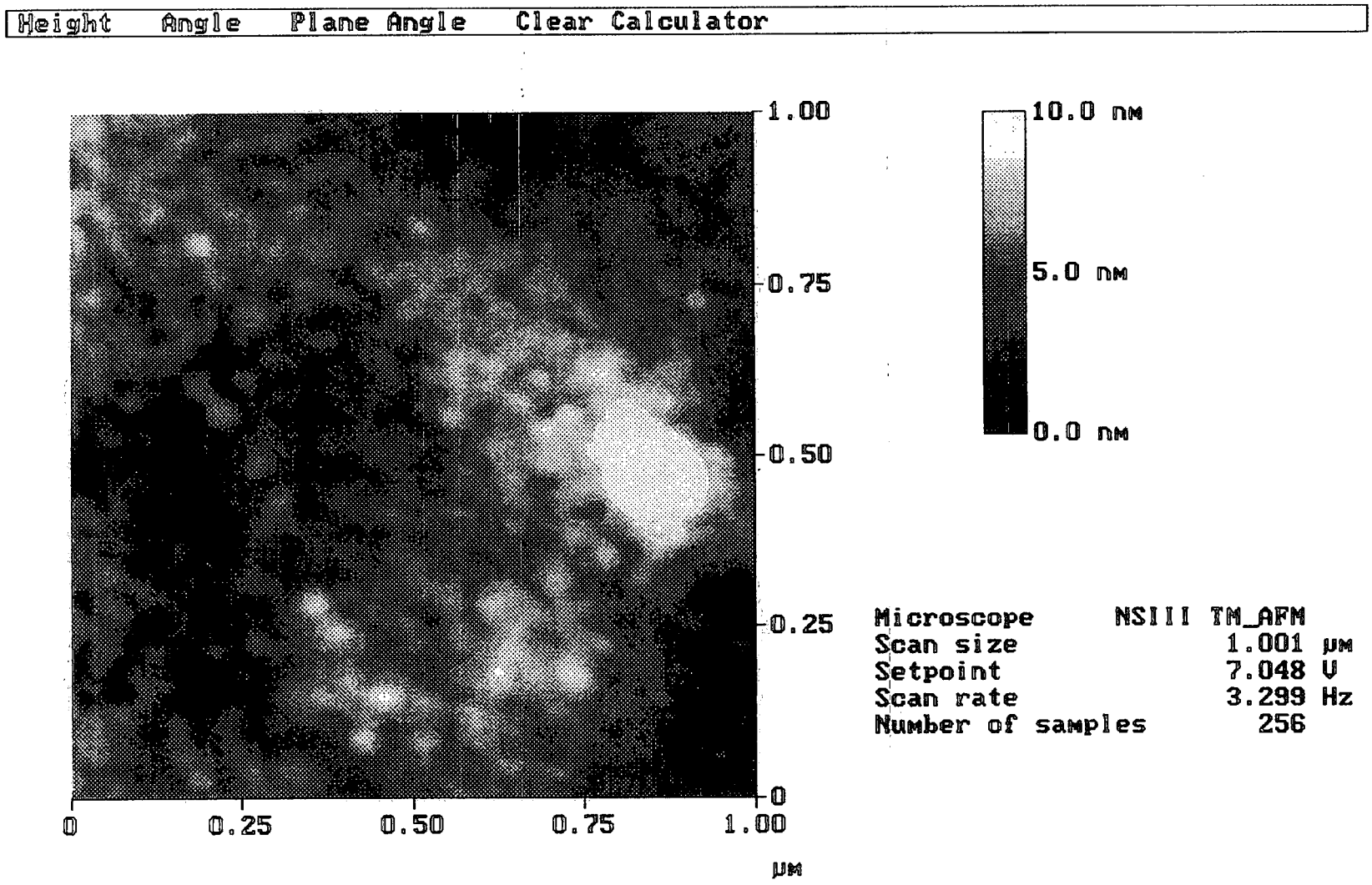

Figure 4.3.2.1: AFM of uncoated PET.

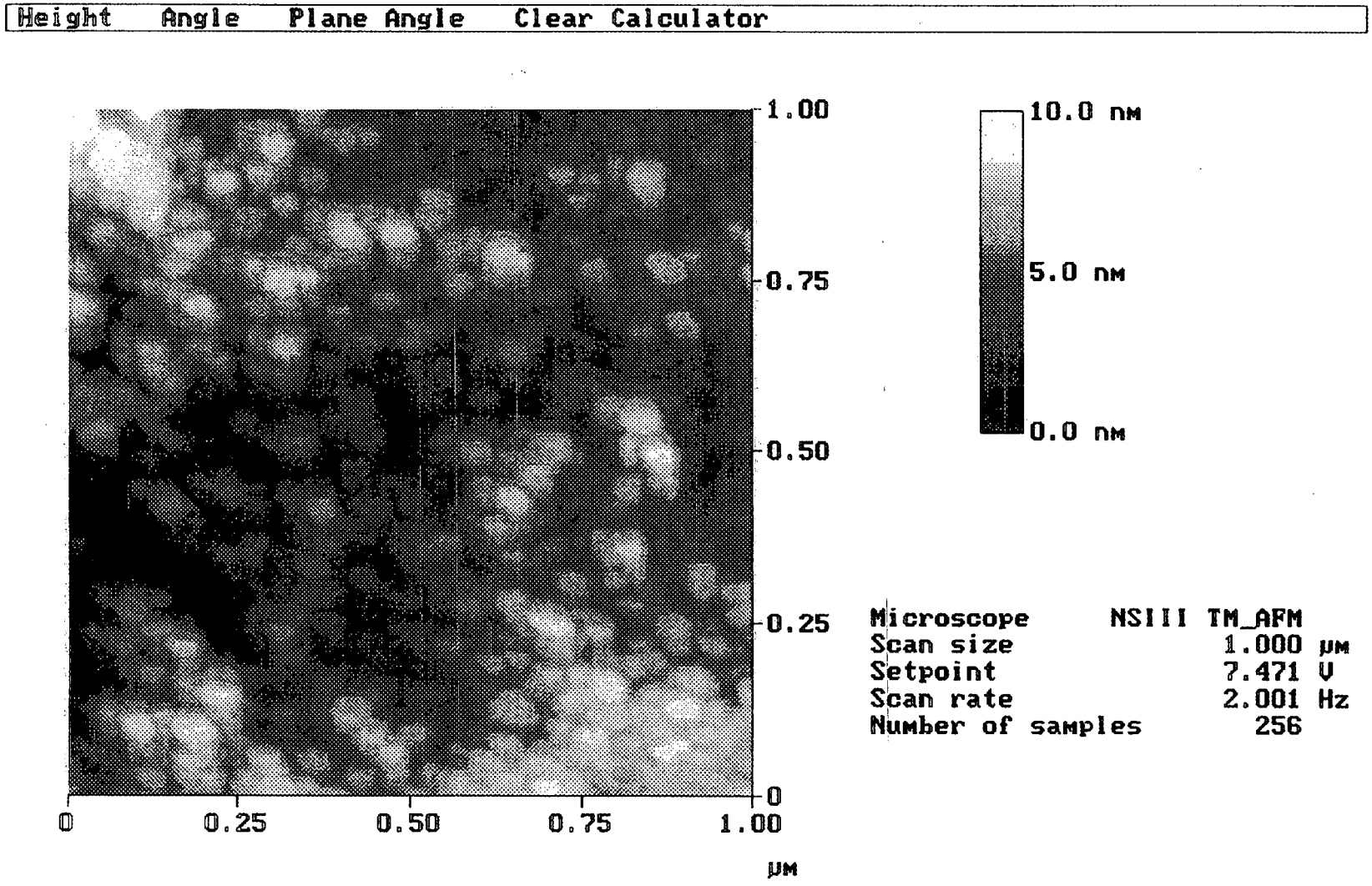

Figure 4.3.2.2: AFM of Al/PET.

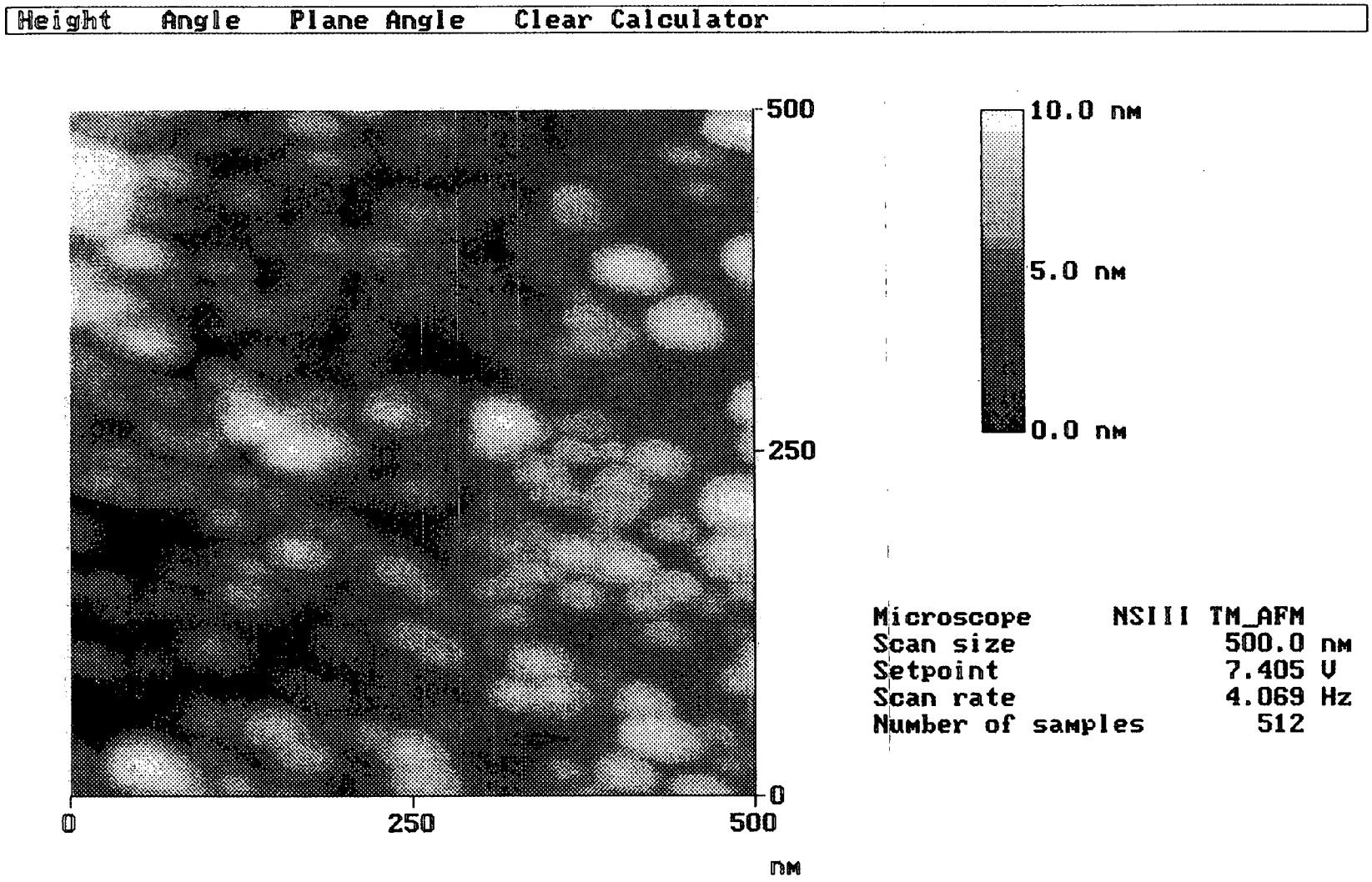

Figure 4.3.2.3: AFM of metal-rich AlO_x/PET.

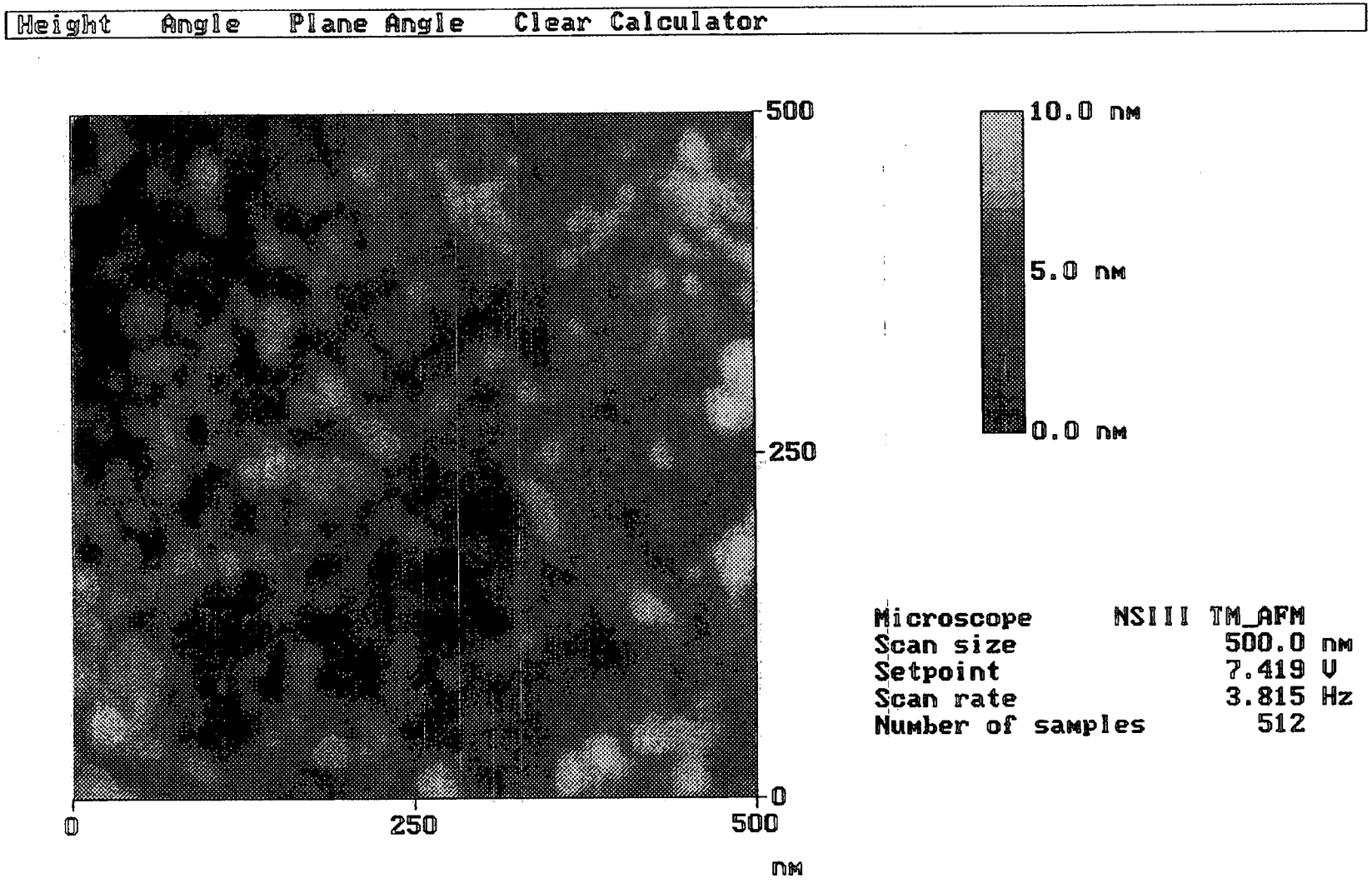

Figure 4.3.2.4: AFM of oxygen-rich AlO_x/PET.

4.4 DISCUSSION

Fine-grained morphologies, similar to those observed in this study, have been reported for the deposition of aluminium films grown under relatively high pressures of either oxygen or water vapour [23,24]. Such effects were rationalized in terms of oxide formation inhibiting the growth of metal grains. However, in this case the growing grains are not necessarily metallic. There may therefore be other effects in play. As defined in Chapter 1, the base pressure of the deposition chamber is in the range covered by the cited references, and the major component of its atmosphere is likely to be water vapour [28]. Clearly the introduction of oxygen has enhanced the effect of reducing grain size since those on the oxygen-rich AlO_x/PET surface are smaller than those on the metal-rich variant. Although deposited at higher deposition rates, the Al/PET morphology also follows this trend.

Few AFM studies have been made on condensed thin films such as aluminium or aluminium oxide. Those that have, upon evaporated indium tin oxide [29], indium [12], silica [30] and electron beam evaporated Al_2O_3 [31] all show grain sizes in the 10-100 nm region. Furthermore, studies [12,31] have highlighted the semispherical nature of the deposits. The results on aluminium and aluminium oxide presented in this chapter are clearly consistent with the literature.

Defects in the layers of the kinds observed by Jamieson and Windle [32], and Mercea *et al.* [33-35] , such as pinholes and cracks, are not found for any of the materials in accordance with a recent study on electron beam evaporated Al_2O_3 gas barrier films [31]. However, nanometer-scale gaps in the coating are observed. Another common factor is the presence of protrusions characteristic of the base polymer morphology. Deposition chemistry will not change their effect upon the coating process since any

effect that they do exert will be one of physical masking similar to that proposed by Jamieson and Windle [32]. The smaller grain size found for increasing oxygen content of the deposited layer will lead to a greater proportion of grain boundaries in those coatings. This has been known to effect the physical properties of ceramic systems [36]. From such an argument one would expect a gradient of properties to be observed since as the proportion of metal in the coatings is increased the size of the grains increases, thereby reducing the proportion of grain boundaries. This is not the case. Chapter 2 showed that the coatings' gas barrier characteristics fall into two groups: firstly, those coatings that contain free metal, Al/PET and metal-rich AlO_X/PET; and that which does not, oxygen-rich AlO_X/PET.

4.5 CONCLUSIONS

- At large scales (10μm) the surface morphologies of all PET films, both uncoated and AlO_x coated, are dominated by protrusions assigned to filler particles in the base polymer.

- AlO_x/PET films consist of globular nanometer-scale particles. The size of these features decreases with increasing oxygen content of the layer consistent with previous studies on the morphologies of evaporated films.

- No defects such as pinholes or cracks were observed for any of the coated films. Nanometer-scale gaps in the coatings may be present.

4.6 REFERENCES

[1] G. Binnig, C. F. Quate, C. Gerber, *Phys. Rev. Lett.* **56** (1986), 930.

[2] D. Sarid, *Scanning Force Microscopy with Applications to Electric, Magnetic and Atomic Forces*, Oxford University Press, Oxford, 1991.

[3] S. N. Magonov, *Applied Spectroscopy Reviews* **28** (1993), 1.

[4] D. M. Eigler, E. K. Schweizer, *Nature* **344** (1990), 524.

[5] G. Dujardin, R. E. Walkup, P. Avouris, *Science* **255** (1992), 1232.

[6] E. Meyer, *Progress in Surface Science* **41** (1992), 3.

[7] H. J. Greisser, R. C. Chatelier, T. R. Gengenbach, Z. R. Vasic, G. Johnson, J. G. Steele, *Polym. Int.* **27** (1992), 109.

[8] H. Hansma, F. Motamedi, P. Smith, P. Hansma, J. C. Wittman, *Polymer* **33** (1992), 647.

[9] P. Markiewicz, M. C. Goh, *Langmuir* **10** (1994), 5.

[10] N. A. Burnham, R. J. Colton, H. M. Pollock, *J. Vac. Sci. Technol.* **A9** (1991), 2548.

[11] C. F. Quate, *Surf. Sci.* **299/300** (1994), 980.

[12] R. Wurster, B. Ocker, *Scanning* **15** (1993), 130.

[13] T. A. Jung, A. Moser, H. J. Hug, D. Brodbeck, R. Hofer, H. R. Hidber, U. D. Schwarz, *Ultramicroscopy* **42-44** (1992), 1446.

[14] S. M. Hues, R. J. Colton, E. Meyer, H.-J. Guntherodt, *MRS Bulletin* **18** (1993), 41.

[15] O. M. Leung, M. C. Goh, *Science* **255** (1992), 64.

[16] K. D. Jandt, T. J. McMaster, M. J. Miles, J. Petermann, *Macromolecules* **26** (1993), 6552.

[17] Digital Instruments, NanoScope III technical information.

[18] Q. Zhong, D. Inniss, K. Kjoller, V. B. Elings, *Surf. Sci. Lett.* **290** (1993), L688.

[19] J.-E. Sundgren, H. T. G. Hentzell, *J. Vac. Sci. Technol.* **A4** (1986), 2259.

[20] J. Weiss, C. Leppin, W. Mader, U. Salzberger, *Thin Solid Films* **174** (1989), 155.

[21] J. F. Silvain, A. Arzur, M. Alnot, J. J. Ehrhardt, P. Lutgen, *Surf. Sci.* **251-252** (1991), 787.

[22] Y. de Puydt, P. Bertrand, *Nuclear Instruments and Methods in Physics Research* **B 39** (1989), 86.

[23] M. J. Verkerk, W. A. M. C. Brankaert, *Thin Solid Films* **139** (1986), 77.

[24] M. J. Verkerk, G. J. van der Kolk, *J. Vac. Sci. Technol.* **A4** (1986), 3101.

[25] W. Lang, *J. Vac. Sci. Technol.* **A8** (1990), 4108.

[26] A. Renou, M. Gillet, *Surf. Sci.* **106** (1981), 27.

[27] B. G. de Boer, G. D. Stein, *Surf. Sci.* **106** (1981), 84.

[28] J. E. Curran, J. S. Page, U. Pick, *Thin Solid Films* **97** (1982), 259.

[29] R. Hiesgen, D. Meissner, *Ultramicroscopy* **42-44** (1992), 1403.

[30] R. I. Hedge, M. A. Chonko, P. J. Tobin, *Mat. Res. Soc. Symp. Proc.* **295** (1993), 65.

[31] R. W. Phillips, T. Markantes, C. LeGallee, *Society of Vacuum Coaters' 36th Annual Technical Conference* (1993), 293.

[32] E. H. H. jamieson, A. H. Windle, *J. Mater. Sci.* **18** (1985), 64.

[33] P. Mercea, L. Muresan, V. Mercea, *J. Memb. Sci.* **24** (1985), 297.

[34] P. Mercea, L. Muresan, V. Mercea, D. Silipas, I. Ursu, *J. Memb. Sci.* **35** (1988), 291.

[35] T. A. Beu, P. Mercea, *Mater. Chem. Phys.* **26** (1990), 309.

[36] J. Karch, R. Birringer, H. Gleiter, *Nature* **330** (1987), 556.

CHAPTER 5

OPTICAL EMISSION SPECTROSCOPY OF AlO_x THIN FILM DEPOSITION

5.1 INTRODUCTION

Characteristic glows observed during AlO_x deposition (absent during metallization) suggest that the hot aluminium vapour reacting with oxygen is producing a flame, a phenomenon which belongs to the family of plasma effects [1] and can be experimentally probed using light emission and absorption spectroscopies [2-5].

So far, the work in this thesis has shown that the physical and chemical properties of AlO_x/PET gas barrier composites can be modified by changing the relative amounts of aluminium and oxygen present during film deposition. It is the aim of this chapter to investigate how the gas phase processes within the deposition chamber are affected by the introduction of oxygen. Two approaches, those of fundamental thermochemistry and metal combustion, have previously been applied to the oxidation reactions of metals in the literature. Both are outlined below.

The chemical physics of metal/oxygen reactions has been extensively studied using optical emission and absorption techniques as non-intrusive probes of both reactant and product species, and reaction pathways and mechanisms [6]. The principal driving force behind such studies has been fundamental research into basic reaction dynamics, metal oxide thermochemistry and atmospheric chemistry [7]. The main applications have been in the areas of solid propellants and explosives which typically

contain between 10 - 30% aluminium and 70 - 90% ammonium perchlorate, and the development of lasers [7].

Another approach is to consider the system as one of metal combustion. This has uses as diverse as continuous steel making, flash bulbs for photography and solid propellant [8,9]. Light metal combustion is often characterized by particle, or smoke, formation [10] and the emission of continuum radiation [11]. Particulate effects are important in many of these applications as well as in other systems: transient carbon particles in flames [12,13]; alumina and beryllia particles in rocket combustion chambers, expansion nozzles and supersonic systems [12]; and contamination of chemical vapour deposition [14] and semiconductor manufacturing processes [15].

Particle formation in semiconductor microfabrication plasmas is currently of great interest [16,17], typical pressures being in the 10^{-3} Torr range for SiH_4/He plasmas. Cold microwave plasmas [18] are thought to affect particulates by their heating effect. Radio frequency silane plasmas are known to contain silicon-containing radicals, and the distribution of particles follows the silicon density of the plasma [19]. Nitridation of aluminium [20], using thermal plasmas of aluminium vapour, argon and ammonia, exhibited nucleation and growth of aluminium nitride particles along the reactor, size approximately 20 nm. Without the presence of ammonia, aluminium particles of 30-40 nm diameter were observed.

5.1.1. Homogeneous Al + O_2 reaction

Aluminium reacting with oxygen, O_2, in the gas phase, leading to the formation of gaseous AlO, is exothermic [21]. Many of the studies probing Al + O_2 kinetics cited [22-25] have used high temperature fast flow reactors. The apparatus is a thermally insulated gas flow system with observation

ports for optical reaction monitoring techniques. Aluminium is produced by direct evaporation of metal downstream of an inert carrier gas inlet. Metal concentrations are low leading to pseudo-first order kinetics. Carrier gas is used to control the total pressure in the system (typically 1-100 Torr) and the reaction temperature. The reactive gas is introduced downstream of the metal source. Most importantly, the reaction zone is isothermal. The pressure range 10-100 Torr was used in these studies because it was found to favour the homogeneous reaction pathway [26].

Beam-gas studies of this system under more controlled conditions (*i.e.*, velocity and state-selective reactions) are achieved using atomic beams [21] of aluminium passed through a chamber of oxygen at pressures lower than 2×10^{-4} Torr (i.e., single collision conditions [27,28]).

Observed rate constants for the Al + O_2 reaction (see Table 5.1.1.1) are similar to those determined for other metal-oxygen reactions [22] such as those of Fe, U, Sr and Ba, all of which have values between 10^{-2} and 10^{0} of the gaseous collision frequency (~10^{-10} ml molecule^{-1} s^{-1}) [23]. If a collision between a gaseous atom of these metals and an oxygen molecule occurs, reaction is likely.

Method of Al prod'n	k ($cm^3\ s^{-1}$)	E_a (kJ mol^{-1})	ΔH (kJ mol^{-1})	Ref.
Direct evaporat'n	$(3 \pm 2) \times 10^{-11}$	small/0	-	22
Direct evaporat'n	$(3.42 \pm 2.2) \times 10^{-11}$	-	-	25
Direct evaporat'n	$(1.6 \pm 0.14) \times 10^{-10}$	-0.71 ± 0.38	-15.1	29
Direct evaporat'n	$\rightarrow 1 \times 10^{-10}$	-	-14 (298 K)	23

Table 5.1.1.1: Kinetic and thermodynamic data summary for Al + O_2 reaction.

Kinetic studies are used to probe the reaction mechanism. In this case, rate constant determinations show no change in value in the 10-100 Torr range [22,23,29], with slight change over the 1-6 Torr range [22]. Lack of pressure-dependence is consistent with a simple oxygen-transfer mechanism [29].

Matrix isolation [2] experiments have supported the formation of both cyclic AlO_2 and bent OAlO structures. Thermodynamic data [30] also points to the formation of an intermediate with stoichiometry Al:O::1:2. Standard heats of formation ($\Delta H^o_f(0K)$) for AlO and AlO_2 are 67 ± 8 and -84 ± 33 kJ mol^{-1}, respectively.

Theoretical calculations [31] show that side-on attack of the oxygen molecule by the aluminium atom to give a cyclic intermediate is most favourable: the importance of aluminium interacting with both oxygen atoms was stressed. Reaction rate constants for Al + $O_2 \rightarrow$ OAlO were calculated [31] at 6.5×10^{-11} $cm^3\ s^{-1}.T^{1/6}$, with no barriers to either the formation or dissociation of OAlO. Two possible decomposition reactions were postulated, giving Al + O_2 or AlO + O as products, with a rate constant ratio of 1:5.

To summarize, the reaction mechanism for Al + O_2 involves the formation of a triatomic intermediate, either cyclic or bent, with little or no barrier to its formation or dissociation. The latter facet of its behaviour is responsible for the fact that no OAlO is formed (except under matrix isolation conditions) since this species decomposes rapidly to give either AlO + O or Al + O_2. The observed rate constant for Al + O_2 → AlO + O is therefore determined by the rate constant for OAlO intermediate formation.

Only one aluminium gas-phase reaction found in the literature [32] has a greater rate constant: Al + N_2O → AlO + N_2, k = (1.1 ± 0.1) x 10^{-11} cm^3 s^{-1}. Aluminium reacting with oxygen would appear to be one of the most favourable gas-phase aluminium reactions.

Of more direct interest to the system under discussion is the reaction of AlO with oxygen: rate constants are quoted [24,25] as (3.1 ± 1.7) x 10^{-13} cm^3 s^{-1} and (7.2 ± 3.6) x 10^{-13} cm^3 s^{-1}. This reaction is therefore approximately one hundred times slower than that of Al + O_2.

5.1.2 Heterogeneous metal oxidation reactions

Heterogeneous combustion usually occurs in the vapour phase [12], in which reaction products condense and produce a large amount of energy (the latent heat of condensation). This is especially important in aluminium-oxygen systems since most of the energetic driving force of solid aluminium oxide formation comes from this process of condensation [10]. Particles produced by such methods are typically between 5 and 50 nm in diameter although sizes as large as 0.1-5 μm have been found in the exhausts of aluminized propellants.

Condensed product formation is a characteristic of many gas-phase metal reactions, and one study [33] describes a macrokinetic approach towards calculating the effect of kinetics, diffusion and heat transfer on both

homogeneous gas phase and heterogeneous gas-particle processes for the Mg + O_2 system. Although not directly applicable to the Al + O_2 system, this reference does outline the principles involved in particle formation during nominally gas-phase processing. Reaction zone modelling assumes that the system is isothermal. Pressures considered in this study are in the range between approximately 15 Torr and atmospheric pressure.

Critical stages in the process are: gas phase reactions leading to product vapour formation; homogeneous nucleation in saturated product vapour; dispersed particle growth through product vapour condensation; and particle growth through heterogeneous reaction of metal and oxygen adsorbed on particle surfaces. A generalized reaction scheme is outlined below for metal M + oxidant X_2:

- Gas-phase reactions: $M_{(g)} + X_{2(g)} \rightarrow MX_{(g)} + X_{(g)}$
  $MX_{(g)} + X_{2(g)} \rightarrow MX_{2(g)} + X_{(g)}$
- Nucleation: $nMX_{(g)} \rightarrow (MX)_{n(s)}$
  $nMX_{2(g)} \rightarrow (MX_2)_{n(s)}$
- Particle growth: $MX_{(g)} + (MX)_{n(s)} \rightarrow (MX)_{n+1(s)}$
  $MX_{2(g)} + (MX_2)_{n(s)} \rightarrow (MX_2)_{n+1(s)}$
- Heterogeneous reactions: $M_{(g)} + X_{(ads)}(MX)_{m+1(s)} \rightarrow (MX)_{m+2(s)}$
  $M_{(g)} + X_{2(ads)}(MX_2)_{m+1(s)} \rightarrow (MX_2)_{m+2(s)}$
- Recombination: $X_{(g)} + X_{(g)} \rightarrow X_{2(g)}$

Simulations show that particle sizes are of the order of tens of nanometers. Pressure increases promote particle growth. The authors conclude that the reaction zone of the Mg + O_2 system is complex.

5.1.2.1 Mechanisms of particle growth

A generalized set of reaction mechanisms has been proposed for metal oxidation [34], one of which covers the situation encountered in AlO_x thin film deposition. This incorporates homogeneous and heterogeneous processes.

Having defined T_r as the temperature of reaction, T_{bo} as the boiling point of the metal oxide, and T_{bm} as the boiling point of the metal, the three generalized cases of metal oxidation can be expressed as:

- $T_r < T_{bm}, T_{bo}$ Low temperature oxidation;
- $T_r \sim T_{bo} < T_{bm}$ Surface burning;
- $T_{bm} < T_r \leq T_{bo}, T_{bm} < T_{bo}$ Vapour phase burning.

Reactive evaporation of aluminium meets the conditions of the last category of metal oxidation, vapour phase burning. A schematic mechanism of the physical and chemical processes involved in such reactions is presented in Figure 5.1.2.1.1. The reaction pathway involving the formation of stoichiometric oxide vapour is not possible in the aluminium system, but the remainder of the processes can be readily envisaged. The exact relationship between, and relative importances of, the individual processes is not clear.

5.1.2.2 Particle nucleation

Particle nucleation can occur by two mechanisms: homogeneous and heterogeneous [10]. The former depends upon the formation of droplets of greater than the critical size by statistical fluctuations in the gas phase, and is the most likely mechanism for metal vapour flames, while the latter

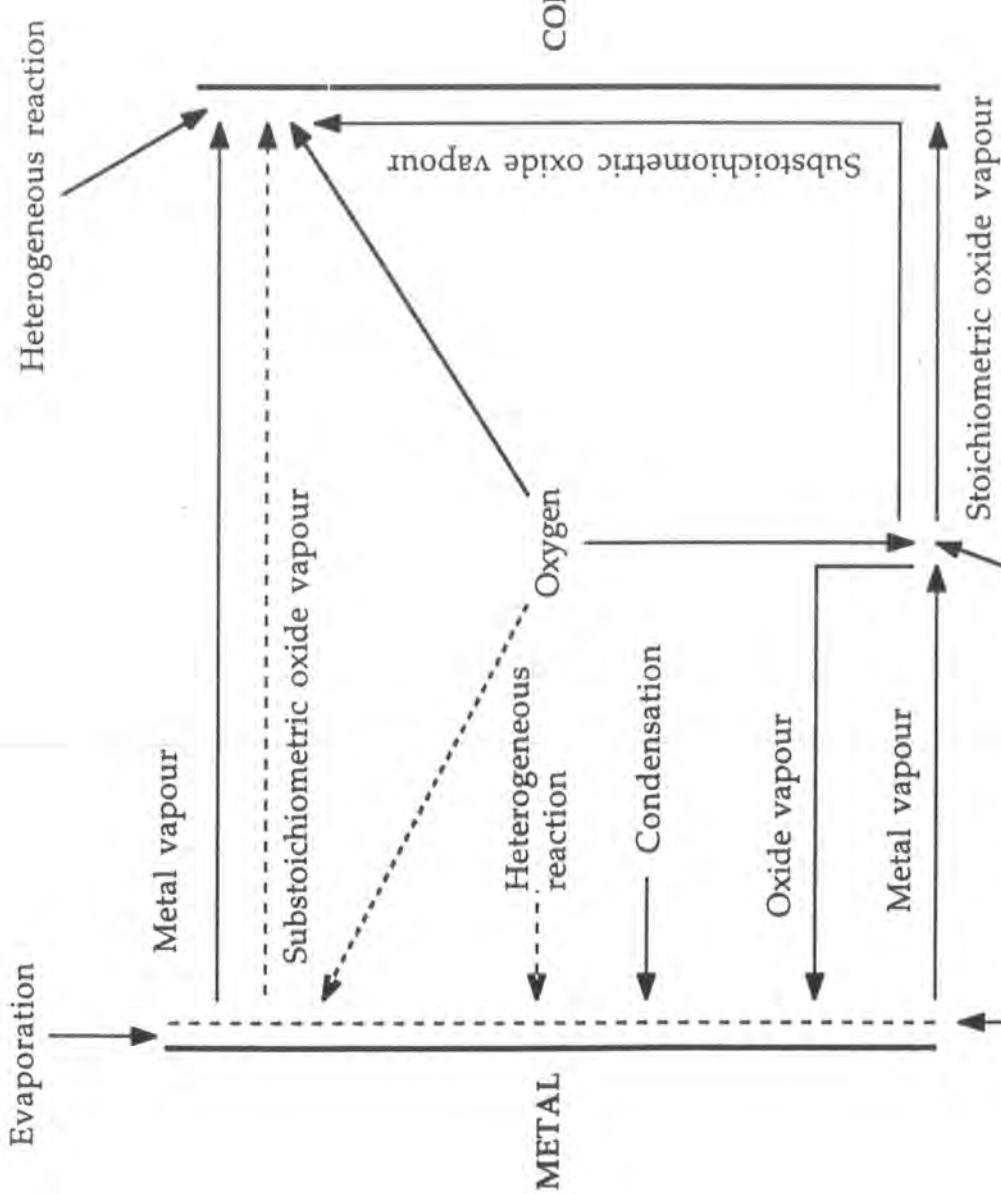

FIGURE 5.1.2.1.1: Schematic vapour phase burning mechanism.

depends upon the presence of foreign particles to initiate nucleation. This discussion will be limited to homogeneous nucleation.

Modification of Frenkel's classical nucleation theory yields the number of embryonic droplets of alumina per unit volume (V), per unit time that pass through the free energy barrier of nucleation and grow to larger sizes.

- $I = (2\pi\sigma/m)^{1/2}.v.S.(p^o/kT)^2.\exp[-16\pi\sigma^3v^2/3(kT)^3.\ln S]$

where: σ is the surface tension of liquid alumina; m is the molar mass of aluminium; v is the volume per molecule of liquid alumina; S is an effective supersaturation coefficient; and p^o is the equilibrium partial pressure of aluminium in the vaporization products of alumina.

The radius of particles at the critical point (when they can pass through the nucleation energy barrier), r^*, is given by:

- $r^* = 2\sigma v/kT.\ln S$

Supersaturation is not easily defined for the aluminium + oxygen system since there is no vapour phase species of stoichiometry Al_2O_3 [10,34], and the extent of supersaturation will depend upon knowledge of the reaction path which is not available. However, supersaturation can be seen to be of great importance in the nucleation of these systems.

Hecht *et al.* have shown that supersaturations greater than 10^5 were required at between 1-50 Torr for Na, K and Zn systems [35]. Clusters can contain as many as 650 atoms [36].

5.1.2.3 Rate of Particle Growth

Phenomena associated with particle growth are [10]: diffusion of condensing species to the particle surface; condensation on the surface; and the transfer of the latent heat of condensation away from the particle. Complex condensation processes are believed to dominate [10,34]. The rate of particle radius growth through the balance of a supersaturation driving force and resistances arising from heat transfer and diffusional phenomena [10].

- dr/dt = driving force/sum of two resistances
- driving force = $(1-r^*/r).\ln S$
- heat transfer resistance $\propto l_v^2/\chi$
- diffusional resistance $\propto 1/pD$

where r is the instantaneous radius of the particle; S is the supersaturation; l_v is the heat of condensation of alumina; χ is the thermal conductivity of the gas phase; p is the sum of the partial pressures of the condensing species; and D is an appropriate mean diffusion coefficient. Again the concept of supersaturation is important.

5.1.2.4 Continuum radiation effects

Metal vapour/oxygen flames exhibit characteristic continuum emissions under many conditions, e.g., magnesium/oxygen diffusion flames [37], trimethylaluminium (TMA)/oxygen flames [38], zirconium/oxygen flame [8], and the detonation of aluminium-containing grenades in the upper atmosphere [34]. The characteristics of these

emissions can be linked to the heterogeneous combustion and condensation rates (which are greatly interdependent) [12].

Magnesium/oxygen diffusion flames (total pressure 2-10 Torr, oxygen partial pressure 0.2-1.1 Torr) yield an emission spectrum consisting entirely of continuum radiation with broad maxima and a complete lack of the well-known Mg + O_2 spectral features [37]. This is taken as evidence of a heterogeneous reaction with electronic excitation of the surface layer [34]. Deposition of a 'fluffy' white deposit occurs throughout the vacuum chamber: adhesion was poor everywhere except the regions closest to the diffusion orifice; and individual particle size as observed by SEM was ~10 nm.

TMA/oxygen flame emission spectra [38] contain features of both continuous and discrete natures: the former is the only feature observed in the initial stages of reaction with maximum intensity at ~500 nm and is assigned to radiative combination of AlO and O (see below); and the latter, discrete, assignable features are superimposed upon the continuum.

The mechanism proposed for radiative combination of AlO and O, as observed after the release of TMA in the upper atmosphere, is outlined below:

- $AlO + O \rightarrow AlO_2^*$ Excited state formation
- $AlO_2^* \rightarrow AlO_2 + h\nu$ Pseudo-continuum emission
- $AlO_2^* + M \rightarrow AlO_2$ Collisional deactivation
- $AlO_2 + O \rightarrow AlO + O_2$ Regeneration of reactants

For the more generalized case of solid grain vaporization and reaction in the gas phase it is assumed that dust particles can be treated as a radiating continuum [39], the radiative flux of which is dependent upon the number density of particles.

Intensities at given wavelengths can be calculated from the equation[12]:

- $I_\lambda = I_b.(\sigma_a/\sigma_t).[1- \exp(-\sigma_t.c_p.z)].\tau$

where: I_λ is the intensity of light of wavelength l; I_b is the intensity of the equivalent black body radiation; σ_a and σ_t are the Mie absorption (emission) and total cross-sections of the particles; c_p is the particle concentration; z is the path length; and τ is a factor to account for the scattering of light in a particle cloud. Thus, all else being equal, for a given system the intensity of radiation increases with particle concentration.

5.1.3 Optical emission spectroscopy

Fundamental to the optical emission process is the structure of molecules [40]. When a molecule forms there is an energetic balance between attractive and repulsive forces. The Morse function is an empirical description of the anharmonic behaviour of a diatomic molecule:

- $E = D_{eq}.[1 - \exp\{a(r_{eq} - r)\}]^2$

where D_{eq} is the equilibrium dissociation energy, a is a constant for a particular molecule, r_{eq} and r are the equilibrium and actual internuclear distances, respectively. The vibrational energy is then given by:

- $\varepsilon_{vibration} = (v + 1/2)\omega_e - x_e(v + 1/2)^2\omega_e$

where $\varepsilon_{vibration}$ is the energy in wavenumbers, v is the vibrational quantum number, ω_e is the vibrational frequency constant, and x_e is the

anharmonicity constant. The latter is usually small and positive, accounting for the crowding together of vibrational levels at high v.

Optical emission spectroscopy is suitable for elucidation of molecular structure and interactions [41] since it studies light emitted from processes originating in the electronic, vibrational and rotational structure of molecules.

Max Planck's quantization of energy led to the development and understanding of molecular energy [42]. The Born-Oppenheimer approximation states that the total energy of a system can be described as the sum of its constituent parts:

- $E_{total} = E_{electronic} + E_{vibration} + E_{rotation}$

and that these components are independent of each other. The relative orders of magnitude of the energy changes associated with each phenomenon are:

- $\Delta E_{electronic} >> \Delta E_{vibration} >>> \Delta E_{rotation}$

Vibrational and rotational energy changes are the coarse and fine structure to the spectrum of electronic transitions, respectively. The large number of available initial and final states means that optical emission can be very complicated. This discussion will be limited to the vibrational structure.

From the partitioning of energy outlined above, the energy of the system can be expressed in terms of the vibrational states of the molecule:

- $\varepsilon_{total} = \varepsilon_{electronic} + (v + 1/2)\ddot{\omega}_e - x_e(v + 1/2)^2\omega_e$

There is essentially no selection rule for vibrational transitions, hence every transition has some probability. The Franck-Condon Principle, however, does limit the intensities of the observed transitions. It states that an electronic transition occurs so rapidly that a vibrating molecule does not change its internuclear distance appreciably during the transition. The probability distributions as a function of internuclear separation for the different vibrational levels dictate the likelihood of a given transition.

5.2 EXPERIMENTAL

5.2.1 Deposition parameters

Deposition parameters used in the optical emission experiments are shown below in Table 5.2.1.1. In addition to those (standard) parameters shown in Chapter 1, experiments were also performed at higher oxygen flow rates. Upon any change in conditions the measured parameters were allowed to equilibrate prior to spectral accumulation.

Film type	Optical density	O_2 flow rate /l min^{-1}	Constant Al wire feed rate /inch min^{-1}	Constant PET web speed/ m min^{-1}	Constant heater voltage/ V	Chamber pressure/ 10^{-3} Torr
Al/PET	0.8	0	6	250	5.5	4
Metal-rich AlO_x/PET	0.4	2-3	6	250	5.5	4
Oxygen-rich AlO_x/PET	0.2	3-5	6	250	5.5	3
-	0.15	4	6	250	5.5	3
-	0.12	5-6	6	250	5.5	3

Table 5.2.1.1: Production parameters associated with characteristic AlO_x barrier film products.

5.2.2 Optical emission spectroscopy

All optical emission measurements were performed over the 200-900 nm wavelength range using a Rees Instruments Monolight Optical Spectrum Analyzer configured for plasma analysis with a Model 6107 scanning monochromator, represented schematically in Figure 5.2.2.1. Data was accumulated with a full width at half maximum intensity (FWHM) of 3 nm. Helium-neon laser emission provided the reference for wavelength calibration. Spectra were accumulated by directing the optical head at the

visible glow through the chamber's observation window (1" toughened glass, light transmission cut-off typically ~300 nm).

5.3 RESULTS

Optical emission spectra accumulated during the deposition of Al/PET, and metal- and oxygen-rich AlO_x/PET under experimental conditions outlined above, Section 5.2.1, are presented in Figure 5.3.1. Two features are observed for all three spectra: a continuous background of emitted radiation; and sharp peaks superimposed upon that background.

Continuous radiation emission changes upon the introduction of oxygen into the aluminium evaporant stream: emission shifts from a smooth continuum ranging from ~400-850 nm, peaking in intensity at ~700 nm, to lower wavelengths, ~350-850 nm peaking at ~500 nm.

Extra oxygen introduction at constant aluminium wire feed rate, to flow rates of 4 and 5 l min^{-1}, yield shapes of continuum radiation similar to but of greater intensity than those at lower flow rates for the deposition of metal- and oxygen-rich AlO_x/PET, Figure 5.3.2.

Two prominent peaks are observed at λ ~436 and ~546 nm. None of these features has been assigned despite considerable attention to the literature. All features are observed for all deposition conditions, including that of no oxygen flow. Their intensities, taken as that above the level of the background radiation, are tabulated in Tables 5.3.1 and 5.3.2, corresponding to the spectra in Figures 5.3.1 and 5.3.2, respectively.

Deposited film	436 nm intensity (a.u.)	546 nm intensity (a.u.)
Al/PET	555	425
Metal-rich AlO_x/PET	386	390
Oxygen-rich AlO_x/PET	458	373

Table 5.3.1: 436 and 546 nm line intensities for AlO_x gas barrier film deposition.

While the intensity of the 436 nm line does not follow the trend of oxygen introduction, that of the 546 nm line decreases with oxygen introduction.

Further experiments performed at constant aluminium wire feed rate allowed the effect of oxygen introduction alone to be evaluated. Intensity data for the 436 and 546 nm lines are:

Film deposited	Oxygen flow rate/l min^{-1}	436 nm intensity (a.u.)	546 nm intensity (a.u.)
Metal-rich AlO_x/PET	2-3	386	390
Oxygen-rich AlO_x/PET	3-5	458	373
-	4	570	528
-	5-6	577	483

Table 5.3.2: 436 and 546 nm line intensities as a function of oxygen flow rate at constant aluminium wire feed rate.

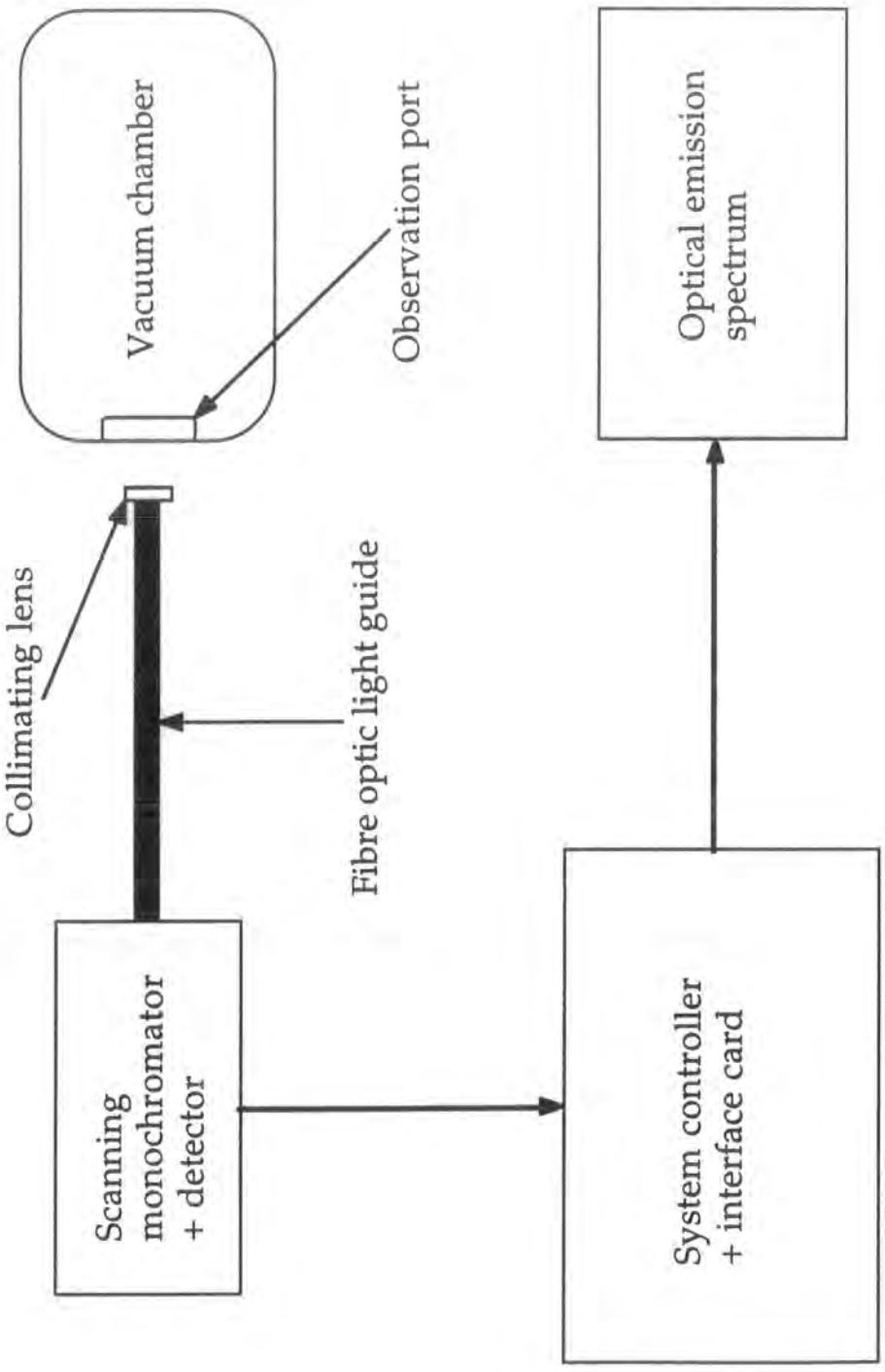

Figure 5.2.2.1: Schematic representation of experimental apparatus for optical emission spectroscopy

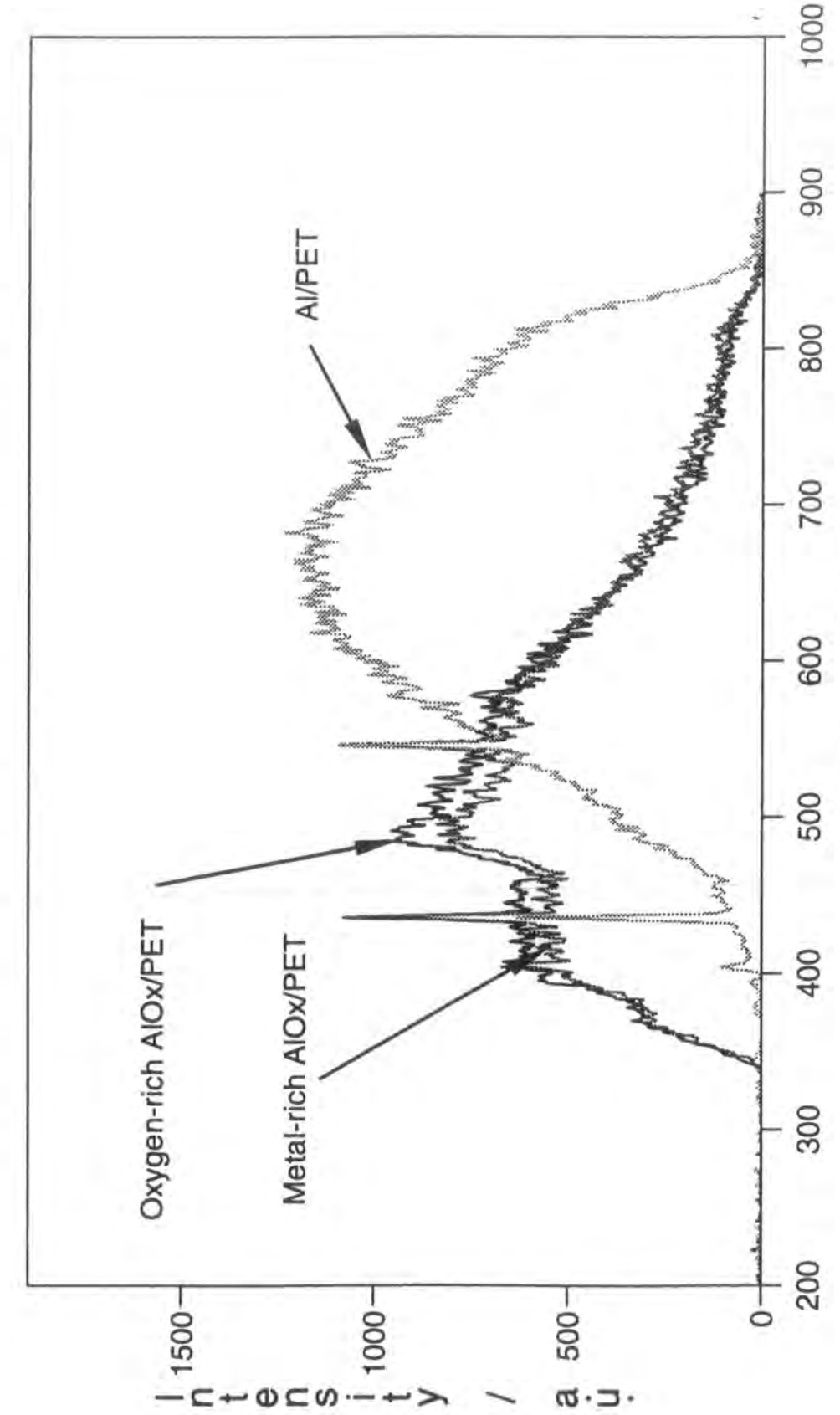

Figure 5.3.1: OES of AlOx gas barrier film deposition.

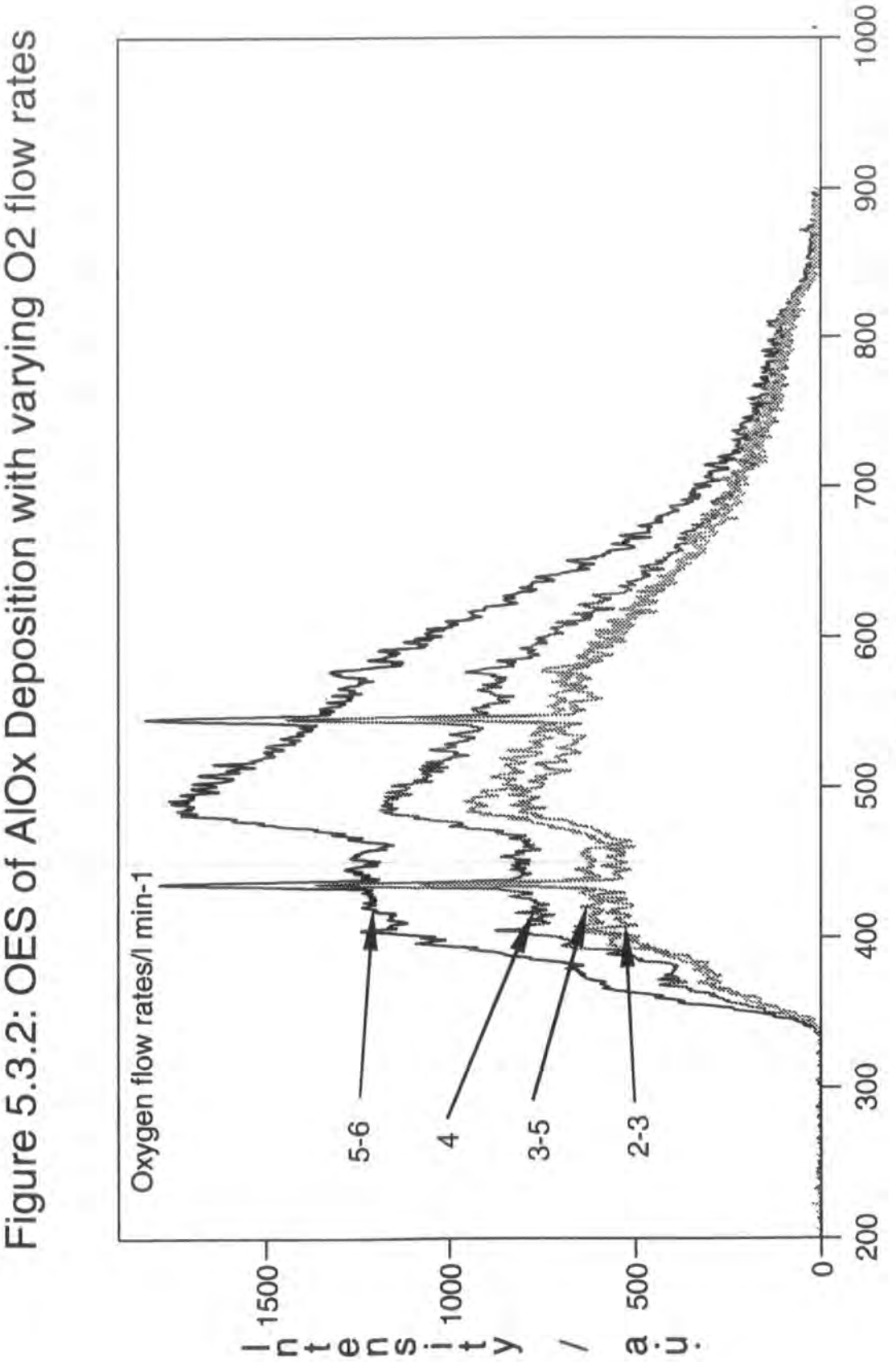

Figure 5.3.2: OES of AlOx Deposition with varying O2 flow rates

Under these conditions it is the 436 nm line intensity that follows the experimental variable, increasing with oxygen flow rate.

The significance of these trends is unclear without further work in this field.

5.4 DISCUSSION

Metals are thought to evaporate atomically [43] although it has been shown, in this and previous chapters that this is not always the case. It was hoped that upon the introduction of oxygen into the metallizing chamber features corresponding to those of homogeneous gas phase reactions of aluminium atoms would be found. Clearly they have not, and the system is more complicated than anticipated. As will be shown below, there are several possible explanations for this behaviour.

Two important points are raised by these results. Firstly, the discrete emission lines observed occur at the same wavelengths for all conditions employed. The reaction responsible for these features is therefore common to all conditions. The principal factor common to all experiments is the presence of aluminium in a vacuum, the residual atmosphere of which is predominantly water vapour [44]. Indeed, pressures of water vapour similar to those possible for these experiments are found to dramatically influence the properties of deposited Al layers, see Chapter 4. It is possible that these features arise from the reaction of aluminium with the residual atmosphere of the chamber.

Secondly, pseudo-continuum radiation emission is found. For the case of Al/PET deposition (zero oxygen flow rate) the spectral shape is consistent with black body radiation. One study of the kinetics of gas phase aluminium reactions found this effect in the 600-850 nm range [45].

Continuum radiation emission is well known in aluminium oxidation reactions [5,45-47]. AlO emission is sometimes seen as a very strong continuum because of the formation of AlO in high vibrational states (with small energy spacings between them), emission from which appears to be continuous when observed at low resolution, e.g., 3 nm FWHM. Continuum emission is also characteristic of particle formation reactions, Section 5.1.2.4. However, at sufficiently low resolutions, similar to those used in these experiments, even reactions occuring under single collisions such as Bi + F_2 [48] and Ti + O_2, N_2O or NO_2 [28] can yield pseudo-continuum radiation. In the latter example titanium evaporating effusively into a chamber containing ~10^{-4} Torr of reactive gas gave rise to pseudo-continual radiation over the range of 300-700 nm, varying in shape with the nature of the oxidant.

With regard to the varying intensities of emitted radiation observed in these experiments, again both homogeneous and heterogeneous systems would show an increase with oxygen flow rate, the former due to the formation of more product and the latter due to the presence of more particles [39]. Figure 5.3.2 showed that the trends in emission intensity for variants of AlO_x coatings at constant aluminium feed rate appear to follow the changes in oxygen flow rate; it is feasible that the increased proportion of oxygen yields greater amounts of aluminium-oxygen products and hence increases the degree of supersaturation in the system, leading to more particle formation [10].

Having established that gas phase reactions are occuring, how do they relate to the observation of previous chapters? The similarity between the optical emission spectra of metal- and oxygen-rich AlO_x/PET deposition conditions correlates with the similar chemistry of the coating/polymer interphases, Chapter 3.

5.5 CONCLUSIONS

- Introduction of oxygen into a conventional metallizing chamber leads to a visible 'glow'; reaction between aluminium and oxygen is therefore occuring in the gas phase.

- Emitted radiation during metallization is consistent with black body emission, caused by the heat of the aluminium vapour, whereas that observed for AlO_x coating matches that found for the combustion (either homo- or heterogeneous) of aluminium to yield aluminium oxide products.

- Differences between conditions employed for metal- and oxygen-rich AlO_x deposition affect the emission line intensities although these cannot be interpreted without further work in this area.

- Oxide species observed in Chapter 3 via XPS and argon ion sputter depth profiles can be rationalized in terms of these optical emission results. The primary difference between Al/PET and metal- and oxygen-rich AlO_x/PET is the presence of oxide in excess of that observed for aerial oxidation in the subsurface region of the latter two deposits. This corresponds to the observation of similar oxide formation *via* OES.

5.6 REFERENCES

[1] A. T. Bell in *Techniques and Applications of Plasma Chemistry*, Eds. J. R. Hollahan, A. T. Bell, Wiley, New York, 1974, Chapter 1.

[2] N. L. Garland, H. H. Nelson, *Chem. Phys. Lett.* **191** (1992), 269.

[3] D. M. Lindsay, J. L. Gole, *J. Chem. Phys.* **66** (1977), 3886.

[4] D. E. Jensen, G. A. Jones, *J. Chem. Soc. Farad. Trans. 1* **68** (1972), 259.

[5] S. Rosenwaks, R. E. Steele, H. P. Broida, *J. Chem. Phys.* **63** (1975), 1963.

[6] C. Naulin, M. Costes, G. Dorthe in *Gas Phase Metal Reactions*, Ed. A. Fontijn, Elsevier, Amsterdam, 1992, 189.

[7] M. E. Weber, J. L. Elkind, P. B. Armentrout, *J. Chem. Phys.* **84** (1986), 1521.

[8] L. S. Nelson, D. E. Rosner, S. C. Kurzius, H. S. Levine, *12th Symp. (Intl.) on Combustion*, The Combustion Institute, Pittsburgh, 1969, 59.

[9] W. A. Hardy, J. W. Linnett, *11th Symp. (Intl.) on Combustion*, The Combustion Institute, Pittsburgh, 1966, 203.

[10] R. W. Hermsen, R. Dunlap, *Combust. Flame* **13** (1969), 253.

[11] R. N. Newman, J. F. B Payne, *Combust. Flame* **68** (1987), 31.

[12] W. G. Courtney, *11th Symp. (Intl.) on Combustion*, The Combustion Institute, Pittsburgh, 1966, 237.

[13] I. M. Kennedy, W. Kollmann, J.-Y. Chen, *Combust. Flame* **81** (1990), 73.

[14] S. L. Chung, J. L. Katz, *Combust. Flame* **61** (1985), 271.

[15] S. R. Turns, M. J. Funari, A. Khan, *Combust. Flame* **75** (1989), 183.

[16] A. Garscadden, *Proc. Int. Symp. Plasma Chem. 11* (1993), 785.

[17] T. Fukuzawa, M. Shiratani, Y. Watanabe, *Proc. Int. Symp. Plasma Chem. 11* (1993), 1125.

[18] Y. Nakano, K. Sugiyama, Y. Takeuchi, T. Matsuda, *Proc. Int. Symp. Plasma Chem. 11* (1993), 1422.

[19] M. Shiratani, H. Tsuroka, T. Fukuzawa, H. Kawasaki, Y. Watanabe, *Proc. Int. Symp. Plasma Chem. 11* (1993), 1469.

[20] J.-F. Bilodeau, P. Proulx, F. J. Moura, R. J. Munz, *Proc. Int. Symp. Plasma Chem. 11* (1993), 356.

[21] P. J. Dagdigian, H. W. Cruse, R. N. Zare, *J. Chem. Phys.* 62 (1975), 1824.

[22] A. Fontijn, W. Felder, J. J. Houghton, *Chem. Phys. Lett.* 27 (1974), 365.

[23] A. Fontijn, P. M. Futerko in *Gas Phase Metal Reactions*, Ed. A. Fontijn, Elsevier, Amsterdam, 1992, 93.

[24] W. Felder, A. Fontijn, *J. Chem. Phys.* 64 (1976), 1977.

[25] A. Fontijn, W. Felder in *Reactive Intermediates in the Gas Phase: Generation and Monitoring*, Ed. D. W. Setser, Academic Press, New York, 1979, Chapter 2.

[26] A. Fontijn, S. C. Kurzius, J. J. Houghton, *11th Symp. (Intl.) on Combustion*, The Combustion Institute, Pittsburgh, 1966, 167.

[27] D. R. Preuss, J. L. Gole, *J. Chem. Phys.* 66 (1977), 2994.

[28] L. H. Dubois, J. L. Gole, *J. Chem. Phys.* 66 (1977), 779.

[29] N. L. Garland in *Gas Phase Metal Reactions*, Ed. A. Fontijn, Elsevier, Amsterdam, 1992, 73.

[30] W. Chen, W. L. Hase, H. B. Schlegel in *Gas Phase Metal Reactions*, Ed. A. Fontijn, Elsevier, Amsterdam, 1992, 179.

[31] P. Marshall, P. B. O'Connor, W.-T. Chan, P. V. Kristof, J. D. Goddard in *Gas Phase Metal Reactions*, Ed. A. Fontijn, Elsevier, Amsterdam, 1992, 147.

[32] J. M. Parnis, S. A. Mitchell, T. S. Kanigan, P. A. Hackett, *J. Phys. Chem.* 93 (1989), 8045.

[33] O. E. Kashireninov in *Gas Phase Metal Reactions*, Ed. A. Fontijn, Elsevier, Amsterdam, 1992, 621.

[34] G. H. Markstein, *11th Symp. (Intl.) on Combustion*, The Combustion Institute, Pittsburgh, 1966, 219.

[35] J. Hecht, W. P. West, M. A. Norton, *Surf. Sci.* **106** (1981), 131.

[36] J. Muhlbach, E. Recknagel, K. Sattler, *Surf. Sci.* **106** (1981), 188.

[37] G. H. Markstein, *9th Symp. (Intl.) on Combustion*, Academic Press, London, 1963, 137.

[38] M. Vanpee, T. F. Seamans, *11th Symp. (Intl.) on Combustion*, The Combustion Institute, Pittsburgh, 1966, 931.

[39] G. A. Marxman, *11th Symp. (Intl.) on Combustion*, The Combustion Institute, Pittsburgh, 1966, 269.

[40] C. N. Banwell, *Fundamentals of Molecular Spectroscopy*, 3rd Edition, McGraw-Hill, London, 1983, Chapter 3.

[41] N. H. March, J. F. Mucci, *Chemical Physics of Free Molecules*, Plenum Press, New York, 1993, Chapter 1.

[42] C. N. Banwell, *Fundamentals of Molecular Spectroscopy*, 3rd Edition, McGraw-Hill, London, 1983, Chapter 6.

[43] K. J. Klabunde, *Chemistry of Free Atoms and Particles*, Academic Press, New York, 1980, Chapter 7.

[44] J. E. Curran, J. S. Page, U. Pick, *Thin Solid Films* **97** (1982), 259.

[45] J. L. Gole, S. A. Pace, *J. Chem. Phys.* **73** (1980), 836.

[46] C. E. Kolb, M. E. Gersh, D. R. Herschbach, *Combust. Flame* **25** (1975), 31.

[47] D. M. Lindsay, J. L. Gole, *J. Chem. Phys.* **66** (1977), 3886.

[48] B. S. Cheong, M. D. Oberlander, R. P. Kampf, J. M. Parson, *J. Chem. Phys.* **99** (1993), 5104.

CHAPTER 6

PROCESS-RELATED GAS BARRIER DETERIORATION OF AlO_x/PET FILMS

6.1 INTRODUCTION

So far this thesis has examined properties of the as-deposited gas barrier films. When used commercially, the 'processability' of the films is a key factor to product success [1]. For flexible coated polymer films post-production processing typically entails passage of the material through laminating/coating machines which move the film *via* rollers and the tension placed upon the film by them. Industrially it has been determined that the gas barrier of such films can be lost during post-production processing. An understanding of how deposition stoichiometry (and therefore coating properties) affects the processability of coated polymer films is therefore desirable. Mechanistic studies of gas barrier loss were initiated. Recalling the work presented in Chapter 2, it was shown that helium is the most sensitive gas for determining microstructural differences between coated films.

As in previous chapters, Al/PET and metal- and oxygen-rich AlO_x/PET gas barrier composites are studied. Permeability and surface morphology were studied as a function of uniaxial stretching in the direction of film spooling as in post-production processing.

Not only did the gas barrier of the AlO_x-coated polymer films deteriorate upon stretching, both under industrial and simulated conditions, but some form of 'healing' was observed when oxygen-rich AlO_x/PET films were tested (under ambient or humid conditions) for shelf-

AlO_X/PET films were tested (under ambient or humid conditions) for shelf-life. Experiments were therefore carried out to probe whether this was in fact a real effect characteristic of AlO_X/PET composite structures.

6.1.1 Fracture and cracking phenomena in thin coatings adhering to high-elongation substrates

Relatively little work has been performed on the elongation of thin films adhering to high-elongation substrates such as polymers (Wojciechowski and Mendolia [2], Lee [3] and Hosaka [4]). The AlO_X/PET gas barrier composites featured in this thesis fit into this category of materials, as do the SiO_X coated PET substrates studied by Felts [1]. Wojciechowski and Mendolia [2] have recently reviewed progress in this area. Fundamental to their approach is the idea that, for systems where two dissimilar materials are bonded together, the properties of the individual materials are influenced by each other, resulting in a 'composite material' with its own properties. Applying this concept to brittle films vacuum-deposited onto weak modulus substrates, they propose that cracking phenomena can be used to characterize thin-film adhesion.

Cohesive failure is typified by cracking of the low-elongation film. The exact mechanism of stress relief is unclear since, although the film has cracked, there are substantial proportions of the film still adhered to the substrate. Grosskreutz and McNeil [5] interpreted their results in terms of stress relaxation of the film, proportional to the stress induced in the substrate which decreases with increasing distance from the crack. The film therefore does not return to its unstrained state after cracking but some of the energy is released.

Stress relaxation mechanisms start to occur when the film-substrate elastic limit is reached, and they include: plastic flow of the substrate; plastic

flow of the film; film tensile fracture; compressive buckling of the film; and film adhesive failure at the film-substrate interface. Substrate stresses are transferred to the overlying film through the interface, hence, by monitoring cracking, information concerning the physical properties of the interface should be available. Cracking patterns of well-adhered films are characterized by a regular and parallel nature as opposed to the irregular features seen for poorly-adhered films [2].

Mathematical treatment of adhesion between μm-range brittle films and low modulus polymeric substrates [6,7] was used to probe the critical stress required to change the behaviour of the system from that of perfect adhesion, and therefore only cohesive failure of the brittle film, to adhesive failure, upon which the film starts to peel away from the substrate.

Since it is closely analogous to the work performed on AlO_x/PET composites, the Kapton case study contained within Wojciechowski and Mendolia's [2] review will be described. 76 μm high strength polyimide film (Kapton, Du Pont) was coated with 40-200 nm of Permalloy (Ni-Fe alloy) and uniaxially stretched. Film failure occurred in stages: at low strains (<0.8%) no cracks were visible; cohesive failure, evidenced by film cracking, commenced at ~0.85% strain, the point of crack onset; as strain was increased up to 5% the number of cracks increases; and, finally, at strains > 6% secondary crack formation and buckling of the film is observed. Buckling of the film leads to the observation (by SEM) of three-dimensional 'tents'.

6.1.2 Permeabilities of stretched gas barrier films

Felts has demonstrated the application of an almost *in situ* method of determining the onset strain and rate of gas barrier loss of various gas barrier composites [1]. Critical to the onset of gas barrier loss is the thickness of the coating: for SiO_x coatings the two are inversely proportional. Felts

determined that the gas barrier degradation of evaporated materials occurred at lower extents of stretching than for plasma-deposited materials. However, these results were undoubtedly influenced by his choice of samples. For example, taking into account the stated facts relating to failure onset and coating thickness, the aluminium oxide samples used were 60 nm thick compared to the 20-25 nm samples studied in this thesis, Chapter 1.

6.2 EXPERIMENTAL

6.2.1 Sample definition

All stretched samples were prepared by Hoechst using coated films prepared by Camvac, Chapter 1. Samples were uniaxially stretched on a linear stretching apparatus, schematically represented in Figure 6.2.1.1, by 1%, 2%, 3%, 5%, 7% and 10%, and were stored under ambient conditions. They were analyzed many months after preparation; it is fair to assume that they have reached equilibrium. Stretchings of between 1 and 2% are thought to occur during processing [8]. The stretching apparatus, analogous to a 'rack', consists of two sample clamps, one of which is fixed and the other movable by means of threaded rods connecting the two components of the apparatus. Sample films are securely clamped and then marked at points corresponding to the length scale of the apparatus, and then the threaded rods are rotated to effect elongation of the film. Once the desired degree of stretching is reached the sample film is released.

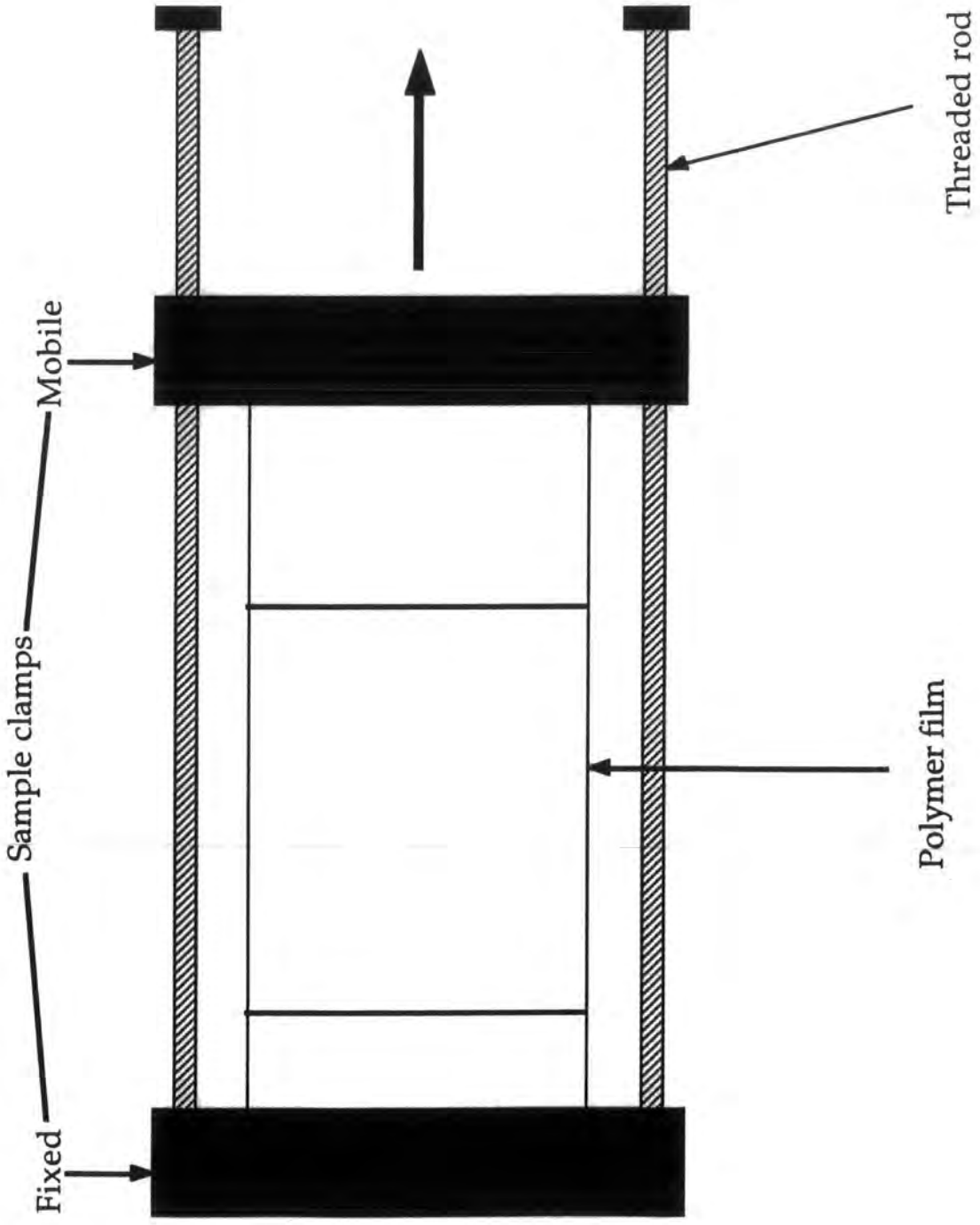

Figure 6.2.1.1: Schematic diagram of uniaxial stretching apparatus

6.2.2 Permeability

All permeability experiments were carried out as described in Chapter 2. Supplementary experiments concerning the 'healing' effect of exposure to water vapour required additional apparatus and a different experimental protocol.

Water vapour exposure experiments required apparatus which would allow a known water vapour pressure to be attained under a controlled atmosphere with ready attachment to existing equipment. A plan view diagram of the apparatus is presented in Figure 6.2.2.1.

A glass tube, sealed at one end and attached to a Young's teflon tap and ground glass joint at the other, and filled with water was chosen as the water vapour supply. The water vapour pressure is known (from standard tables) if the temperature of the water is kept constant. Water used was of ultra-high purity.

Oxygen carrier gas is required to provide an ambient atmosphere of known composition, and to purge the system of any unwanted gaseous/vapour species prior to experimentation. Since, unlike the gaseous permeability apparatus, the gas/vapour inlet system is not connected to a vacuum line it was necessary, in order to control gas composition and pressure, to have both a gas inlet and exhaust; this was accomplished by fitting two bleed valves to the system, one as a gas inlet and the other as an exhaust. Pressure of the gas supply was directly controlled by the gas cylinder regulator. The pressure of gas exposed to the membrane is set at approximately atmospheric pressure by momentarily venting the gaseous exhaust after the gas supply has been isolated, thus allowing the system to equilibrate at ambient pressure.

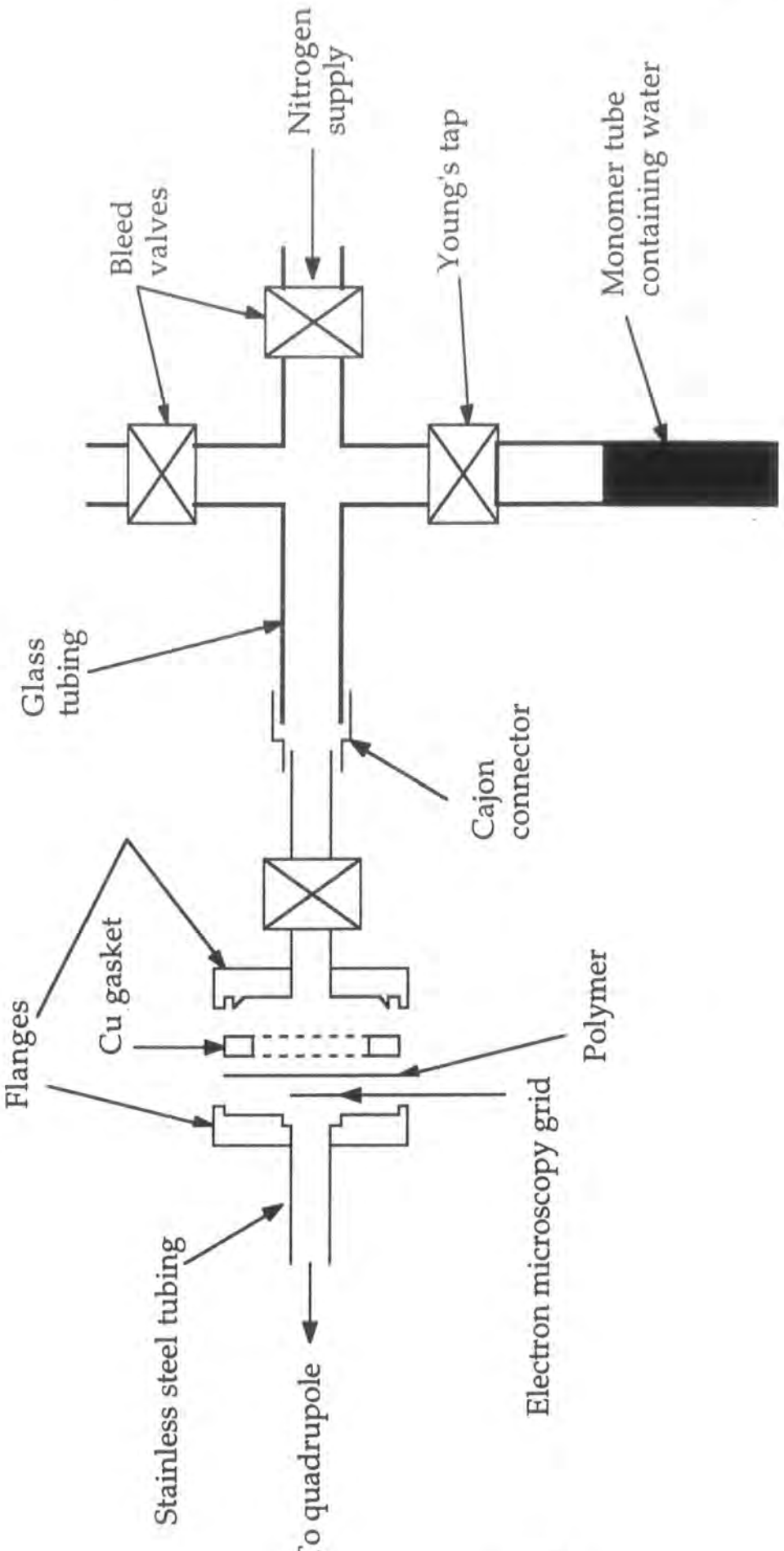

Figure 6.2.2.1: Schematic representation of water vapour healing permeability apparatus.

Samples are handled and introduced into the vacuum chamber as reported previously, Chapter 2 MEPPPs of Ar and He were determined prior to water vapour exposure using the standard apparatus. The sample was then removed from the vacuum chamber and the gas supply was replaced by the water vapour supply, and the sample reintroduced. The water vapour supply was purged with oxygen and then opened up to the sample for 24 hours, after which period the sample was again extracted from the machine and the gas supply replaced prior to sample reintroduction for MEPPP determination in order to probe the extent of gas barrier healing.

Room temperature was 24°C during these experiments, giving a water vapour pressure of 22.4 Torr [9].

6.2.3 AFM

All atomic force micrographs were accumulated as described in Chapter 4, with additional care being taken to avoid scanning-induced artefacts caused by the large-scale nature of the features observed by changing the scanning directions.

6.3 RESULTS

6.3.1 Permeability of stretched AlO_X/PET films

Data for Ar, He and O_2 MEPPPs of stretched Al/PET, metal- and oxygen-rich AlO_X/PET are tabulated in Tables 6.3.1.1 (a)-(c).

(a)

Al/PET sample	MEPPP (10^{-9} Torr)		
	Ar	He	O_2
0%	0.029 ± 0.003	1.36 ± 0.12	0.027 ± 0.002
1%	0.029 ± 0.001	1.17 ± 0.01	0.024 ± 0.001
2%	0.037 ± 0.003	1.66 ± 0.10	0.031 ± 0.001
3%	0.29 ± 0.01	7.41 ± 0.49	0.20 ± 0.05
5%	0.64 ± 0.10	28.43 ± 1.38	0.75 ± 0.01
7%	1.00 ± 0.04	44.63 ± 0.49	0.87 ± 0.01
PET	0.93 ± 0.01	53.7 ± 0.6	1.02 ± 0.01

(b)

Metal-rich AlO_x /PET sample	MEPPP (10^{-9} Torr)		
	Ar	He	O_2
0%	0.035 ± 0.001	1.03 ± 0.06	0.025 ± 0.003
1%	0.041 ± 0.003	1.88 ± 0.15	0.030 ± 0.020
2%	0.064 ± 0.004	1.59 ± 0.01	0.040 ± 0.006
3%	0.88 ± 0.09	52.7 ± 4.5	0.66 ± 0.02
5%	0.92 ± 0.06	44.4 ± 3.8	0.88 ± 0.02
7%	1.08 ± 0.03	51.7 ± 1.8	1.13 ± 0.02
PET	0.93 ± 0.01	53.7 ± 0.6	1.02 ± 0.01

(c)

Oxygen-rich AlO_X /PET sample	MEPPP (10^{-9} Torr)		
	Ar	He	O_2
0%	0.034 ± 0.001	1.86 ± 0.05	0.025 ± 0.002
1%	0.029 ± 0.001	1.27 ± 0.03	0.022 ± 0.001
2%	0.135 ± 0.001	7.46 ± 0.70	0.091 ± 0.010
3%	0.73 ± 0.03	31.06 ± 0.25	0.627 ± 0.014
5%	1.08 ± 0.02	54.05 ± 2.19	1.04 ± 0.09
7%	1.16 ± 0.01	59.84 ± 2.45	1.06 ± 0.03
PET	0.93 ± 0.01	53.7 ± 0.6	1.02 ± 0.01

Table 6.3.1.1: Ar, He and O_2 MEPPP data for stretched: (a) Al/PET; (b) metal-rich AlO_X/PET; and (c) oxygen-rich AlO_X/PET samples.

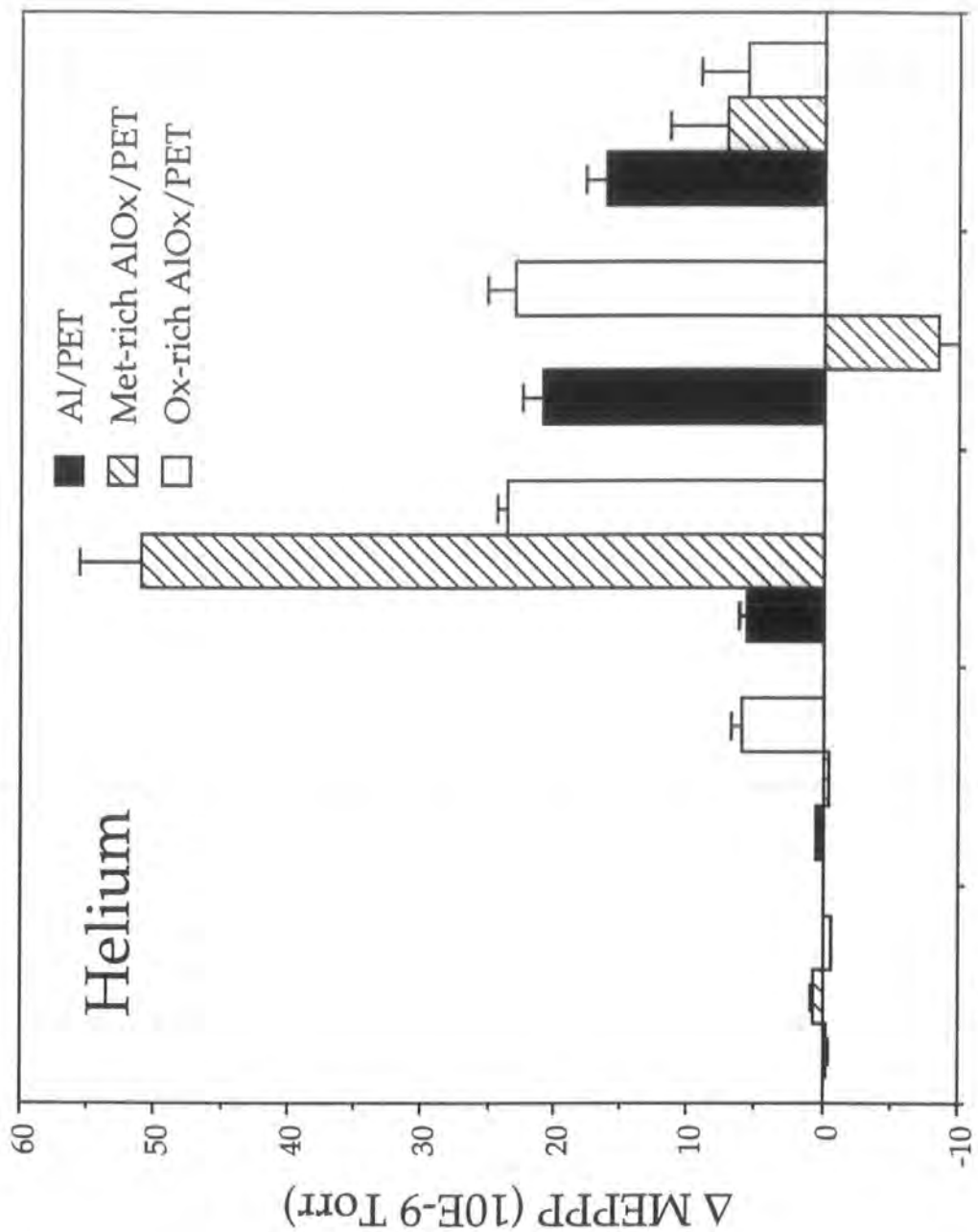

Figure 6.3.1.1: Incremental changes in He MEPPP as a function of stretching.

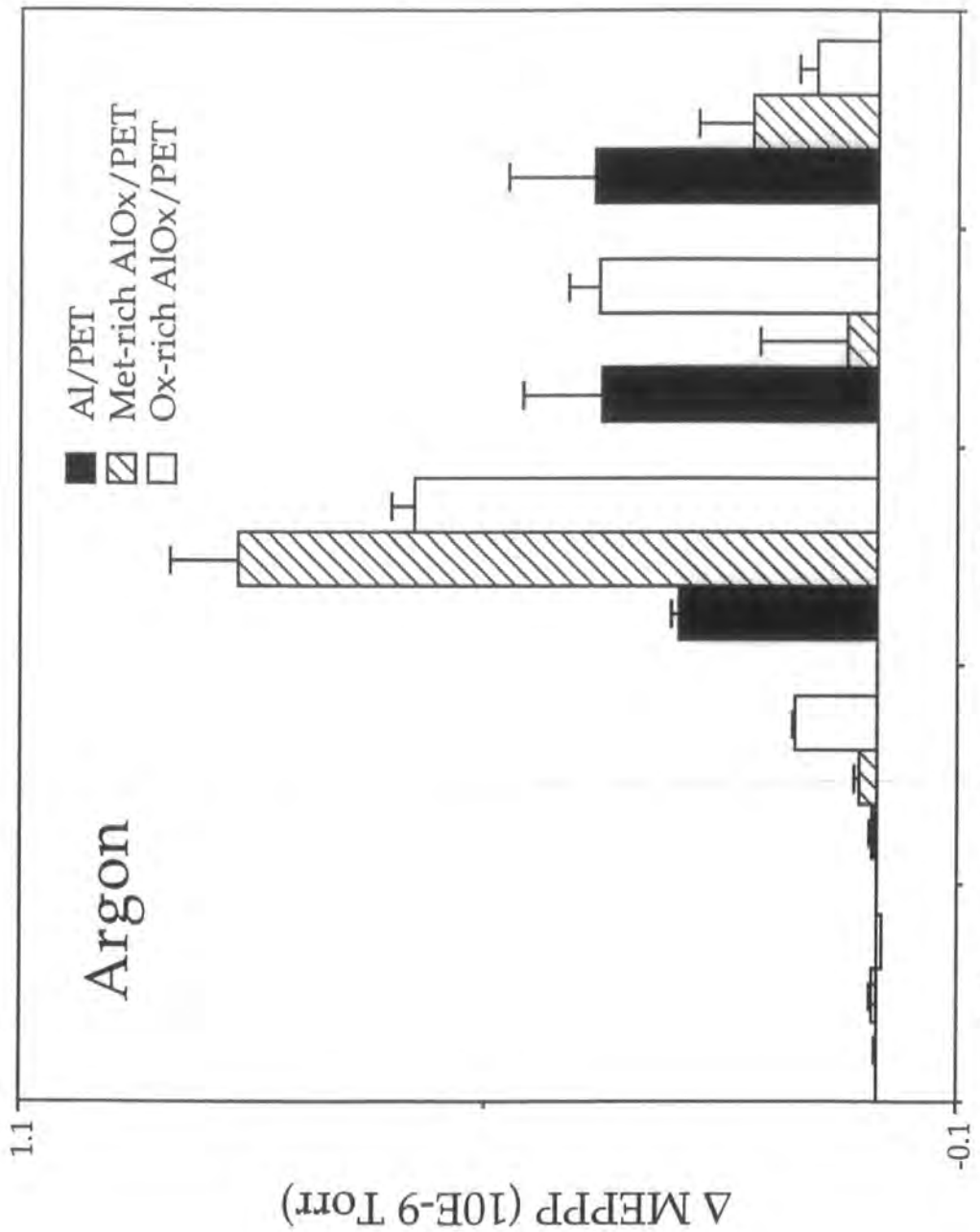

Figure 6.3.1.2: Incremental changes in Ar MEPPP as a function of stretching.

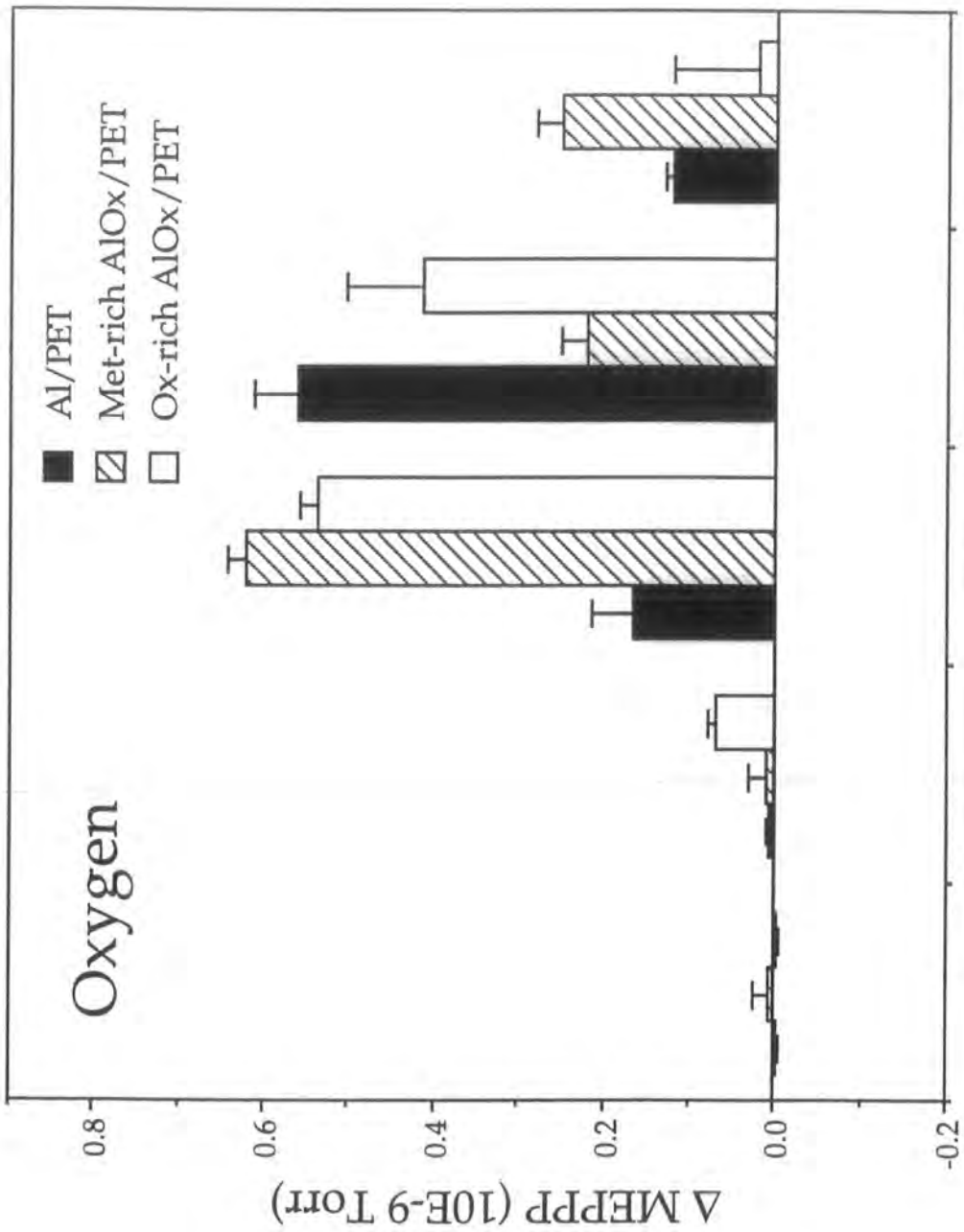

Figure 6.3.1.3: Incremental changes in O2 MEPPP as a function of stretching.

Figures 6.3.1.1-3 are graphs of the incremental MEPPP increase as a function of stretching for He, Ar and O_2, respectively. Between 0 and 1% stretching only small changes in MEPPP are seen; indeed, a slight improvement in gas barrier is noted for the oxygen-rich AlO_x/PET composite. As stretching is increased to 2%, the two types of oxide coated polymer film start to differ in behaviour: oxygen-rich AlO_x/PET's barrier starts to deteriorate earlier, the effect being most prominent for He, followed by Ar, and then O_2, and continues to deteriorate as higher extents of stretching are reached. Al/PET and metal-rich AlO_x/PET only start to exhibit deterioration at greater extents of stretching (between 2 and 3%); metal-rich AlO_x/PET loses its helium barrier much more abruptly than its oxygen-rich counterpart, while Al/PET's degradation is similarly gradual.

6.3.2 Gas barrier 'healing'

Data for 'healing' experiments is presented below, Figures 6.3.2.1-2 for Ar and He. Oxygen-rich AlO_x/PET after 2% stretching, and metal-rich AlO_x/PET after 3% were studied since these values correspond to the onset of barrier deterioration in each case. Metal-rich AlO_x/PET's gas barriers do not change significantly after water vapour/oxygen exposure. The oxygen-rich variant, however, exhibits a clear recovery of its He gas barrier after 24 hours exposure. Clearly the response of oxygen-rich AlO_x/PET to water vapour under an oxygen atmosphere has not reached equilibrium even after extended exposure to ambient atmospheric conditions, and any physicochemical changes that are occurring modify the permeabilities of different gases to different extents. This data is consistent with results in Chapter 2, and the literature, which show that helium is more greatly affected by microstructural changes than the larger penetrants.

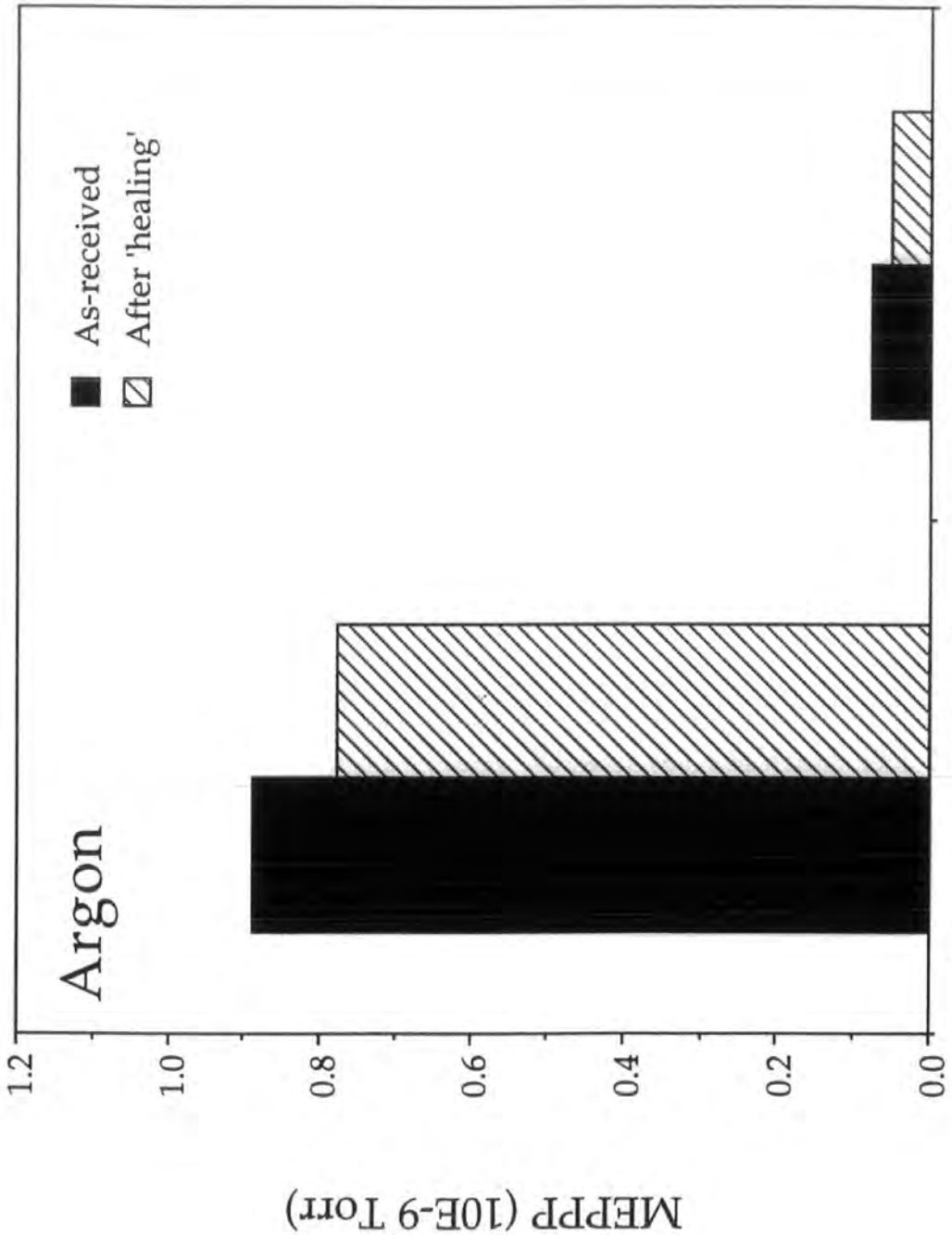

Figure 6.3.2.1: Ar MEPPP data for 'healing' experiments.

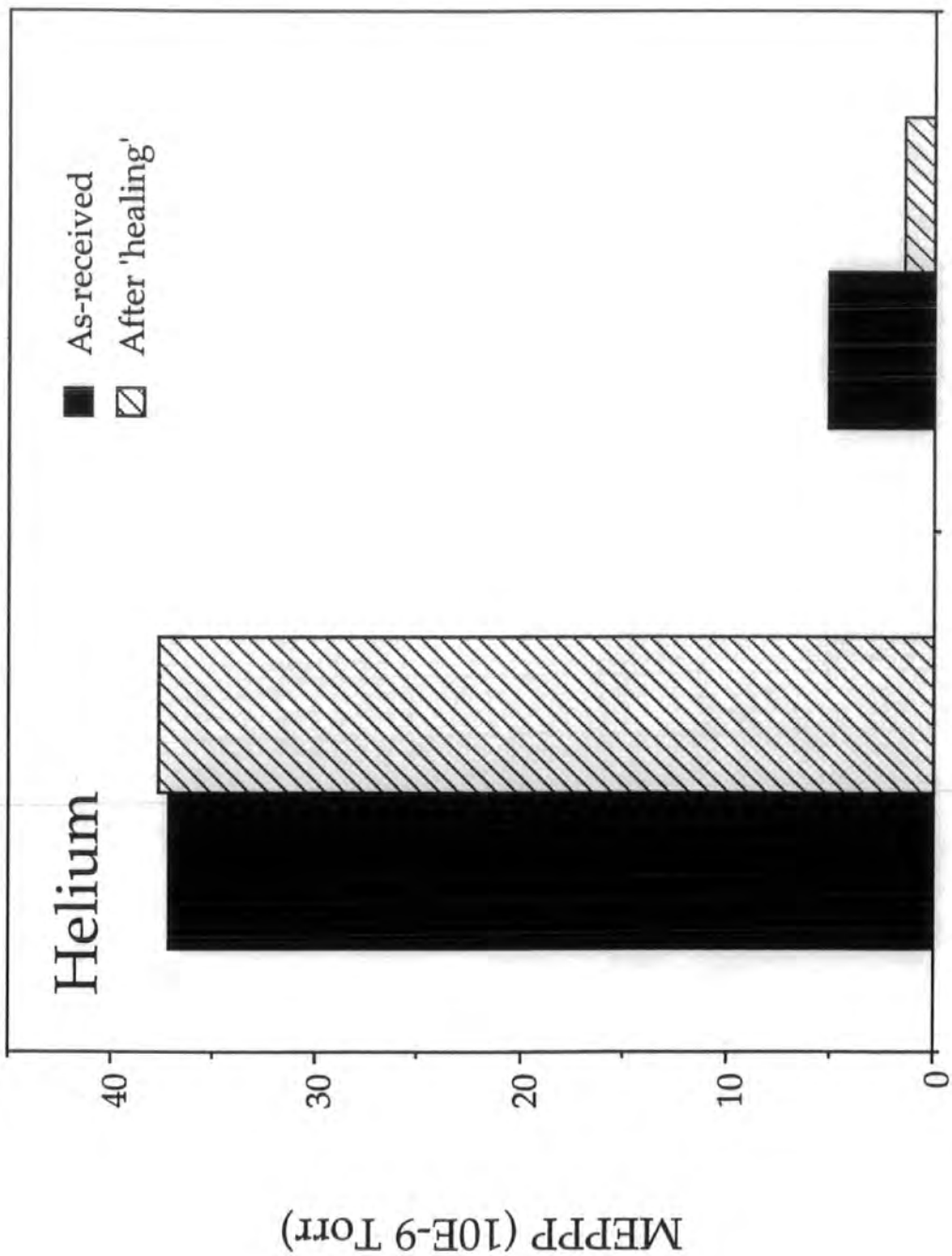

Figure 6.3.2.2: He MEPPP data for 'healing' experiments.

6.3.3 AFM of stretched AlO_X/PET composites

Cracking onset is observed for all AlO_X/PET films after 3% stretching, Figures 6.3.3.1-3 for Al/PET, metal- and oxygen-rich AlO_X/PET, respectively. The nature of the cracking is different, however. Al/PET's cracking is irregular whereas the metal- and oxygen-rich AlO_X/PET composites exhibit straight, parallel cracks. For Al/PET the cracks are in the lower part of Figure 6.3.3.1. Figure 6.3.3.2, metal-rich AlO_X/PET, has just one vertical crack to the right of centre of the figure. Figure 6.3.3.3, oxygen-rich AlO_X/PET, exhibits two parallel cracks running almost vertically down the diagram. Note that SEM performed by Hoechst confirms these observations and showed that the cracks form perpendicular to the direction of stretching.

After 10% elongation the difference in behaviour between the films is more pronounced. Figures 6.3.3.4-6 are AFMs of 10% stretched Al/PET, metal- and oxygen-rich AlO_X/PET, respectively. Al/PET exhibits an irregular cracking pattern. Metal- and oxygen-rich AlO_X/PET, on the other hand, both exhibit a regular parallel arrangement of cracks linked by ~1 μm wide, ~0.1 μm high protrusions, the lighter regions of the diagrams. A summary of the measurements of the surface features is presented in Table 6.3.3.1. The only significant difference between the two reactively evaporated coatings is the width of the protrusions; they are larger for the oxygen-rich variant.

Topographical Feature	10% Oxygen-rich AlO_x (nm)	10% Metal-rich AlO_x (nm)
Protusion Height	115 ± 47	108 ± 25
Protusion Width	618 ± 147	228 ± 21
Protusion Breadth	1317 ± 482	1753 ± 387
Crack Size	302 ± 82	449 ± 81

Table 6.3.3.1: Summary of measurements of protrusions from AFMs of metal- and oxygen-rich AlO_x/PET.

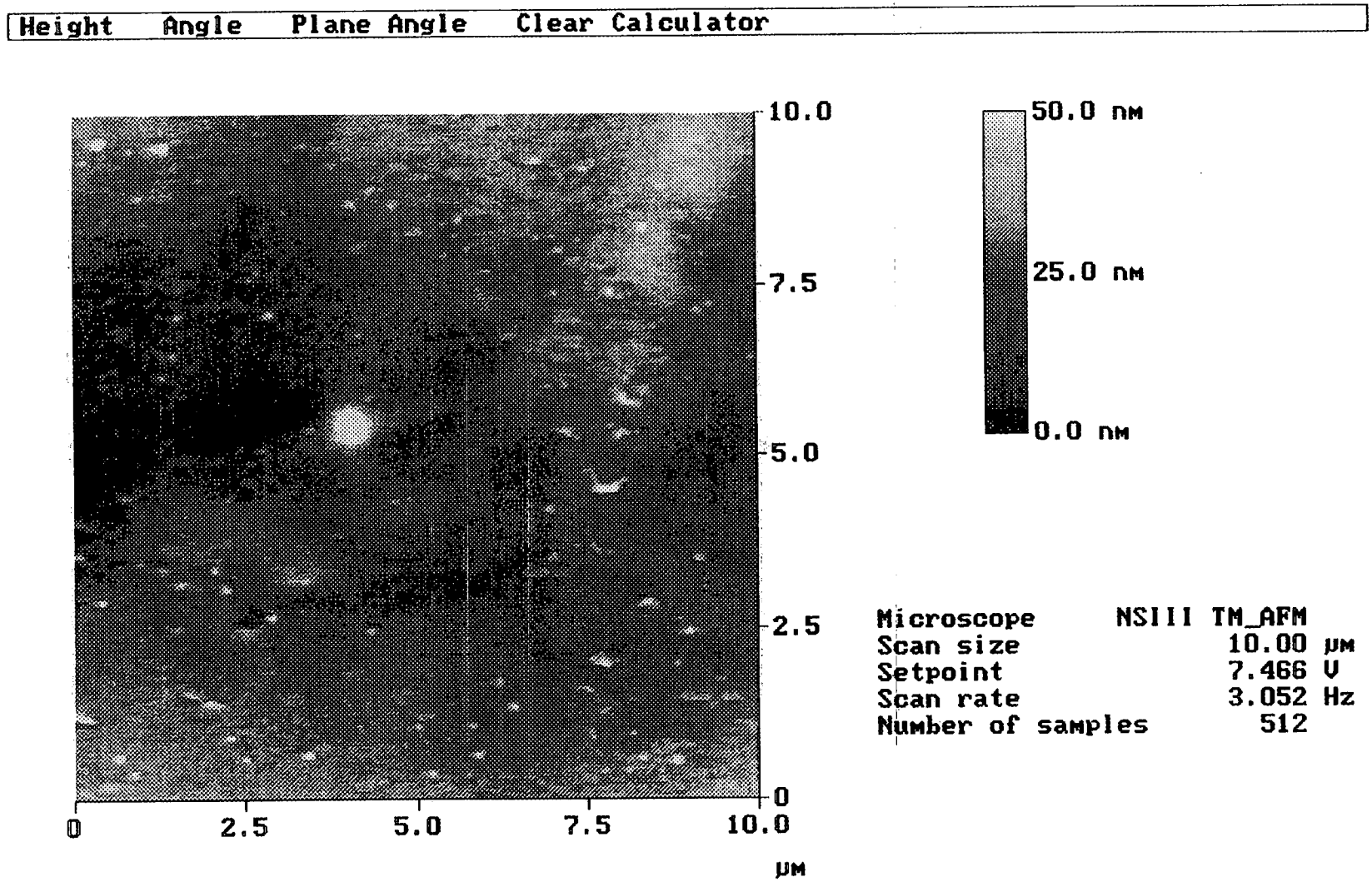

Figure 6.3.3.1: AFM of 3% stretched Al/PET.

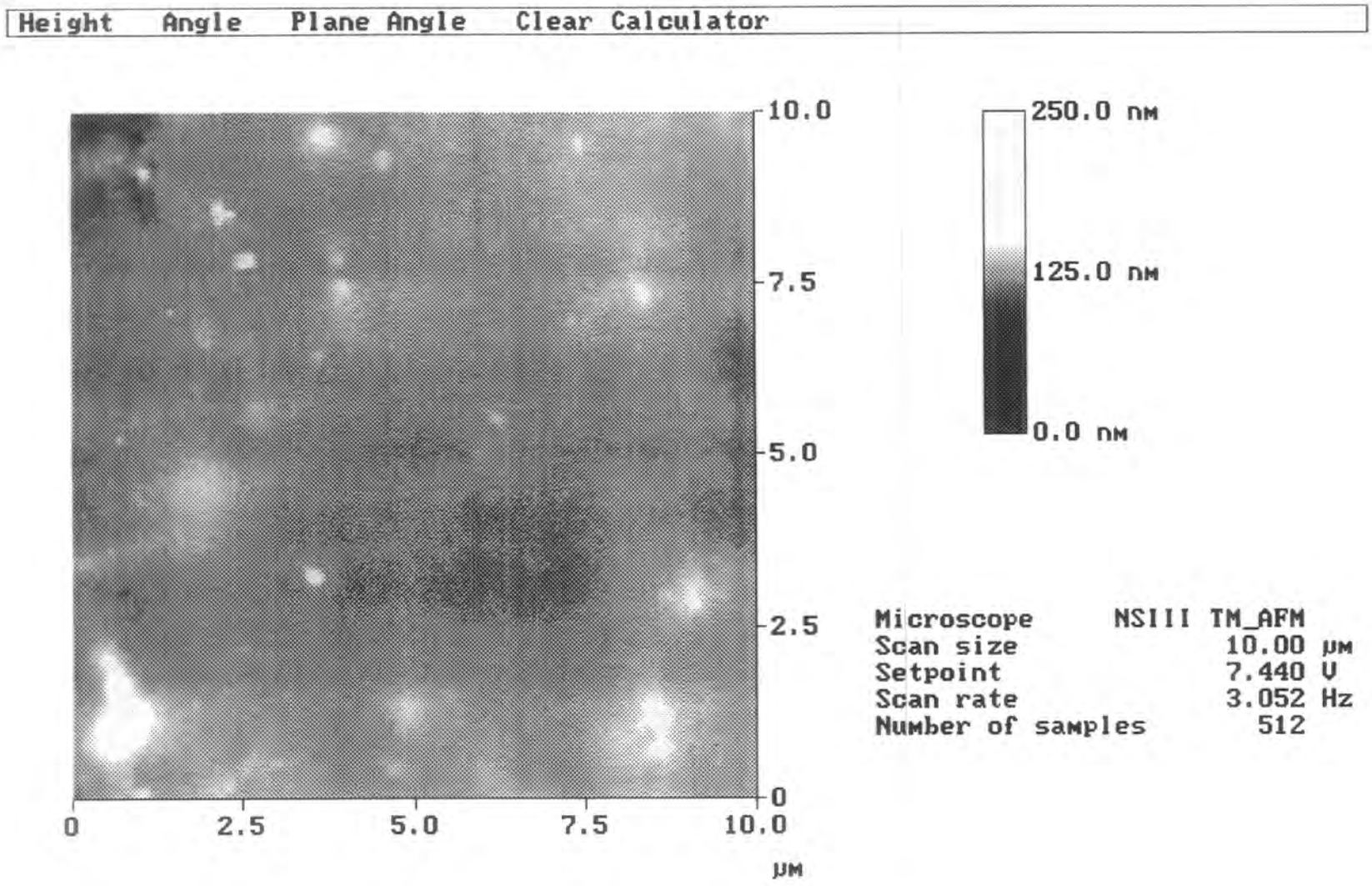

Figure 6.3.3.2: AFM of 3% stretched metal-rich AlO_x/PET.

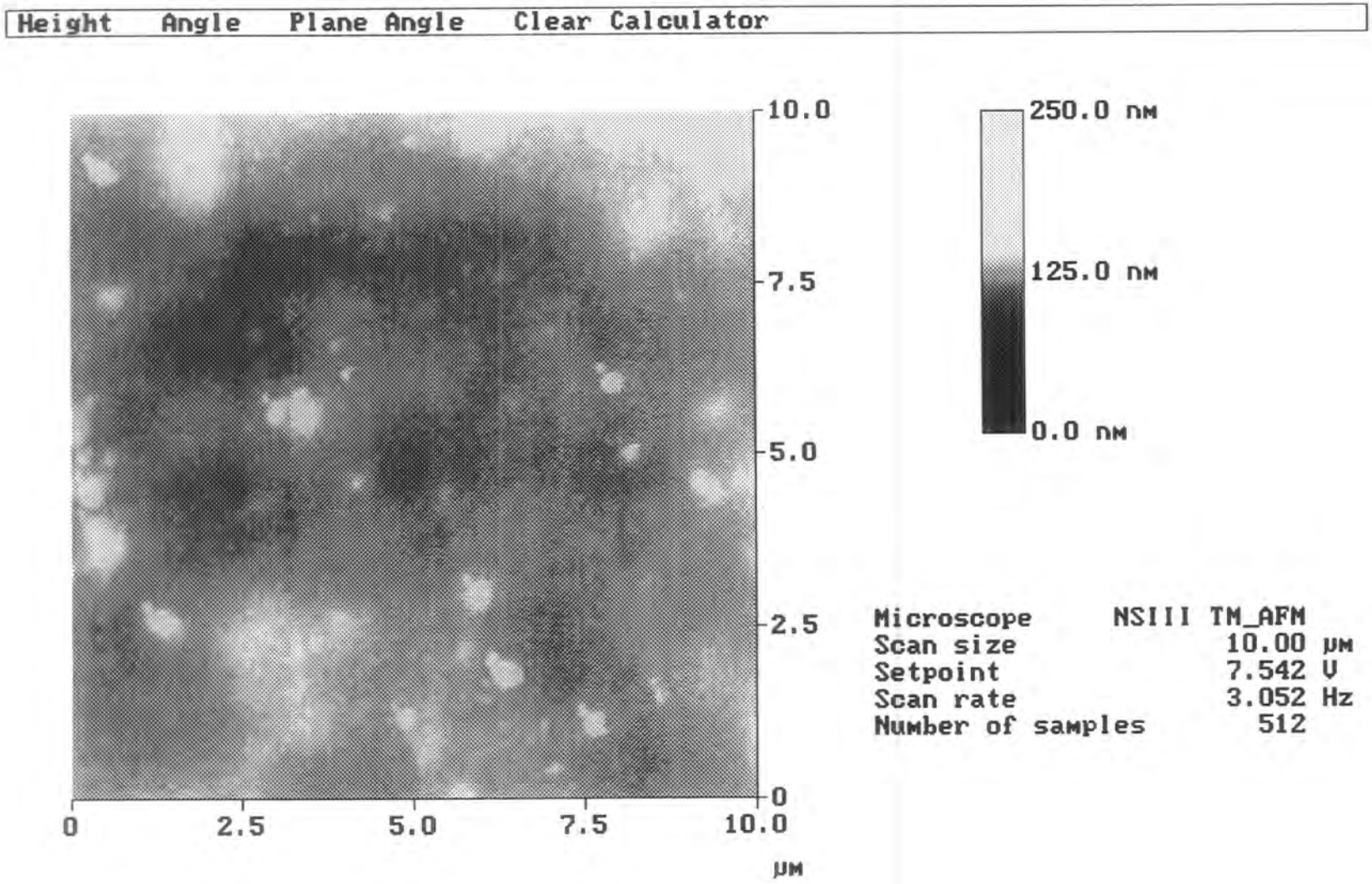

Figure 6.3.3.3: AFM of 3% stretched oxygen-rich AlO_x/PET.

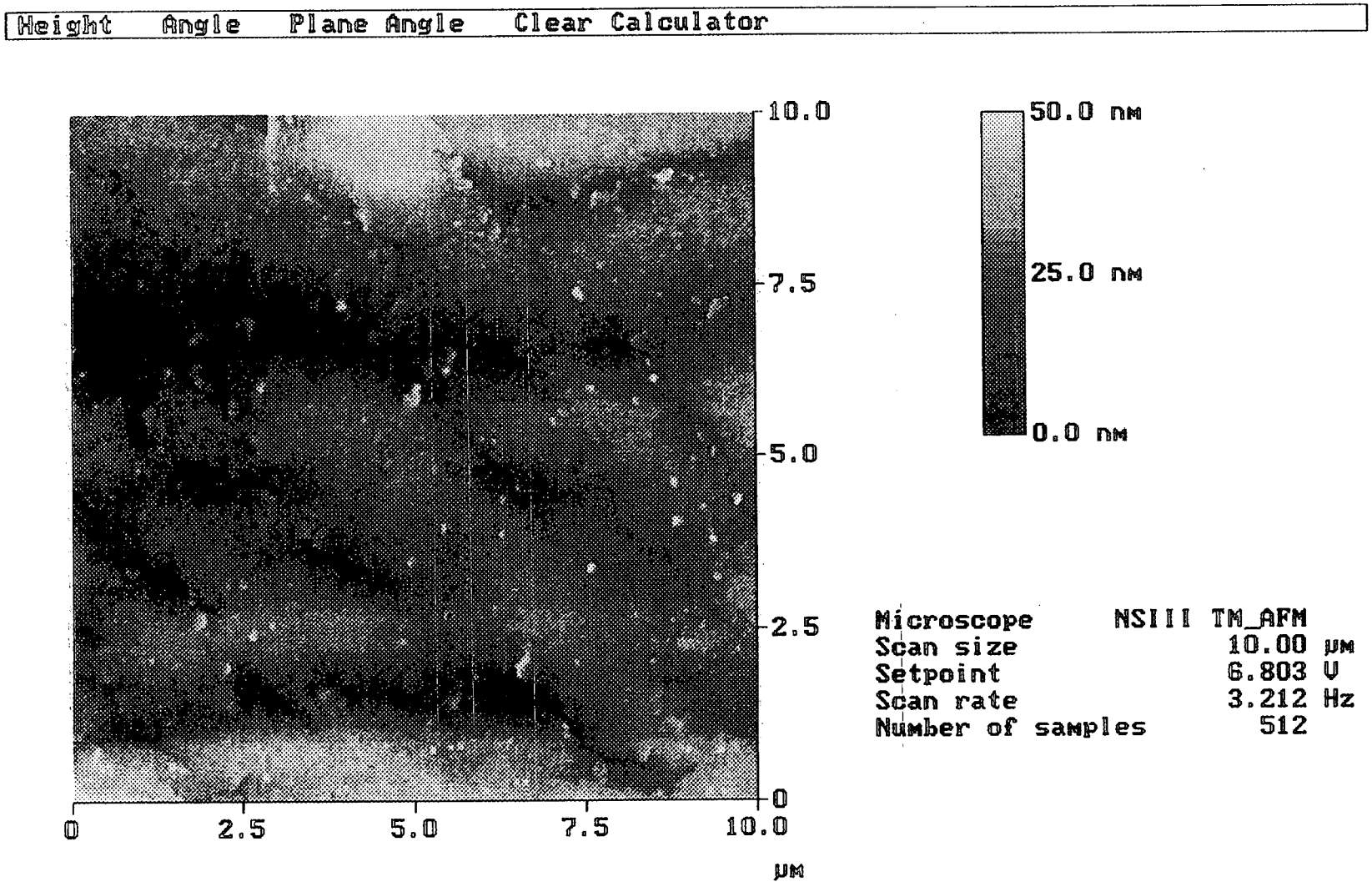

Figure 6.3.3.4: AFM of 10% stretched Al/PET.

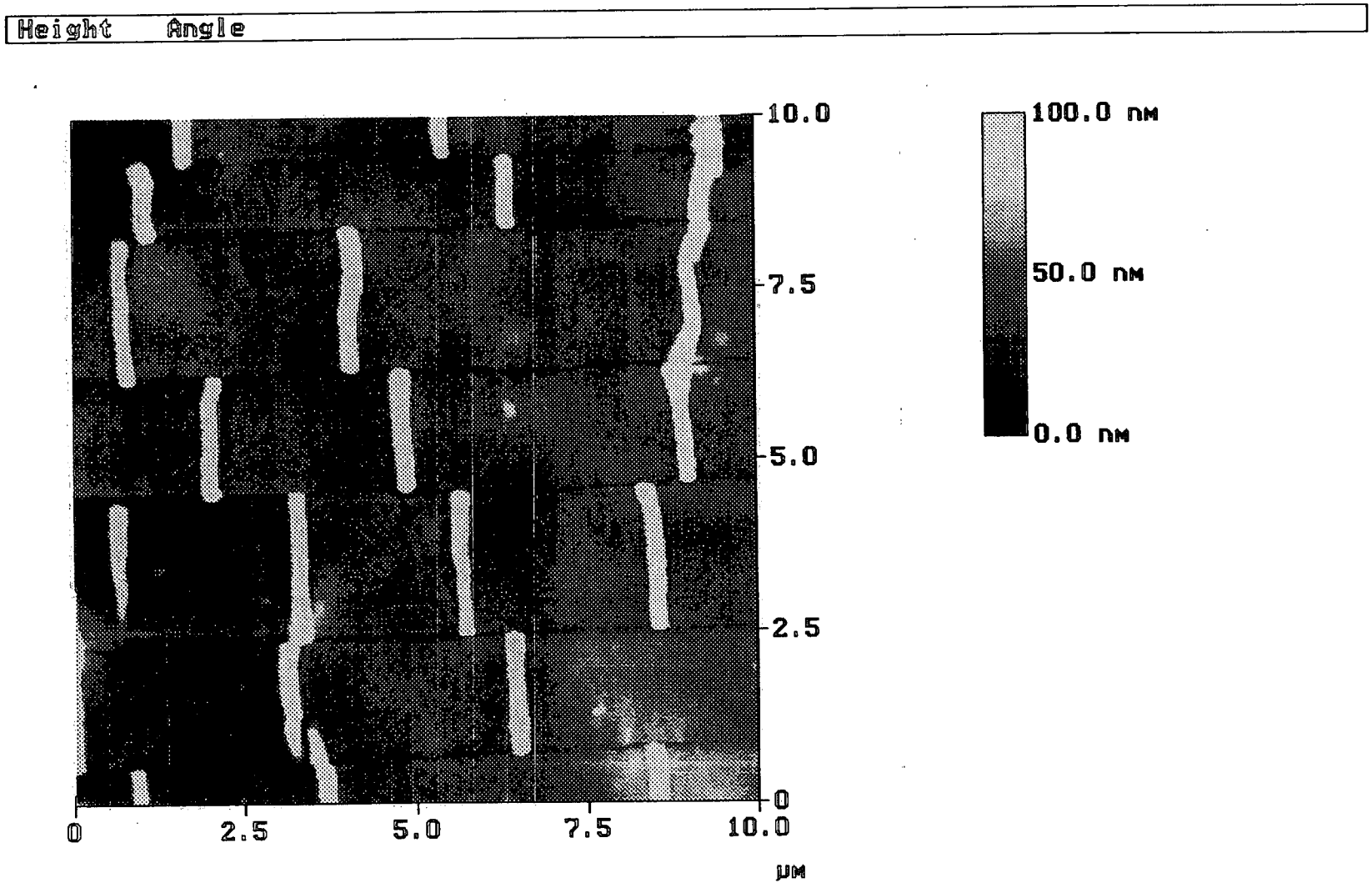

Figure 6.3.3.5: AFM of 10% stretched metal-rich AlO_x/PET.

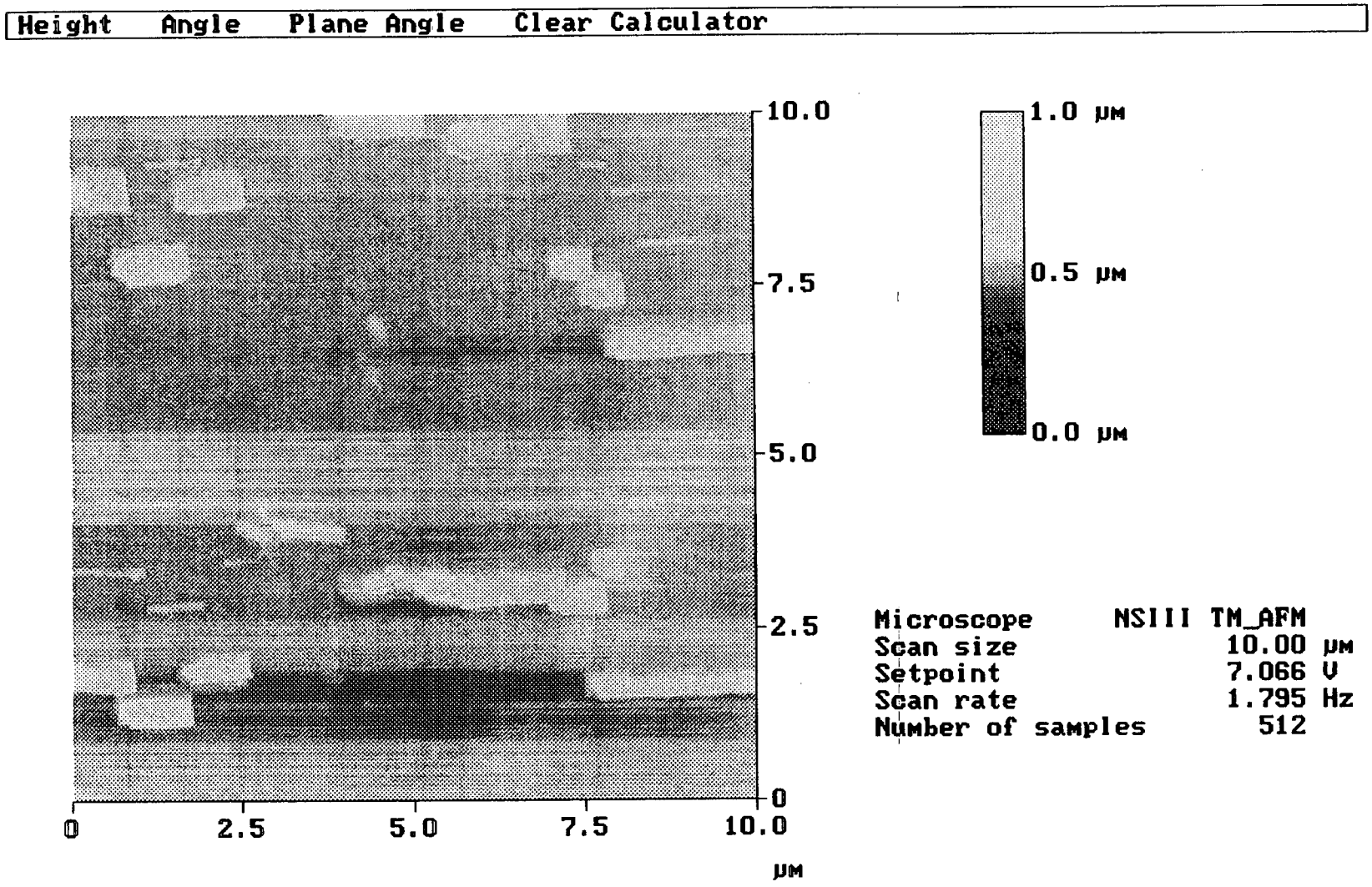

Figure 6.3.3.6: AFM of 10% stretched oxygen-rich AlO_x/PET.

6.4 DISCUSSION

6.4.1 Gas barrier loss upon uniaxial stretching

Incremental MEPPP changes, it is hoped, can help to elucidate the mechanism of gas barrier loss of these composite films. It is noteworthy that very little change in permeability is reported to occur in the PET substrate itself for the relatively low draw ratios employed in this study [10].

Firstly, there is the onset of gas barrier loss. For oxygen-rich AlO_X/PET this occurs at lower extents of stretching than for the other films, and is at extents of stretching where no crack formation is observed. This suggests that the mechanism responsible for this degradation relies upon microscopic changes in the coating morphology not detected under the conditions employed. Metal-rich AlO_X PET's gas barrier starts to deteriorate at higher extents of stretching, as does that of Al/PET. Furthermore, the latter's is far more gradual than the former's. Both correlate with the formation of cracks.

Chapter 3 showed the differences in the layer chemistries of these three composites. The gas barrier deterioration onset can be rationalized in terms of that chemistry. For Al/PET the interface with the PET is substantially substoichiometric, and therefore potentially more 'metallic' and ductile, hence the greater extent of stretching required for deterioration. For metal- and oxygen-rich AlO_X/PET, the interfacial chemistries are substantially the same. Why the different behaviour of the gas barriers upon stretching? The chemical difference between the layers is the presence of metallic aluminium in the subsurface of the metal-rich composite. This will be more ductile than a purely oxide region. The abrupt loss is explained by considering the metal as a mask for the true, and limiting, properties of the interface (its elastic limit) which can only be countered to a limited

extent. Once the 'glueing' properties of the metal have been overcome by the applied external stress the system's behaviour reverts abruptly to that dictated by the interfacial chemistry.

The relative variation in gas barrier deterioration during uniaxial stretching between the films is most pronounced for helium (to which the PET substrate is itself most permeable), amply demonstrating this gas' use as an incisive probe into the behaviours of gas barrier coatings.

6.4.2 Gas barrier 'healing'

Partial regeneration of oxygen-rich AlO_X/PET's barrier to helium occurs at 2% stretching, at which point cracks in the coating have not yet developed. 3% stretching causes cracks in the metal-rich AlO_X layer, and gas barrier is not regained upon exposure to conditions responsible for the healing of the oxygen-rich variant.

Correlating the permeability and AFM results for oxygen-rich AlO_X/PET would indicate that the potential mechanism is that of particle displacement relative to each other at 2% stretching, and that subsequent regeneration of barrier is consistent with 'swelling' of the oxide. Two possible mechanisms can be envisaged dependent upon the nature of gas barrier loss. Firstly, if the coating undergoes no fracture and no unhydrated oxide is exposed, but the particles are displaced relative to one another, then the observed healing can be assigned to a shift in the equilibrium of hydration upon exposure to higher levels of water vapour pressure. On the other hand, if fresh oxide were exposed upon stretching, healing could be explained by the hydration [11], and concomitant expansion, of this oxide because of the greater molar volume of the hydroxide species [12].

At 3% stretching for the metal-rich coating the barrier cannot be regained and is consistent with the inability of oxide 'swelling' to close previously opened large-scale cracks.

These results confirm that the mechanisms of barrier loss can be subdivided into two categories, as in the previous section: firstly, displacement of particles relative to one another at low extents of stretching, as found with oxygen-rich AlO_X/PET and passage of gas through the defects thus introduced; and, secondly, cracking of the coating to produce relatively large defects through which gas can pass relatively unhindered into the base polymer.

6.4.3 Surface morphology

During the stretching of such composite materials as discussed in the introduction to this chapter, the film-substrate composite elastic limit can be reached, after which point stress relaxation mechanisms are evidenced by changes in the surface morphology. These are evidenced by, typically, initial tensile fracture (cracking perpendicular to the direction of the applied principal stress), characteristic of cohesive film failure, followed by compressive buckling (protrusion formation) and delamination of the film, both characteristic of adhesive film failure. The mechanical properties of the composite material will clearly influence the behaviour upon stretching. Atomic force micrographs show that, indeed, the AlO_X/PET composite structures under study do follow these mechanisms, and that the chemistry of these systems influences their behaviour. The substantially metallic nature of the Al/PET coating and interphase leads to the more ductile and irregular development of its surface morphology. The oxide-like nature of the metal- and oxygen-rich AlO_X/PET interphase accounts for the regular cracking and similar surface morphologies of these two composites.

As evidenced by the onset of cracking, the interphases' elastic limits appear to be similar for all three coated films. What does differ between the coatings is their response to larger extents of stretching, namely 10%. The buckling seen as protrusions for metal- and oxygen-rich AlO_X/PET is characteristic of adhesive failure. No such protrusions are seen for the Al/PET structure. Comparing this with the fact that regular cracking indicates good adherence and irregular cracking bad, there appears to be a contradiction with this author's observations. These protrusions are due to adhesive failure of the composite, and, since they are broader for the oxygen-rich film, it is possible that the oxygen-rich composite is less well adhered than the metal-rich.

6.5 CONCLUSIONS

- Permeability and AFM analyses have been performed on uniaxially stretched gas barrier composites, and the onset and rates of gas barrier loss correlated with surface morphology for Al/PET, and metal- and oxygen-rich AlO_x/PET.

- Onset of gas barrier loss occurs most readily for oxygen-rich AlO_x/PET (between 1 and 2% elongation). Both Al/PET and metal-rich AlO_x/PET start to lose barrier at higher elongation (between 2 and 3%). Cracks in all three coatings are observed at 3% elongation.

- Helium permeability is most sensitive to differences between the films, and has been used to monitor differences in the rates of gas barrier loss. Al/PET and oxygen-rich AlO_x/PET lose barrier more gradually than the metal-rich variant.

- Onset and rate of gas barrier loss, and changes in surface morphology can be elucidated by considering the layer chemistries. Al/PET's 'metallic' interphase is more ductile than the oxide-like interphases of metal- and oxygen-rich AlO_x/PET. The presence of metal in the subsurface of the metal-rich variant accounts for the difference in behaviour from its oxygen-rich counterpart. The metal leads to a 'masking' of the properties of the interphase (identical to that of the oxygen-rich composite) because of its greater ductility. When this effect is overcome at higher extents of stretching the gas barrier reverts to that dictated by the interphase, giving rise to an abrupt change in gas barrier.

6.6 REFERENCES

[1] J. T. Felts, Airco Coating Technology, Concord, California.

[2] P. H. Wojciechowski, M. S. Mendolia, *Physics of Thin Films* 16 (1992), 271.

[3] P. S. Ho, R. Haight, R. C. White, B. D. Silverman, F. Faupel, in *Fundamentals of Adhesion*, Ed. L.-H. Lee, Plenum Press, New York, 1991, Chapter 14.

[4] T. Hosaka, *J. Vac. Soc. Jap.* 31 (1988), 687.

[5] J. C. Grosskreutz, M. B. McNeil, *J. Appl. Phys.* 40 (1969), 355.

[6] T. S. Chow, *J. Appl. Phys.* 46 (1975), 219.

[7] R. C. Penwell, K. S. Liang, T. S. Chow, *Thin Solid Films* 60 (1979), 133.

[8] K.-H. Kochem, Hoechst AG, private communication.

[9] *CRC Handbook of Chemistry and Physics*, Ed. R. C. Weast, CRC Press, Boca Raton, 1982, D-196.

[10] J. A. Slee, G. A. J. Orchard, D. I. Bower, I. M. Ward, *J. Polym. Sci. Polym. Phys.* 27 (1989), 71.

[11] W. Vedder, D. A. Vermilyea, *Trans. Farad. Soc.* 65 (1969), 561.

[12] *CRC Handbook of Chemistry and Physics*, Ed. R. C. Weast, CRC Press, Boca Raton, 1982, B-218.

CHAPTER 7

POLYPROPYLENE SURFACE ENGINEERING *VIA* RESIN ADDITION AND CORONA TREATMENT

7.1 INTRODUCTION

Polymer surface chemistry and morphology control is an area of great interest because of their influence on properties such as adhesion [1]. Surface roughness is one of the important factors influencing adhesion [2] since it will affect the degree of mechanical interlocking achievable. Corona [3] and plasma treatment [4], and UV irradiation [5,6] are used to modify both chemistry and morphology. Corona treatments of PP and PET proceed *via* free radical mechanisms and can introduce a wide range of oxidized functionalities, including alcohol, ketone, acid, ester, epoxy and hydroperoxide groups [7]. Critical parameters for the use of corona treated polymers are: ageing effects; the extent of chain scission and low molecular weight oxidized material formation; and the quantity and distribution of oxidized groups.

With respect to this project, the control of polypropylene surface chemistry and morphology is fundamental to the development of a polypropylene substrate suitable for AlO_X film deposition. Such an advance is desirable since lamination of coated materials to polyolefins is common practice, and a 'monomaterial' laminate would be more easily recyclable than one containing several materials. Transfer of AlOx coating technology from PET to PP is therefore an important goal.

Coextruded polypropylene films (ABA structure) containing low molecular weight saturated hydrocarbon resin in both the base film and coextruded layer were the only samples to give gas barriers approaching those of metallized PP upon oxide coating, so variants of these new materials were prepared by Hoechst in order to assess the effect of resin content and location within the films upon their chemistry and morphology.

This chapter does not aim to be a mechanistic study of corona discharge treatment of polymers, but rather the first step towards an understanding of how correct manipulation of polymer film composition can lead to a harnessing of polymer surface properties.

7.1.1 Corona discharges

Corona discharge processes have been used for more than one hundred years [8]. Modern applications include: electrostatic precipitation; electrophotography; static control in semiconductor manufacture; destruction of toxic compounds; and ozone generation.

A corona discharge is a relatively low power (200-1000 Wm^{-2}) electrical discharge occurring at or near atmospheric pressure, and is produced by the generation of strong electric fields (frequencies typically in the range 3-30 kHz) associated with sharp edges of electrodes. The term 'corona' (meaning crown) is derived from sea-farers' observations of discharges from masts during electrical storms. Their physical appearance is of filamentary discharges between the electrodes of the system.

Some typical parameters for corona discharges are compared with those of low pressure glow discharges (or plasmas) in Table 7.1.1.1 [9].

Discharge	Pressure (mbar)	Electric field (V/cm)	Electron temp. (eV)	Electron density (cm^{-3})	Degree of ionization
Corona	1000	500-50000	~5	10^{13}	10^{-5}
Glow	$< 10^{-2}$	10	0.5-2	10^{8}-10^{11}	10^{-6}

Table 7.1.1.1: Typical parameters characterizing corona and glow discharges.

The lack of vacuum requirement for corona discharges makes their use appealing since processing is therefore much simpler.

As electrons are ~100 times more mobile than ions yet carry the same magnitude of charge they play the major role in coupling the electrical energy from the applied field to the discharge itself. As the pressure is increased the electron mean free path decreases, and they undergo more frequent collisions with neutral species. This leads to the greater electron density in atmospheric pressure discharges.

Also because of the increased number of collisions, the breakdown threshold voltage increases with pressure. The reduced electric field at breakdown, E/n, where E is the electric field and n the gas density, is typically ~50 for a low pressure plasma and up to 200 for corona discharges. This more intense electric field at atmospheric pressure results in higher energy free electrons than those found at lower pressures, with their kinetic energy being efficiently transferred to other species [10]. In low pressure plasmas, collisions are not as frequent as at higher pressures, and energy is coupled less effectively to the species within the discharge.

Models of atmospheric pressure discharges has shown that, in atmospheres of oxygen and air [10,11], ozone (O_3) is the dominant species.

Its concentration is at least 10^2 greater than that of any other species present, and it is by far the most long-lived.

7.1.1.1 Corona discharge treatment of polymers

Corona discharge treatment of polymers is characterized by the formation of oxidized functionalities [12]. Oxidation is also characterized by the production of low molecular weight oxidized material (LMWOM) which is water-soluble in the cases of PP and PET [13,14]. These surfaces may not be stable as evidenced by ageing phenomena, when the surface chemistry of the system changes. For PP the surface composition is found to remain virtually unchanged after storage under ambient conditions. This is in contrast with PET, for which XPS has shown that the oxidized functionalities (LMWOM) migrate into the polymer surface below the depth penetrable by XPS.

7.1.1.2 Ozonolysis of polymers

Ozone is a highly unstable and oxidative gas, and is known to degrade polymers along with other reactive gases such as SO_2, Cl_2 and NO_x [15].

Polymer reactions with ozone can be delineated in to those of saturated and unsaturated polymers. The former are thought to react by the free radical mechanism, and the latter by the Criegee addition mechanism.

Application of electron spin resonance to the ozonolysis of saturated polyolefins [16] showed that oxidation proceeds *via* a peroxy radical, Figure 7.1.1.2.1.

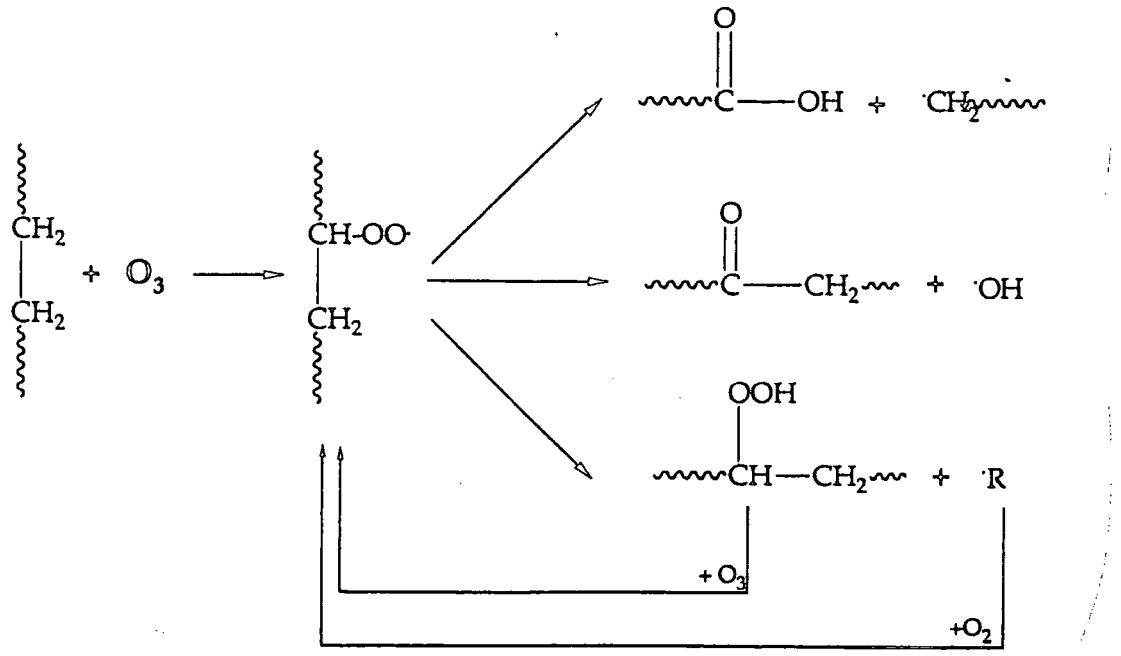

Figure 7.1.1.2.1: Free radical mechanism of saturated polymer ozonolysis.

This mechanism leads to the formation of low molecular weight oxidized material.

For unsaturated polymers, ozone adds across a carbon-carbon double bond to give an unstable primary ozonide (molozonide) which then decomposes yielding and rearranges to give a stable ozonide

7.1.2 AFM of corona-treated polymers

Recently, attention has been directed at the surface morphologies of corona-treated polymers, especially polypropylene [17,18]. Of special interest was the observation of droplets physisorbed onto the surface, ~500 nm in diameter and 60 nm in height [17]. The nature of the protrusions is dependent upon the corona dose [18]. Mechanisms proposed for their formation are the oxidative degradation of the polymer leading to the

formation of low molecular weight material (~16 carbon atoms per molecule) [18], local surface melting or sublimation [17]. The material can be washed off by rinsing in water [19].

Corona treatment of PET and PS also leads to the formation of low molecular weight material [19,20]. In the case of PET, this material is found to migrate into the film upon ageing [20].

7.1.3 Polymer-polymer diffusion

The mutual diffusion of polymers is important in applications such as polymer welding [21] as well as areas of academic interest [22-24]. Experimental probes include infrared spectroscopy, nuclear magnetic resonance spectroscopy, Rutherford back-scattering and small-angle neutron scattering.

The samples considered in this chapter cannot be termed polymer blends since these are characterized by the large molecular weight of both components.

For a binary mixture A + B the transfer of species per unit area is proportional to the concentration gradient [21]. If the two components of the mixture are chemically identical and one is of much lower molecular weight than the other then diffusion occurs *via* reptation [22-24]. This mechanism is envisaged thus: the low molecular weight species' diffusion path is constrained by the topological restrictions of the high molecular weight 'host' matrix.

Low energy components tend to adsorb preferentially at the surface of polymers so as to lower the surface energy [25]. The surface energy of polypropylene is typically ~30 dyn cm^{-1} while that of oxygen-containing polymers is higher, ~42 dyn cm^{-1} for polyethylene terephthalate. One approach to lowering the interfacial energy between two polymers has been

to incorporate low molecular weight additives containing functional groups characteristic of both polymers into the mixture. Such additives act as a gradient of chemical properties bridging the gap between the two original polymers and reducing the system's energy.

7.2 EXPERIMENTAL

7.2.1 Sample preparation

All films have the same basic formulation: base film is a C_3 homopolymer with small amounts of anti-static, stabilizing and neutralizing agents; coextruded layers are comprised of the same homopolymer as the base film but with anti-blocking agent (silica particles).

The resin is a saturated hydrocarbon of low molecular weight. No further information concerning either the components or treatments of the samples was made available by Hoechst AG apart from the fact that they were corona treated in a continuous, in-line process. All samples were analyzed as-received so as to probe the surface to which the AlO_x gas barrier film deposition is applied.

Sample designation	Base film resin content (%)	Coextruded layer resin content (%)
Resin 0/0	0	0
Resin 0/10	0	10
Resin 0/20	0	20
Resin 15/0	15	0
Resin 15/15	15	15
Resin 25/25	25	25

Table 7.2.1.1: Sample definition and nomenclature for resin-containing polypropylene films.

7.2.2 XPS

All experiments were performed as described in Chapter 3 using an electron take-off angle of 30°, and data analysis was performed using elemental sensitivity factors, Chapter 3.

7.2.3 AFM

All samples were analyzed using a Digital Instruments NanoScope III atomic force microscope in the Tapping Mode as described in Chapter 4. Surface roughnesses are measured as root-mean-square (rms) values.

7.3 RESULTS

7.3.1 X-ray photoelectron spectroscopy

Elemental compositions of the surface layers of the polypropylene samples as determined by XPS for the surface layers shows that only carbon and oxygen functionalities were detected. The percentage of oxygen incorporation is presented graphically in Figure 7.3.1.1.

Both the untreated and corona-treated sides of the polypropylene films exhibit oxygenated functionalities, consistent with the transfer of low molecular weight oxygenated species from the treated to the reverse side of the film. Introduction of resin into the coextruded layer of the ABA structure, whether the base layer contains resin or not, reduces the extent of such transfer.

Resin content of the coextruded layer does not affect the proportion of oxygen incorporation whereas an increase in the resin content of the base film from 0 to 15 or 25% leads to a slight increase in the extent of oxygenation from 14.2 - 14.5% in the former to 16.0 - 16.7% in the latter. Experimental data for the 25/25 sample is within the limits of experimental error for the 15/0 and 15/15 samples, indicating an insensitivity of the degree of oxygen incorporation to the precise proportion of resin incorporated into the film.

7.3.2 AFM

Atomic force micrographs of the untreated sides of the polypropylene films containing no resin in the base film, Figures 7.3.2.1-3 for 0/0, 0/10 and 0/20, respectively, indicate that increasing resin content in the coextruded layer results in a 'smearing' of the surface morphology. Resin addition to

the base film alone does not change the surface morphology, Figure 7.3.2.4. Surprisingly, the presence of resin in the base layer results in little, if any, change to the surface morphology as the resin content of the coextruded layer is increased, Figures 7.3.2.5-6, in contrast to the results observed for samples 0/0, 0/10, 0/20.

Corona treatment of the 0/0 sample leads to the formation of globular structures, probably low molecular weight oxidized material, Figure 7.3.2.7. As the resin content of the coextruded layer increases from 0 through 10 to 20% these globules become smaller, Figures 7.3.2.8-9. Incorporation of resin into the base film as well as the coextruded layer enhances this effect: the globular structures of the 15/0 sample are smaller than those for the 0/0 sample, Figure 7.3.2.10; and the addition of resin to the coextruded layer decreases their size further, Figures 7.3.2.11-12. Initial studies showed that these globular features could be washed off with chloroform.

Sizes of the globules were not determined because they were of irregular size and shape.

Surface roughness data, Table 7.3.2.1, shows that the addition of resin to the coextruded layer increases the surface roughness when none is present in the base film. Corona-treatment induces a rougher surface for 10 % resin in the coextruded layer but a smoother surface for 20 % incorporation. Surface roughnesses determined for samples containing resin in both the base film and coextruded layer are increased slightly with increasing resin content but to a lesser degree than for the samples containing resin in the coextruded layer only. Corona treatment of these samples decreases the roughnesses, the extent of decrease decreasing with increasing resin content.

Sample designation	Untreated side rms surface roughness (nm)	Corona treated side rms surface roughness (nm)
Resin 0/0	7.46	8.39
Resin 0/10	8.43	14.42
Resin 0/20	11.34	7.61
Resin 15/0	7.52	5.38
Resin 15/15	8.02	6.95
Resin 25/25	8.37	7.14

Table 7.3.2.1: Surface roughness data for PP+resin variants.

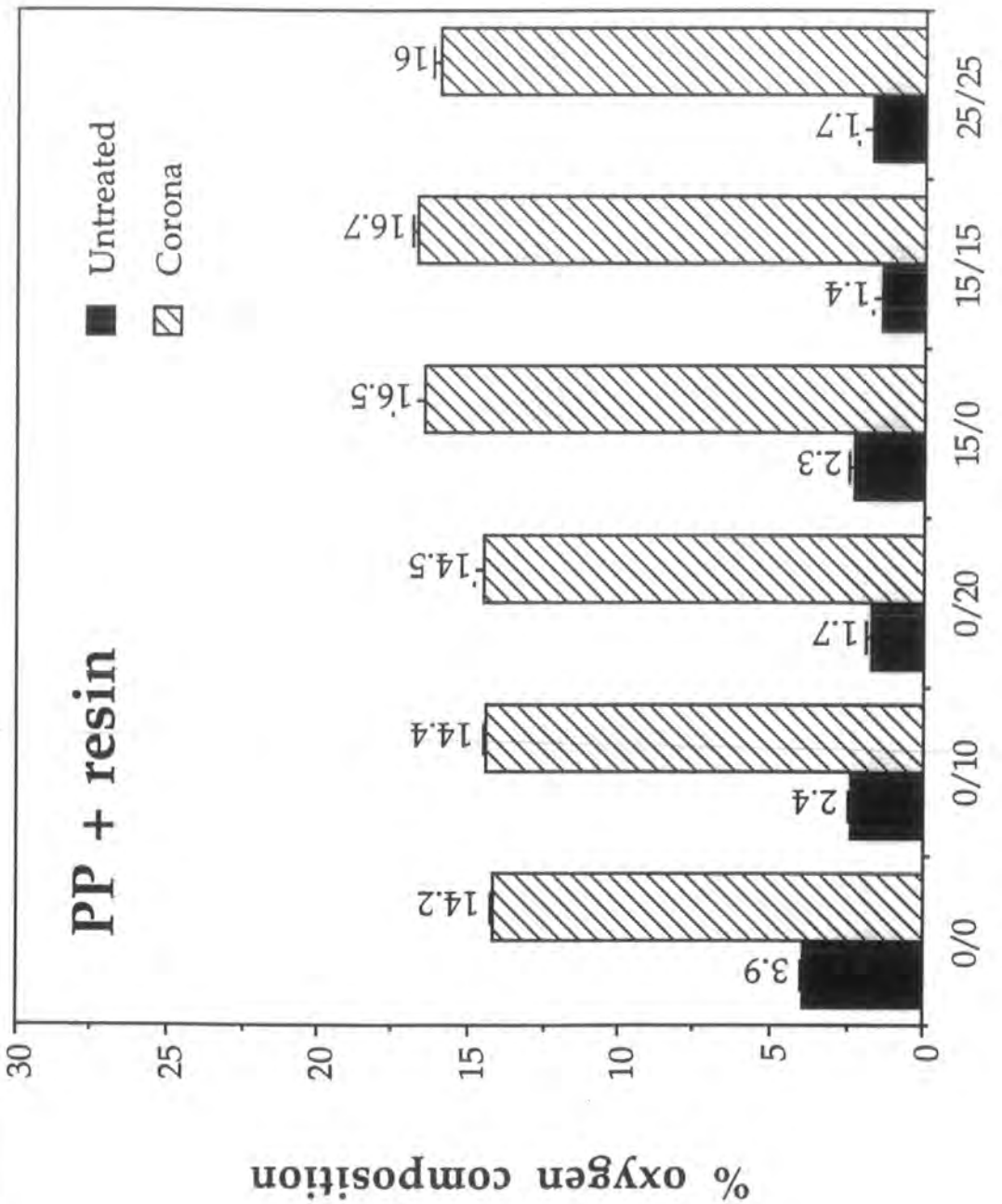

Figure 7.3.1.1: Percentage oxygen incorporation for PP+resin samples.

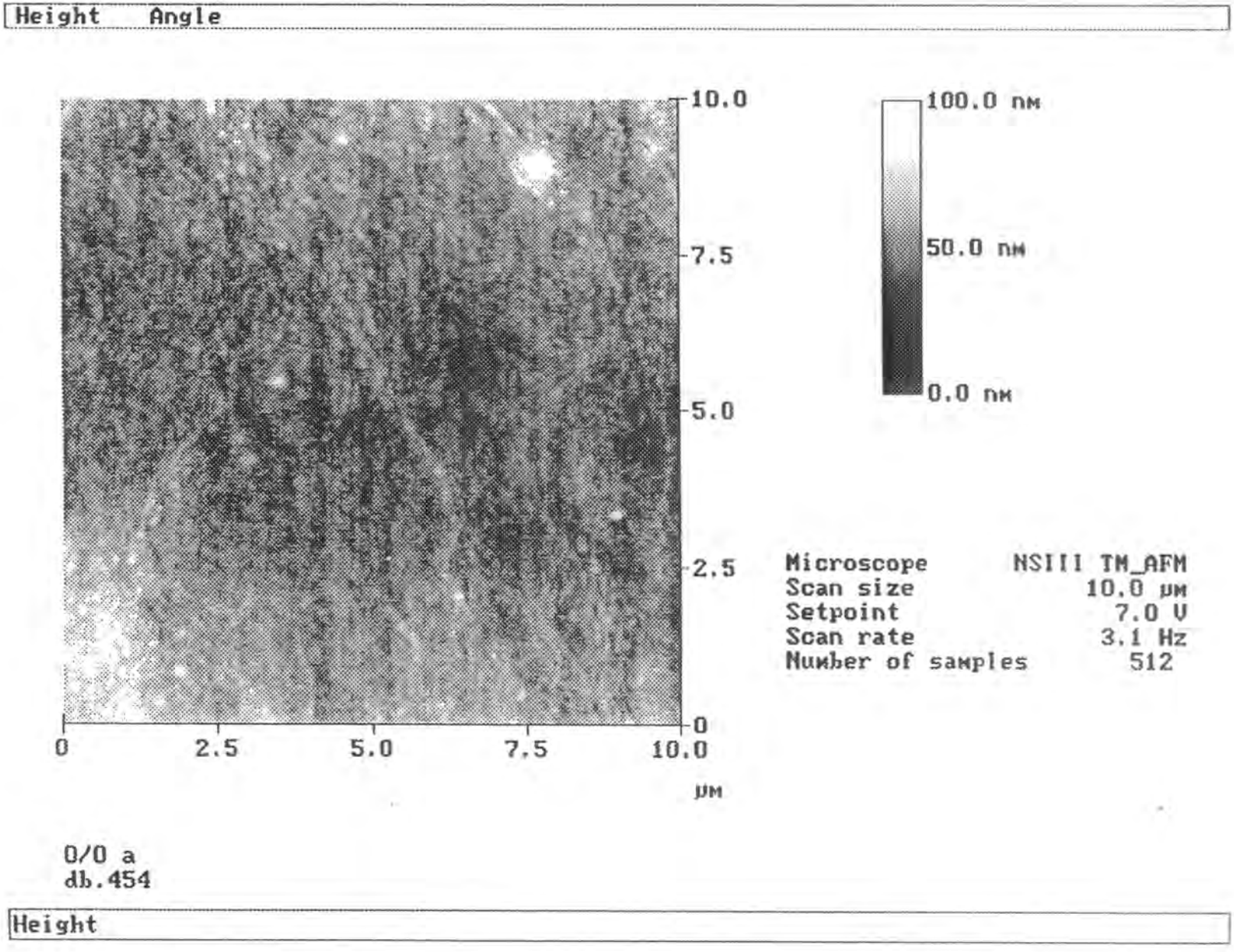

Figure 7.3.2.1: AFM of 0/0 resin-containing polypropylene sample.

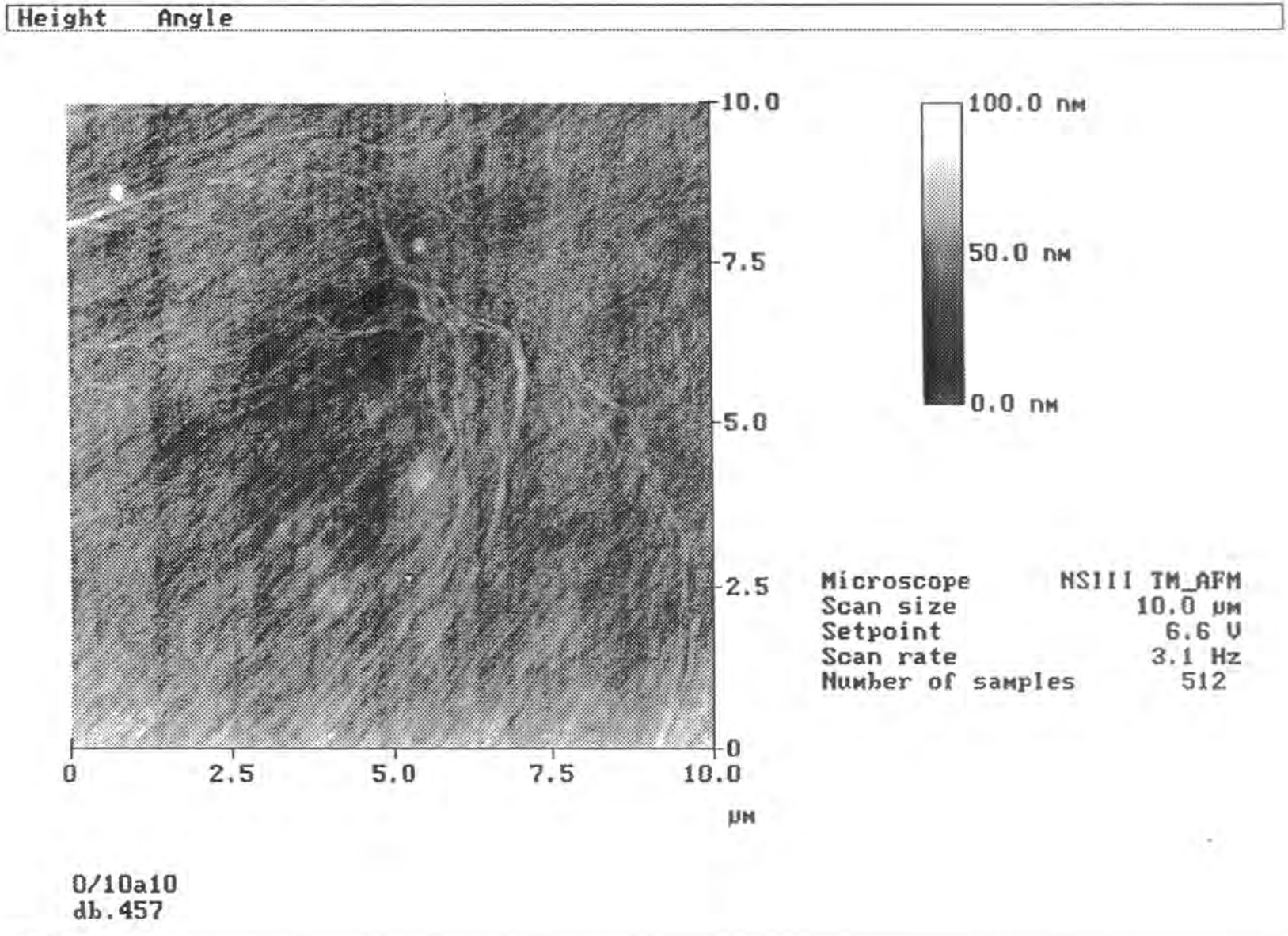

Figure 7.3.2.2: AFM of 0/10 resin-containing polypropylene sample.

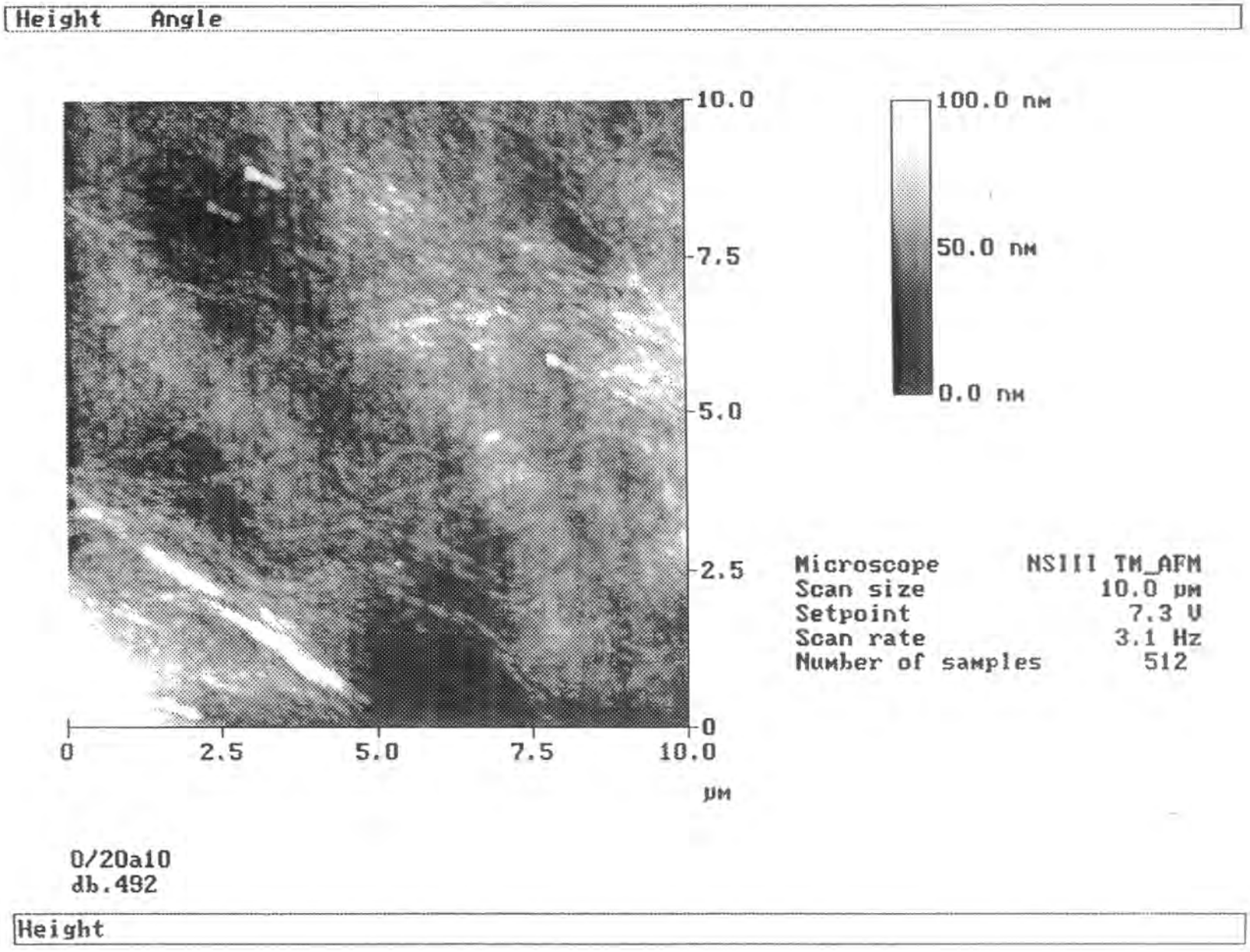

Figure 7.3.2.3: AFM of 0/20 resin-containing polypropylene sample.

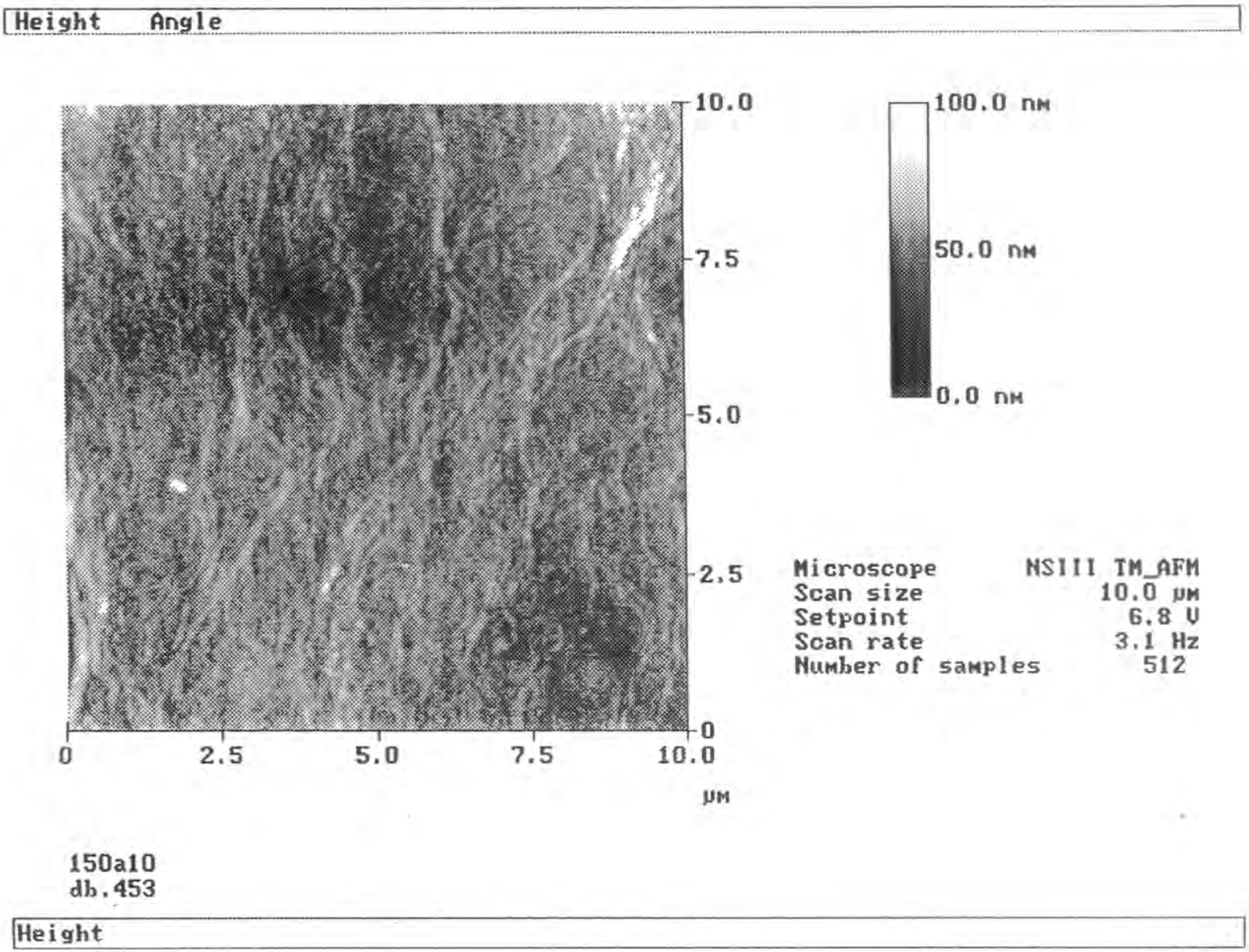

Figure 7.3.2.4: AFM of 15/0 resin-containing polypropylene sample.

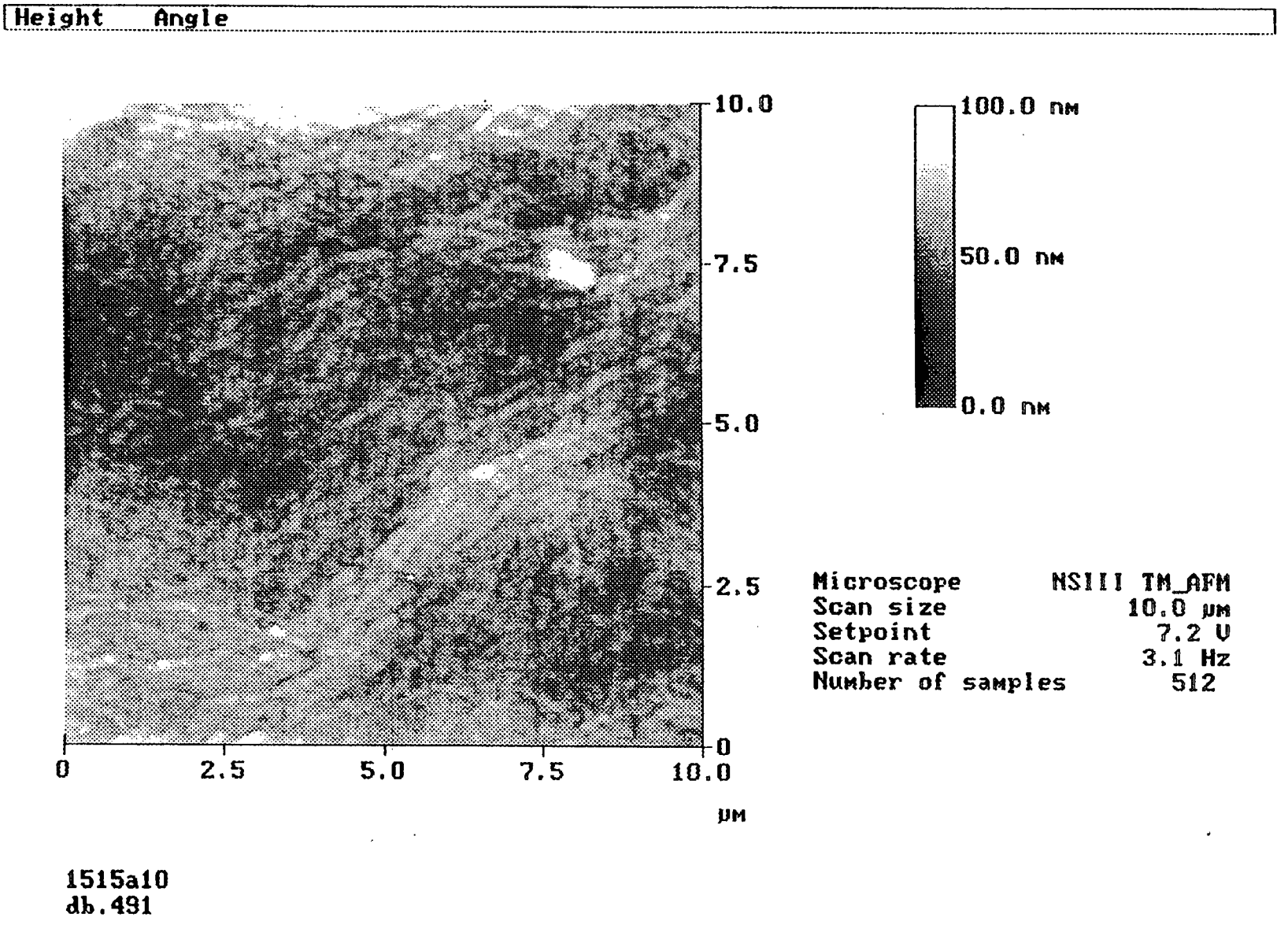

Figure 7.3.2.5: AFM of 15/15 resin-containing polypropylene sample.

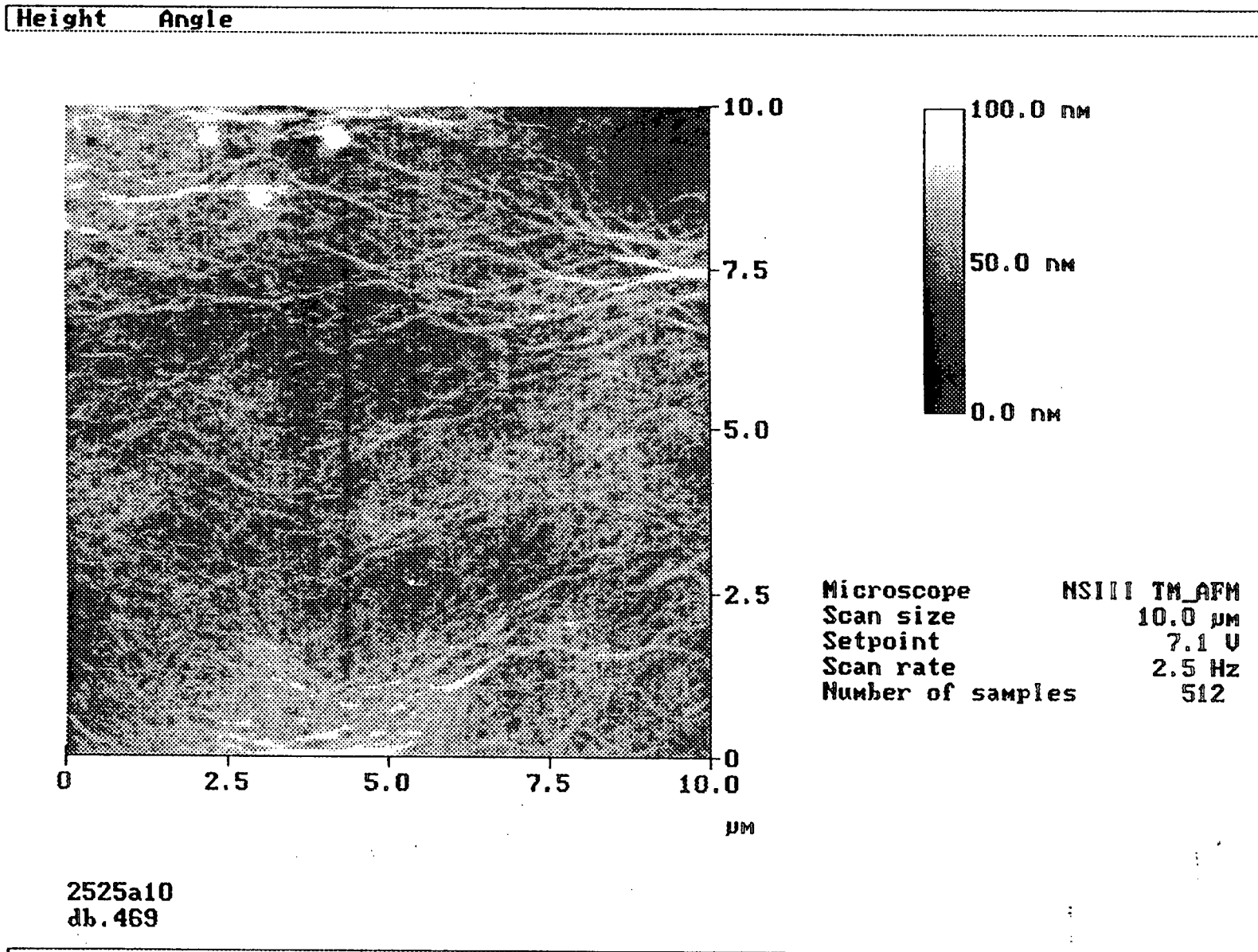

Figure 7.3.2.6: AFM of 25/25 resin-containing polypropylene sample.

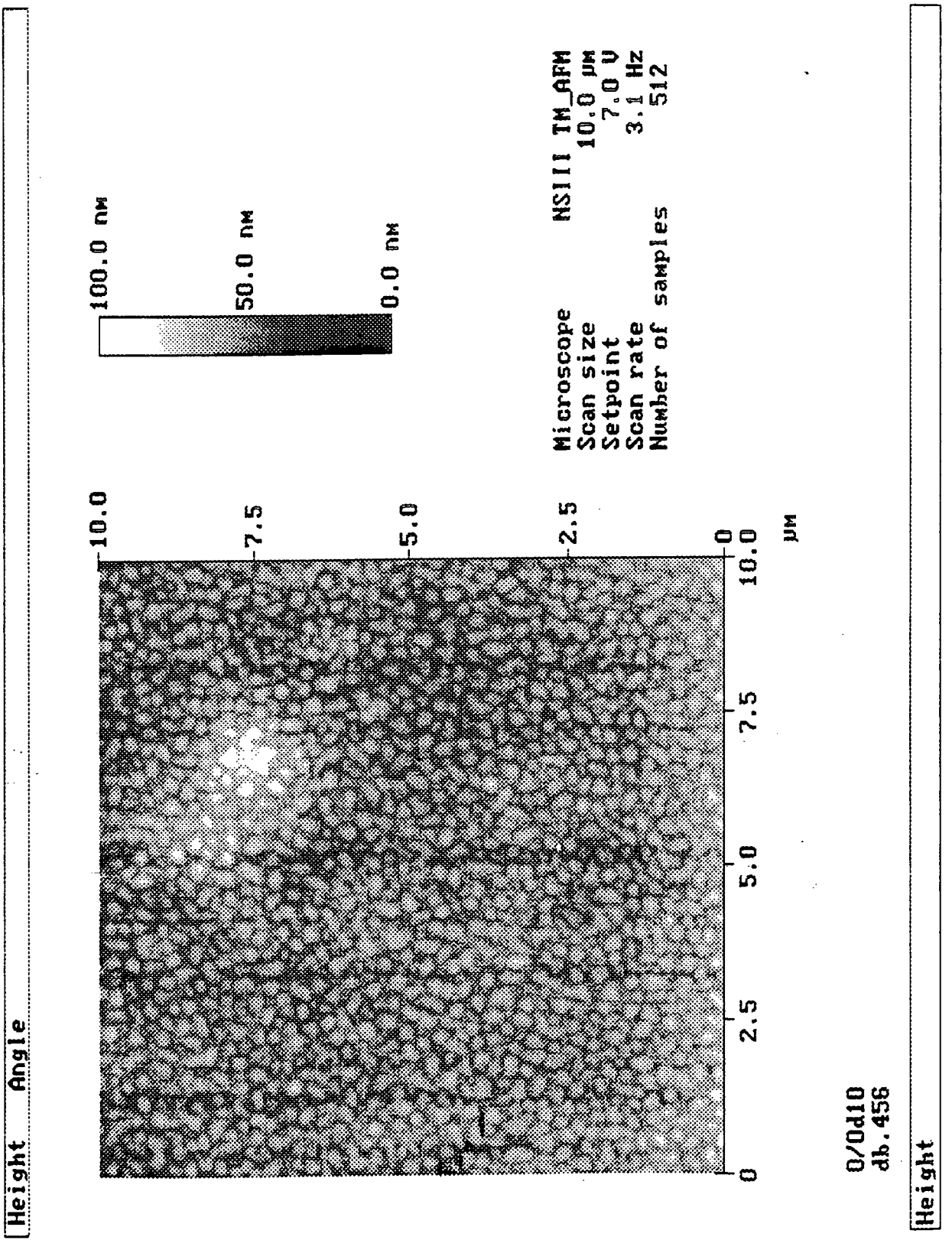

Figure 7.3.2.7: AFM of corona treated 0/0 resin-containing polypropylene sample.

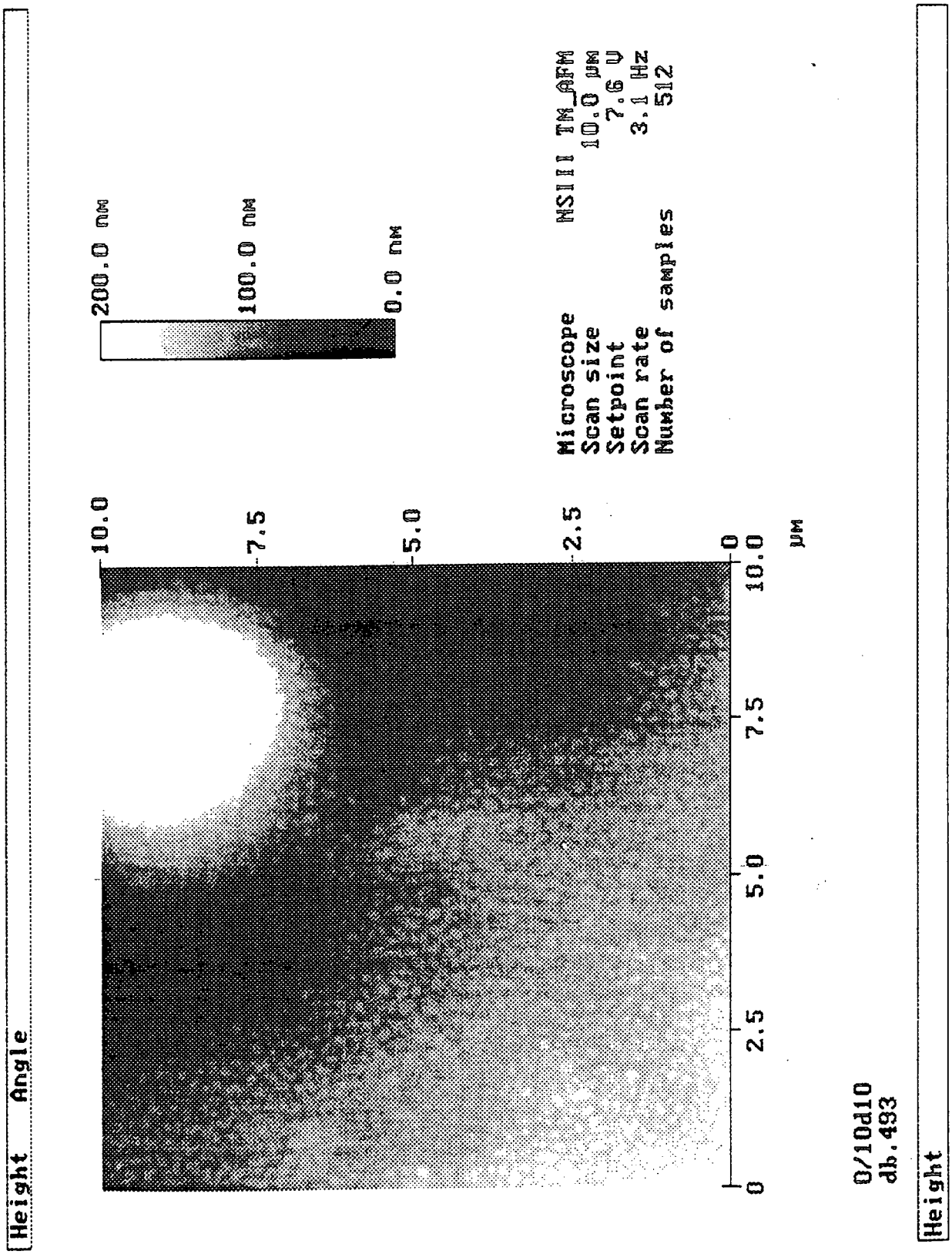

Figure 7.3.2.8: AFM of corona treated 0/10 resin-containing polypropylene sample.

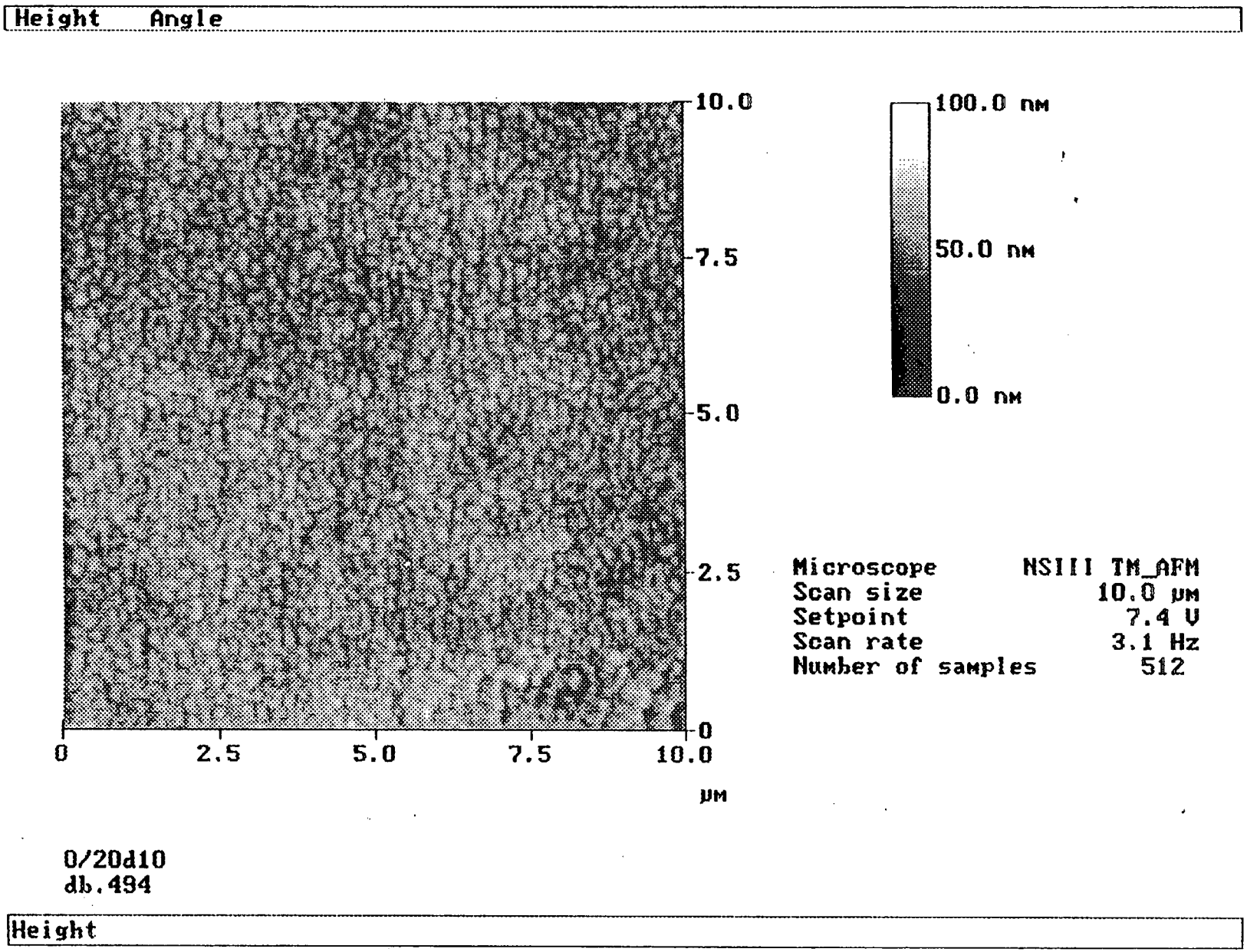

Figure 7.3.2.9: AFM of corona treated 0/20 resin-containing polypropylene sample.

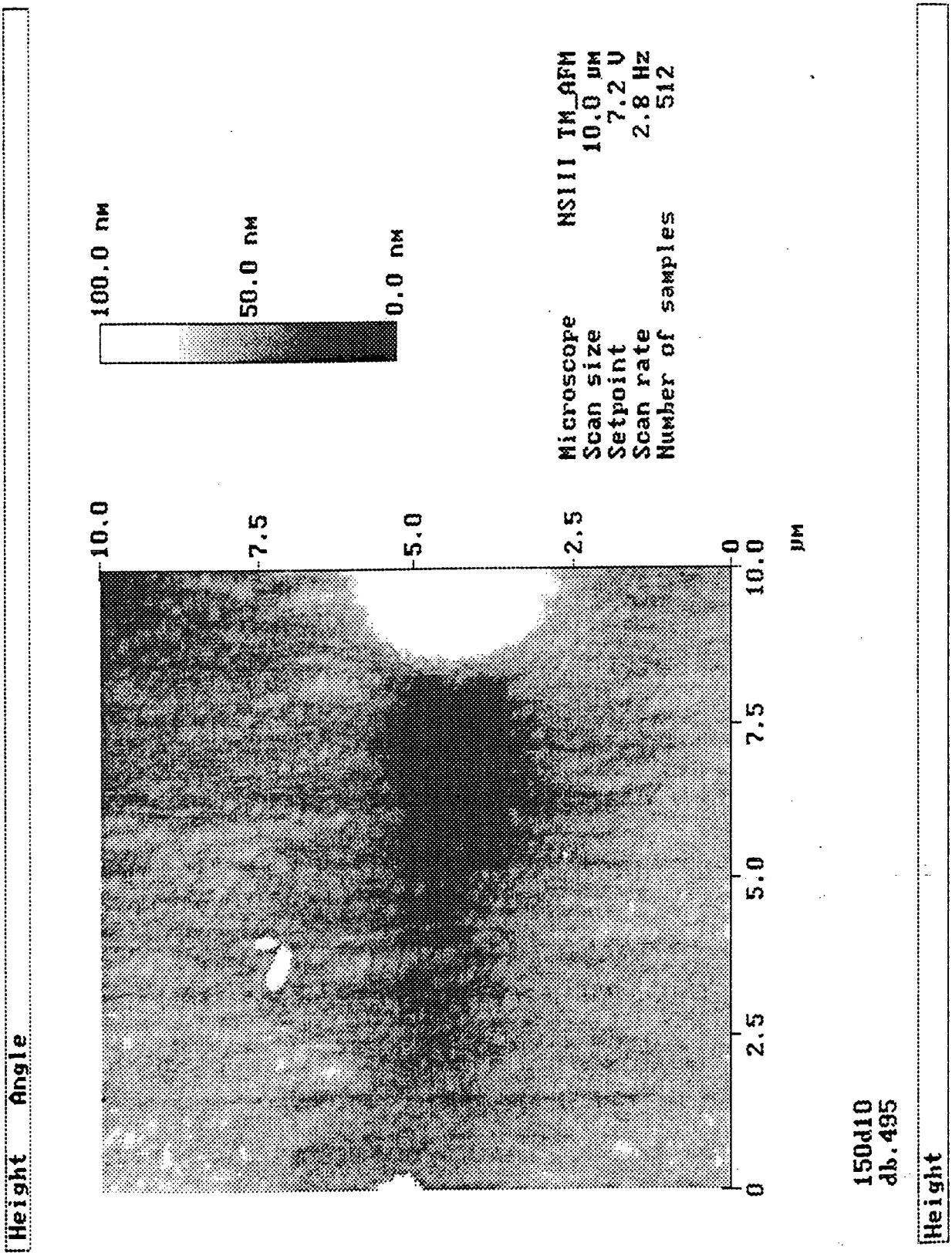

Figure 7.3.2.10: AFM of corona treated 15/0 resin-containing polypropylene sample.

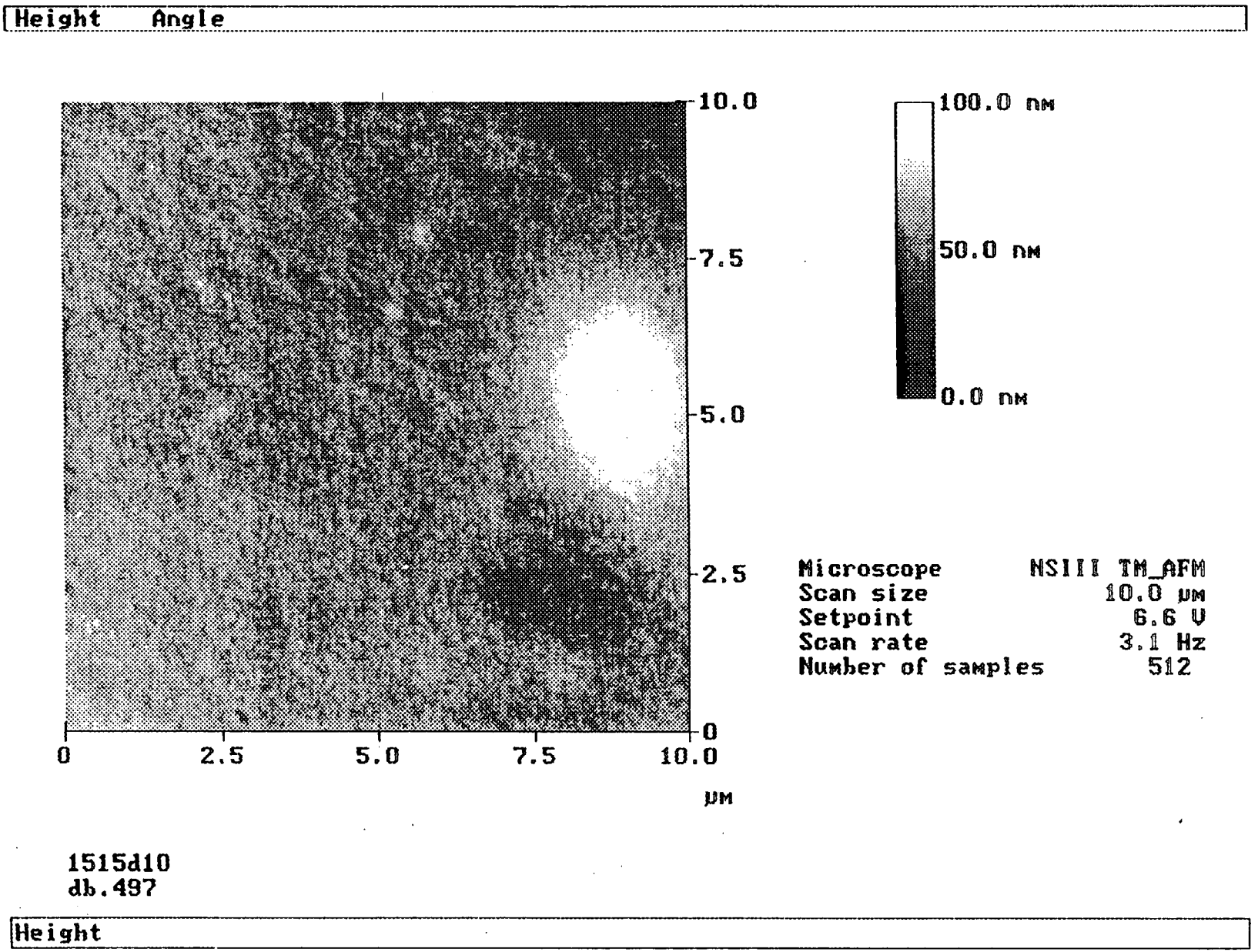

Figure 7.3.2.11: AFM of corona treated 15/15 resin-containing polypropylene sample.

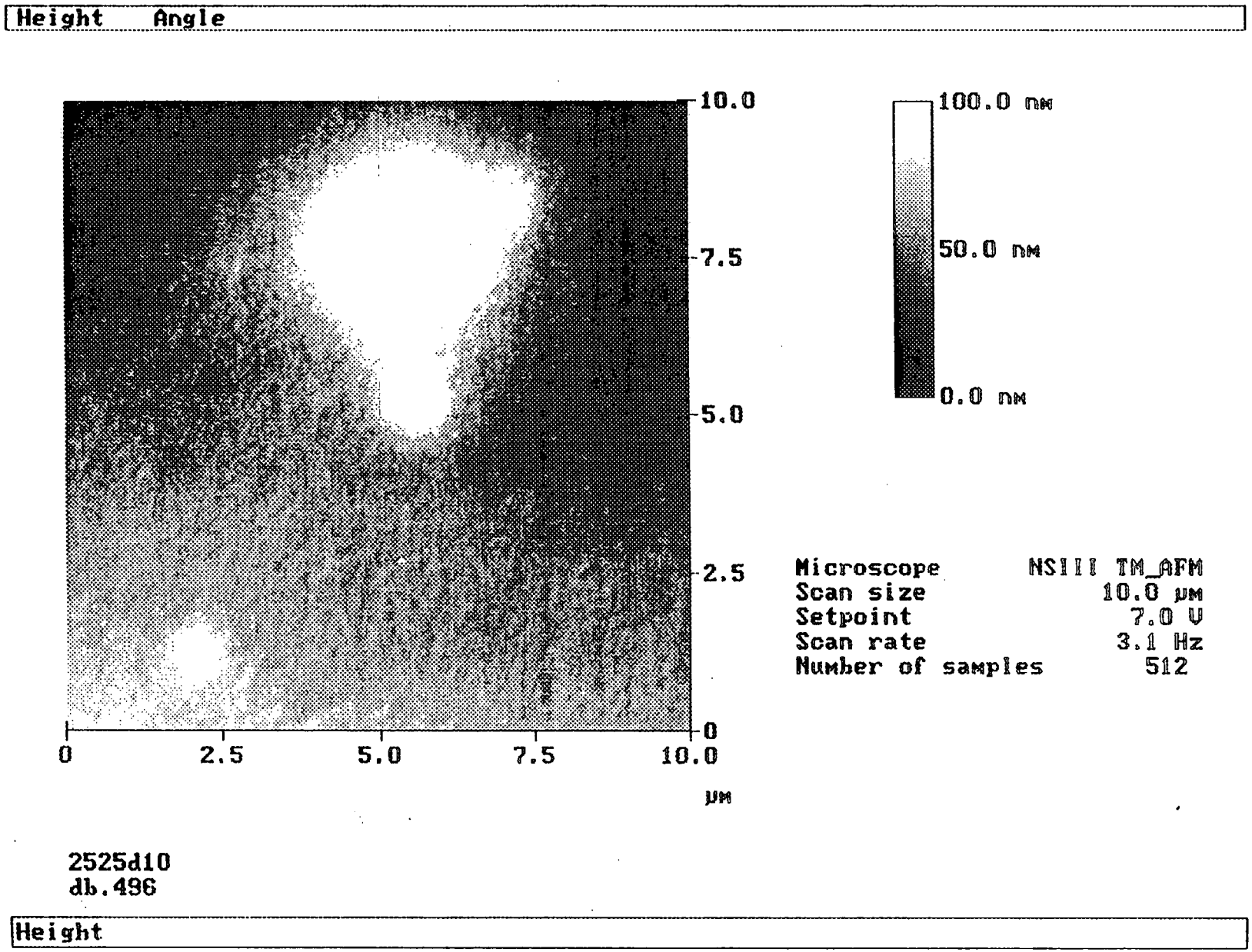

Figure 7.3.2.12: AFM of corona treated 25/25 resin-containing polypropylene sample.

7.4 DISCUSSION

As stated in the introduction to this chapter, it is important to note that this study does not aim to examine the mechanism of corona discharge treatment of polymers (outlined in the introduction). Rather it is to show that corona discharge treatment of this resin-containing polypropylene system allows control of polymer surface morphology.

XPS data for the untreated films oxygenated functionalities is consistent with transfer of low molecular weight oxidized material from the treated side after winding-up of the film when the two sides come into contact. Hence these samples cannot be treated as untreated films *per se.* However, they do represent a useful set of reference samples for the corona discharge treatment as evidenced by their atomic force micrographs which show relatively small differences from those of the untreated, resin-free film.

As resin content is increased in the untreated films, the slight smearing of the AFMs is consistent with the presence of a low molecular weight species, more mobile than the host polymer. The smearing may well be due to disruption of the potentially low molecular weight surface species by the AFM tip.

Corona treatment of the 0/0 PP sample (i.e., no resin) shows the same effects as observed in the literature, namely the introduction of oxygenated functionalities and the removal of these 'globules' by washing. These globules are therefore due to the presence of low molecular weight oxidized material (LMWOM). The overall mechanism responsible for globule formation is not known. It will, however, involve both the formation of the LMWOM and its formation into the observed globules. The wettability of the post-treatment polymer surface by such species will have an effect.

Increasing extents of oxygenation of corona treated samples is achieved by the presence of low molecular weight resin in the base layer. There are several possibilities for the mechanism of this process: firstly, that the presence of resin enhances the reactivity of the polymer surface to the corona treatment; or, secondly, that oxygen incorporation of the surface layer is enhanced by the removal of low molecular weight hydrocarbon moieties.

Putting these chemical effects into context, Strobel *et al.* [7] concluded from their XPS work on corona treated PP that its surface properties do not change significantly with ageing, as opposed to the large changes observed for the more mobile PET polymer. Any differences upon the addition of resin can therefore be thought to be induced by the resin and its properties, most notably its ability to diffuse through the polymer matrix.

AFM results for corona treated samples show that the size of the globular features upon the surface of the polymer films decreases as the proportion of resin increases, and that surface roughnesses increase when resin is present in the coextruded layer only, and decrease when it is present in both layers. This could be accounted for by two (limiting case) mechanisms: firstly, that the presence of resin in the polymer leads to the formation of smaller globules; or, secondly, that these globules are a manifestation of post-treatment migration of low molecular weight species. In this case, the latter hypothesis is favoured since very little effect on the surface morphology was seen for the 15/0 untreated sample whereas a marked reduction of globule size (relative to the 0/0 sample) was observed following corona treatment. As shown in Section 7.1.3, the migration of low energy species to the surface is most likely.

It is noteworthy that the physical and chemical effects of the resin in the corona treated samples cannot be divorced from each other in this work since analyses were performed upon aged samples. In order to probe these

effects a time-dependent study would be required. Monitoring the surface morphology with time after treatment would hopefully allow any diffusion effects of the low molecular weight resin to be observed.

This study throws light upon the difference between the AlO_X coating performance of PET and PP films. PET can be oxide coated to give good gas barrier performance without corona treatment since its surface is already oxygenated. PP on the other hand requires activation of the surface by a corona discharge before conventional metallization can give the required barrier. The further difficulties associated with oxide coating of PP may be derived from the LMWOM material associated with corona treated PP surfaces. This approach, of controlling the surface morphology *via* the addition of resin, will aid the understanding of this phenomenon.

7.5 CONCLUSIONS

- Surface chemistry and morphology of coextruded PP films has been controlled *via* the addition of low molecular weight, saturated hydrocarbon resin.

- Surface oxygen content upon corona treatment is increased by the presence of resin in the base film.

- Corona treatment gives rise to globular features (LMWOM) on the polymer surface as described by previous workers. Their size is reduced by the addition of resin. The greater the resin content, the greater the reduction in globule size.

- Diffusion of low molecular weight species will dictate the final structure. In this case the situation is complicated by the presence of low molecular weight hydrocarbon resin and oxidized material, the individual effects of which cannot be divorced.

- The mechanism by which these globules are formed will require further work.

7.5. REFERENCES

[1] L.-H. Lee, in *New Trends in Physics and Physical Chemistry of Polymers*, Ed. L.-H. Lee, Plenum, New York, 1989, 95.

[2] L.-H. Lee, in *Fundamentals of Adhesion*, Ed. L.-H. Lee, Plenum, New York, 1992, Chapter 1.

[3 B. Leclercq, M. Sotton, A. Baszkin, L. Ter-Minassian-Saraga, *Polymer* **18** (1977), 675.

[4] E. Liston, L. Martinue, M. Wertheimer, *J. Adh. Sci. Technol.* **7** (1993), 1091.

[5] W. Kesting, D. Knittel, T. Bahners, E. Schollmeyer, *Appl. Surf. Sci.* **69** (1993), 299.

[6] J.-Y. Zhang, H. Esrom, U. Kogelschatz, G. Ennig, *Appl. Surf. Sci.* **69** (1993), 299.

[7] M. Strobel, C. S. Lyons, J. M. Strobel, R. S. Kapaun, in *Contact Angle, Wettability and Adhesion*, Ed. K. L. Mittal, VSP, Holland, 1993, 493.

[8] J.-S. Chang, *IEEE Trans. Plasma Sci.* **19** (1991), 1152.

[9] B. Eliasson, *IEEE Trans. Plasma Sci.* **19** (1991), 1063.

[10] B. Eliasson, U. Kogelschatz, *IEEE Trans. Plasma Sci.* **19** (1991), 309.

[11] B. Eliasson, B. Gellert, *J. Appl. Phys.* **68** (1990), 2026.

[12] D. Briggs, in *Practical Surface Analysis by Auger and X-ray Photoelectron Spectroscopy*, Eds. D. Briggs, M. P. Seah, John Wiley & Sons, Chichester, 1983, Chapter 9.

[13] D. Briggs, C. R. Kendall, A. R. Blythe, A. B. Wootton, *Polymer* **24** (1983), 47.

[14] M. Strobel, C. Dunatov, J. M. Strobel, C. S. Lyons, S. J. Perron, M. C. Morgen, *J. Adhesion Sci. Technol.* **3** (1989), 321.

[15] S. D. Razumovskii, A. A. Kefeli, G. E. Zaikov, *Europ. Polym. J.* **7** (1971), 275.

[16] T. N. Pokholak, P. M. Vohlyaev, O. N. Karphukin, S. D. Razumovskii, *Vysokomol. Soedin.* **B11** (1969), 692.

[17] R. M. Overney, R. Luthi, H. Haefke, J. Frommer, E. Meyer, H.-J. Guntherodt, S. Hild, J. Fuhrmann, *Appl. Surf. Sci.* **64** (1993), 197.

[18] R. M. Overney, H.-J. Guntherodt, S. Hild, *J. Appl. Phys.* **75** (1994), 1401.

[19] E. C. Onyiriuka, L. S. Hersh, W. Hertl, *J. Coll. Interf. Sci.* **144** (1991), 98.

[20] D. Briggs, D. G. Rance, C. R. Kendall, A. R. Blythe, *Polymer* **21** (1980), 895.

[21] F. Brochard-Wyart, in *Fundamentals of Adhesion*, Ed. L.-H. Lee, Plenum, New York, 1992, Chapter 6.

[22] P. J. Mills, P. F. Green, C. J. Palmstrom, J. W. Mayer, E. J. Kramer, *Appl. Phys. Lett.* **45** (1984), 957.

[23] F. Brochard, P. G. de Gennel, *Europhys. Lett.* **1** (1986), 221.

[24] E. A. Jordan, R. C. Ball, A. M. Donald, L. J. Fetters, R. A. L. Jones, J. Klein, *Macromolecules* **21** (1988), 235.

[25] D. W. van Krevelen, *Properties of Polymers*, 3rd Edition, Elsevier, Amsterdam, Chapter 8.

CHAPTER 8

CONCLUSIONS

8.1 INTRODUCTION

This final chapter brings together the work described in the bulk of the thesis, and describes this author's interpretation and understanding of the whole project. Potential mechanisms consistent with the experimental data are presented, and future areas of work are discussed.

8.2 COATING CHEMISTRY

Chapters 1 and 3 contain information concerning the *in situ* and post-production oxidized chemistries of the gas barrier composites. Figure 8.2.1 is a *schematic* mechanism of the chemistries of the coatings consistent with experimental data.

Case (a) is that of Al/PET. Literature data, Chapter 3, shows that Al reacts with PET to give an interfacial complex. The remainder of the layer is metallic aluminium, possibly with some oxide species incorporated at grain boundaries, Chapters 4 and 5. Upon post-production aerial oxidation both the surface and interfacial metal species react. Those at the surface oxidize to give an oxide species while those at the interface yield a substoichiometric product due to their partial reaction with the polymer to form the interfacial complex. Oxidizing species can permeate through the base polymer to the interface. The resultant layer is therefore substantially metallic.

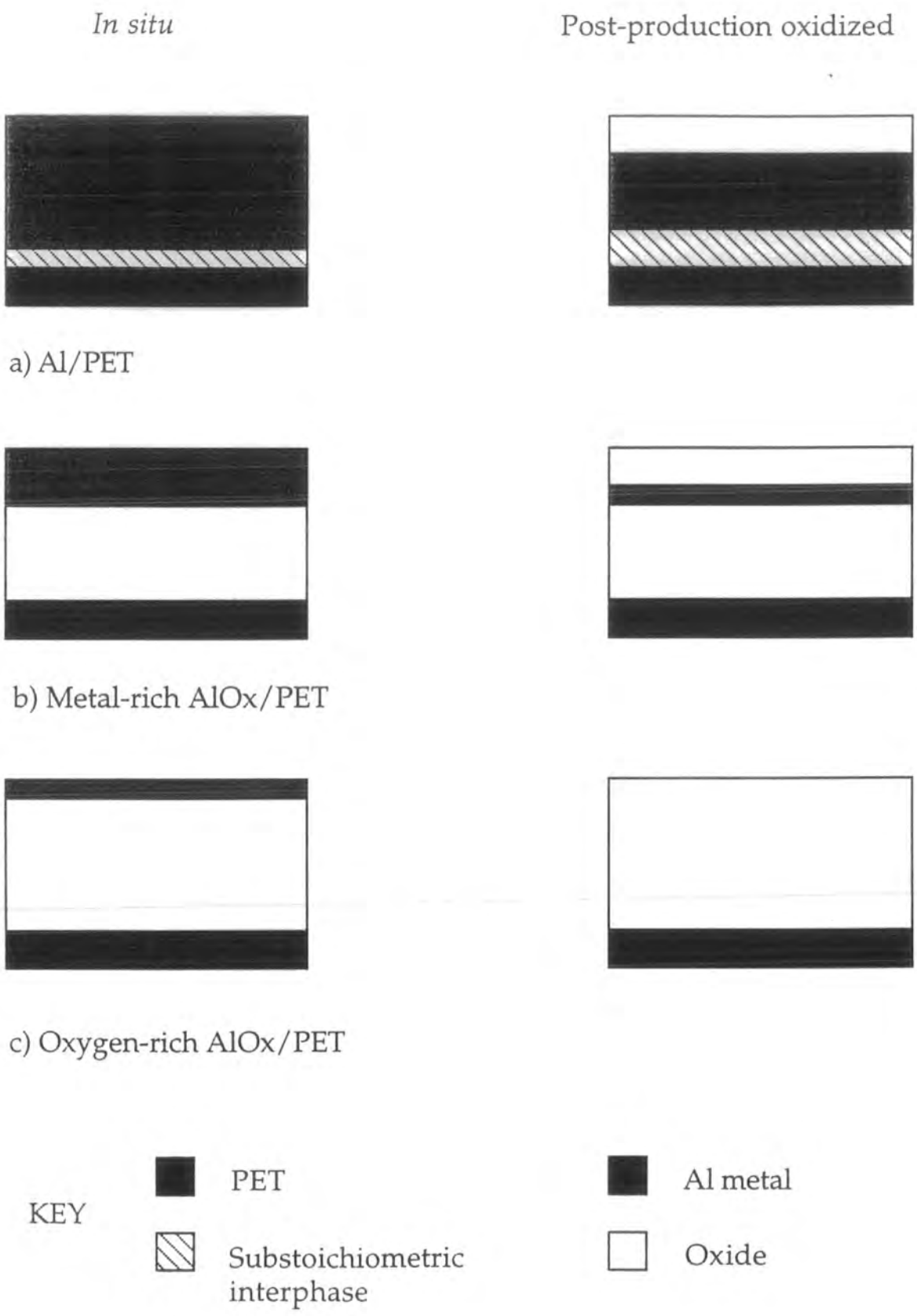

Figure 8.2.1: Schematic mechanism of coating chemistry.

Upon the introduction of oxygen into the deposition process, metal-rich AlO_X/PET, case (b), gas phase reactions occur and lead to the formation of oxide at the coating/polymer interface, Chapter 3. Metal present in this layer is observed on top of the oxide as if the deposition chamber was zoned. Aerial oxidation of this layer leads to the observation of oxidize at the surface. The thickness of the initially deposited metal-containing portion of the coating is therefore not much greater than the depth of aerial oxidation. No comment concerning the state of the metal prior to atmospheric exposure can be made although it is present as metal clusters after exposure.

At higher oxygen flow rates, oxygen-rich AlO_X/PET, case (c), gas phase reactions again lead to the formation of a substantially oxide layer. OD data, Chapter 1, indicates that the metal content of the *in situ* oxygen-rich layer is the same as the *ex situ* metal-rich one. The thickness of this metal layer is less than the depth of aerial oxidation. Post-production aerial oxidation would account for the fact that none of the metal is observed.

8.3 COATING MORPHOLOGY

At large scales (> 10 μm) the morphologies of the AlO_X layers are dictated by the base film morphology. No defects (e.g., pinholes, cracks) were found apart from protrusions assigned to filler particles from the base film. These can be thought of as defects in the layer.

All three AlO_X films exhibit the same globular morphology at higher magnifications (~1 μm scale). This is found in the literature for films grown under single and multiple collision conditions, Chapters 4 and 5. Without direct evidence to determine whether particles are formed in the gas phase or not, no definite statement can be made concerning the origin of these morphologies.

Background information on the deposition process does provide some useful information. Al/PET cannot be deposited evenly at the aluminium wire feed rates employed in the production of the other two coatings. This is because the deposit does not evenly cover the substrate. Introduction of oxygen leads to an even coating. Gas phase interactions are therefore important. The nature of the product of these interactions is not clear, and may be either molecular or particulate in nature.

No precise comparison can be made between the Al/PET layer and the metal- and oxygen-rich AlO_X/PET layers since they are deposited at different evaporation rates of aluminium. However, the morphologies are still surprisingly similar.

Direct comparison between the metal- and oxygen-rich films shows that whatever mechanism is responsible for the formation of the globular features, higher degrees of oxygen introduction into the deposition process result in smaller features. A classical explanation of this situation would be that the deposited metal and/or substoichiometric oxide species (*i.e.*, not Al_2O_3) have reduced mobility in a more oxidizing environment.

8.4 GAS BARRIER

Two effects must be considered here: the chemistry of the layer; and filler particles in the base film protruding through the deposited layer.

Helium gas was found to be the most sensitive gas to differences in the layers, and was therefore used as a probing tool.

Al/PET and metal-rich AlO_X/PET both exhibit similar helium gas transport properties, and they both contain a metal/oxide interface in the subsurface regions of their coatings. The interfacial chemistries are different. It is proposed that it is the metal/oxide interface, resulting in a

compressive stress, which closes microscopic gaps between the deposited grains/particles, thus inhibiting the flow of helium. The transport of other gases, argon and oxygen, are not affected by these differences.

Oxygen-rich AlO_x/PET lacks the metal/oxide interface and exhibits different, and greater, helium gas transport properties than the metal/oxide interface containing variants.

As for the effect of filler particles in the base film protruding through the deposited layer, this will be the same for all films since they were all deposited onto the same substrate. If such a mechanism is in operation then it is likely to give a 'baseline' effect, *i.e.*, the observed gas transport properties will be the summation of contributions from both layer chemistry and filler particle protrusions.

8.5 GAS BARRIER DETERIORATION

This phenomenon is dependent upon both the interfacial and surface chemistries of the barrier layers.

The interfacial structure dictates the point at which the interphase fails upon uniaxial stretching. The more ductile, substoichiometric Al/PET interphase can withstand greater stretching than the oxide-like interphase of metal- and oxygen-rich AlO_x/PET. The presence of metal in the subsurface region of the metal-rich variant allows this composite to undergo slightly more stretching prior to failure than its purely oxide counterpart since it 'glues' the component oxide particles together. This idea can be elucidate by reference to Figure 8.2.1.

8.6 POLYPROPYLENE SURFACE ENGINEERING

Addition of varying amounts of low molecular weight saturated hydrocarbon resin to, and subsequent corona treatment of, coextruded PP films leads to control over the characteristic globular surface morphology as observed by AFM. Chemistry and morphology of the low molecular weight oxidized material has been controlled. The exact mechanism is not clear since diffusion effects are complicated by the oxidation and fragmentation processes occurring upon corona treatment. However, any effects are likely to be driven by the lowering of surface energy associated with the diffusion of low surface energy components to the surface.

8.7 FUTURE WORK

This section will outline some of the next steps that could be taken towards a better understanding of the effects observed during the course of this project.

The chemistry at the coating/polymer interfaces could be elucidated by firstly performing *in situ* analysis of deposited aluminium oxide at low coverages on PET to complement the existing literature data on the deposition of aluminium. Also of importance in this work has been the process of aerial oxidation since this gives rise to the chemical structure that finds practical application. *In situ* deposition of aluminium and aluminium oxide onto PET followed by controlled exposure to air and/or oxygen would permit chemical changes at the interface to be observed. Both of these approaches could be extended to other polymers.

As for the gas barrier, coating morphology and state of the metal in these coatings, production of coatings under a more finely divided range of

oxygen flow rates would determine the evolution of the coating from metallized to oxide coated, and hopefully observe the point at which behaviour changes (such as gas barrier) occur.

Mechanical properties of the composite structures have played a role in the process of gas barrier deterioration. Full characterization of the mechanical properties of these systems, such as the changes in force *versus* elongation curves upon coating deposition and differences caused by changes in coating chemistry, may shed light upon the differences in processability between the films deposited onto PET, and, perhaps, the difficulty of oxide coating PP.

Corona treatment of polymers is an area of great interest. There are two main approaches to future work in this area. Firstly, further study of the globular material formed upon treatment and, secondly, studies of the wetting of polymer surfaces by low molecular weight oxidized material.

To put the study of globular features into context a little background is necessary. When first studied, surface modification of polymers was thought to be a purely surface effect and was supported by XPS. The development of atomic force microscopy and its application to polymer surfaces has clearly shown that the changes effected by corona discharge treatment are on a much larger scale than the XPS sampling depth (a few nanometres). The modification mechanism has now moved away from a purely surface phenomenon. Application of conventional techniques to these films and their low molecular weight material, such as nuclear magnetic resonance spectroscopy, especially of the solid state, would show the extent of modification relative to the bulk of the film. This would give researchers a true perspective of the extent of modification.

The second area of interest, the wetting of polymer surfaces by low molecular weight oxidized material, would be an area of model studies for the surface morphology effects observed by AFM and XPS. By varying the

chemistry of both the base film and the wetting layer it may be possible to reproduce the structures found for corona discharge treated films, or at least to understand the effects of these variables.

APPENDIX

COLLOQUIA, LECTURES AND SEMINARS FROM INVITED SPEAKERS

COURSES ATTENDED

- Chemistry Department induction courses;
- Laboratory techniques, 6 lectures;
- Basic electronics, 6 lectures.

LECTURES (* denotes attendance)

1991

Sept. 17 — Prof. R. D. Fischer, University of Hamburg, Germany
Organo-f-element Systems to Organo-Main-Group Polymers

October 17 — Dr. J. A. Salthouse, University of Manchester
Son et Lumiere - a Demonstration Lecture

October 31 — Dr. R. Keeley, Metropolitan Police Forensic Science
Modern Forensic Science

Nov. 6 — Prof. B. F. G. Johnson, Edinburgh University
Cluster-Surface Analogies*

Nov. 7 — Dr. A. R. Butler, University of St. Andrews
Traditional Chinese Herbal Drugs: a Different Way of Treating Disease

Nov. 13 — Prof. D. Gani, University of St. Andrews
The Chemistry of PLP-dependent Enzymes*

Nov. 20 — Dr. R. M. O'Ferral, University College, Dublin
Some Acid-catalyzed Rearrangements in Organic Chemistry*

Nov. 28 Prof. I. M. Ward, IRC in Polymer Science, University of Leeds
The Science and Technology of Orientated Polymers

Dec. 4 Prof. R. Grigg, Leeds University
Palladium-catalyzed Cyclization and Ion Capture Processes*

Dec. 5 Dr. W. D. Cooper, Shell Research
Colloid Science, Theory and Practice*

Dec. 5 Prof. A. L. Smith, ex Unilever
Soap, Detergents and Black Puddings*

1992

January 22 Dr. K. D. M Harris, University of St. Andrews
Understanding the Properties of Solid Inclusion Compounds*

January 29 Dr. A. Holmes, Cambridge University
Cycloaddition Reactions in the Service of the Synthesis of Piperidine and Indolizidine Natural Products*

January 30 Dr. M. Anderson, Shell Research
Recent Advances in the Safe and Selective Chemical Control of Insect Pests

February 12 Prof. D. E. Fenton, Sheffield University
Polynuclear Complexes of Molecular Clefts as Models for Copper Biosites

February 13 Dr. J. Saunders, Glaxo Group Research
Molecular Modelling in Drug Discovery

February 19 Prof. E. J. Thomas, Manchester University
Applications of Organostannanes to Organic Synthesis

February 20 Prof. E. Vogel, University of Cologne
Porphyrins, Molecules of Interdisciplinary Interest

February 25 Prof. J. F. Nixon, University of Sussex
PHosphalkynes, New Building Blocks in Inorganic and Organometallic Chemistry

March 5 Dr. N. C. Billingham, University of Sussex
Degradable Plastic - Myth or Magic

March 11 Dr. S. E. Thomas, Imperial College
Recent Advances in Organoiron Chemistry

March 12 Dr. R. A. Hann, ICI Imagedata
Electronic Photography - An Image of the Future

March 18 Dr. H. Maskill, Newcastle University
Concerted or Step-wise Fragmentation in a Deamination-type Reaction

April 7 D. M. Knight, University of Durham
Interpreting Experiments: the Beginning of Electrochemistry*

May 6 Prof. T. Marder, University of Waterloo
Metal-catalyzed Alkene Hydroboration

May 6 Dr. J. C. Gehret, Ciba-Geigy
Some Aspects of Industrial Agrochemical Research

October 15 Dr M. Glazer & Dr. S. Tarling, Oxford University & Birbeck College, London
It Pays to be British! - The Chemist's Role as an Expert Witness in Patent Litigation

October 20 Dr. H. E. Bryndza, Du Pont Central Research
Synthesis, Reactions and Thermochemistry of Metal (Alkyl) Cyanide Complexesand Their Impact on Olefin Hydrocyanation Catalysis

October 22 Prof. A. Davies, University College London

The Behaviour of Hydrogen as a Pseudometal*

October 28 Dr. J. K . Cockcroft, University of Durham
Recent Developments in Powder Diffraction

October 29 Dr. J. Emsley, Imperial College, London
The Shocking History of Phosphorus

Nov. 4 Dr. T. P. Kee, University of Leeds
Synthesis and Co-ordination Chemistry of Silylated Phosphites

Nov. 5 Dr. C. J. Ludman, University of Durham
Explosions, A Demonstration Lecture

Nov. 11 Prof. D. Robins, Glasgow University
Pyrrolizidine Alkaloids : Biological Activity, Biosynthesis and Benefits

Nov. 12 Prof. M. R. Truter, University College, London
Luck and Logic in Host - Guest Chemistry

Nov. 18 Dr. R. Nix, Queen Mary College, London
Characterisation of Heterogeneous Catalysts*

Nov. 25 Prof. Y. Vallee. University of Caen
Reactive Thiocarbonyl Compounds

Nov. 25 Prof. L. D. Quin, University of Massachusetts, Amherst
Fragmentation of Phosphorous Heterocycles as a Route to Phosphoryl Species with Uncommon Bonding

Nov. 26 Dr. D. Humber, Glaxo, Greenford
AIDS - The Development of a Novel Series of Inhibitors of HIV

Dec. 2 Prof. A. F. Hegarty, University College, Dublin
Highly Reactive Enols Stabilised by Steric Protection

Dec. 2 Dr. R. A. Aitken, University of St. Andrews
The Versatile Cycloaddition Chemistry of $Bu_3P.CS_2$

Dec. 3 Prof. P. Edwards, Birmingham University
The SCI Lecture - What is Metal?

Dec. 9 Dr. A. N. Burgess, ICI Runcorn
The Structure of Perfluorinated Ionomer Membranes*

1993

January 20 Dr. D. C. Clary, University of Cambridge
Energy Flow in Chemical Reactions*

January 21 Prof. L. Hall, Cambridge
NMR - Window to the Human Body

January 27 Dr. W. Kerr, University of Strathclyde
Development of the Pauson-Khand Annulation Reaction : Organocobalt Mediated Synthesis of Natural and Unnatural Products

January 28 Prof. J. Mann, University of Reading
Murder, Magic and Medicine

February 3 Prof. S. M. Roberts, University of Exeter
Enzymes in Organic Synthesis

February 10 Dr. D. Gillies, University of Surrey
NMR and Molecular Motion in Solution*

February 11 Prof. S. Knox, Bristol University
The Tilden Lecture Organic Chemistry at Polynuclear Metal Centres

February 17 Dr. R. W. Kemmitt, University of Leicester
Oxatrimethylenemethane Metal Complexes

February 18 Dr. I. Fraser, ICI Wilton
Reactive Processing of Composite Materials

February 22 Prof. D. M. Grant, University of Utah
Single Crystals, Molecular Structure, and Chemical-Shift Anisotropy

February 24 Prof. C. J. M. Stirling, University of Sheffield
Chemistry on the Flat-Reactivity of Ordered Systems

March 10 Dr. P. K. Baker, University College of North Wales, Bangor
Chemistry of Highly Versatile 7-Coordinate Complexes

March 11 Dr. R. A. Y. Jones, University of East Anglia
The Chemistry of Wine Making

March 17 Dr. R. J. K. Taylor, University of East Anglia
Adventures in Natural Product Synthesis

March 24 Prof. I. O. Sutherland, University of Liverpool
Chromogenic Reagents for Cations*

May 13 Prof. J. A. Pople, Carnegie-Mellon University, Pittsburgh, USA
Applications of Molecular Orbital Theory*

May 21 Prof. L. Weber, University of Bielefeld
Metallo-phospha Alkenes as Synthons in Organometallic Chemistry

June 1 Prof. J. P. Konopelski, University of California, Santa Cruz
Synthetic Adventures with Enantiomerically Pure Acetals

June 2 Prof. F. Ciardelli, University of Pisa
Chiral Discrimination in the Stereospecific Polymerisation of Alpha Olefins

June 7 Prof. R. S. Stein, University of Massachusetts

Scattering Studies of Crystalline and Liquid Crystalline Polymers

June 16 — Prof. A. K. Covington, University of Newcastle
Use of Ion Selective Electrodes as Detectors in Ion Chromatography

June 17 — Prof. O. F. Nielsen, H. C. Ørsted Institute, University of Copenhagen
Low-Frequency IR - and Raman Studies of Hydrogen Bonded Liquids

Sept. 13 — Prof. Dr. A.D. Schlüter, Freie Universität Berlin, Germany
Synthesis and Characterisation of Molecular Rods and Ribbons

Sept. 13 — Dr. K.J. Wynne, Office of Naval Research, Washington, USA
Polymer Surface Design for Minimal Adhesion

Sept. 14 — Prof. J.M. DeSimone, University of North Carolina, Chapel Hill, USA
Homogeneous and Heterogeneous Polymerisations in Environmentally Responsible Carbon Dioxide

Sept. 28 — Prof. H. Ila, North Eastern Hill University, India
Synthetic Strategies for Cyclopentanoids via Oxoketene Dithioacetals

October 4 — Prof. F.J. Feher, University of California, Irvine, USA
Bridging the Gap between Surfaces and Solution with Sessilquioxanes

October 14 — Dr. P. Hubberstey, University of Nottingham
Alkali Metals: Alchemist's Nightmare, Biochemist's Puzzle and Technologist's Dream

October 20 — Dr. P. Quayle, University of Manchester
Aspects of Aqueous ROMP Chemistry

October 21 Prof. R. Adams, University of South Carolina, USA
Chemistry of Metal Carbonyl Cluster Complexes :
Development of Cluster Based Alkyne Hydrogenation Catalysts

October 27 Dr. R.A.L. Jones, Cavendish Laboratory, Cambridge
Perambulating Polymers*

Nov. 10 Prof. M.N.R. Ashfold, University of Bristol
High Resolution Photofragment Translational Spectroscopy : A New Way to Watch Photodissociation*

Nov. 17 Dr. A. Parker, Rutherford Appleton Laboratory, Didcot
Applications of Time Resolved Resonance Raman Spectroscopy to Chemical and Biochemical Problems*

Nov. 24 Dr. P.G. Bruce, University of St. Andrews
Structure and Properties of Inorganic Solids and Polymers

Nov. 25 Dr. R.P. Wayne, University of Oxford
The Origin and Evolution of the Atmosphere

Dec. 1 Prof. M.A. McKervey, Queen's University, Belfast
Synthesis and Applications of Chemically Modified Calixarenes

Dec. 8 Prof. O. Meth-Cohn, University of Sunderland
Friedel's Folly Revisited - A Super Way to Fused Pyridines

Dec. 16 Prof. R.F. Hudson, University of Kent
Close Encounters of the Second Kind

1994

January 26 Prof. J. Evans, University of Southampton
Shining Light on Catalysts*

February 2 Dr. A. Masters, University of Manchester

Modelling Water Without Using Pair Potentials

February 9 Prof. D. Young, University of Sussex
Chemical and Biological Studies on the Coenzyme Tetrahydrofolic Acid

February 16 Prof. K.H. Theopold, University of Delaware, USA
Paramagnetic Chromium Alkyls : Synthesis and Reactivity

February 23 Prof. P.M. Maitlis, University of Sheffield
Across the Border : From Homogeneous to Heterogeneous Catalysis*

March 2 Dr. C. Hunter, University of Sheffield
Noncovalent Interactions between Aromatic Molecules

March 9 Prof. F. Wilkinson, Loughborough University of Technology
Nanosecond and Picosecond Laser Flash Photolysis

March 10 Prof. S.V. Ley, University of Cambridge
New Methods for Organic Synthesis

March 25 Dr. J. Dilworth, University of Essex
Technetium and Rhenium Compounds with Applications as Imaging Agents

April 28 Prof. R. J. Gillespie, McMaster University, Canada
The Molecular Structure of some Metal Fluorides and Oxofluorides: Apparent Exceptions to the VSEPR Model.

May 12 Prof. D. A. Humphreys, McMaster University, Canada
Bringing Knowledge to Life